

# Characterization and tracking of the three-dimensional translational motion and rotation of single nanoparticles using a fiber-based microcavity with high finesse

Larissa Anne-Marie Kohler



Karlsruhe 2021



Characterization and tracking of the  
three-dimensional translational motion  
and rotation of single nanoparticles  
using a fiber-based microcavity with  
high finesse

Zur Erlangung des akademischen Grades einer  
DOKTORIN DER NATURWISSENSCHAFTEN (Dr. rer. nat.)

von der KIT-Fakultät für Physik des  
Karlsruher Instituts für Technologie (KIT)  
angenommene

DISSERTATION

von

M.Sc. Larissa Anne-Marie Kohler

Erster Gutachter: Prof. Dr. David Hunger  
Zweiter Gutachter: Prof. Dr. Heinz Kalt  
Tag der mündlichen Prüfung: 16.07.2021

## Abstract

Sophisticated new sensor techniques have to be developed to enable the detection of the temporal dynamics of single nanoparticles and molecules. Some of the new microscopy techniques are based on nanoparticle labeling, achieving high sensitivity on the single nanometer scale, but also changing the nanoparticle's natural behavior. In this work, a fiber-based Fabry-Pérot (FP) microcavity with high finesse is presented, which allows the detection of unlabeled nanoparticles. Single nanoparticle resolution is achieved by forcing the light to thousands of round trips between two high-reflective mirrors of micrometer size and consequently enhancing the interaction between light and nanoparticle.

So far, fiber-based FP cavities in air, vacuum and liquid helium have been reported in the past. In order to enable single nanoparticle measurements in liquids, two different microfluidic channels are demonstrated. Both channels allow an easy integration of the fiber-based FP cavity, provide a controllable laminar flow, and the measurement of small sample volumes. Furthermore the microfluidic channel and the integrated FP cavity are embedded in a sensing platform, that provides a high passive stability of  $\sim 1$  pm and a low root-mean-square measurement noise of 0.39 pm. Combined with a high Cooperativity of the FP cavity in water of  $C \sim Q\lambda_0^3/(n_m^3 V_m) = 2.1 \cdot 10^4$  single SiO<sub>2</sub> nanospheres with a hydrodynamic radius down to 11.7 nm can already be detected. In this work, it is shown that the FP cavity allows the detection of hundreds of single SiO<sub>2</sub> nanosphere transit events within a few hours. From the derived statistical data, the SiO<sub>2</sub> nanosphere's mean polarizability, as well as the mean effective refractive index, are deduced. Here, the first important finding is the detection of the nanosphere's expanded size in pure water originating from a hydrate shell. This allows the estimation of the mean thickness as well as the mean refractive index of the hydrate shell of different SiO<sub>2</sub> nanosphere samples. Besides, the effect of salt on the hydrate shell is investigated. Already small salt concentrations presumably lead to a suppression of the formation of the hydrate shell and give indications of the significantly lower polarizability of the bare nanosphere. Furthermore, by improving the measurement time resolution, the polarizability of a single SiO<sub>2</sub> nanosphere is determined. In addition, the autocorrelation of the dispersive signal of several SiO<sub>2</sub> nanosphere transit events is compared with the theoretical numerical autocorrelation of a punctiform nanosphere and the Monte Carlo simulated autocorrelation of several nanosphere transit events with expanded size. As a result, a purely diffusive motion is identified.

Completely new is the detection of the three-dimensional Brownian motion of a single nanosphere with a microcavity. By the simultaneous measurement of the dispersive shifts of the fundamental and two higher-order transverse modes, the three-dimensional coordinate of the nanosphere can be derived with a high spatial resolution of 8 nm and a high temporal resolution of 0.3 ms. This is first analyzed by simulations and then demonstrated with measured signals. From the three-dimensional track, the nanosphere's diffusivity, as well

as its hydrodynamic radius, is deduced. The rotational diffusion of single anisotropically shaped nanoparticles is measured by the polarization-split fundamental mode with a high temporal resolution of 0.07 ms. Already nanospheres with a specified roundness of  $>0.98$  can be investigated in their rotational diffusion, showing that this detection method is highly sensitive.

The presented FP microcavity already achieves a sensitivity, which allows the detection of different molecules like viruses, ribosomes, and exosomes. Therefore, it is a promising candidate for a future detection of the dynamics of single, unlabeled molecules with a small molecular mass.

# Contents

<b>Abstract</b> . . . . .	<b>i</b>
<b>1. Nanoparticles and their detection on a single particle level</b> . . . . .	<b>1</b>
1.1. Nanoparticles in our everyday life . . . . .	1
1.2. Methods for the detection of single nanoparticles dispersed in liquids . . . . .	3
1.2.1. Fluorescence microscopes . . . . .	3
1.2.2. Interference scattering microscopy . . . . .	4
1.2.3. Optical cavities . . . . .	5
1.3. Fiber-based Fabry-Pérot microcavity with high finesse . . . . .	10
1.4. Scope of this work . . . . .	12
<b>2. Fundamentals of single polarizable nanoparticles inside a fiber-based Fabry-Pérot microcavity</b> . . . . .	<b>15</b>
2.1. Fiber-based Fabry-Pérot cavity modes . . . . .	15
2.1.1. Planar cavity mirrors . . . . .	16
2.1.2. Spherical cavity mirrors . . . . .	18
2.1.3. Birefringent cavity mirrors . . . . .	20
2.2. Nanoparticles in a homogeneous electrical field . . . . .	22
2.2.1. Nanosphere . . . . .	22
2.2.2. Anisotropically shaped nanoparticle . . . . .	24
2.3. Interaction of nanoparticles with a cavity mode . . . . .	26
2.3.1. Scattering and absorption losses . . . . .	26
2.3.2. Resonance frequency shift . . . . .	28
2.3.3. Hydrate shell of quartz glass nanospheres dispersed in water . . . . .	31
2.4. Simulation of the nanoparticle's translational diffusion probed by a Fabry-Pérot microcavity . . . . .	33
2.4.1. Simulation of the measured signal generated by a nanoparticle diffusing in water and verification of the tracking algorithm . . . . .	34
2.4.2. Mean squared displacement . . . . .	39
2.5. Autocorrelation function for a punctiform particle moving through the Fabry-Pérot standing-wave light field . . . . .	42
2.6. Rotational diffusion of an anisotropic, homogeneous nanoparticle probed by a Fabry-Pérot cavity with birefringent mirrors . . . . .	45
<b>3. Realization and performance of the Fabry-Pérot microcavity sensing platform</b> . . . . .	<b>49</b>
3.1. The core of the Fabry-Pérot sensor . . . . .	49
3.1.1. Fiber-based Fabry-Pérot cavity . . . . .	50

3.1.2.	Microfluidic channel . . . . .	56
3.2.	Combining all elements into the Fabry-Pérot sensing platform . . . . .	60
3.2.1.	Cavity A . . . . .	60
3.2.2.	Cavity B . . . . .	62
3.2.3.	Cavity C . . . . .	63
3.3.	Detection of the cavity finesse . . . . .	65
3.3.1.	Measurement of the full width half maximum . . . . .	66
3.3.2.	Measurement of the cavity length . . . . .	66
3.4.	Detection of nanoparticle signals . . . . .	70
3.4.1.	Preparation of the nanoparticle colloidal solution . . . . .	70
3.4.2.	Optical and electrical components . . . . .	71
3.4.3.	Measurement principle . . . . .	72
3.5.	Resolution limit of the different cavity versions . . . . .	74
3.5.1.	Passive stability and measurement noise . . . . .	75
3.5.2.	Resolution limit . . . . .	77
3.6.	Cavity geometries and signal enhancement of each cavity version . . . . .	79
3.7.	Discussion . . . . .	79
<b>4.</b>	<b>Properties of quartz glass nanospheres dispersed in liquids and probed by the Fabry-Pérot cavity light field . . . . .</b>	<b>81</b>
4.1.	Single nanoparticle transit events . . . . .	82
4.2.	Quantitative evaluation of the nanoparticle optical properties . . . . .	85
4.2.1.	Polarizability and effective refractive index . . . . .	85
4.2.2.	Refractive index of the hydrate shell . . . . .	89
4.2.3.	Discussion . . . . .	89
4.3.	Optical properties of a single quartz glass nanosphere . . . . .	91
4.4.	The impact of salt ions on the formation of the hydrate shell . . . . .	93
4.4.1.	Hydrate shell of 25 nm quartz glass nanoparticles . . . . .	95
4.4.2.	Hydrate shell of 60 nm quartz glass nanoparticles . . . . .	97
4.5.	Towards the determination of the hydrodynamic radius via the autocorrelation of the frequency shift signal . . . . .	98
4.6.	Discussion . . . . .	101
<b>5.</b>	<b>Three-dimensional tracking of a single quartz glass nanoparticle . . . . .</b>	<b>103</b>
5.1.	Reduction of the measurement noise by two probe lasers . . . . .	103
5.2.	Selection of a single transit event . . . . .	104
5.3.	Characterization of the cavity and tracking resolution . . . . .	105
5.4.	Three-dimensional track and mean squared displacement . . . . .	108
5.5.	Discussion . . . . .	111
<b>6.</b>	<b>Towards the determination of the rotational diffusion of nanoparticles . . . . .</b>	<b>113</b>
6.1.	Rotational diffusion of 25 nm quartz glass nanoparticles . . . . .	114
6.2.	Rotational diffusion of 60 nm quartz glass nanoparticles . . . . .	118
6.3.	Discussion . . . . .	121

---

<b>7. Summary and outlook</b>	<b>123</b>
7.1. Characterization of the cavity	123
7.2. Characterization of different quartz glass nanospheres	124
7.3. Three-dimensional tracking of the Brownian motion	125
7.4. Rotational diffusion	125
7.5. Outlook	126
<b>A. Appendix</b>	<b>129</b>
A.1. The first fiber-based Fabry-Pérot cavity for sensing in liquids	129
A.2. Construction of the core sensor	130
A.2.1. Protection of electronics from getting wet	130
A.2.2. Construction of the different cavity versions	132
A.3. Pressure inside the microfluidic channel	136
A.4. CAD design for the electric current and temperature control of the laser	137
A.5. Quartz glass nanoparticle samples	139
A.5.1. Sample A	139
A.5.2. Sample B	142
A.5.3. Sample C	145
A.6. Raw data of the single quartz glass nanosphere transit event	147
A.7. Cavity preparation and occurring sensor problems	147
A.8. Silanization	152
A.9. Fast Fourier transformation and power spectral density	154
A.10. Possible acting forces inside the Fabry-Pérot cavity	154
A.10.1. Optical tweezer force	154
A.10.2. Mirror movement	156
<b>B. Abbreviations and symbols</b>	<b>159</b>
B.1. Abbreviations	159
B.2. Symbols	160
<b>Bibliography</b>	<b>163</b>



# **1. Nanoparticles and their detection on a single particle level**

## **1.1. Nanoparticles in our everyday life**

Nanoparticles play an important role in our everyday life. When we are walking through the streets, ultrafine dust containing nanometer-sized particles can fill the air which we breathe in and which stem from the exhaust air of diesel engines, from wood combustion in stoves, or are contained in tobacco smoke [1, 2]. When we season our food with salt, anticaking agents such as silicon dioxide nanoparticles can be included as an additive to prevent the salt from clumping. The food industry doesn't only use nanoparticles for changing the food's consistency, but also to exploit their preservation properties and to use them for the prevention of pathogens [3, 4]. Nanoparticles can also be found in our clothes. In sportswear, the antibacterial properties of silver nanoparticles are exploited to combat otherwise developing perspiration odors [5]. Maybe soon we will even be able to buy cotton clothes containing carbon nanotubes, which can improve the cotton's mechanical stability, make it water repellent, reduce flammability and the UV light permeability [6]. We also carry nanoparticles onto our bodies via cosmetics, such as sunscreens [7] or anti-wrinkle creams [8]. Nanoparticles do not only exist as a result of artificial production, but they also occur naturally. For example by a volcanic eruption or by a forest fire nano fine dust is blown into the air. We are also made of various nanometer-sized objects, which are responsible for important vital processes. For example, we produce catalytic enzymes for a better digestion of food [9, 10, 11] or we build antibodies in order to defend against invading viruses [12, 13]. If our immune system is not sufficient to fight off diseases, we are forced to rely on drugs and vaccinations. In cancer therapy, cytostatics are used to prevent the cancer cells from multiplying, but they also have a toxic effect on healthy cells. Great hope is being placed here in nanomedicine. Various organic and inorganic nanoparticles can be used to transport the drug directly to the cancer cells. Here, the nanoparticles specifically bind to the cancer cell's surface and release the drugs there. This has the positive effect that lower drug doses can be used and healthy cells are less affected [14]. This increased efficacy through nanoparticles also finds its application in the development of effective vaccines [15]. While a great potential is seen in nanoparticles, it is unclear, to which extent some of the used nanoparticles also have a harmful effect on people and the environment. But there are already several indications [16, 17, 18, 19].

Per definition, particles with the size range between 1 nm and 100 nm are called nanoparticles. Due to the small size, they consist of a very large surface area to volume ratio. As a result, the surface properties become more prominent and consequently, the nanoparticles' properties can totally differ from the properties of the bulk material. For example, water as we know it

is harmless. However, when water drops reach a nanometer size, they can destroy the cell membranes of the *M. parafortuitum* bacteria [20]. This means, in the nanoworld, the rules are different from the ones we know. To be able to learn more from this exciting world and use it for our own benefit, we need ways to make nanoparticles visible.

**Different nanoparticle detection methods.** When we look at our hand, we can't see any viruses that are probably on its surface at that moment. Even if we place our hand under a light microscope, the viruses can't be resolved due to the Rayleigh limited resolution of about 200 nm [21]. The resolution can be improved by decreasing the wavelength. For example electron microscopes, such as scanning electron microscopes (SEM) and transmission electron microscopes (TEM) achieve sub-nanometer resolution and provide information about the nanoparticle's size and morphology by the scattered electrons at the nanoparticle [22, 23]. However, the electrons are also scattered by the particles in air, thus the measurements are usually operated in vacuum. Consequently, the nanoparticles' natural behavior is changed and their dynamical motion can't be detected. In terms of biological processes, where molecules play an important role, detection methods in liquids are necessary. There are several different approaches, such as electrochemical, electrical and optical sensors. Electrochemical sensors detect nanoparticles by their reduction or oxidation at electrode surfaces and the resulting voltage, current, potential or resistance change [24, 25]. On the other hand, electric sensors such as field-effect transistors (FETs) consist of a functionalized gate surface, where the nanoparticles can bind. This results into a change of the gate voltage and consequently into a change of the source-drain current [26]. Both, electrochemical, as well as electric sensors, allow nanoparticle concentration measurements, but based on their measurement principles, they change the nanoparticle properties and rely on either electrochemical processes or laborious surface functionalization. Optical detection methods instead only require a non-zero electrical polarizability of the nanoparticle and they allow a label-free detection of its temporal dynamics without a change of its intrinsic properties. At ensemble measurements, e.g. dynamic light scattering (DLS), the scattered light of several nanoparticles gives information about the averaged nanoparticle size distribution [27]. On the other hand, fluorescence quenching allows the detection of molecule concentrations [28].

**Advantage of single nanoparticle detection.** Of particular interest, however, are those optical sensors that enable the resolution of single nanoparticles. The reason for this is that in ensemble measurements, individual anomalous behaving nanoparticles can't be registered. But exactly those nanoparticles could be responsible for individual important processes that could, for example in the case of anomalous molecules, cause diseases in the long term. Therefore, in the following, only such optical sensors are presented, which allow the detection of single nanoparticles.

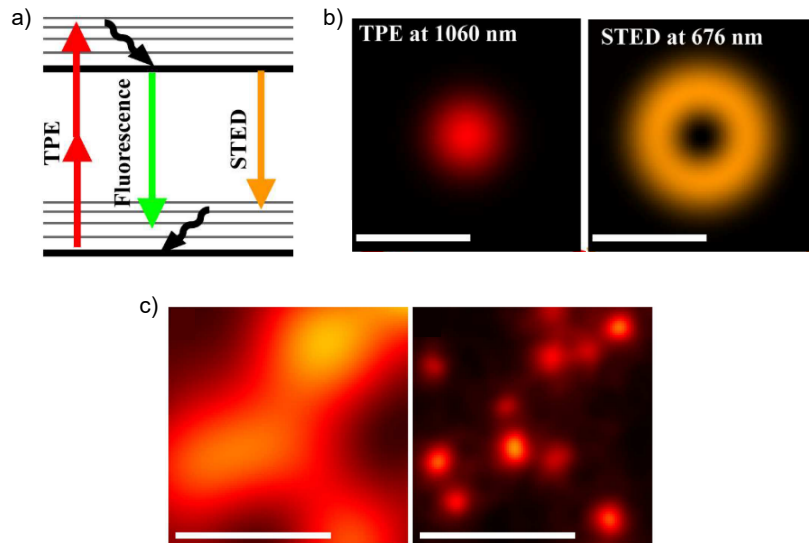


**Figure 1.1.:** Principle of the STED microscopy. **a)** Energy diagram of the three different processes. TPE (red arrow): Two-photon excitation of the fluorophore. Green arrow: Spontaneous emission of fluorescence light. STED (orange arrow): Stimulated emission depletion. **b)** Intensity distribution of the TPE laser (left) and the STED doughnut (right). Scale bars: 500 nm. **c)** Diffraction-limited resolution (left, confocal microscopy) versus sub-diffraction resolution (right, STED). Scale bars: 500 nm. All images were taken from [29].

## 1.2. Methods for the detection of single nanoparticles dispersed in liquids

In this work, a so-called Fabry-Pérot (FP) fiber-based sensor is presented that allows us to detect the dynamics of single nanoparticles with a size of a virus. But before going into this in more detail, other types of optical microscopes and sensors will be introduced, which can also give us insights into the nanoworld. All these optical sensing methods have in common that the optical interaction between light and nanoparticle is exploited. Here, the general challenge is to increase the nanoparticle signal-to-measurement-noise ratio. As the nanoparticle is tiny, only a tiny amount of light is scattered, absorbed, re-emitted or frequency shifted by it<sup>1</sup>. The following sections present different optical sensors and their individual tricks for being able to resolve single nanoparticles.

### 1.2.1. Fluorescence microscopes

Fluorescence microscopes are based on the detecting of the fluorescent light of nanoscaled sources, the so-called fluorophores [30, 31, 32]. When the fluorophore is excited with a certain light wavelength, it first absorbs the light, and then it re-emits the light at a longer wavelength after a typical time scale of  $10^{-9}$ - $10^{-7}$  s [33]. The emitted light is diffraction limited, but

<sup>1</sup> If the nanoparticle is a nanosphere, its cross-sections scales with its radius  $r$  as follows: The scattering cross-section  $\sigma_s$  is proportional to  $|\alpha|^2 \sim r^6$  and the absorption cross-section  $\sigma_a$  is proportional to  $\Im(\alpha) \sim r^3$ .

superresolution is achieved by different techniques [34, 35]. For example, the photoactivated localization microscopy (PALM) [36] and the stochastic optical reconstruction microscopy (STORM) [37] enable a resolution limit down to 20 nm. In both techniques, this high resolution is achieved by the usage of fluorophores which can be actively turned on and off. The stimulated emission depletion (STED) microscopy [29, 38] (see Fig. 1.1) or its further developed versions the MINFLUX [39, 40] and the MINSTED [41] microscopy even reach a spatial resolution down to 1 nm. The basic idea is the depletion of the excited fluorophore by a doughnut-shaped focal laser spot with a longer wavelength than the excitation laser. Consequently, the fluorophore molecules in the doughnut-shaped region are forced to stimulated emission, but the molecules in the very center are undisturbed and therefore emit the fluorescent light, which has another wavelength than the emitted light by stimulated emission. To investigate biological actually non-fluorescent processes by either a diffraction limited fluorescence microscope or by the different superresolution microscopy techniques, the so-called targets are labeled with different kinds of fluorophores. The usage of fluorophores has the advantage of selectivity. That means they only bind to a specific target. This allows the imaging of the target's location and shape [21]. Besides, parallel sensing of several fluorophores over a large area is possible. However, the labeling of the target is a complicated process and it can be also expensive. In addition, the labeling might change the chemical structure of the target to such an extent that its natural behavior is disturbed. Fluorescence microscopy does not only allow the imaging of the fluorophore, but it also enables the detection of its three-dimensional motion. As the fluorophores suffer from photobleaching and saturation, both the spatial as well as the temporal resolution are limited. The best tracking fluorescence microscopy is MINFLUX [39], which provides a 2 nm spatial and a  $4 \cdot 10^{-4}$  s temporal resolution.

### 1.2.2. Interference scattering microscopy

The interference scattering (iSCAT) microscopy is based on the interferometric measurement of the Rayleigh scattered light from a nanoparticle. The nanoparticles dispersed in liquid are located on a glass substrate and are illuminated from below with a laser beam (see Fig. 1.2). At the substrate-liquid interface, the laser beam is partially reflected and the transmitted fraction

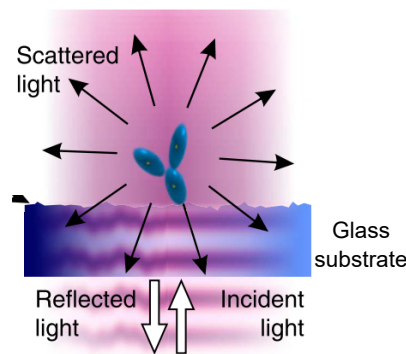


**Figure 1.2.:** Principle of the iSCAT microscopy. The incident laser beam is partially reflected at the glass plate and the transmitted fraction is partially Rayleigh scattered at the nanoparticle. The figure was taken from [42].

is partially Rayleigh scattered at the nanoparticle. Eventually, the interference between the reflected beam and the Rayleigh back-scattered beam is detected. This is also called "homodyne interferometric detection" [43]. By this method, the position of single metallic nanoparticles can be detected with a spatial resolution limit down to 1.9 nm [44]. As molecules of the same size have a smaller effective refractive index and thus a smaller scattering cross-section than metallic nanoparticles, either only relatively large molecules can be detected [42, 45] or in the case of smaller molecules, the resolution can be improved by their labeling with metallic nanoparticles [46]. The disadvantages of labeling were already described in Chapter 1.2.1. In terms of motion detection, iSCAT microscopy allows the two-dimensional tracking of single nanoparticles. A reduction of noise and thus an improvement of the signal-to-noise ratio is achieved by the integration over several frames. This enables an improved spatial resolution, but at the same time, the temporal resolution gets worse [42]. At a spatial resolution of 1.9 nm, thus, gold nanoparticles with a radius of 10-20 nm can be tracked with a time resolution of 1 ms [44]. A larger gold nanoparticle with a radius between 20-40 nm can be tracked with a similar spatial resolution of about 2 nm, but an improved time resolution of  $2 \cdot 10^{-5}$  s [47]. The tracking of an unlabeled single Ferritin protein, though, is possible with a spatial resolution of 12 nm and a relatively long resolution time of 35 ms [45]. As for the fluorescence microscope, the iSCAT microscopy can be operated in a wide-field mode. This allows the parallel sensing of multiple nanoparticles [42].

### 1.2.3. Optical cavities

There are different types of optical cavities, which can be used for nanoparticle detection: The micrometer-sized whispering gallery mode (WGM), photonic crystal (PhC), and Fabry-Pérot (FP) cavities, and the nanometer-sized surface plasmon resonance (SPR) cavity. Each cavity-type detects the single nanoparticle in the same way: The cavity enhances the interaction between the cavity light field and the nanoparticle. In general, the excitation light of wavelength  $\lambda$  is trapped inside the cavity, which forces the light to several round trips until it can leave the cavity. This leads to a standing-wave structure and therefore to regions with high electrical fields. When the nanoparticle resides inside such a high electrical field, it partially absorbs and scatters the light and shifts the resonance frequency of the cavity<sup>2</sup> each time when the light passes the nanoparticle [48, 49]. Thereby, the amount of cavity light field change depends on the shape, size, and material of the nanoparticle. This is described in Chapter 2.3 for the case of a FP resonator in more detail. The enhancement of the nanoparticles signal and thus the resolution limit of the optical microresonator depends on the number of light round trips inside the cavity and the light confinement in the mode volume  $V_m$ . Hence, the figure of merit is the cooperativity  $C \sim Q\lambda_0^3/(n_m^3 V_m)$ . A high quality factor  $Q$  means that the cavity photon lifetime is longer and therefore it interacts more frequently with the nanoparticle. A small mode volume implies a highly localized mode field. As a result, more photons interact with the nanoparticle at one round trip. In the following,

<sup>2</sup> This is also called "refractive shift", because the light's optical path length changes due to the different refractive index of the nanoparticle in comparison to the liquid.

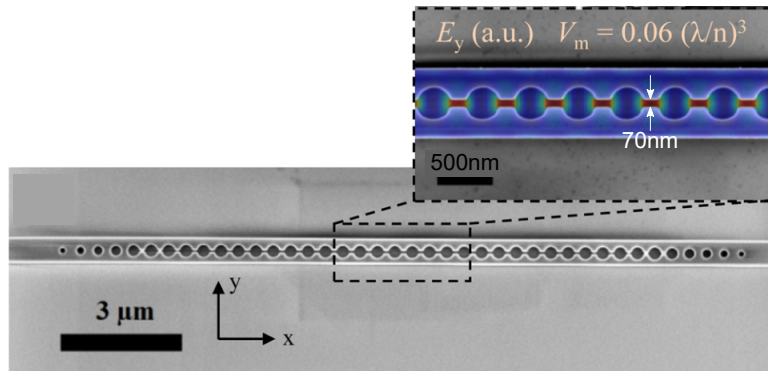


**Figure 1.3.:** SEM image of a slot-mode photonic crystal (PhC). Due to the slot-mode design, high electric fields are generated in the slots. The figure was taken from [50].

the three different resonator types are presented and compared in terms of their enhancements.

**Photonic crystal (PhC) cavity.** PhCs consist of a periodic lattice structure with two alternating materials of a high and a low refractive index. In the case of single nanoparticle sensing in liquids, the material with the lower refractive index is the liquid. Due to the periodicity, the photonic crystal band structure consists of a bandgap. By inducing a defect into the lattice structure or by changing locally the periodicity, an allowed state of a specific frequency within the band structure is created. That means photons with this frequency are not allowed to propagate in the PhC structure and therefore they are forced to execute round trips. Consequently, a cavity is created (see Fig. 1.3). There are many different PhC cavity designs. An overview is given in [51, 49]. Since for the high refractive index material typically silicon, silicon nitride, or gallium arsenide is used, the PhC cavities are operated in the infrared range around  $\lambda = 1.5 \mu\text{m}$  and therefore suffer from a strong water absorption [52, 51]. Thus, with a PhC cavity filled with water, typically low quality factors of  $Q \approx 10^3$  are achieved [53, 52]. However, PhCs consist of very small mode volumes. In Ref. [50], a PhC with a mode volume of  $V_m = 0.06 \cdot (\lambda/n_{\text{H}_2\text{O}})^3 \approx 0.08 \mu\text{m}^3$  and filled with heavy water ( $\text{D}_2\text{O}$ ) is presented. In this case, with a  $Q$ -factor of  $1.2 \cdot 10^4$ , a  $Q\lambda_0^3/(n_m^3 V_m)$  ratio of  $\approx 4.7 \cdot 10^5$  is achieved, and single Polystyrene nanoparticles with a radius of 20 nm can be detected. However, this best reported  $Q\lambda_0^3/(n_m^3 V_m)$  ratio in liquids should be treated with caution since the high  $Q$ -value is only achieved by the usage of heavy water and therefore the light absorption is reduced. In terms of biological measurements, heavy water is toxic. For example, at medium concentration, it slows down cell division (mitosis) and at high concentration, it can destroy the cell [54]. By using normal water instead for biosensing applications, the  $Q$  factor is below 6000 [50] and the  $Q\lambda_0^3/(n_m^3 V_m)$  ratio is  $2.4 \cdot 10^5$ . This value is still high and promising for the future detection of small molecules. However, in terms of statistical measurements, the small sensing volume limits the detection of several single nanoparticle events within a reasonable time. Besides, due to the proximity to the dielectric surface, the nanoparticle could experience forces influencing its movement. In general, PhCs can be easily integrated into a lab-on-a-chip device, and also label-free sensing is possible.

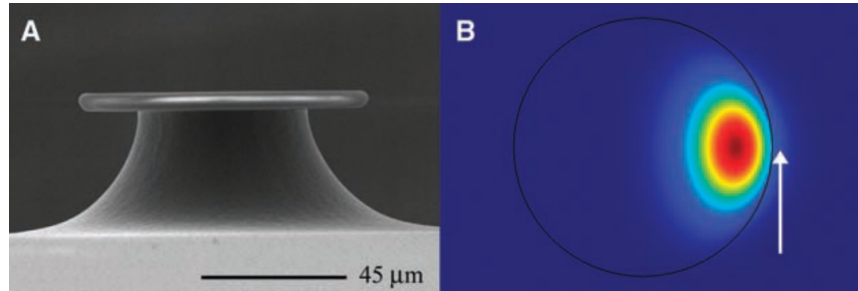


**Figure 1.4.:** Microtoroid whispering gallery mode (WGM) microresonator. **A:** SEM image of a microtoroid. **B:** Electrical field distribution of the fundamental mode. The majority of the electrical field is located inside the dielectric material. Only a fraction of the electrical field leaks out of the material and can interact with nanoparticles and molecules residing close to the surface. The figure was taken from [55].

**Whispering Gallery mode (WGM) cavity.** WGM resonators consist of a dielectric material, which have a circular shape and usually have an extension in the micrometer range. In order to excite the resonator, a laser with a certain light wavelength is coupled into the resonator by an evanescent field. For the in-coupling, typically a tapered fiber or a prism is used. Due to total internal reflection, the light propagates inside the WGM resonator along the periphery. If the diameter of the WGM cavity hits resonance condition<sup>3</sup>, the propagating wave interferes constructively with itself after one round trip. Thus, a standing-wave propagates inside the dielectric material. The main part of the resonance mode is extended inside the dielectric material, where it is unreachable for the nanoparticle (see Fig. 1.4). However, an evanescent field leaks out of the material, allowing the nanoparticle to interact with the mode. [56]

There are different WGM cavity geometries, such as rings [57], disks [58], spheres [59, 60, 61, 56], bubbles [62] and toroids [63, 64, 55, 65, 66, 67]. In the case of WGM cavities, the effective sensing volume has to be introduced. As only a small fraction of the cavity mode can interact with the nanoparticle, the figure of merit for the cavity enhancement is not the mode volume  $V_m$ , but the effective sensing volume  $V_s$ . The latter takes into account the reduced maximal electrical field outside of the dielectric material at the surface. Comparing the different WGM geometries filled with water, the best nanoparticle signal enhancement is achieved with microtoroids. Although the  $Q$  factor is similar to that of microspheres on the order of  $Q \approx 10^6 \dots 10^8$ , the effective sensing volume is reduced in microtoroids due to the different geometry. Here, typical values for the effective sensing volume are in the range  $V_s \approx 630 \dots 3200 \mu\text{m}^3$  [52, 66]. Therefore, with microtoroids  $Q\lambda_0^3/(n_m^3 V_s)$  ratios of up to  $\approx 9.7 \cdot 10^3 \dots 2.2 \cdot 10^4$  are achievable [55, 65, 66]. This allows the studying of single, unlabeled nanoparticles and molecules [55, 68]. As the excitation of the WGM cavity by an evanescent field is very sensitive, its integration into a microfluidic channel is challenging. But there are different approaches published [69, 70]. In comparison to PhCs, WGM cavities have an up to five orders larger quality factor, when both are filled with normal water, but due to a less confined mode, the  $Q\lambda_0^3/(n_m^3 V_s)$  ratio is about an order of magnitude lower. In general, single nanoparticles can be measured

<sup>3</sup> The diameter is approximately a multiple of half light wavelengths.

label-free with WGM cavities. However, usually the WGM cavity surface is functionalized in order to introduce specificity. This leads to an irreversible binding of the nanoparticles and consequently to a contamination and damage of the sensor.

**Surface plasmon (SP) resonances.** SP resonances can be excited in metallic surfaces as well as in metallic nanoparticles. In the first case, the conduction electrons are excited to a resonant oscillation along the metallic surface by an evanescent light field. Thereby both, the electrical field of the incident light and the induced electrical field interfere constructively. Consequently, close to the metallic surface, the electrical field is enhanced ( $\approx 150\text{-}300$  nm field extension length perpendicular to the surface [72]). In the second case, localized surface plasmon (LSP) resonances are excited in metallic nanoparticles<sup>4</sup> of a size much smaller than the incident light wavelength. The incident, non-evanescent, linearly polarized light field forces the conduction electrons to a resonant and coherent oscillation along the whole particle. Consequently, a dipole field is induced. At the nanoparticle poles, the electrical field vectors of the dipole point in the same direction as the electrical field of the excitation light, and at the equator the field vectors point in opposite directions. The thus generated constructive interference at the poles results in so-called "hot spots". Here, the electrical field is highly confined to a small mode volume and the field strength is increased (see Fig. 1.5a). When a nanoparticle or molecule resides inside a hot spot, the wavelength for resonance condition is shifted due to a change in refractive index (see Fig. 1.5b) and also the light-scattered intensity is changed. [73, 74, 75]

SP sensors allow the detection of single virus-like particles<sup>5</sup> with a radius between 50-100 nm and the detection of single Polystyrol (PS) nanoparticles with a radius of 40 nm, both dispersed in distilled water or phosphate-buffered saline (PBS) [76]. In this case, the gold surface is functionalized with different labels, in order to achieve a binding of the virus-like particles or

<sup>4</sup> Typically gold and silver nanoparticles are used.

<sup>5</sup> "Virus-like particles are self-assembling, non-replicating, non-pathogenic particles similar in size, morphology, and conformation to intact viruses. However, in contrast to viruses, virus-like particles are not infectious because they assemble without in-corporating genetic material." [76]

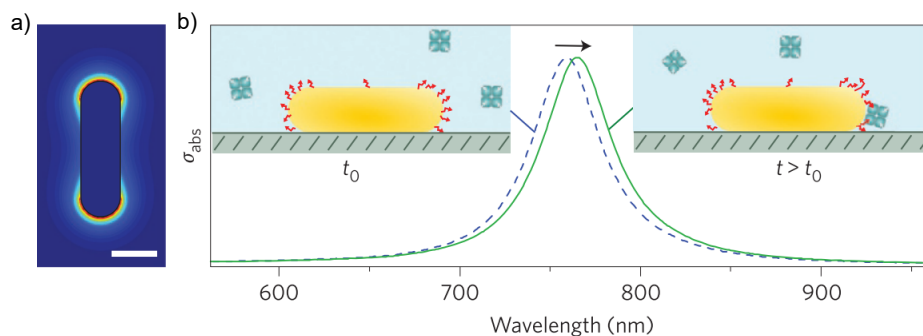


**Figure 1.5.:** Localized surface plasmon (LSP) resonator. **a)** Simulated electrical field distribution when LSP resonances are excited along the vertical axis. The highest electrical field intensity is in the red regions ("hot spots"). Scale bar: 10 nm. **b)** Produced plasmon resonance shift in the photothermal signal (absorption cross-section) when biotin binds to the functionalized surface of the gold nanorod. The figures were taken from [71].

the PS nanoparticles to the surface. Besides, a parallel sensing of several single nanoparticles can be achieved with a wide-field SP microscopy [77]. The best resolution, however, is accomplished with LSP sensors. They allow a label-free detection of single proteins with a mass down to 53 kDa [71]. The high sensitivity is achieved by the induced LSPs inside a gold nanorod and the resulting strong confinement of the mode. In this case, the ultra-small mode volume is "of the same order as the volume of a typical protein" [71]. In [78] a mode volume of  $\approx 6 \cdot 10^{-5} \mu\text{m}^3$  is achieved. However, LSP resonances suffer from large propagation losses. Therefore, the  $Q$ -factor is small and of the order  $\approx 10$ -50 [79, 80]. In total, with LSP resonances a high  $Q\lambda_0^3/(n_m^3 V_m)$  ratio of  $\approx 4 \cdot 10^5$  can be achieved. Furthermore, the LSP resonance sensor can be easily integrated into a microfluidic device [81, 82] and also a parallelized detection of several single LSP resonances is possible [83]. The parallelization has the advantage of increasing the total sensing area, which is quite small for a single LSP sensor and is in the range of  $10^{-3} \mu\text{m}^2$  [52].

Finally, single-molecule sensitivity in the measured Raman signal is also achieved in surface-enhanced Raman scattering. When the molecule is attached to a hot spot region of the plasmonic structure, the molecule starts to vibrate and emits wavelength shifted photons due to inelastic scattering. Thus, the weak Raman cross-section<sup>6</sup> is enhanced. For instance, in Ref. [85] the Raman signals of single Bovin serum albumin molecules with a molecular mass of 66.5 kDa could be detected. However, the measurement technique itself doesn't allow the detection of the molecule's natural behavior as the molecule is forced to vibrations.

**Fabry Pérot (FP) microcavity.** FP microcavities consist of two highly reflective mirrors of micrometer size, which allow a small fraction of light to be transmitted through each mirror. In the case of planar mirrors, they are aligned parallel to each other. Through one of the mirrors, a laser with a specific wavelength is transmitted and reflected back and forth between the two mirrors. If the mirror distance hits resonance condition<sup>7</sup>, the propagating waves interfere constructively and a standing-wave occurs. Consequently, when a nanoparticle resides inside the cavity standing-wave light field, the light-nanoparticle-interaction leads to a change of the intracavity field (see Chapter 2).

FP microcavities itself are well known [87, 88, 89, 90, 91, 92, 93], however, their usage for single nanoparticle sensing in liquids is relatively new. In 2014 a FP microcavity for a refractive index sensing of different liquids was published [94]. The FP cavity consists of a planar mirror and a second concave mirror with a small radius of curvature in order to simplify the alignment of the mirrors and to realize a stable cavity<sup>8</sup>. Two years later, the same group introduced nanospheres with a minimum radius of  $\approx 45$  nm (PS) into the FP cavity (see Fig. 1.6). In this case, the  $Q$ -factor of  $1.8 \cdot 10^4$  and the mode volume of  $V_m \approx 0.4 \mu\text{m}^3$  allowed the trapping of unlabeled nanospheres inside the confined mode and the investigation of resonance shift and linewidth broadening produced by the nanosphere. However, in their approach, the  $Q$  factor

<sup>6</sup> The Raman cross-section is on the order  $10^{-29}$  to  $10^{-32}$  [84] and about 7 orders smaller than the Rayleigh cross-section.

<sup>7</sup> The optical path length has to be a multiple of half of the wavelength.

<sup>8</sup> If two planar mirrors are used, already small misalignments reduce the  $Q$ -factor dramatically, as the light can leave the cavity after a few reflections. Spherical mirrors instead are more robust against small misalignments and the condition for a stable cavity is  $0 \leq (1 + d/r_{c,1})(1 + d/r_{c,2}) \leq 1$ , with the mirror radii of curvature  $r_{c,i}$  and the cavity length  $d$ .

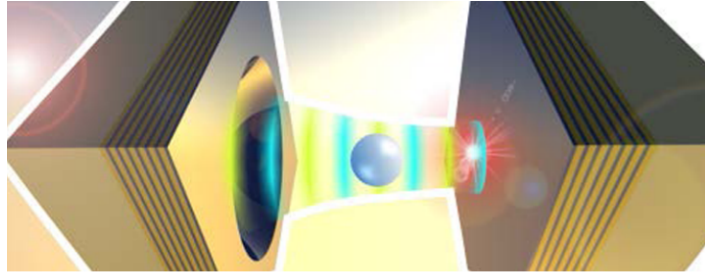


**Figure 1.6.:** Fabry-Pérot cavity consisting of a planar mirror (right) and a second mirror with an ion beam milled spherical profile (left). Between the two mirrors, a nanoparticle is trapped inside an antinode of the standing-wave cavity light field. The figure was taken from Ref. [86].

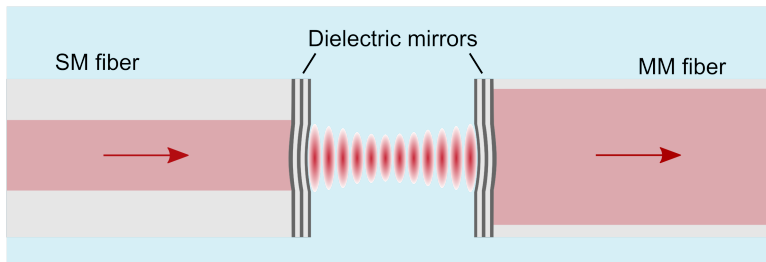


**Figure 1.7.:** Sketch of a fiber-based Fabry-Pérot (FP) cavity. The laser beam is guided through a single-mode (SM) glass fiber, which has a depression inside the end-facet and a dielectric mirror attached. A small fraction of the laser beam is transmitted through the mirror and reflected back and forth between the two mirrors. At discrete distances, a standing-wave occurs with high electrical fields at the center of the antinodes. A fraction of the intracavity light is transmitted through the second mirror into the multi-mode (MM) fiber.

is limited due to the focused ion beam milled mirror profiles and accordingly the high surface roughness. Therefore, the  $Q\lambda_0^3/(n_m^3 V_m)$  ratio of  $\approx 1.1 \cdot 10^4$  is less than that of PhC, WGM, and SP cavities. In addition, for this kind of FP cavity, free-space in-coupling optics is needed and the cavity was not yet integrated into a microfluidic device in order to provide a controllable laminar flow.

The advantage of FP cavities in comparison to PhC, WGM, and SP cavities is the open-access design. The cavity standing-wave light field is formed between the two mirrors, thus the nanoparticle has open access to the light field without the requirement for being close to the mirror surface. Hence, the nanoparticle's motion isn't influenced by surface forces, and in contrast to WGM resonators, it has full access to the field maximum.

### 1.3. Fiber-based Fabry-Pérot microcavity with high finesse

Within this work, a fiber-based FP cavity is presented, which consists of two concave, dielectric, mirrors on the end facets of glass fibers (see Fig. 1.7). In the following, they are called fiber cavity mirrors. In this section, at first, the fiber-based FP cavity is compared with other optical cavities. Second, the new achievements presented in this work are summarized. Third, the tracking of a single nanoparticle with the FP microcavity is compared with other detection

methods and finally the limitations of this detection method are briefly discussed.

**Comparison of the FP microcavity with other optical cavities.** Due to the fabrication of the concave profile with CO<sub>2</sub> laser pulses instead of ion beam milling, the surface roughness is very low [87]. Therefore, a high quality factor of  $1 \cdot 10^6$  is achieved for a fiber-based FP cavity filled with water. Simultaneously, the mode volume amounts to  $V_m = 10 \mu\text{m}^3$  resulting into a  $Q\lambda_0^3/(n_m^3 V_m)$  ratio of  $2.1 \cdot 10^4$  [95]. Although this sensor type is new in the area of single nanoparticle sensing in liquids, the  $Q\lambda_0^3/(n_m^3 V_m)$  ratio is already similar or better than the best WGM cavity and it is only a factor of 5 worse than the best PhC cavity and a factor of 8.5 worse than the best LSP cavity. In contrast to WGM cavities and FP cavities consisting of two macroscopic mirrors, it is shown that a fiber-based FP cavity can be easily integrated into a microfluidic channel.

**New achievements.** Within this work, a novel and compact cavity setup consisting of a 3D laser-written polymer microfluidic channel is presented, which enables a customized design of the channel and consequently ensures a controllable laminar flow. Thus, hundreds of single, unlabeled nanoparticle transit events can be detected within a few hours. From the measured dispersive shifts of several single nanosphere transit events, the autocorrelation of their motion through a FP cavity standing-wave light field could be investigated. The two arising slopes were in accordance with Monte Carlo simulations of the Brownian motion of single nanospheres of the same size. Whereas the numerical autocorrelation for a focused beam is widely understood (see fluorescence correlation spectroscopy [96]), the autocorrelation for a standing-wave light field is not yet investigated. Only Ref. [97] offers a numerical result, which, however, contradicted the double-slope structure of the measured autocorrelation. Instead, within this work, a new numerical result for a punctiform nanoparticle was derived, which described the two slopes. Via the refractive index sensing of single nanospheres, the effective refractive index of the expanded nanosphere size in water could be determined and the refractive index of the hydrate shell estimated [95]. The presumption in Ref. [98] that salt reduces the expansion of the hydrate shell could be verified and probably small amounts of salt already suppressed the formation of the whole hydrate shell as the same polarizability as the intrinsic polarizability of the bare nanosphere could be measured. Completely new is the tracking of the three-dimensional Brownian motion of a single, unlabeled nanosphere by an optical cavity in general and especially by a FP cavity. The nanosphere's motion could be tracked with a time-resolution of  $3 \cdot 10^{-4}$  ms and a maximal spatial resolution of 8 nm [95]. The track gave rise to estimate the nanosphere's hydrodynamic radius independently from its refractive index and besides the normal diffusive motion, this technique should also allow the detection of anomalous diffusion in the future. In addition to the translational movement, for the first time, also the rotational diffusion of anisotropic-shaped single nanoparticles was investigated with the fiber-based FP cavity. This is shown within this work with a time resolution of  $7 \cdot 10^{-5}$  s.

**Comparison of the single particle tracking with other detection methods.** In comparison to the spatial resolution of 2 nm of the fluorescence microscope MINIFLUX, the maximal spatial resolution of 8 nm of the fiber-based FP cavity is worse. However, the use of labels is

avoided, the method enables tracking in three instead of two dimensions, and the translational movement is purely diffusive and not disturbed by the measurement. In addition, the time resolution of the fiber-based FP cavity is an order of magnitude better. With the fluorescence microscopy TSUNAMI [99] a better time resolution of  $5 \cdot 10^{-5}$  s is achieved, though the spatial resolution is worse with 16...35 nm. With iSCAT microscopes, a spatial resolution of 2 nm and a time resolution of  $2 \cdot 10^{-5}$  for larger gold nanoparticles is achieved. Both resolution limits are better than those obtained with the fiber-based FP cavity, however, the tracking is limited to two dimensions and fast tracking is only possible with labels (strong scatterers) or larger nanoparticles.

The current time and spatial resolution of the fiber-based FP cavity could be significantly improved by an active stabilization of the cavity length and a heterodyne detection of the resonance phase shift. Then, the time resolution would only depend on the bandwidth of the photodetector and the cavity decay rate ( $\approx 10^8$  Hz). The spatial resolution would be improved at the same time due to the lower measurement noise and consequently the increased signal-to-noise ratio.

**Limitations.** Besides the advantages, the disadvantages of FP cavities should not be concealed. As with all optical microcavities, a single FP cavity doesn't allow the parallel observation of several single nanoparticles. Multiple single nanoparticles could be observed by the integration of several single FP cavities into one microfluidic channel. This is theoretically possible by the usage of multi-core fibers, however, this also complicates the handling. Moreover, the sensing area is relatively small in comparison to fluorescence microscopes and iSCAT.

#### 1.4. Scope of this work

In **Chapter 2**, after the basic introduction to FP cavities and nanoparticles in the Rayleigh regime, the interaction between the FP standing-wave light field and a single, homogeneous nanoparticle are discussed. First, the resonance amplitude decrease and frequency shift produced by a nanosphere are considered. Then, a  $\text{SiO}_2$  nanosphere dispersed in water is discussed. Afterward, the diffusive motion of the nanosphere in water probed by the cavity light field is numerically simulated and it is shown that the simultaneous detection of the fundamental mode and the two higher-order transverse modes reveal the nanosphere's Brownian motion and thus the information about its diffusivity and hydrodynamic radius. In the next subchapter, the theoretical autocorrelation of the signal produced by a punctiform nanosphere, which transits the FP standing-wave light field is derived. Finally, the investigation of the rotational motion of anisotropic-shaped nanoparticles via the polarization-split fundamental modes is discussed.

The next **Chapter 3** deals with different experimental sensing platforms and their performance. The sensing platforms, where different kind of microfluidic channels and the FP cavity are embedded, are discussed in detail. In addition, the principle of finesse and nanoparticles measurements are presented. Furthermore, the different sensing platforms are compared in terms of their passive stability, measurement noise and resolution limit. At the end of

this chapter, an overview of the different cavity geometries is given, that were used for the conducted experiments.

**Chapter 4** is about the sensing of the mean polarizability of several single nanosphere transit events of different SiO<sub>2</sub> samples. Furthermore, for each sample, the refractive index of the hydrate shell is determined. In addition, it is shown that an improved time resolution already enables the determination of the polarizability of a single, freely diffusing nanosphere. The next sub-chapter covers the impact of salt on the hydrate shell of SiO<sub>2</sub> nanospheres. It is shown that salt decreases the thickness of the hydrate shell and probably already very low salt concentrations could cause a removal of the shell. In the last sub-chapter, the experimentally derived autocorrelation of several nanosphere transit events is compared with the theoretical autocorrelation function of a punctiform nanosphere and the simulated autocorrelation derived by several Monte Carlo tracks.

In **Chapter 5** the three-dimensional single nanosphere track is derived from the simultaneously measured frequency shifts of the fundamental and two higher-order transverse modes. From the three-dimensional track, the mean squared displacement is determined, which contains the information about the nanosphere's diffusivity and its hydrodynamic radius.

In **Chapter 6** the rotational diffusion of an almost spherical nanoparticle, a dimer, and a larger agglomerate is investigated by the polarization-split fundamental modes. This technique is highly sensitive as already nanospheres with a specified roundness of >0.98 can be tracked in their rotational motion.

Finally, in **Chapter 7**, all results are briefly summarized and possible future steps are discussed in an outlook.

Last but not least, references should be made to the appendix. In **Appendix A** detailed descriptions and mathematical derivations are given, as well as assistance for possible problems arising in practice. **Appendix B** contains a list of abbreviations and a list of symbols.



## **2. Fundamentals of single polarizable nanoparticles inside a fiber-based Fabry-Pérot microcavity**

In this chapter, at first, the fundamentals of fiber-based Fabry-Pérot (FP) cavities are discussed (Chapter 2.1). The next Chapter 2.2 deals with the properties of nanoparticles much smaller than the wavelength of incident light (Rayleigh regime). For a homogeneous nanosphere, the polarizability is derived and its response to an external oscillating electrical field is considered. In addition to a homogeneous sphere, anisotropically shaped nanoparticles are also discussed. Finally, the interaction of a nanoparticle with the standing-wave light field of a FP cavity is considered. Several aspects are highlighted. In Chapter 2.3 the change in cavity resonance is explained when a spherical nanoparticle resides inside the cavity mode. The resonance change is directly related to the polarizability of the nanosphere. Chapter 2.4 deals with the Monte Carlo simulation of the Brownian motion of nanoparticles. It is theoretically shown that the simultaneous measurement of the  $TEM_{00}$ ,  $TEM_{01}$  and  $TEM_{10}$  allows the three-dimensional tracking of a single nanosphere. From the three-dimensional track, the diffusivity and hence the hydrodynamic radius of the nanosphere can be deduced via the mean squared displacement. In Chapter 2.5 the autocorrelation function is derived for a punctiform nanosphere moving through the FP standing-wave light field. In general, the autocorrelation provides information about the type of motion (e.g. diffusion, drift or rotation). In this case, diffusion and drift are considered. Finally, Chapter 2.6 deals with the rotational diffusion of anisotropically shaped nanoparticles. It is explained, how the polarization splitting of the fundamental modes can be exploited to obtain information about the rotational diffusion of the nanoparticles.

### **2.1. Fiber-based Fabry-Pérot cavity modes**

In this chapter, the general properties of a fiber-based Fabry-Pérot cavity are briefly summarized. If there is no prior knowledge of FP resonators in general, the reader is motivated to acquire a deeper understanding for the basics e.g. by reading the corresponding chapters in the standard literature [100].

A fiber-based FP cavity consists of two highly reflective dielectric mirrors attached to the end facets of two glass fibers (see. Fig. 1.7). Before the mirrors are attached, a depression is micromachined into each cleaved fiber end facet by  $CO_2$  laser pulses [87, 101]. The resulting

mirror profiles have a low surface roughness of  $\approx 0.2$  nm and the depression inside the surface can be approximated by a Gaussian profile. At the center, the depression is almost spherical. Accordingly, the mirror curvature is defined by the radius of curvature  $r_c$ . In general, different mirrors with different radii of curvature  $r_{c,1}$  and  $r_{c,2}$  are used. In the real case, the mirrors are slightly elliptical. Therefore, each mirror consists of two radii of curvature  $r_{c,1,1}$ ,  $r_{c,1,2}$  for mirror 1 and  $r_{c,2,1}$ ,  $r_{c,2,2}$  for mirror 2. Before going into details of FP cavities with spherical and elliptical mirrors, at first, a FP cavity with planar mirrors is considered.

### 2.1.1. Planar cavity mirrors

A cavity is created by a parallel alignment of the two mirrors. When laser light with vacuum wavelength  $\lambda_0$  is coupled into the mirror gap through one of the mirrors ("input mirror"), the light is reflected back and forth between the two mirrors. At mirror separations of

$$d_{\text{geom}} = q \left( \frac{\lambda_0}{2n_m} - 2d_{\text{pen}}(n_m) \right) \frac{1}{n_m}, \quad q \in \mathbb{N}, \quad (2.1)$$

with " $d_{\text{geom}}$ " called geometric cavity length, the reflected light propagates in phase after one round trip and a standing-wave with a constant amplitude occurs between the two mirrors. In Eq. (2.1), the cavity is filled with a liquid of refractive index  $n_m$  and  $d_{\text{pen}}(n_m)$  denotes the penetration depth of light into each mirror with the same dielectric coating. Hence, the optical cavity length can also be expressed as

$$d_{\text{opt}} = d_{\text{geom}}n_m + 2d_{\text{pen}}. \quad (2.2)$$

This simplifies Eq. (2.1) to

$$d_{\text{opt}} = q \frac{\lambda_0}{2n_m}, \quad q \in \mathbb{N}. \quad (2.3)$$

If the mirrors are highly reflective and cavity losses are neglected, light is only transmitted through the second mirror ("output mirror") at resonance condition. Otherwise, the transmittance is zero. Thus, the light intensity distribution detected by the APD is a delta distribution and the distance between two consecutive delta peaks is called **free spectral range (FSR)**

$$\Delta\nu_{\text{FSR}} = \frac{c_0}{2d_{\text{opt}}n_m}. \quad (2.4)$$

Here,  $c_0$  is the light velocity in vacuum.

In the real case, different loss channels inside the cavity lead to a broadening of the transmitted intensity. In Fig. 2.1 the losses inside a cavity are shown. Light with the incident electrical field  $E_0$  enters the cavity through mirror 1 and is reflected back and forth between both mirrors. As mirrors have a reflectivity smaller than one, with  $R_i = 1 - T_i - A_i$  and where  $T_i$  is the transmission and  $A_i$  are the absorption and scattering losses of mirror  $i = [1, 2]$ , a fraction of the intracavity light can also leave the cavity through each mirror. In the following, only the transmission through the second mirror is considered. At each reflection at mirror 2, a

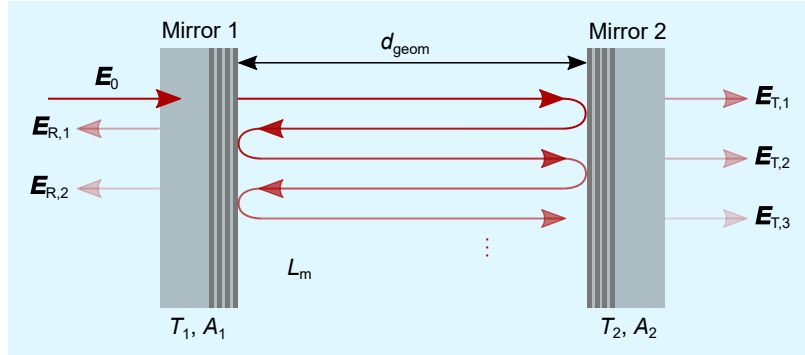


**Figure 2.1.:** Loss channels inside a FP cavity. The incident light  $E_0$  is coupled into the cavity through mirror 1. Inside the cavity, the light is reflected back and forth between the mirrors. At each round trip, a fraction of the light is lost. The liquid into which the mirrors are immersed absorbs a fraction of the light ( $L_m$ ). Besides, the mirrors absorb and scatter a fraction of the light as well ( $A_1, A_2$ ) and enable partial transmittance ( $T_1, T_2$ ).

fraction of the light is transmitted  $E_{T,k}$ . The overall transmission through mirror 2 is then given by the sum over all transmitted fractions

$$T_{\text{cav}} = \frac{|\sum_{k=1}^{\infty} E_{T,k}|^2}{|E_0|^2} . \quad (2.5)$$

A fraction of the intracavity light does not only get lost due to the transmission and absorption through each mirror but also due to the absorption of the liquid  $L_m$ , by which the cavity is filled. The amount of absorption is described by the Lambert absorption coefficient  $\alpha_m$  and the overall loss at each round trip caused by the medium is

$$L_m(\lambda, d_{\text{geom}}) = 2 \cdot \alpha_m(\lambda) \cdot d_{\text{geom}} . \quad (2.6)$$

Hence, a larger geometric cavity length  $d_{\text{geom}}$  leads to a greater absorption inside the medium and therefore to a decreased cavity transmission and finesse. In case of water and the wavelength  $\lambda = 775 \text{ nm}$ , the absorption coefficient is  $\alpha_m = 2.38 \text{ ppm}/\mu\text{m}$  [102]. The exact result for the transmission amplitude is an **Airy-function**, where the transmission doesn't decrease to zero at off-resonance condition. If only highly reflective mirrors are considered with  $R \approx 1$ , the transmission amplitude  $T_{\text{cav}}$  can be approximated as [103]

$$T \approx T_{\text{max}} \frac{\left(\frac{\delta\nu}{2}\right)^2}{\left(\frac{\delta\nu}{2}\right)^2 + (q\Delta\nu_{\text{FSR}} - \nu)^2} , q \in \mathbb{N} . \quad (2.7)$$

Consequently, the intensity distribution detected by the APD has a **Lorentzian** shape with the **full width half maximum (FWHM)**

$$\delta\nu = \Delta\nu_{\text{FSR}} \frac{T_1 + T_2 + A_1 + A_2 + L_m}{2\pi} \quad (2.8)$$

and the maximal amplitude at resonance condition  $\nu_q = q\Delta\nu_{\text{FSR}}$  is

$$T_{\text{max}} = \frac{4T_1T_2}{(L_m + A_1 + A_2 + T_1 + T_2)^2} . \quad (2.9)$$

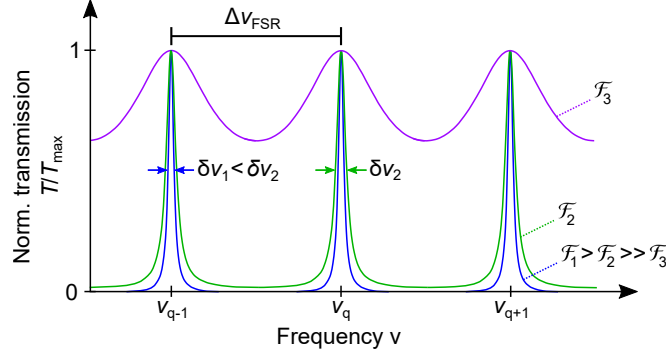


**Figure 2.2.:** Schematic illustration of the FP cavity transmission spectrum with planar mirrors and different finesse. The transmission spectrum of a low finesse cavity is described by an Airy function ( $\mathcal{F}_3$ , purple). When the finesse of the cavity is high ( $\mathcal{F}_1, \mathcal{F}_2 \gg \mathcal{F}_3$ , green and blue), the transmission spectrum decreases to approximately zero at non-resonance condition. At resonance condition, resonances occur with a Lorentzian shape. The higher the finesse, the narrower are the resonances (full width half maximum  $\delta\nu_1 < \delta\nu_2$ ). The distance between two consecutive resonances is called free spectral range  $\Delta\nu_{\text{FSR}}$ .

The cavity **finesse** is defined as the ratio between FSR and FWHM

$$\mathcal{F} = \frac{\Delta\nu_{\text{FSR}}}{\delta\nu} = \frac{c_0}{2d_{\text{opt}}n_m\delta\nu} \quad (2.10)$$

For the transformation, Eq. (2.4) was inserted. Inserting Eq. (2.4) and Eq. (2.8) into Eq. (2.10) gives the important relation

$$\mathcal{F} = \frac{2\pi}{L_m + A_1 + A_2 + T_1 + T_2} \quad (2.11)$$

for the finesse [104]. In Fig. 2.2 the transmitted light is sketched for different finesse. The lower the losses, the greater is the finesse and the sharper are the resonances. The finesse is only used in the context of FP cavities. For other resonator types, including mechanical and electrical resonant circuits, the figure of merit is the **quality factor**  $Q$ . It is related to the finesse as follows:

$$Q = \frac{\nu_q}{\delta\nu} = q\mathcal{F} \quad , q \in \mathbb{N} \quad (2.12)$$

### 2.1.2. Spherical cavity mirrors

When the two planar mirrors are exchanged by two spherical mirrors, the amplitude of the standing-wave isn't a constant anymore, but it is a complex quantity depending on the spatial coordinate  $\vec{r} = (x, y, z)^T$ . The new cavity modes can be found by solving the paraxial Helmholtz equation. The simplest solution is a Gaussian amplitude distribution and the overall intensity distribution of the cavity standing-wave light field is

$$I_{00}(x, y, z) = I_G(x, y, z) \cos^2\left(\frac{2\pi n_m}{\lambda_0} \cdot z\right), \quad (2.13)$$

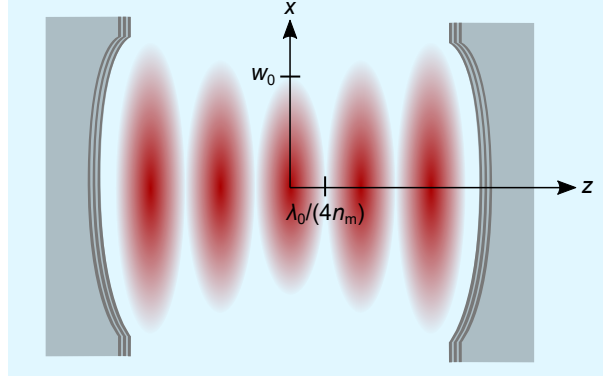


**Figure 2.3.:** Illustration of the cavity standing-wave light field distribution if spherical cavity mirrors are used with the same radii of curvatures and if the fundamental mode  $\text{TEM}_{00}$  is excited. The expansion of an antinode in the longitudinal direction between two nodes is  $\lambda_0/(2n_m)$ . The smallest size of the beam is called waist  $w_0$  and its expansion is defined where the light field drops from its maximal value at the center of the antinode  $I_0$  to  $I_0/e$  in the lateral direction. In this case, the waist is located at the center between the two mirrors. By the usage of different mirror radii of curvatures, the waist would be located away from the center closer to the mirror with the larger radius of curvature. Similar to [95]

with

$$I_G(x, y, z) = I_0 \frac{w_0^2}{w(z)^2} \exp\left(\frac{-2(x^2 + y^2)}{w(z)^2}\right) \quad (2.14)$$

and

$$w(z)^2 = w_0^2 \left(1 + \left(\frac{z}{z_0}\right)^2\right) \quad (2.15)$$

Here, the Rayleigh length is defined as  $z_0 = \pi n_m w_0^2 / \lambda_0$ , where  $w_0$  is the waist of the Gaussian beam

$$w_0 = \sqrt{\sqrt{\frac{-d_{\text{opt}}(r_{c,1} + d_{\text{opt}})(r_{c,2} + d_{\text{opt}})(r_{c,1} + r_{c,2} + d_{\text{opt}})}{r_{c,1} + r_{c,2} + 2d_{\text{opt}}}} \frac{\lambda_0}{n_m \pi}} \quad (2.16)$$

and  $I_0$  is the light field amplitude at  $z = 0$ . The waist depends on the geometry of the two spherical mirrors with the radius of curvature  $r_{c,1}$  ( $r_{c,2}$ ) of the first and second mirror. In Fig. 2.3, the intensity distribution of the  $\text{TEM}_{00}$  mode is sketched. Due to the complex amplitude, the light propagating between the two mirrors collects an additional phase of  $2\Delta\xi$  along the optical axis at  $x, y = 0$ . This phase difference is also called the Gouy-phase difference between the Gouy-phases at mirror 1 and mirror 2. Therefore, the resonances, called **fundamental modes**  $\text{TEM}_{00}$ , occur at slightly different frequencies in contrast to the resonances of a FP resonator with planar mirrors, namely at

$$\nu_q = q\Delta\nu_{\text{FSR}} + \Delta\nu_{\text{FSR}} \frac{\Delta\xi}{\pi} \quad (2.17)$$

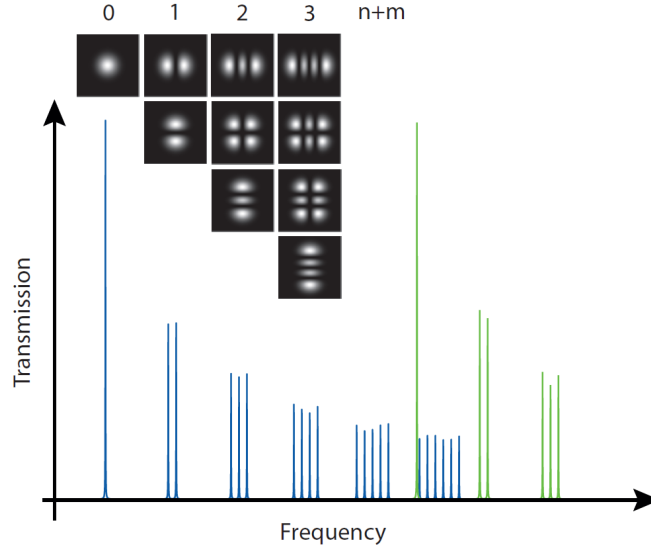


**Figure 2.4.:** "Schematic illustration of the cavity transmission as a function of frequency. Blue and green denote different longitudinal orders  $q$ . Inset: intensity distribution of the transverse modes up to order 3." Image and description were taken from [103].

In addition to the fundamental mode, also the Hermite-Gaussian modes are solutions of the paraxial Helmholtz equation. By introducing the Hermite-Gauss functions  $G_m$ , the overall intensity distribution can be described by

$$I_{m,n}(x, y, z) = I_G(x, y, z) \cdot G_m^2\left(\frac{\sqrt{2}x}{w(z)}\right) G_n^2\left(\frac{\sqrt{2}y}{w(z)}\right) \cos^2\left(\frac{2\pi n_m}{\lambda_0} \cdot z\right) . \quad (2.18)$$

In the following, they are called the **higher-order transverse modes**  $\text{TEM}_{mn}$ . The collected Gouy-phase of  $(m+n+1)\Delta\xi\Delta\nu_{\text{FSR}}/\pi$  leads to the resonance condition

$$\nu_{q,m,n} = q\Delta\nu_{\text{FSR}} + (m+n+1)\frac{\Delta\xi}{\pi}\Delta\nu_{\text{FSR}} . \quad (2.19)$$

For the condition  $m, n = 0$ , the resonance frequencies of the fundamental modes are obtained. Fig. 2.4 shows a schematic illustration of the transmission spectrum of a FP cavity with almost spherical mirrors. The fundamental mode as well as the higher-order modes occur at different resonance frequencies and the inset depicts the intensity distributions of the different modes. Because of a slightly elliptical mirror shape, the modes of the same order  $m+n$  are not degenerated and therefore appear at different frequencies.

### 2.1.3. Birefringent cavity mirrors

Each resonance is splitted into two polarization modes if either the mirror profiles are not perfectly spherical, but have an elliptical shape, or if the mirror coating is birefringent. In the following, this is explained for elliptically shaped mirrors with different radii of curvature

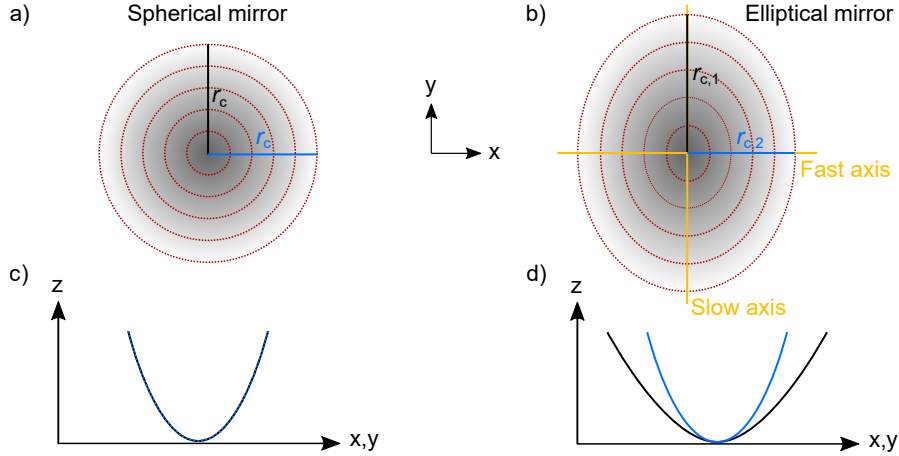


**Figure 2.5.:** Sketch of a spherical and elliptical-shaped mirror. **a)** Contour plot of a spherical, concave mirror with radius of curvature  $r_c$ . **b)** Contour plot of an elliptical, concave mirror. The largest (smallest) radius of curvature is defined as  $r_{c,1}$  ( $r_{c,2}$ ). Due to the non-spherical shape, the mirror consists of a slow and fast axis and therefore causes birefringence. **c)** Cut through the spherical mirror. **d)** Cut through the elliptical mirror.

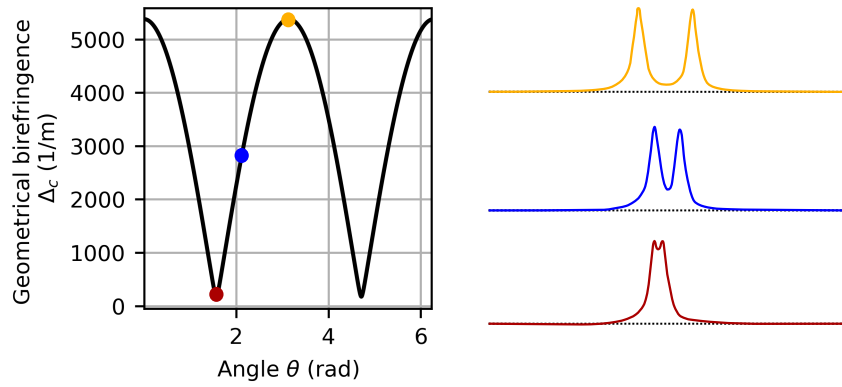


**Figure 2.6.:** Geometrical Birefringence depending on the rotation angle  $\theta$  of the birefringent mirrors to each other. The radii of curvature used for the simulation are  $r_{c,M1,1} = 40.0 \mu\text{m}$ ,  $r_{c,M1,2} = 70.0 \mu\text{m}$ ,  $r_{c,M2,1} = 45.0 \mu\text{m}$  and  $r_{c,M2,2} = 85.6 \mu\text{m}$ . Marked in colors are the two extreme values as well as a value in between. On the right hand-side the corresponding frequency splitting of the fundamental mode is sketched.

along the two principal axes  $r_{c,1}$  and  $r_{c,2}$  (see Fig. 2.5):

If both mirrors are elliptical and the mirrors differ from each other in their curvature ( $r_{c,M1,1} \neq r_{c,M2,1}$  and  $r_{c,M1,2} \neq r_{c,M2,2}$ ) and if the radii of curvature are much larger than the wavelength of light, the frequency splitting  $\Delta\nu$  between the two linearly and orthogonally polarization-split fundamental modes is given by [92, 105]

$$\Delta\nu = \frac{\lambda_0 \mathcal{F} \delta\nu}{2n_m \pi^2} \Delta_c(\theta) = \frac{c\lambda_0}{8n_m \pi^2 d_{\text{opt}}} \Delta_c(\theta) \quad , \quad (2.20)$$

with the geometrical birefringence

$$\Delta_c(\theta) = \sqrt{\delta_1^2 + \delta_2^2 + 2\delta_1\delta_2 \cos(2\theta)} \quad . \quad (2.21)$$

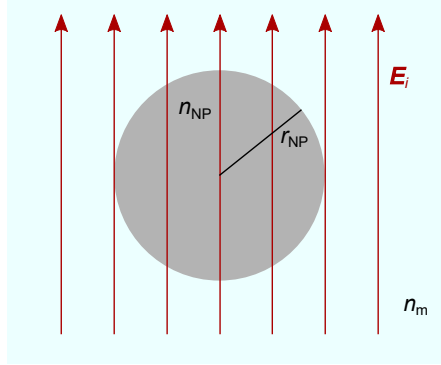


**Figure 2.7.:** Respond of an homogeneous, dielectric nanosphere residing inside a static, homogeneous electrical field  $\vec{E}_i = E_0 \hat{e}_z$ . The nanosphere has a radius of  $r_{NP}$ , a refractive index of  $n_{NP}$  and is surrounded by a medium with refractive index  $n_m$ .

The latter depends on the radii of curvature of each mirror  $M$

$$\delta_M = \frac{1}{r_{c,M,1}} - \frac{1}{r_{c,M,2}} \quad , \quad (2.22)$$

with  $M = 1, 2$  for mirror 1 and 2, and on the rotation angle  $\theta$  of the mirrors to each other (see Fig. 2.6).

## 2.2. Nanoparticles in a homogeneous electrical field

The electrical polarizability of a nanoparticle is in general a tensor and a complex quantity, which takes into account the nanoparticle's shape, expansion and refractive index. Ultimately, the polarizability describes the response of the nanoparticle to an external electrical field, e.g. to an electromagnetic wave. In the following, two special cases are discussed: A homogeneous nanosphere and a homogeneous, anisotropically shaped nanoparticle. In both cases, the expansion of the nanoparticle is much smaller than the wavelength of light of an electromagnetic wave. Therefore, the electrical field can be considered as approximately constant over the whole nanoparticle (Rayleigh regime).

### 2.2.1. Nanosphere

The case for a homogeneous, dielectric nanosphere with refractive index  $n_{NP}$  and radius  $r_{NP}$  residing inside a homogeneous electrical field  $\vec{E}_i = E_0 \hat{e}_z$  and in the external medium with refractive index  $n_m$  is depicted in Fig. 2.7. In order to derive the polarizability of the nanosphere, the Laplace equation

$$\Delta \Phi = 0 \quad (2.23)$$

has to be solved. Here,  $\Phi$  is the potential and the electrical field depends on the potential as  $\vec{E} = -\nabla \Phi$ . Different boundary conditions have to be taken into account:

First, the potential outside the nanosphere has to become the potential of the incident field at infinity:

$$\lim_{r \rightarrow \infty} \Phi_{\text{out}} = -E_0 z \quad . \quad (2.24)$$

Second, at the interface between the nanosphere and the environmental medium, the tangential component of the electrical fields has to stay constant

$$E_{t,\text{out}}(|\vec{r}| = r_{\text{NP}}) = E_{t,\text{in}}(|\vec{r}| = r_{\text{NP}}) \quad (2.25)$$

and finally, the normal component of the electric displacement has to be constant as well:

$$D_{n,\text{out}}(|\vec{r}| = r_{\text{NP}}) = D_{n,\text{in}}(|\vec{r}| = r_{\text{NP}}) \quad . \quad (2.26)$$

Solving the Laplace equation with these boundary conditions gives the solution [52, 106]:

$$\Phi_{\text{in}} = -\frac{3n_{\text{m}}^2}{n_{\text{NP}}^2 + 2n_{\text{m}}^2} E_0 z \quad (2.27)$$

and

$$\Phi_{\text{out}} = -E_0 z + r_{\text{NP}}^3 \frac{n_{\text{NP}}^2 - n_{\text{m}}^2}{n_{\text{NP}}^2 + 2n_{\text{m}}^2} E_0 \frac{z}{|\vec{r}|^3} \quad . \quad (2.28)$$

Consequently, the incident electrical field induces a constant electrical field inside the nanosphere and a static dipole field outside the nanosphere. By introducing the induced dipole moment  $\vec{p}$ , the potential outside the nanosphere can be written as

$$\Phi_{\text{out}} = -\Phi_i + \Phi_{\text{dipole}} \quad (2.29)$$

$$= -E_0 z + \frac{\vec{p} \cdot \vec{r}}{4\pi\epsilon_0 n_{\text{m}}^2 |\vec{r}|^3} \quad , \quad (2.30)$$

with

$$\vec{p} = n_{\text{m}}^2 \alpha E_0 \hat{e}_z \quad , \quad (2.31)$$

the complex electrical polarizability

$$\alpha = 4\pi r_{\text{NP}}^3 \epsilon_0 \frac{n_{\text{NP}}^2 - n_{\text{m}}^2}{n_{\text{NP}}^2 + 2n_{\text{m}}^2} \quad (2.32)$$

and with  $\epsilon_0$  as the vacuum permittivity. The electrical field outside of the sphere at distance  $|\vec{r}|$  and direction  $\hat{e}_r = \vec{r}/|\vec{r}|$  is given by [106]

$$\vec{E}_{\text{out}} = -\nabla\Phi_{\text{out}} = \vec{E}_i + \frac{3(\vec{p} \cdot \hat{e}_r)\hat{e}_r - \vec{p}}{4\pi\epsilon_0 n_{\text{m}}^2 |\vec{r}|^3} \quad . \quad (2.33)$$

In general, expect for the temporal oscillation, this is the solution as for an oscillating dipole in the near field [107].

**Extinction, scattering and absorption.** In case of a nanosphere residing inside a constant homogeneous field, the nanoparticle's polarizability can be deduced (Eq. (2.32)). In the next step, the constant field is changed by an oscillating electrical field

$$\vec{E}_i = E_0 \hat{e}_z e^{i(k_{\text{m}} r - \omega t)} \quad , \quad (2.34)$$

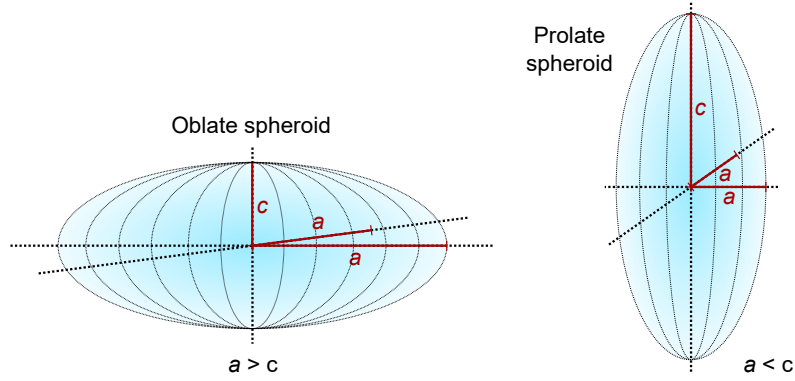


**Figure 2.8.:** Sketch of an oblate ( $a > c$ ) and a prolate ( $a < c$ ) spheroid.

with the wavenumber  $k_m = 2\pi n_m/\lambda_0$ . The nanosphere is considered to be so small that at a specific time the electrical field is approximately constant over the hole nanoparticle. Again, due to the external field, surface charges are induced, causing a dipole moment inside the sphere. Due to the oscillation of the external field, the surface charges oscillate with the same frequency. This can be described by a harmonic oscillator. Due to damping caused by friction, a fraction of the external field energy is absorbed by the nanoparticle. This is described by the absorption cross-section  $\sigma_{\text{abs}}$ . On the other hand, the incident light is also scattered at the nanosphere, which is described by the scattering-cross section  $\sigma_{\text{scat}}$ . Both, the absorption and scattering cross-sections can be summed up to the extinction cross-section

$$\sigma_{\text{ext}} = \sigma_{\text{abs}} + \sigma_{\text{scat}} \quad . \quad (2.35)$$

The derivation of the different cross-section is discussed in Ref. [108]. Here, the results are directly given for the scattering-cross section

$$\sigma_{\text{scat}} = \frac{k_m^4}{6\pi\epsilon_0^2} |\alpha|^2 \quad (2.36)$$

and the absorption cross-section

$$\sigma_{\text{abs}} = \frac{k_m}{\epsilon_0} \Im(\alpha) \quad . \quad (2.37)$$

### 2.2.2. Anisotropically shaped nanoparticle

If a homogeneous nanoparticle consists of an anisotropic shape, its polarizability depends on the polarization direction of the external field ("birefringence"). This is explained using the example of a spheroid.

A spheroid is a special type of an ellipsoid, consisting of two semiaxes of the same length ( $a \neq c, a = b$ ). Here, two different types of spheroids can be distinguished by  $a > c$  ("oblate spheroid") and  $a < c$  ("prolate spheroid") (see Fig. 2.8). Due to the different semi-axis lengths,

different optical polarizabilities occur. The optical polarizability of the general case of an ellipsoid ( $a \neq b \neq c$ ) can be described as [109, 110]

$$\alpha = \epsilon_0 V_e \alpha_j \quad , \quad (2.38)$$

with the ellipsoid volume  $V_e = 4\pi abc/3$  and the normalized polarizability  $\alpha_j$  for the different half axes directions  $j = [a, b, c]$ . If the external electrical field is polarized in the direction of half axis  $j$ , the normalized polarizability is given by

$$\alpha_j = \frac{n_e^2 - n_m^2}{n_m^2 + N_j(n_e^2 - n_m^2)} \quad . \quad (2.39)$$

Here,  $n_e$  is the refractive index of the homogeneous ellipsoid and the depolarization factor  $N_j$  is defined by

$$N_j = \frac{abc}{2} \int_{s=0}^{\infty} \frac{ds}{(s+j^2)\sqrt{(s+a^2)(s+b^2)(s+c^2)}} \quad (2.40)$$

and fulfills

$$N_a + N_b + N_c = 1 \quad . \quad (2.41)$$

Hence, for an *oblate spheroid* with  $a = b$  and  $a > c$ , the depolarization factor in  $c$ -direction is

$$N_c = \frac{a^2}{a^2 - c^2} \left( 1 - \frac{c}{\sqrt{a^2 - c^2}} \arctan \left( \sqrt{\frac{a^2}{c^2} - 1} \right) \right) \quad (2.42)$$

and for a *prolate spheroid* with  $a = b$  and  $a < c$  it is

$$N_c = \frac{a^2}{c^2 - a^2} \left( -1 + \frac{c}{2\sqrt{c^2 - a^2}} \ln \left( \frac{c + \sqrt{c^2 - a^2}}{c - \sqrt{c^2 - a^2}} \right) \right) \quad . \quad (2.43)$$

The respective depolarization factors in  $a$ -direction result from Eq. (2.41).

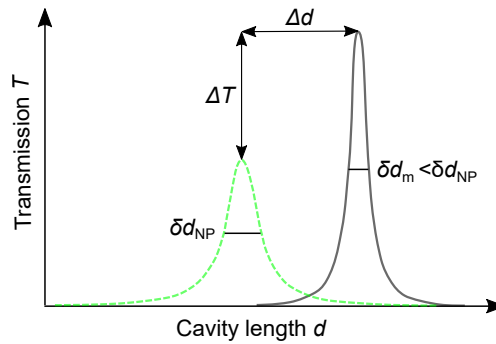


**Figure 2.9.:** Change of the cavity length at which the resonance of the excited mode occurs, when a nanoparticle enters the cavity standing-wave light field. The nanoparticle produces a shift  $\Delta d$  of the unperturbed resonance (black) to a smaller cavity length (green resonance) and also the resonance amplitude decreases by  $\Delta T$  and the linewidth broadens to  $\delta d_{NP} > \delta d_m$ .

### 2.3. Interaction of nanoparticles with a cavity mode

When a polarizable and non-fluorescent nanoparticle of complex refractive index  $n_{\text{NP}} = n_{\text{R}} + in_{\text{I}}$  enters the cavity standing-wave light field (see Chapter 2.1), the resonance of the excited mode changes (see Fig. 2.9). A fraction of the intracavity light is absorbed and another fraction is scattered by the nanoparticle (see Chapter 2.2), both producing a decrease of the resonance amplitude  $\Delta T$  and broadening of its linewidth  $\delta d_{\text{NP}} > \delta d_{\text{m}}$ . Since the refractive index  $n_{\text{NP}}$  is larger than the refractive index of the cavity medium  $n_{\text{m}}$ , the total optical path length increases and thus the resonance shifts to a smaller cavity length  $d$ . Thereby, the strength of the overall resonance change depends on the optical polarizability tensor of the nanoparticle (see Chapter 2.2). Consequently, the detection of the resonance change allows the investigation of individual nanoparticles' properties. In the following subsections, the three effects, decrease of amplitude, linewidth broadening and resonance shift, are explained in more detail for a spherical, homogeneous nanoparticle with radius  $r_{\text{NP}}$ . Besides, the hydration shell of a  $\text{SiO}_2$  nanosphere is considered. This knowledge is important since the later measurement results show that the FP sensor is sensitive to the increased size and the effective refractive index of the dispersed  $\text{SiO}_2$  nanoparticles in water.

#### 2.3.1. Scattering and absorption losses

When a nanoparticle resides in the cavity standing-wave light field, it produces a decrease of the resonance amplitude and a broadening of its linewidth, because the nanoparticle absorbs and scatters a fraction of the light (see Chapter 2.2). The amount of scattering depends on the scattering cross-section  $\sigma_{\text{scat}}$  and the amount of absorption depends on the absorption cross-section  $\sigma_{\text{abs}}$  of the nanoparticle. Since the change of the resonance is an effect of both, the cross-sections can be summed up to the extinction cross-section  $\sigma_{\text{ext}} = \sigma_{\text{scat}} + \sigma_{\text{abs}}$ . At first, the relation between the extinction cross-section and the decrease of the amplitude is derived and then the linewidth broadening is discussed.

**Decrease of the transmission amplitude.** In the following, the connection between the amplitude change and nanoparticle extinction cross-section is derived briefly. If the reader is interested in a detailed derivation, they can find more detailed descriptions in [100, 108, 111]. The following derivations are also based on these sources.

In Chapter 2.1 the losses inside an empty cavity are discussed and an expression for the overall transmission is derived (Eq. (2.9)). Now, a nanosphere inside the FP resonator is considered, thus leading to an additional loss  $2L_{\text{NP}}$  for one round trip of the reflected light inside the cavity (see Fig. 2.10). As a result, the overall transmission can be approximated as

$$T_{\text{cav}}(L_{\text{NP}}) \propto \frac{4T_1 T_2}{(2L_{\text{NP}} + L_{\text{m}} + A_1 + A_2 + T_1 + T_2)^2} \quad , \quad (2.44)$$

if only low losses of the mirrors are considered. Since it is difficult to determine the absorption and scattering losses of the mirrors, the intrinsic cavity losses can be derived from the finesse

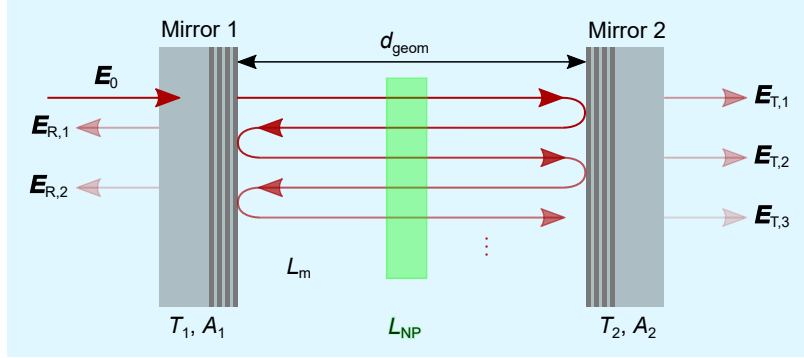


**Figure 2.10.:** Loss channels inside a FP cavity. The incident light  $E_0$  is coupled into the cavity through mirror 1. Inside the cavity, the light is reflected back and forth between the mirrors. At each round trip, a fraction of the light is lost. The liquid into which the mirrors are immersed absorbs a fraction of the light ( $L_m$ ), the nanoparticle scatters and absorbs a part of the light, leading to the loss  $L_{NP}$  and the mirrors absorb and scatter a fraction of the light as well ( $A_1, A_2$ ) and enable partial transmittance ( $T_1, T_2$ ).

of the empty cavity  $\mathcal{F}$  in Eq. (2.11). If spherical cavity mirrors are used and the fundamental mode ( $TEM_{00}$ ) is excited, the intracavity light field distribution has in the lateral direction the shape of a Gaussian beam with the beam waist  $w_0$  and in longitudinal direction it is a standing-wave (see Fig. 2.3 and Eq. (2.13) for the mathematical description). At the center of the antinode of the standing-wave, the intensity is maximal, and therefore the nanoparticle produces maximum loss, when it resides there. The maximum loss  $L_{NP,max}$  is then given by [110]

$$L_{NP,max} \approx \frac{4\sigma_{ext}}{\pi w_0^2} \quad (2.45)$$

if  $\sigma_{ext}$  is much smaller than  $w_0$ .

If the nanoparticle size can't be neglected, the extinction cross-section of a nanoparticle with a given size and refractive index can be derived by Mie theory. More information can be taken from various literature as [112, 113, 114].

In the later shown experimental results, the percentage change of the transmission amplitude due to a nanoparticle is investigated. Therefore, the decrease of amplitude ( $DOA$ ) is introduced:

$$DOA = 100\% \left( 1 - \frac{T_{cav}(L_{NP})}{T_{cav}(0)} \right) . \quad (2.46)$$

**Linewidth broadening.** The additional loss  $L_{NP}$  produced by the nanoparticle leads not only to the decrease of the resonance amplitude, but also to a linewidth broadening. Eq. (2.8) changes to the following expression for the FWHM:

$$\delta\nu = \Delta\nu_{FSR} \frac{T_1 + T_2 + A_1 + A_2 + L_m + 2L_{NP}}{2\pi} . \quad (2.47)$$

### 2.3.2. Resonance frequency shift

The optical cavity length changes, when a nanoparticle enters the cavity standing-wave light field. Therefore, the mirror separation has to be adapted, when the resonance condition should be maintained and the laser wavelength is kept constant. In the following, the optical length change  $\Delta d$  is described as a frequency shift  $\Delta\nu$ , but both relate to each other by

$$\Delta d = \frac{\Delta\nu}{\delta\nu} \cdot \delta d \quad , \text{ with} \quad (2.48)$$

$$\delta d = \frac{d_{\text{opt}} \cdot \delta\nu \cdot \lambda_0}{c_0} \quad . \quad (2.49)$$

First, a spherical, homogeneous nanoparticle with polarizability  $\alpha$  and a size much smaller than the wavelength ( $r_{\text{NP}} \ll \lambda$ ) is considered (Rayleigh limit, see Chapter 2.2). Both cases, the empty cavity ( $k_m = k_0/n_m$ ,  $\vec{E}_0$ ,  $\epsilon_m = n_m^2$ ) as well as the same cavity with a nanosphere residing inside the light field ( $k_{\text{NP}} = k_0/n_{\text{NP}}$ ,  $\vec{E}$ ,  $\epsilon_{\text{NP}} = n_{\text{NP}}^2$ ) obey the Helmholtz equation

$$[\Delta + \epsilon_0 \epsilon_m k_m^2] \vec{E}_0 = 0 \quad \text{and} \quad (2.50)$$

$$[\Delta + \epsilon_0 \epsilon_{\text{NP}} k_{\text{NP}}^2] \vec{E} = 0 \quad . \quad (2.51)$$

In first order perturbation theory, the permittivity  $\epsilon_m$  as well as the wavenumber  $k_m$  of the empty cavity only change slightly when the nanoparticle resides in the cavity:

$$\epsilon_{\text{NP}} \approx \epsilon_m + \delta\epsilon \quad \text{and} \quad (2.52)$$

$$k_{\text{NP}} \approx k_m + \delta k \quad . \quad (2.53)$$

By an integration of the Helmholtz equations, the important relation for frequency shift in first order perturbation theory is derived [52]

$$\frac{\delta\nu}{\nu_0} = \frac{\delta k}{k_0} \approx -\frac{1}{2} \frac{\int_{V_{\text{NP}}} \delta\epsilon |E_0|^2 d\vec{r}}{\int_V \epsilon_m |E_0|^2 d\vec{r}} \quad (2.54)$$

Taking into account the geometry of the nanosphere, the electrical field inside the nanosphere has to be considered. According to Eq. (2.27), the electrical field is [52]

$$\vec{E}_{\text{in}} = -\nabla\Phi_{\text{in}} \quad (2.55)$$

$$= \frac{3n_m^2}{n_{\text{NP}}^2 + 2n_m^2} E_0 \quad . \quad (2.56)$$

Consequently, with

$$\delta\epsilon = \frac{3n_m^2 (n_{\text{NP}}^2 - n_m^2)}{n_{\text{NP}}^2 + 2n_m^2} \delta(\vec{r} - \vec{r}_{\text{NP}}) \quad (2.57)$$

the frequency shift produced by a nanosphere is

$$\frac{\delta\nu}{\nu_0} \approx -\frac{3}{2} \Re \left[ \frac{n_{\text{NP}}^2 - n_m^2}{n_{\text{NP}}^2 + 2n_m^2} \right] \frac{|E_0(\vec{r}_{\text{NP}})|^2 V_{\text{NP}}}{\int_V |E_0|^2 d\vec{r}} \quad (2.58)$$

Inserting the polarizability of a nanosphere (see Eq. 2.32) and introducing  $\vec{r}_{\text{NP}} = (x_0, y_0, z_0)^T$  for its position the produced frequency shift  $\Delta\nu_{00}$  of the fundamental mode ( $\text{TEM}_{00}$ ) can be transformed to [59, 115]

$$\Delta\nu_{00}(x_0, y_0, z_0) = \frac{\Re(\alpha) \cdot c_0}{2\lambda_m \epsilon_0 V_m} \frac{I_{00}(x_0, y_0, z_0)}{I_0}, \quad (2.59)$$

with  $\lambda_m = \lambda_0/n_m$  being the wavelength in medium. Here,  $\delta\nu$  was replaced by  $\Delta\nu$  as in the following  $\delta\nu$  is defined as the full width half maximum and  $\Delta\nu$  as the frequency shift. The intracavity light field of the fundamental mode in Eq. (2.13) is normalized to the maximal intensity  $I_{00}(0, 0, 0) = I_0$  and the phase terms of the cavity standing-wave light field are neglected. The cavity mode volume  $V_m$  can be approximated by [116, 103]

$$V_m = \frac{\pi w_0^2 d_{\text{opt}}}{4}. \quad (2.60)$$

If the the size of the nanosphere is not negligible, but sufficiently small (in the order of  $\left| \frac{n_{\text{NP}}}{n_m} \right| \frac{2\pi r_{\text{NP}}}{\lambda_m} \approx 1$  [108]), an integration over the nanosphere's volume  $V_{\text{NP}}$  is demanded and the frequency shift is described by [86]:

$$\Delta\nu_{00}(x_0, y_0, z_0) = \frac{\Re(\alpha) \cdot c_0}{2\lambda_m \epsilon_0 V_m} \int_{V_{\text{NP}}} dV_{\text{NP}} \cdot \frac{I_{00}(x - x_0, y - y_0, z - z_0)}{I_0}. \quad (2.61)$$

With equations (2.3), (2.4), (2.10), (2.12) and (2.60) this can be transformed to

$$\Delta\nu_{00}(x_0, y_0, z_0) = \frac{\Re(\alpha) \cdot n_m}{2\epsilon_0} \int_{V_{\text{NP}}} dV_{\text{NP}} \cdot \frac{I_{00}(x - x_0, y - y_0, z - z_0)}{I_0} \frac{\delta\nu \cdot Q}{V_m}. \quad (2.62)$$

**Resonance frequency shifts produced by a single nanosphere residing in the  $\text{TEM}_{00}$  mode.** Fig. 2.11 shows the simulated frequency shifts when a nanosphere resides in the  $\text{TEM}_{00}$  mode at different positions. According to Eq. (2.61), the frequency shift is maximal at the center of the antinode ( $z_0=0, y_0=0, x_0=0$ ) and is smaller when the nanosphere is at lower intensities. If a single nanosphere diffuses in water and is probed by the cavity standing-wave light field, the probability to measure a smaller frequency shift is greater than measuring a larger frequency shift. This is regarded to be obvious by considering the schematic in Fig. 2.12 a). The contour lines represent areas of equal intensity and consequently, at those locations, the same frequency shifts are produced by the nanosphere. Fig. 2.12 b) shows histograms of the produced frequency shifts if the nanosphere was exactly once at every position in the standing-wave light field. This result was obtained by the simulation of different frequency shift matrices (Fig. 2.11) with the same nanoparticle radius, but for different refractive indices. Subsequently, the frequency shift values of the matrix were plotted in an histogram. In Fig. 2.12, each histogram has a steep decay at the maximal occurring frequency shift. Besides, a larger refractive index leads to a larger frequency shift.

**Frequency shifts of the higher-order transverse modes  $\text{TEM}_{01}$  and  $\text{TEM}_{10}$ .** If the nanosphere resides in the higher-order transverse modes, the intensity distribution of the

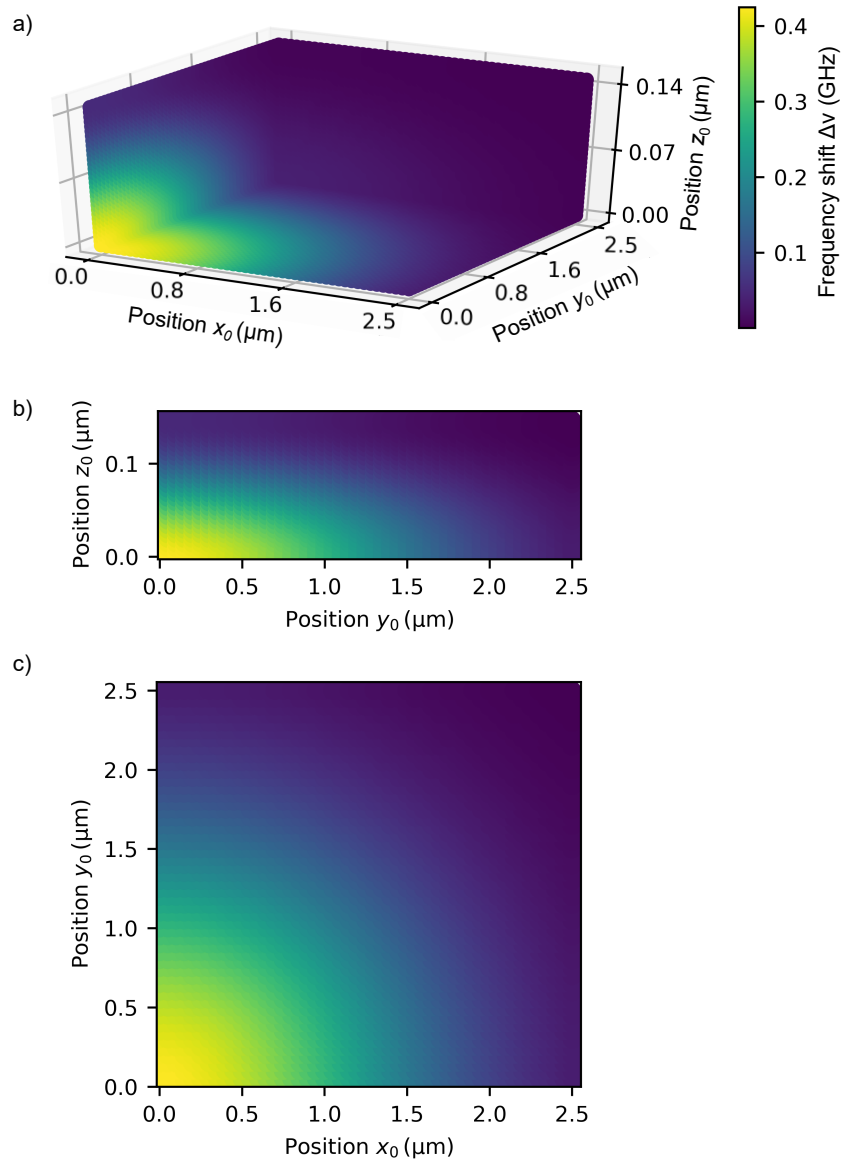


**Figure 2.11.:** The in Python simulated frequency shifts produced by a spherical, homogeneous  $\text{SiO}_2$  nanoparticle at different residential positions inside the fundamental mode light field ( $\text{TEM}_{00}$ ) and which is dispersed in water. For the simulation a nanosphere radius of  $r_{\text{NP}} = 71.5 \text{ nm}$ , a refractive index of  $n_{\text{NP}} = 1.42$ , a cavity quality factor of  $Q = 1.7 \cdot 10^6$ , a mode volume of  $V_m = 110 \mu\text{m}^3$  and a vacuum wavelength of  $\lambda_0 = 780 \text{ nm}$  were assumed. The remaining cavity parameters can be taken from Table 3.6, CP1. For reasons of symmetry, only one octant of the antinode is shown (also see Fig. 2.12a). **a)** Three dimensional representation of the frequency shift matrix. **b)** Cut through the matrix at  $x_0 = 0$ . **c)** Cut through the matrix at  $z_0 = 0$ .

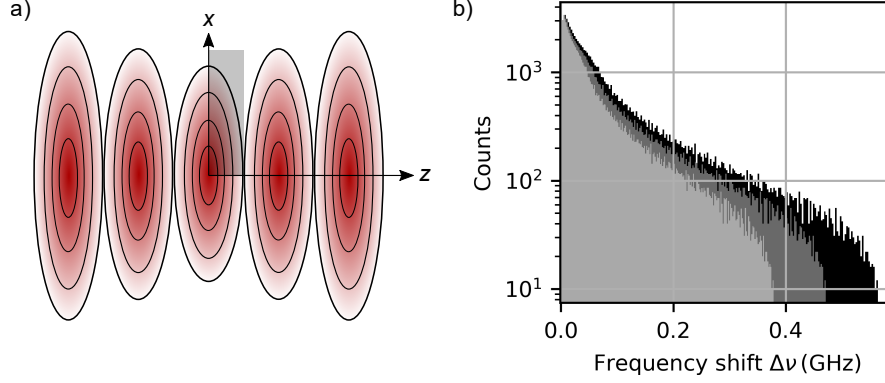


**Figure 2.12.:** Density of states inside the cavity standing-wave light field and frequency shift probabilities. **a)** Contour plot of the intracavity light field. The gray rectangle marks the section of the antinode (one octant), which is shown in 2.11. **b)** Histograms for the produced frequency shifts of a SiO<sub>2</sub> nanosphere with radius  $r_{\text{NP}} = 71.5$  nm and refractive index  $n_{\text{NP}} = 1.41$  (light gray),  $n_{\text{NP}} = 1.43$  (dark gray) and  $n_{\text{NP}} = 1.45$  (black). The nanosphere was assumed to be exactly once at each position inside the cavity standing-wave light field. The cavity parameters are the same as in Fig. 2.11.

TEM<sub>00</sub> mode in Eq. (2.61) has to be exchanged by the intensity distributions of the higher-order transverse modes (see Eq. (2.18)). Hence, the transverse modes of order 1 are described by

$$I_{01}(x, y, z) = \frac{8(x - x_0)^2}{w_{01}(z - z_0)^2} I_G(x, y, z) \cos^2(k_m \cdot z) \quad (2.63)$$

for the TEM<sub>01</sub> and

$$I_{10}(x, y, z) = \frac{8(y - y_0)^2}{w_{10}(z - z_0)^2} I_G(x, y, z) \cos^2(k_m \cdot z) \quad (2.64)$$

for the TEM<sub>10</sub> mode and their frequency shifts are given by

$$\Delta\nu_{01}(x_0, y_0, z_0) = \frac{\Re(\alpha) \cdot c}{2\lambda_m \epsilon_0 V_m} \int_{V_{\text{NP}}} dV_{\text{NP}} \cdot \frac{I_{01}(x - x_0, y - y_0, z - z_0)}{I_0} \quad (2.65)$$

and

$$\Delta\nu_{10}(x_0, y_0, z_0) = \frac{\Re(\alpha) \cdot c}{2\lambda_m \epsilon_0 V_m} \int_{V_{\text{NP}}} dV_{\text{NP}} \cdot \frac{I_{10}(x - x_0, y - y_0, z - z_0)}{I_0} . \quad (2.66)$$

### 2.3.3. Hydrate shell of quartz glass nanospheres dispersed in water

Within this work, SiO<sub>2</sub> nanospheres were investigated in water. In order to understand the later shown results concerning the hydrodynamic radius and the effective refractive index of the SiO<sub>2</sub> silica nanospheres, the basic understanding is created here.

The surface of SiO<sub>2</sub> nanospheres is covered with silanol groups (hydrophilic) and with hydrophobic siloxane groups. When the nanospheres are immersed in water, a chemical potential difference occurs at the interface between water and nanospheres. In order to minimize the

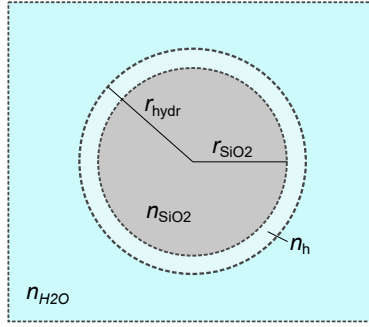


**Figure 2.13.:** Simplified schematic representation of the developed hydrate shell, when a  $\text{SiO}_2$  nanosphere is dispersed in water. Due to the formation of a hydrate shell, the intrinsic radius of the bare nanosphere  $r_{\text{SiO}_2}$  is increased to the hydrodynamic radius  $r_{\text{hydr}}$ . The effective refractive index  $n_{\text{eff}}$  is composed of the intrinsic refractive index  $n_{\text{SiO}_2}$  and the refractive index of the hydrate shell  $n_h$ . [95], supplementary information.

Gibbs free energy, a fraction of the free silanol groups dissociate and acquire a negative surface charge [117, 118, 119]:



For the sake of simplicity, other dissociation processes are not shown. At equilibrium, a static electric field at the surface arises, which attracts water molecules. In the innermost zone, the water molecules adsorb to the nanosphere surface via hydrogen bonding. This so-called Stern layer is rigid and the potential decreases linearly. In the outer zone, a diffusive electric double-layer is developed (Gouy-Chapman layer), where the potential decreases to zero. Consequently, an expanded hydrate shell surrounds the nanosphere, which increases its intrinsic radius  $r_{\text{SiO}_2}$  to the effective radius  $r_{\text{hydr}}$  (see Fig. 2.13) [120, 121, 119].

When  $\text{SiO}_2$  dispersed in water are investigated with the fiber-based FP sensor, the expanded size of the nanoparticle  $r_{\text{hydr}}$  as well as the effective refractive index  $n_{\text{eff}}$ , consisting of the intrinsic refractive index  $n_{\text{SiO}_2}$  and the refractive index of the hydrate shell  $n_h$  is measured (see Chapter 4). Therefore, the effective polarizability of a nanosphere with a surrounding hydrate shell is described by

$$\mathfrak{R}(\alpha) = 4\pi r_{\text{hydr}}^3 \epsilon_0 \frac{n_{\text{eff}}^2 - n_{\text{m}}^2}{n_{\text{eff}}^2 + 2n_{\text{m}}^2} \quad (2.68)$$

(compare with Eq. (2.32)). In Chapter 5 it will be shown that the hydrodynamic radius can be determined independently from the effective refractive index and by the measurement of the effective polarizability (Chapter 4), the effective refractive index can be determined as well. Besides, there are indications that the intrinsic polarizability of the bare nanosphere can be measured by the FP sensor when small concentrations of salt are added to the colloidal solution of the nanosphere (see Chapter 4.4). Accordingly, when the intrinsic radius  $r_{\text{SiO}_2}$  is known (e.g. by scanning electron microscope (SEM) images), presumably the intrinsic refractive index of the bare nanoparticle  $n_{\text{SiO}_2}$  can be derived from the intrinsic polarizability.

Finally, the refractive index of the hydrate shell  $n_h$  can be deduced. According to [122], the polarizability of a core-shell nanosphere is

$$\alpha_{CS} = 4\pi r_{NP}^3 \epsilon_0 \frac{(2n_h^2 + n_{SiO_2}^2)(n_h^2 - n_m^2)r_{hydr}^3 + (n_{SiO_2}^2 - n_h^2)(2n_h^2 + n_m^2)r_{SiO_2}^3}{(2n_h^2 + n_{SiO_2}^2)(2n_m^2 + n_h^2)r_{hydr}^3 + 2(n_{SiO_2}^2 - n_h^2)(n_h^2 - n_m^2)r_{SiO_2}^3} . \quad (2.69)$$

Since the effective polarizability (Eq. (2.68)) and the polarizability of the core-shell nanosphere (Eq. (2.69)) have to be equal, the following relation applies:

$$\frac{n_{eff}^2 - n_m^2}{n_{eff}^2 + 2n_m^2} = \frac{(2n_h^2 + n_{SiO_2}^2)(n_h^2 - n_m^2)r_{hydr}^3 + (n_{SiO_2}^2 - n_h^2)(2n_h^2 + n_m^2)r_{SiO_2}^3}{(2n_h^2 + n_{SiO_2}^2)(2n_m^2 + n_h^2)r_{hydr}^3 + 2(n_{SiO_2}^2 - n_h^2)(n_h^2 - n_m^2)r_{SiO_2}^3} . \quad (2.70)$$

This can be transformed to

$$n_h = \sqrt{-\frac{p}{2} + \sqrt{\frac{p^2}{4} - q}} , \quad (2.71)$$

with

$$p = \frac{n_{eff}^2 (r_{SiO_2}^3 + 2r_{hydr}^3) - n_{SiO_2}^2 (2r_{SiO_2}^3 + r_{hydr}^3)}{2(r_{SiO_2}^3 - r_{hydr}^3)} \quad (2.72)$$

and

$$q = -\frac{n_{SiO_2}^2 n_{eff}^2}{2} . \quad (2.73)$$

## 2.4. Simulation of the nanoparticle's translational diffusion probed by a Fabry-Pérot microcavity

This chapter covers the three-dimensional tracking of the Brownian motion of a single, spherical-shaped nanoparticle within a FP cavity and the information gained from the track about the nanosphere's hydrodynamic radius. Parts of this chapter have been submitted to [95] (supplementary information). The Brownian motion of a nanoparticle is described by its translation as well as by its rotation. If the nanoparticle is spherical, the translational diffusivity is, according to the Stokes-Einstein-relation [123, 124]

$$D_t = \frac{k_B T}{\gamma_t} , \quad (2.74)$$

with the friction coefficient  $\gamma_t = 6\pi\eta r_{hydr}$ . In addition, a nanosphere undergoes diffusive rotational motion, with

$$D_r = \frac{k_B T}{\gamma_r} \quad (2.75)$$

and  $\gamma_r = 8\pi\eta r_{hydr}^3$  for the rotational friction coefficient. The translation and the rotation are induced by the collisions of the fluid molecules (thermal noise) [125]. In order to track

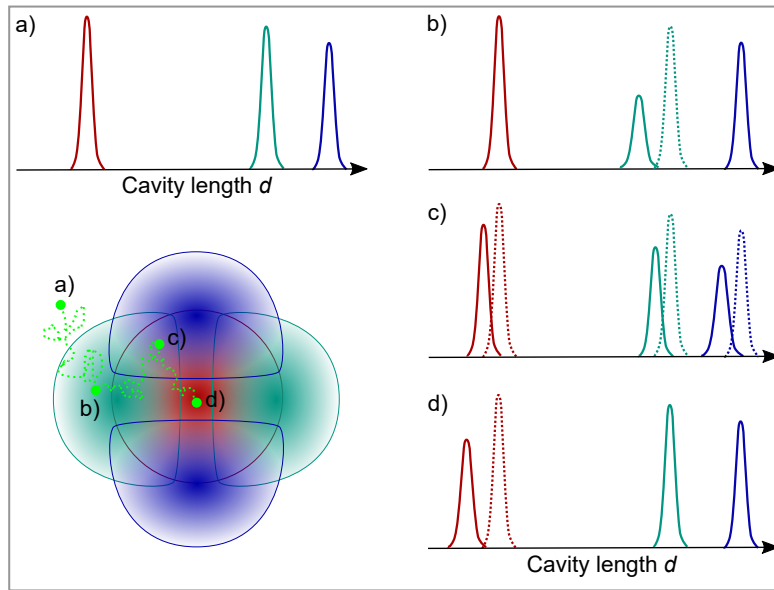


**Figure 2.14.:** Schematic illustration of the different mode shifts depending on the nanosphere's position inside the cavity light field. In red (green, blue) the  $TEM_{00}$  ( $TEM_{01}$ ,  $TEM_{10}$ ) is illustrated as a cross-section through the standing-wave light field at  $z = 0$  (see Fig. 2.3) and as the respective resonances. Depending on the position of the nanosphere (green full circle), the resonances **a)** are not shifted, **b)** only the  $TEM_{01}$  is shifted, **c)** all resonances are shifted and **d)** only the  $TEM_{00}$  mode is shifted. Submitted to [95].

the translational motion of the nanosphere, the fundamental mode  $TEM_{00}$  and the radially expanded higher-order transverse modes  $TEM_{01}$  and  $TEM_{10}$  are scanned simultaneously. In Chapter 2.4.1 it is shown that the three-dimensional track can be extracted from the measured frequency shifts of the three modes. In Chapter 2.4.2 the mean squared displacement is derived from the three-dimensional track and the connection to the nanosphere's diffusivity and hydrodynamic radius is presented.

#### 2.4.1. Simulation of the measured signal generated by a nanoparticle diffusing in water and verification of the tracking algorithm

The simultaneous scanning over the three cavity modes  $TEM_{00}$ ,  $TEM_{01}$  and  $TEM_{10}$  and thereby the differently measured frequency shifts generated by a nanosphere diffusing in water provides information about the nanosphere's position (see Fig. 2.14 and Chapter 2.3.2). Due to the symmetry of the light field, the absolute position of the nanosphere can't be determined as soon as the nanosphere changes the octant within an antinode or changes between antinodes (in Fig. 2.12, an octant of the antinode is marked with a gray rectangle). Instead, the derived three-dimensional path from the detected frequency shifts is folded back into one octant of the antinode. Although the absolute position of the nanosphere gets lost, its performed Brownian motion is still contained in the back-folded track when only short time scales are considered, before the track is back-folded again. But an additional uncertainty comes into play, which demands a tracking algorithm: The measured frequency shifts are superimposed

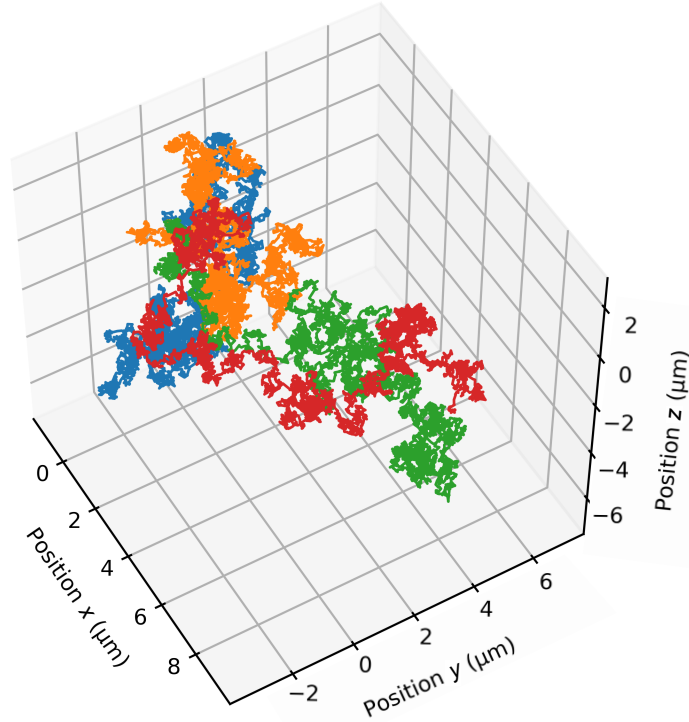


**Figure 2.15.:** Monte Carlo simulation of four exemplary single nanosphere tracks, depicted in different colors. Each track starts at zero position and is simulated for a nanosphere with a hydrodynamic radius of 75.3 nm, which is dispersed in water.

by the measurement noise, which allows the particle to reside in a certain region of the octant at a given time. In the following, the measured frequency shifts are simulated and different tracking algorithms are compared. For this purpose, various steps are carried out in succession: First, a random three-dimensional nanosphere track is Monte Carlo simulated. In the second step, the track is folded back in  $x, y$ -direction into one octant of the standing-wave. In the third step, the theoretically produced frequency shifts for the  $TEM_{00}$ , the  $TEM_{01}$  and the  $TEM_{10}$  are calculated and on each shift, a random measurement noise is added. Finally, from the frequency shifts, the position of the nanosphere inside the light field is derived via different algorithms and compared with the originally simulated path.

**Monte Carlo simulation.** The diffusion time for the free diffusion of the center of the nanosphere is described by [126, 127]

$$\tau_D = \frac{\langle r^2 \rangle}{2b \cdot D} \quad (2.76)$$

Here,  $b$  is the dimension and  $r$  is the moved distance. This can be transformed to a mean stepwise position change within the time step  $\Delta t$  by

$$\sqrt{\langle \Delta \vec{r}^2 \rangle} = \sqrt{2bD\Delta t} \quad . \quad (2.77)$$

At each individual time step, the nanosphere doesn't move exactly  $\sqrt{\langle \Delta \vec{r}^2 \rangle}$ , but the movement is probabilistic and is described by a Gaussian probability distribution  $P(r)$  with the standard deviation  $\sigma = \sqrt{2bD\Delta t}$  [128, 129, 130]:

$$P(r) = \frac{1}{\sigma\sqrt{2\pi}} \exp\left(-\frac{1}{2}\left(\frac{r}{\sigma}\right)^2\right), r \in \mathbb{R}. \quad (2.78)$$

The direction of the nanoparticle movement  $\hat{e}_r$  at time step  $\Delta t$  can be expressed by

$$\hat{e}_r = \frac{(x^{(k)}, y^{(k)}, z^{(k)})^T}{\sqrt{x^{(k)2} + y^{(k)2} + z^{(k)2}}}, \quad (2.79)$$

with  $x^{(k)}$ ,  $y^{(k)}$  and  $z^{(k)}$  randomly chosen from the probability distributions  $P(x)$ ,  $P(y)$  and  $P(z)$  at the  $k$ 'th time step:

$$P(x) = \frac{1}{\sqrt{2\pi}} \exp(-0.5x^2), x \in \mathbb{R}, \quad (2.80)$$

$$P(y) = \frac{1}{\sqrt{2\pi}} \exp(-0.5y^2), y \in \mathbb{R}, \quad (2.81)$$

$$P(z) = \frac{1}{\sqrt{2\pi}} \exp(-0.5z^2), z \in \mathbb{R}. \quad (2.82)$$

Thus, the probabilistic discrete step is given by

$$\Delta \vec{r} = r^{(k)} \cdot \hat{e}_r. \quad (2.83)$$

Here,  $r^{(k)}$  is the randomly selected  $k$ 'th step distance with the Gaussian probability distribution in Eq. (2.78). Finally, the new position  $\vec{r}_k$  can be derived from the position before by

$$\vec{r}_k = \vec{r}_{k-1} + \Delta \vec{r}. \quad (2.84)$$

Fig. 2.15 shows four simulated three-dimensional Brownian motion tracks all starting at zero position and for a nanosphere with a hydrodynamic radius of 75.3 nm, which is dispersed in water. The time step is  $\Delta t = 3.3 \mu\text{s}^1$ .

**Back-folding of the simulated track into one octant for the lateral directions.** To artificially lengthen the residence time of the particle in the standing-wave light field, such a simulated track is folded back into one octant in  $x$ ,  $y$ -direction. This is explained for the

<sup>1</sup> Those parameters were chosen, because the discussed experiments in Chapter 5 were also carried out under these conditions.

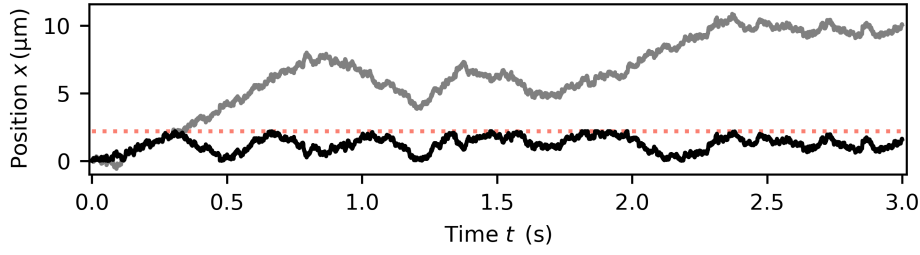


**Figure 2.16.:** The simulated nanoparticle track (gray) is back-folded into the octant  $0 \leq x \leq 2.2 \mu\text{m}$  (black). The red dotted line marks the upper border.

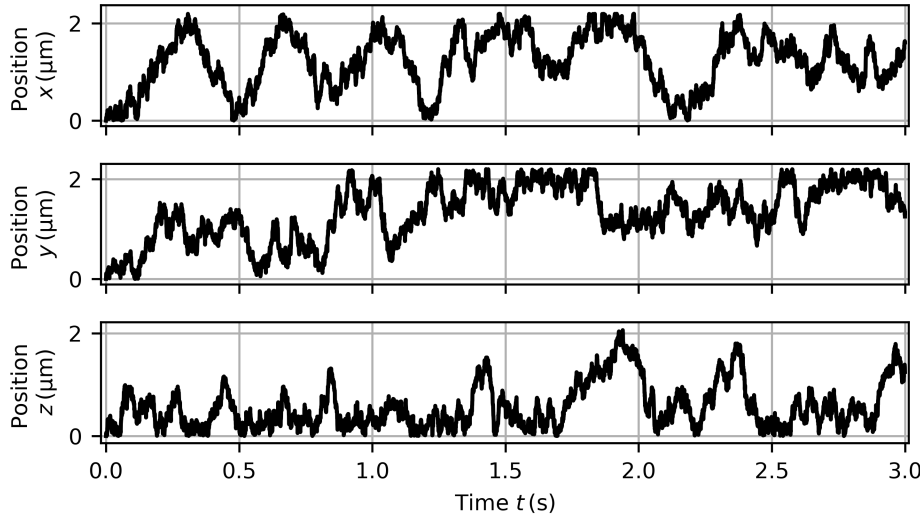


**Figure 2.17.:** Back-folded simulated tracking path for a nanosphere with the hydrodynamic radius  $r_{\text{hydr}} = 75.3 \text{ nm}$  dispersed in water. Submitted to [95].

$x$ -coordinate. When the position of the nanosphere at time  $x(t_k)$  is below 0 or exceeds  $2.2 \mu\text{m}$ <sup>2</sup>, the position  $x(t_k)$  and the following positions  $x(t_{k+1} \dots x(t_N))$  are mirrored on the horizontal line at the height of  $x(t_{k-1})$ :

$$x(t_{k \dots N}) = 2 \cdot x(t_{k-1}) - x(t_{k \dots N}) \quad . \quad (2.85)$$

The back folding of the track in  $x$ -direction is shown in Fig. 2.16 and the final result for all directions is shown in Fig. 2.17. The track in  $z$ -direction is also folded back when the  $z$ -value falls below zero (though it is not necessary). But there isn't an upper border in  $z$ -direction, which demands the particle to stay within the octant in order to simulate both, a change of the octant within an antinode and a change of the antinode itself.

**Theoretically calculated shifts.** In the next step, from the simulated, back-folded nanosphere diffusion track, the expected frequency shifts are calculated for the modes  $\text{TEM}_{00}$ ,  $\text{TEM}_{01}$

<sup>2</sup> This is taken from the experiment: At around  $x = 2.2 \mu\text{m} \approx 1.5w_0$ , the produced frequency shift by the nanosphere is approximately the measurement noise. For smaller values, the signal is greater than the measurement noise.

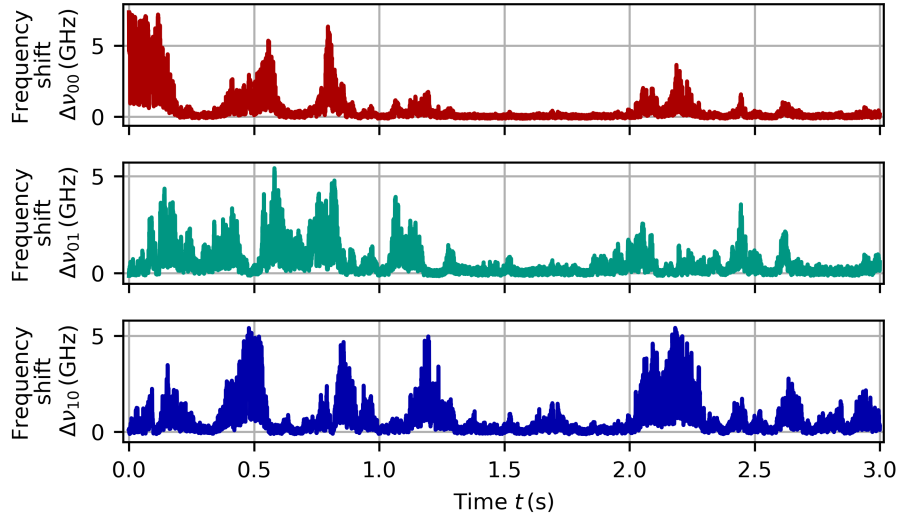


**Figure 2.18.:** Simulated frequency shifts for the nanosphere track shown in Fig. 2.17 including the measurement noise of 0.14 GHz (0.16 GHz, 0.14 GHz) for the TEM<sub>00</sub> (red) (TEM<sub>01</sub> (green), TEM<sub>10</sub> (blue)) mode. Submitted to [95].

and TEM<sub>10</sub>. Equations (2.61), (2.65) and (2.66) show the theoretical relations between the nanosphere's position inside the standing-wave light field and the calculated frequency shifts. For each frequency shift calculated in this way, a measurement noise of  $\sigma_{00} = 0.14$  GHz ( $\sigma_{01} = 0.16$  GHz,  $\sigma_{10} = 0.14$  GHz) is superimposed on the TEM<sub>00</sub> (TEM<sub>01</sub>, TEM<sub>10</sub>) mode by randomly choosing a value within the interval  $[\Delta\nu(t) - \sigma, \Delta\nu(t) + \sigma]$ . The result is depicted in Fig. 2.18 and the noise values are based on experimentally derived data (see Chapter 5).

**Comparison of different tracking algorithms.** In the last step, the nanosphere track is deduced from the simulated frequency shifts by different tracking algorithms. The algorithms' track solutions are compared with the original track in order to evaluate which track deviates least from the original one. As the simulated (and measured) frequency shifts include the measurement noise, the frequency shift triple values lie within a range of uncertainty

$$\Delta\nu_{00}(t) - \sigma_{00} \leq \Delta\nu_{00}(t) \leq \Delta\nu_{00}(t) + \sigma_{00} \quad , \quad (2.86)$$

$$\Delta\nu_{01}(t) - \sigma_{01} \leq \Delta\nu_{01}(t) \leq \Delta\nu_{01}(t) + \sigma_{01} \quad \text{and} \quad (2.87)$$

$$\Delta\nu_{10}(t) - \sigma_{10} \leq \Delta\nu_{10}(t) \leq \Delta\nu_{10}(t) + \sigma_{10} \quad . \quad (2.88)$$

This has the consequence that several nanosphere positions within the octant fulfill this condition. In the following, three different tracking algorithms are tested:

- Algorithm 1: Chooses the position at time  $t$  which has the shortest distance to the position before at  $t - 1$ , but the distance has to be non-zero.
- Algorithm 2: Chooses the position at time  $t$  which has from all possible positions the mean distance to the position before at  $t - 1$ .

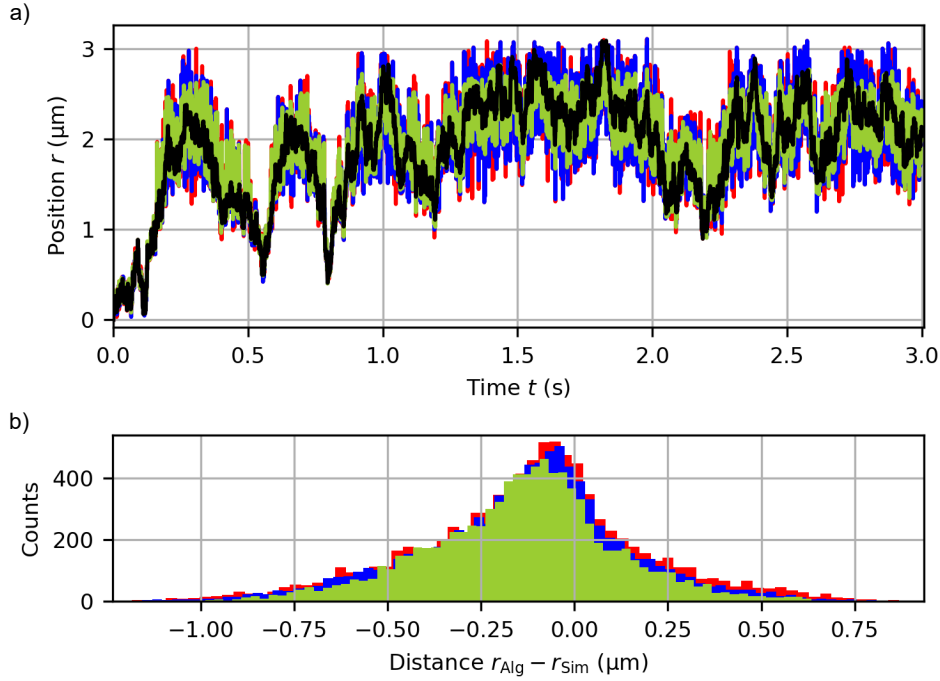


**Figure 2.19.:** Derived tracks from the simulated frequency shifts calculated by different evaluation algorithms. **a)** The black curve is the original track, the green curve is derived from the absolute mean position, the blue curve originates from the minimum distance algorithm, and the red curve from the mean distance to the position before. **b)** Deviations from the original track. At each time the distance between the original track and the track derived by the respective algorithm is calculated and all distances are summarized by the respective histograms. Submitted to [95].

- Algorithm 3: Doesn't take into account the previous position, but takes the absolute mean position of all possible positions at time  $t$ .

Fig. 2.19 shows the result for the different tracking algorithms. Each algorithm follows the original track. However, algorithm 3 deviates the least from the original track with a standard deviation of  $0.26 \mu\text{m}$  instead of  $0.29 \mu\text{m}$  (algorithm 1) and  $0.31 \mu\text{m}$  (algorithm 2). Therefore the absolute mean position is chosen for the evaluation of the experimentally derived data in Chapter 5.

### 2.4.2. Mean squared displacement

In the following it is discussed, how the hydrodynamic radius of the nanosphere can be obtained from its track. This is directly shown for the simulated track in Fig. 2.19, green, which is derived from the simulated frequency shifts and with the third tracking algorithm. The core variable of this analysis is the mean squared displacement (*MSD*). As the simulated track is limited to the antinodes octant ( $x \in [0, 2.2 \mu\text{m}]$ ,  $y \in [0, 2.2 \mu\text{m}]$ ,  $z \in [0, \lambda_0 / (4 \cdot n_m)]$ ), the track is divided into sequences. A new sequence  $i$  starts, when the nanosphere reaches a border of the octant, because here, the information about the absolute distance to the earlier positions is no longer meaningful. The division into sequences is shown in Fig. 2.20 by different colors

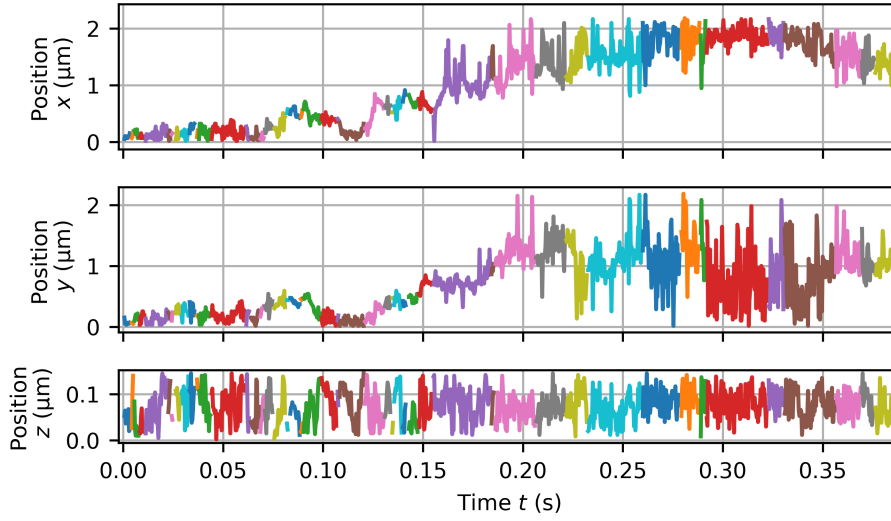


**Figure 2.20.:** Division of the Monte Carlo simulated track in different segments depicted in different colors. A new segment starts, when the nanosphere reaches the border of the octant sensing volume. Shown in [95] for measured data.

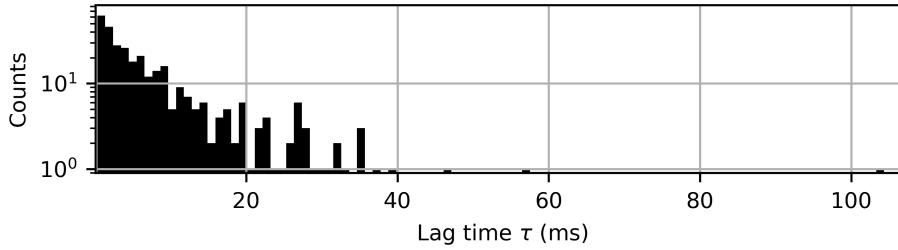


**Figure 2.21.:** Histogram of the segment lengths. Submitted to [95].

and for the first few milliseconds. For each segment, the means squared displacement of the segment  $MSD_s$  is calculated by [126]

$$MSD_s(\tau) = \frac{1}{N_s - k} \sum_{t=0}^{N_s-k} (\vec{r}_s(t + k \cdot dt) - \vec{r}_s(t))^2, \quad \text{with } k = 1, 2, \dots, N_s \text{ .}$$

Here,  $N_s$  is the length of segment  $s$ . The lag time  $\tau$  is an integer multiple of the time bin  $dt$

$$\tau = k \cdot dt \quad (2.89)$$

and  $\vec{r}_s$  represents the three-dimensional coordinates  $\vec{r}_s = (x_s, y_s, z_s)^T$ . Fig. 2.21 shows the statistical distribution of the segment lengths. For the most segments, a border of the sensing octant is reached within less than 10 ms. Responsible for the nanosphere reaching the border in such a short time is mainly the diffusion in  $z$ -direction, because the  $z$ -expansion of the octant is only  $\lambda/(4 \cdot n_m) \approx 0.14 \mu\text{m} \ll w_0 \approx 1.5 \mu\text{m}$ . All calculated  $MSD_s$  are set to start from zero. Hence, the mean  $MSD$  at lag time  $\tau$  can be calculated by

$$\langle MSD(\tau) \rangle = \frac{1}{N(\tau)} \sum_s MSD_s(\tau) \text{ ,}$$

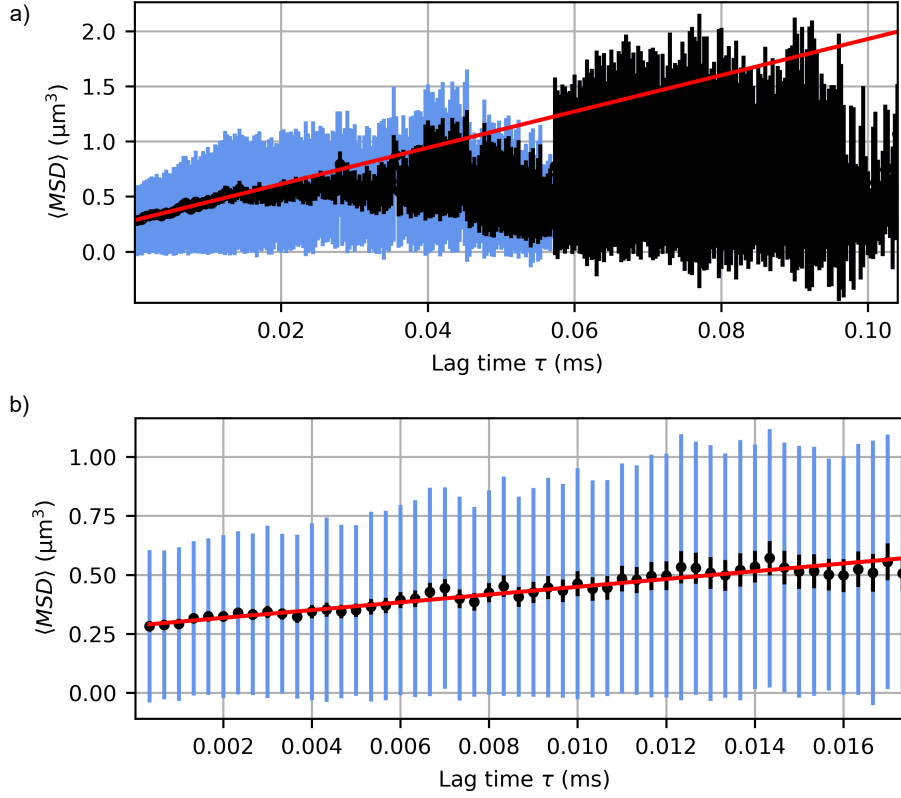


**Figure 2.22.:** Mean squared displacement  $\langle MSD(\tau) \rangle$  of the simulated track in Fig. 2.17 of a nanosphere with  $r_{\text{hydr}} = 75.5$  nm hydrodynamic radius dispersed in water. The blue error bars show the standard deviation and the black error bars show the ten-fold enlarged statistical error  $\Delta x_i$ . The red line is a linear fit to the first 52 data points. **a)** For the first few milliseconds the  $\langle MSD(\tau) \rangle$  increases linearly. With a decreasing statistic at longer lag times, the  $\langle MSD(\tau) \rangle$  deviates from the linear behavior. **b)** Fit to the first 52 data points. Shown in [95] for measured data.

where  $N(\tau)$  is the number of  $MSD_s$  values at the lag time  $\tau$ . The result for  $\langle MSD(\tau) \rangle$  is shown in Fig. 2.22. The blue error bars represent the standard deviation  $\sigma_i$  and the black error bars the ten-fold enlarged statistical error  $\Delta x_i$ , which is given by

$$\Delta x(\tau) = \frac{\frac{1}{N(\tau)} \sum_s^{N(\tau)} \sigma_s(\tau)}{\sqrt{N(\tau)}} . \quad (2.90)$$

The  $y$ -offset of the  $\langle MSD(\tau) \rangle$  arises due to measurement noise and consequently a localization uncertainty of the nanosphere's position. According to Ref. [127], from the  $y$ -offset, the static localization uncertainty  $\sigma_0$  can be estimated by an "unweighted linear fit to the first two or few data points". The obtained  $MSD_{\text{fit}}$ -offset at  $\tau = 0$  is then related to the localization uncertainty by

$$\sigma_0 \approx \left( \frac{MSD_{\text{fit}}(0)}{6} \right)^{1/3} . \quad (2.91)$$

In this case, a fit to the first five data points gives  $MSD_{\text{fit}}(0) = 0.269 \mu\text{m}^3$  and accordingly the statistic localization uncertainty of the simulated track amounts to  $\sigma_0 \approx 355$  nm.

For short lag times,  $\langle MSD(\tau) \rangle$  increases linearly. This is in agreement with the Brownian motion of the nanosphere, and the slope of the linear fitting curve (red) is directly related to the nanosphere's diffusivity by

$$D = \frac{1}{6} \frac{d}{d\tau} \langle MSD(\tau) \rangle .$$

Because of a worsening statistic for increasing lag times, the  $\langle MSD(\tau) \rangle$  deviates from the linear progression. Therefore, a linear fit to a maximal number of data points is necessary. On the other hand, a fit to only the first few data points would lead to a wrong results as well due to the lack of statistics and therefore a larger effect of localization errors. In order to determine the optimal number of fitting data points  $x_{ON}$ , the iterative approach in [127] is followed. In this case,  $x_{ON}$  is 52. By weighting the fit with

$$w(\tau) = \frac{1}{\Delta x(\tau)},$$

in addition, the linear fit to the first 52 data points (see Fig. 2.22b) yields  $D = (2.7 \pm 0.4) \mu\text{m}^2/\text{s}$ . According to the Stokes-Einstein relation (Eq. (2.74) this corresponds to a hydrodynamic radius of  $r_{\text{hydr}} = (78 \pm 11) \text{ nm}$ . The diffusivity error is calculated by the standard error slope of the linear fit and the error for the hydrodynamic radius is calculated via Gaussian error propagation. By comparing the result derived from Monte Carlo simulated single nanosphere diffusion ( $r_{\text{hydr}} = (78 \pm 11) \text{ nm}$ ) with the assumed hydrodynamic radius of  $r_{\text{hydr}} = 75.3 \text{ nm}$ , both values agree very well. Therefore, this is a proof of principle of how the diffusivity and hydrodynamic radius of the nanosphere can be extracted from its track, which in turn is derived from the recorded  $\text{TEM}_{00}$ ,  $\text{TEM}_{01}$  and  $\text{TEM}_{10}$  signals.

## 2.5. Autocorrelation function for a punctiform particle moving through the Fabry-Pérot standing-wave light field

In fluorescence correlation spectroscopy (FCS) the fluorescence light of several nanoparticles is simultaneously detected and autocorrelated. The autocorrelation contains information about the particles' kind of motion (normal and anormal diffusion), about their mean diffusivity and hydrodynamic radius, gives information about the mean particle concentration, allows the detection of single triplet dynamics and enables the detection of chemical reaction rates [96, 131, 132]. This kind of analysis is very sensitive as only a small number of nanoparticles are excited in a small volume of a focused beam. The prerequisite for an accurate determination of the time constants of the present processes is the precise determination of the theoretical autocorrelation function. Here, the intensity distribution of the focused beam is included. In the case of FCS, it is described by a 2D-Gaussian and a 1D-Lorentzian distribution, but usually the approximation of a 2D-Gaussian in lateral and a 1D-Gaussian in longitudinal direction is sufficient. In this work, the transmission signals of several non-fluorescent single nanosphere transit events were measured with a FP cavity and the autocorrelation evaluated in order to determine the nanoparticles' mean diffusivity and mean hydrodynamic radius. However, in this case, an own analytical solution for the theoretical autocorrelation had to be

deduced. On the one hand, the FP cavity light field consists of a 2D-Gaussian distribution and a cosine squared function. Therefore, it can't be approximated by two Gaussians as it is done in FCS. On the other hand, only in Ref. [97] an analytical solution for the autocorrelation of a standing-wave light field is suggested. However, the measurement results presented in Chapter 4.17 contradicted with those results. Therefore, an own analytical solution was derived and is outlined in the following.

The general definition of the autocorrelation function describing the signal produced by punctiform particles

$$G(\tau) \propto \iint W(\vec{r})W(\vec{r}')\Phi(\vec{r}, \vec{r}', \tau)dVdV' \quad , \quad (2.92)$$

with

$$\Phi(\vec{r}, \vec{r}', \tau) = (4\pi D\tau)^{-3/2} e^{-|\vec{r}-\vec{r}'-\vec{v}\tau|^2/(4D\tau)} \quad , \quad (2.93)$$

has to be solved for the FP standing-wave light field

$$W(\vec{r}) = e^{-2\frac{x^2+y^2}{w_0^2}} \cos^2(k_m z) \quad . \quad (2.94)$$

Here,  $k_m = 2\pi/\lambda_m$  is the wavenumber in medium and the additional phase terms  $k_m(x^2 + y^2)/(2R(z)) - \arctan(z/z_0)$  as well as the change of the beam diameter along the longitudinal direction  $w_0^2/w(z)^2$  are neglected. This is well justified since the used cavity geometries are in the quasi-planar regime. The velocity  $\vec{v}$  in Eq. (2.93) describes possible drifts in all directions. Within a collaboration, the numerical solution of the autocorrelation function was solved by Kevin Müller, a PhD student at the École Polytechnique Fédérale de Lausanne (EPFL). His solution path is given below:

The standing-wave term can be written as

$$\cos^2(k_m z) = \frac{1}{4} (2 + e^{2ik_m z} + e^{-2ik_m z}) \quad (2.95)$$

and therefore, according to Eq. (2.92) and (2.94),  $\cos^2(k_m z) \cos^2(k_m z')$  can be converted to the following five terms:

$$\cos^2(k_m z) \cos^2(k_m z') = F_1 + F_2(z) + F_3(z') + F_4(z, z') + F_5(z, z') \quad , \quad (2.96)$$

with

$$\begin{aligned} F_1 &= \frac{1}{4} \quad , \\ F_2(z) &= \frac{1}{4} \Re(e^{2ik_m z}) \\ F_3(z') &= \frac{1}{4} \Re(e^{2ik_m z'}) \quad , \\ F_4(z, z') &= \frac{1}{8} \Re(e^{2ik_m(z+z')}) \quad \text{and} \\ F_5(z, z') &= \frac{1}{8} \Re(e^{2ik_m(z-z')}) \quad . \end{aligned} \quad (2.97)$$

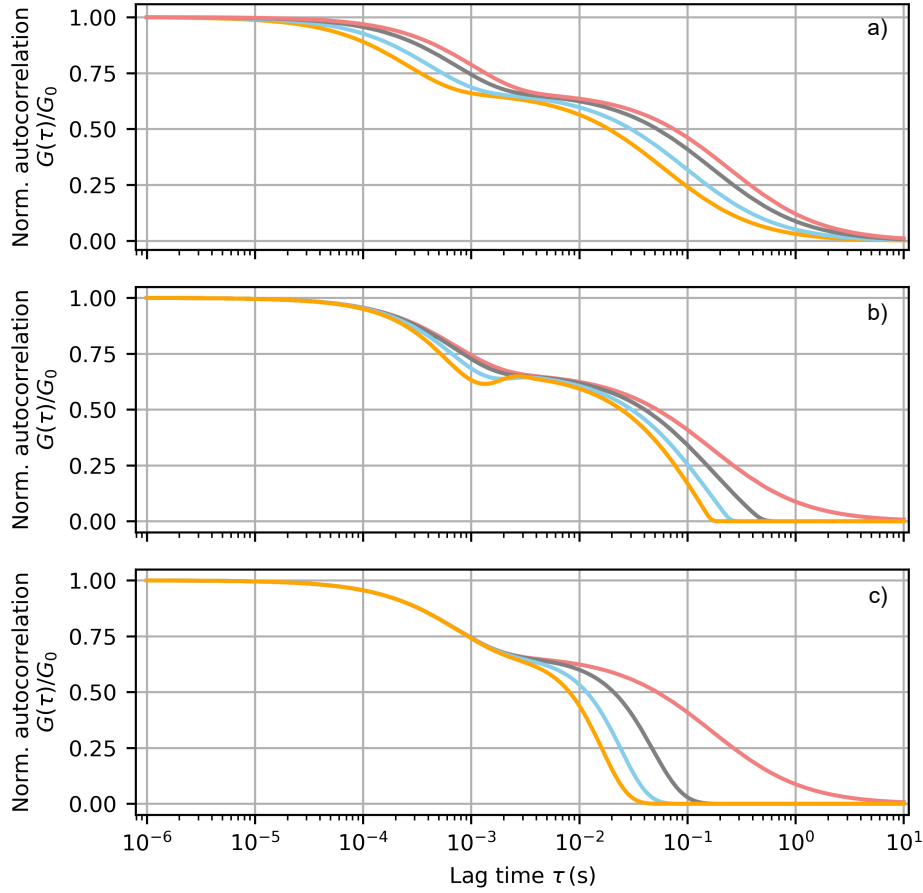


**Figure 2.23.:** Normalized autocorrelation for a punctiform nanoparticle moving through the FP standing-wave light field. From red to orange **a)** the hydrodynamic radius of the nanosphere is decreased from 100 nm to 25 nm and pure diffusion in all directions is considered, **b)** the radius is constant, but the drift velocity in  $z$ -direction is increased from 0 to  $90 \mu\text{m/s}$ , while the other directions are purely diffusive and **c)** the radius is constant, but the drift velocity in  $x$ -direction is increased from 0 to  $90 \mu\text{m/s}$ , while the other directions are purely diffusive.

Here, the relation  $2\Re(z) = z + \tilde{z}$  is used, with  $\tilde{z}$  representing the complex conjugate of the complex number  $z$ . Hence,  $G(\tau)$  can be expressed as

$$\begin{aligned}
 G(\tau) \propto (4\pi D\tau)^{-3/2} & \iint dzdz' e^{-(z-z'-v_z\tau)^2/(4D\tau)} \sum_{m=1}^5 F_m \\
 & \iint_{-\infty}^{\infty} dx dx' e^{-(x-x'-v_x\tau)^2/(4D\tau)} e^{-2\frac{x^2+x'^2}{w_0^2}} \\
 & \iint_{-\infty}^{\infty} dy dy' e^{-(y-y'-v_y\tau)^2/(4D\tau)} e^{-2\frac{y^2+y'^2}{w_0^2}} .
 \end{aligned} \tag{2.98}$$

In  $z$ -direction the light field changes periodically and thus the integrals have to be resolved over several periods in order to obtain a sufficiently accurate solution. The whole integral

in Eq. (2.98) is solved by the commercially available software Wolfram Mathematica<sup>3</sup>. Since the analytical solution is very long, it is not shown here, but instead, the result is plotted for different parameters<sup>4</sup> (see Fig. 2.23). In contrast to Ref. [97], two characteristic slopes at about  $2 \cdot 10^{-4}$  s and  $10^{-1}$  s are visible in the autocorrelation. This already occurs for pure diffusion, without any considered drifts and can be explained by the FP standing-wave light field: In  $z$ -direction, the 1D-movement from antinode to node ( $\lambda_0/(4 \cdot n_m)$ ) generates the shorter time constant, while the 2D-movement from antinode in  $x, y$ -direction ( $w_0 \approx 10 \cdot (\lambda_0/(4 \cdot n_m))$ ) generates the longer time constant. a) shows the change of the autocorrelation for decreasing hydrodynamic radii and a purely diffusive punctiform nanoparticle. According to Eq. (2.74) the diffusivity increases for decreasing radii and the diffusion time is given by Eq. (2.76). Hence, the decreasing diffusion time for decreasing hydrodynamic radii is in agreement with the simulated data in a) (the characteristic slopes shift to the left). The same hydrodynamic radius, but different drift velocities in  $z$ -direction are depicted in b). By increasing the drift velocity, the periodical structure of the standing-wave light field becomes visible in the autocorrelation. In addition, in c) is the change of the autocorrelation for a possible drift in  $x$ -direction shown. Only the longer time constant is affected by decreasing the time for the lateral movement.

## 2.6. Rotational diffusion of an anisotropic, homogeneous nanoparticle probed by a Fabry-Pérot cavity with birefringent mirrors

At the beginning of Chapter 2.4 the Brownian translational and rotational movement of a nanosphere are introduced. If the nanoparticle is not spherical but anisotropic in shape, the movement perpendicular to its long axis  $b$  or perpendicular to its short axis  $a$  causes different friction  $\gamma_{t,b} > \gamma_{t,a}$  with the surrounding medium. Therefore, two translational diffusivities  $D_{t,b} < D_{t,a}$  arise. The rotational diffusivity is described by Eq. (2.75), but with a different friction coefficient. E.g. the friction coefficient of a nanorod with flat ends can be expressed as [133]

$$\gamma_r = \frac{8\pi\eta b^3}{3} \left[ \ln\left(\frac{b}{a}\right) - 0.662 + 0.917\frac{a}{b} - 0.050\left(\frac{a}{b}\right)^2 \right]^{-1}. \quad (2.99)$$

The mean square angular displacement (MSAD)  $\langle \Delta \vec{\varphi}^2(\Delta t) \rangle = \langle (\varphi(t + \Delta t) - \varphi(t))^2 \rangle$  in three dimensions is related to the rotational diffusivity [134] via

$$\langle \Delta \vec{\varphi}^2(\Delta t) \rangle = 4D_r \Delta t \quad (2.100)$$

and thus the diffusion time for a full rotation of the nanoparticle is

$$\tau_{D,r} = \Delta t (2\pi \text{rad}^2) = \frac{\pi^2}{D_r} \text{rad}^2. \quad (2.101)$$

<sup>3</sup> Each of the integral terms is solved individually and then assembled by superposition.

<sup>4</sup> The following fixed parameters are used:  $w_0 = 1.48 \mu\text{m}$ ,  $\lambda = 780 \text{ nm}$ ,  $T = 20 \text{ }^\circ\text{C}$  and  $\eta = 1 \text{ mPa s}$ .

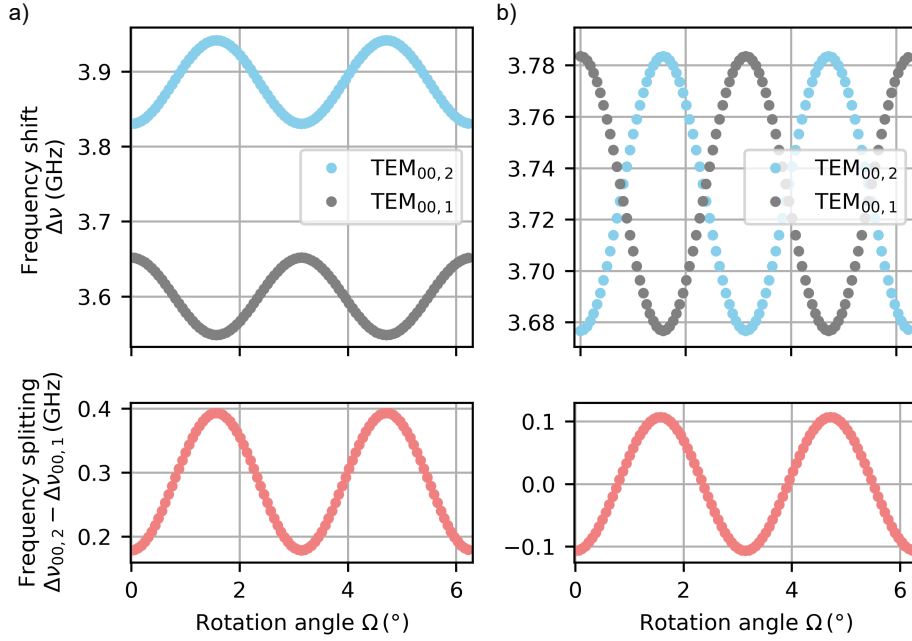


**Figure 2.24.:** Frequency shift and frequency splitting produced by a prolate spheroid with semi-axes  $c = 95.8$  nm and  $a, b = c/2$  and the refractive index  $n = 1.41$ . For the mirror rotation angle, the value  $\theta = 0^\circ$  was chosen. **a)** The radii of curvatures of the elliptical cavity mirrors are different with  $r_{c,M1,1} = 40.0$   $\mu\text{m}$ ,  $r_{c,M1,2} = 70.0$   $\mu\text{m}$ ,  $r_{c,M2,1} = 45.0$   $\mu\text{m}$  and  $r_{c,M2,2} = 85.6$   $\mu\text{m}$ . **b)** The radii of curvatures of the elliptical cavity mirrors are the same with  $r_{c,M1,1} = r_{c,M2,1} = 45.0$   $\mu\text{m}$  and  $r_{c,M1,2} = r_{c,M2,2} = 70.0$   $\mu\text{m}$ .

There are different ways how the rotation of the anisotropic nanoparticle can be detected. Either the direct imaging of its rotation (e.g. see [135, 136, 137, 134, 133]), applying anisotropy to a spherical nanoparticle by labeling with a highly scattering nanoparticle [138], or as investigated in this work, via the polarization-split cavity fundamental mode.

In the following, the detection of the rotational movement of an anisotropically shaped nanoparticle via the polarization-split cavity fundamental mode is explained. The birefringence of an anisotropic nanoparticle is already introduced in Chapter 2.2.2 by the example of a homogeneous spheroid. In addition, the polarization splitting of the fundamental mode is explained in Chapter 2.1.3.

For a fixed mirror rotation angle  $\theta$ , the distance between the two linearly and orthogonally polarization-split fundamental modes  $\text{TEM}_{00,1}$  and  $\text{TEM}_{00,2}$  is constant, when the cavity is empty. When a prolate spheroid resides inside the modes, the amount of shift of each mode is differently and depends on the rotation angle  $\Omega$  of the spheroid. If the long axis  $c$  of the prolate spheroid shows in the direction of  $\text{TEM}_{00,1}$ , the frequency shift of  $\text{TEM}_{00,1}$  resonance is maximal and that of  $\text{TEM}_{00,2}$  is minimal. The other way around is produced by the spheroid for  $c$  parallel to  $\text{TEM}_{00,2}$ . A mathematical description is derived for the case, when the optical polarizabilities  $\alpha_c$  and  $\alpha_a$  are projected on the mode axes [89]

$$\alpha_{00,1} = \sqrt{(\alpha_a \cos(\Omega))^2 + (-\alpha_c \sin(\Omega))^2} \quad , \quad (2.102)$$

$$\alpha_{00,2} = \sqrt{(\alpha_a \sin(\Omega))^2 + (\alpha_c \cos(\Omega))^2} \quad (2.103)$$

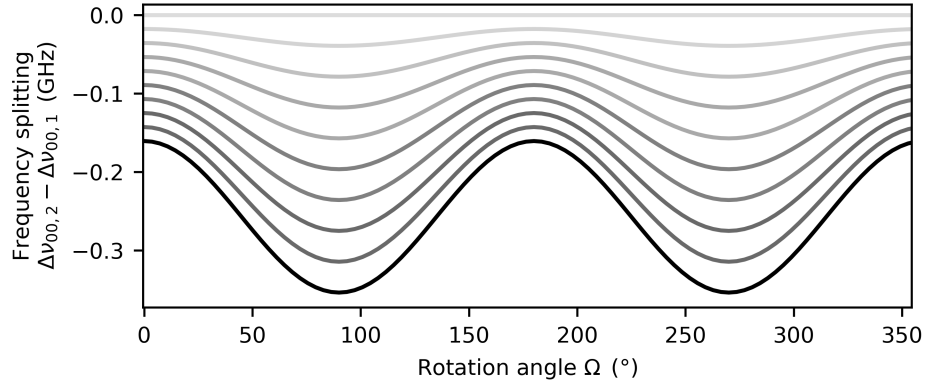


**Figure 2.25.:** Prolate spheroid with the two polarizabilities  $\alpha_c = 18.0 \cdot 10^3 \text{ nm}^3 / (4\pi\epsilon_0)$  and  $\alpha_a = 17.2 \cdot 10^3 \text{ nm}^3 / (4\pi\epsilon_0)$  rotating inside the FP standing-wave light field at different positions. From light gray to black the spheroid approaches the maximum intensity. At the lightest gray color the spheroid is outside the light field and at the black color it resides at the center of the antinode.

and the calculated frequency shifts are accordingly

$$\Delta\nu_{00,1} = \frac{\Re(\alpha_x) \cdot c}{2\lambda_m \epsilon_0 V_m} \int_{V_{\text{Spheroid}}} dV_{\text{Spheroid}} \cdot \frac{I_{00}(x - x_0, y - y_0, z - z_0)}{I_0}, \quad (2.104)$$

$$\Delta\nu_{00,2} = \frac{\Re(\alpha_y) \cdot c}{2\lambda_m \epsilon_0 V_m} \int_{V_{\text{Spheroid}}} dV_{\text{Spheroid}} \cdot \frac{I_{00}(x - x_0, y - y_0, z - z_0)}{I_0}. \quad (2.105)$$

$$(2.106)$$

Fig. 2.24 shows the simulated frequency shifts and the frequency splitting  $\Delta\nu_{00,2} - \Delta\nu_{00,1}$  for a Rayleigh spheroid<sup>5</sup> rotating at the center of the antinode. At a fixed position of the spheroid in the light field, the frequency splitting contains only the information of the spheroid's rotation angle. However, when a spheroid diffuses in water and is probed by the FP cavity standing-wave light field, the intensity at the location of the spheroid changes. Consequently, the strength of the frequency splitting also changes. This is depicted in Fig. 2.25. As the intensity increases, the frequency splitting also increases. Thus, the measured frequency splitting signal generated by a diffusing anisotropically shaped nanoparticle does not only contain the information about the rotation, but also about the translational diffusion.

The projection on the polarization split mode axes (see Eq. (2.102) and (2.103)) is only valid, when the polarization direction isn't changed by the anisotropic-shaped nanoparticle. In Ref. [89] a change in polarization direction isn't observed, although, in [139, 140] a rotation is predicted.

<sup>5</sup>  $\int_{V_{\text{Spheroid}}} dV_{\text{Spheroid}} \cdot \frac{I_{00}(x - x_0, y - y_0, z - z_0)}{I_0} \approx 1$ .



### **3. Realization and performance of the Fabry-Pérot microcavity sensing platform**

In the previous chapter, the fundamentals of a Fabry-Pérot (FP) microresonator and the interaction of the FP standing-wave light field with a nanoparticle were discussed. In order to detect the described effects, an experimental sensing platform had to be developed. The very first sensing platform combining a fiber-based FP sensor with a microfluidic channel was introduced by Matthias Mader [108], a former PhD student of the same research group. With his preliminary work, Matthias Mader could detect the Rayleigh scattered light of SiO<sub>2</sub> spheres with a diameter of 142 nm flowing through the cavity, and simultaneously, he could measure the correlated change of the cavity transmission signal. Since his version of the sensing platform included many time consuming steps for the fabrication and exhibited several problems such as a lack of reproducibility (see Appendix A.1), a new sensing platform had to be developed. This chapter is about the realization of the new fiber-based FP microcavity sensing platform and about its performance in terms of signal enhancement and mechanical stability. Parts of this chapter have been submitted to nature communications [95]. The core of the sensor consists of a fiber-based FP microcavity and a microfluidic channel, which is explained in detail in Chapter 3.1. This core is embedded in different versions of sensing platforms. These are presented in Chapter 3.2. In Chapter 3.3 the detection of the cavity finesse is explained in the case of different optical cavity length regimes. Chapter 3.4 covers the optical and electrical periphery. These components are required to operate the fiber-based cavity sensor. Besides, general aspects for the detection of nanoparticle signals are discussed. In addition, in Chapter 3.5, the different sensing platforms are compared in terms of their mechanical stability and resolution limit. The different cavity geometries, which were used in the different experiments are summarized in Chapter 3.6 and in Chapter 3.7 the results are finally discussed.

#### **3.1. The core of the Fabry-Pérot sensor**

This chapter deals with the core of the FP sensor, which consists of the fiber-based FP cavity and the microfluidic channel (see Fig. 3.1). At first, the fiber-based FP cavity is discussed (Chapter 3.1.1). By micromachining the fiber end facet with CO<sub>2</sub> laser pulses, an approximately Gaussian-shaped depression is achieved with an ultra smooth surface roughness. This low surface roughness in combination with high reflective dielectric mirrors is responsible for the achieved high cavity finesse in the order of  $\mathcal{F} \approx 10^5 \dots 10^6$ . In addition, a fiber-based FP cavity allows a direct coupling of light into the cavity. In this context, the coupling efficiency (mode matching) and the overall transmission efficiency are discussed. In Chapter 3.1.2 two different

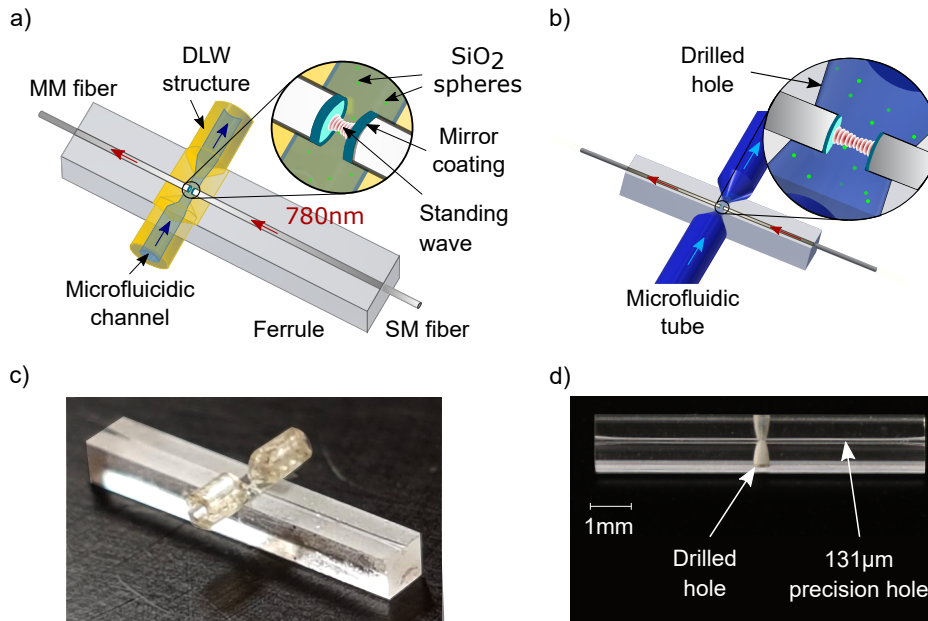


**Figure 3.1.:** Two different versions for the core of the fiber-based FP microfluidic scanning cavity setup. **a)** The precision hole of the glass ferrule causes a direct alignment of the single-mode (SM) and the multi-mode (MM) cavity fibers. On the end facet of the fibers, dielectric mirrors are attached, forming a FP resonator. The cavity fibers protrude into a microfluidic channel, which in this case is created by a direct laser-written (DLW) polymer structure. This setup makes it possible to pump nanoparticles dispersed in water into the microfluidic channel and through the cavity in a flow perpendicular to the orientation of the cavity fibers. **b)** Similar setup as shown in a). Instead of the DLW polymer structure, the microfluidic channel is directly formed by a drilled, conically-shaped hole through the ferrule. Commercial available microfluidic tubes are attached in order to guide the sample solution to the cavity. **c)** Photograph of the ferrule and the DLW polymer structure. **d)** Photograph of the conically-shaped hole inside the ferrule. Submitted to [95].

types of microfluidic channels are presented. Both channels enable the integration of the fiber-based cavity and allow the measurement of nanoparticles dispersed in liquids. Although all measurements were conducted at rest, the liquid flow inside a microfluidic channel with fibers protruding into the channel was simulated and the results are presented within this chapter.

### 3.1.1. Fiber-based Fabry-Pérot cavity

The core of each cavity version consists of a glass ferrule<sup>1</sup>, which has a precision hole of 131 µm in diameter. Into the precision hole, a single-mode (SM) and a multi-mode (MM) fiber are inserted. Both fibers have a depression in their end facets, which is coated by a dielectric high reflective mirror<sup>2</sup>. In the following, such a fiber is called „SM-cavity fiber“ or „MM-cavity fiber“.

<sup>1</sup> OZ Optics, FER 1.225-1.225-131, material: quartz glass

<sup>2</sup> Transmission at 780 nm:  $T = 17.6$  ppm

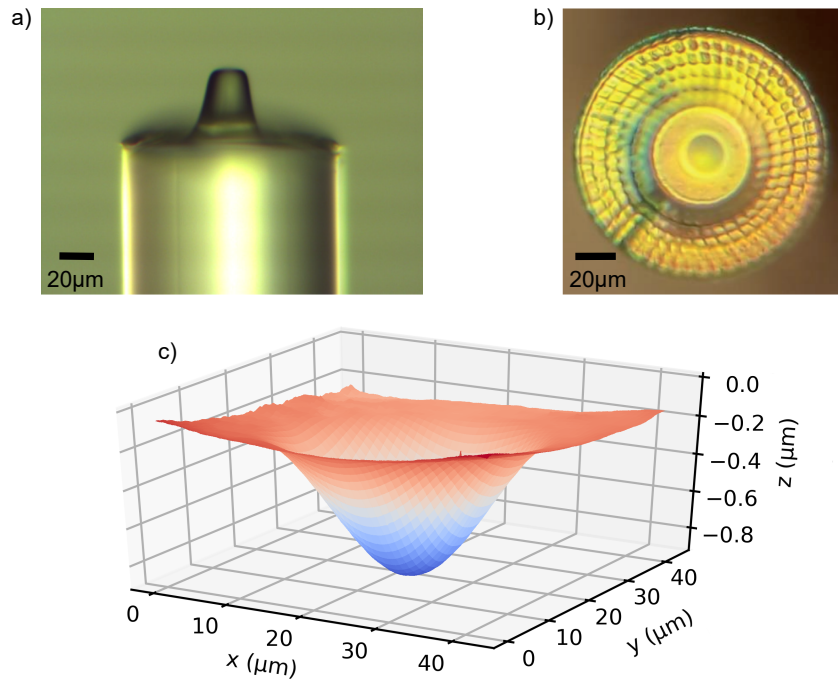


**Figure 3.2.:** CO<sub>2</sub> laser-machined fiber end facets. **a)** Side view from a cropped fiber end. The picture was taken from [141]. **b)** Top view of a cropped fiber end with a Gaussian depression at the center. Due to the already attached dielectric mirror coating for the center wavelength  $\lambda = 585 \text{ nm}$ , the surface appears yellow. The picture was taken from [103]. **c)** White light interferometric (WLI) image of an approximately Gaussian depression at the center. This MM cavity fiber mirror was used for the three-dimensional tracking experiment (Chapter 5) and for the measurement of the rotational movement of single SiO<sub>2</sub> nanospheres with  $r_{\text{geom}} = 25 \text{ nm}$  geometric radius (Chapter 6.1).

**Micromachined fiber end-facet.** A depression in the surface of a glass fiber end-facet can be achieved by one or several CO<sub>2</sub> pulses ( $\lambda = 10.6 \text{ }\mu\text{m}$ ) focused on the cleaved surface. This method was first published by David Hunger and Jakob Reichel [87, 101] and a detailed description can be looked up in the references [141, 108]. The focused CO<sub>2</sub> pulse on the glass fiber-end facet is thermally absorbed by the silica and depending on the intensity distribution of the pulse, the silica evaporates. Consequently, an approximately Gaussian depression in the surface remains. In order to enable short cavity distances and an angular alignment of the cavity mirrors, the rim of the fiber end is removed with CO<sub>2</sub> pulses. This process leaves a freestanding cone behind that contains the depression at the Gaussian center. In Fig. 3.2 such a cropped cavity fiber end-facet with an approximately depression at the center is shown. The depression is not perfectly rotationally symmetrical and the profile is more like an elliptical shape. A  $x$ - and  $y$ -cut through such an elliptically-shaped depression is shown in Fig. 3.3. In this case, the depression was machined with a single CO<sub>2</sub> laser pulse and the radii of curvature are  $r_{c,x}^{\text{MM}} \approx 79.2 \text{ }\mu\text{m}$  and  $r_{c,y}^{\text{MM}} \approx 87.8 \text{ }\mu\text{m}$ . However if the depression is machined with multiple CO<sub>2</sub> pulses, also spherical profiles can be achieved. This was shown by Jonathan Körber, a former Bachelor student of the same research group [142]. All cavity fiber mirrors used in this work had an elliptical shape and had a radius of curvature between  $r_c = 29 \text{ }\mu\text{m}$  and  $31 \text{ }\mu\text{m}$  (see Chapter 3.6). In principle also radii of curvatures below  $10 \text{ }\mu\text{m}$  can be fabricated by CO<sub>2</sub> laser

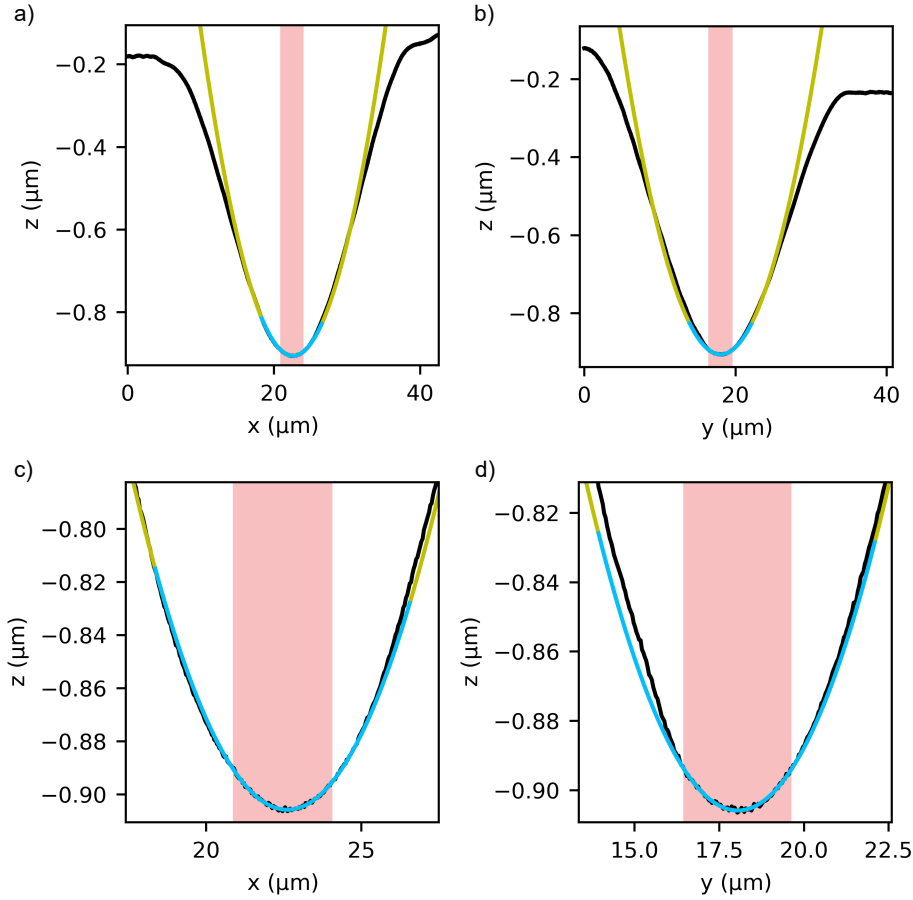


**Figure 3.3.:** Cut through the WLI profile (black) shown in Fig. 3.2 at  $y = 0$  (a,c) and  $x = 0$  (b,d). The expansion of the cavity  $TEM_{00}$  mode on the mirror surface is assumed to be  $3.2 \mu\text{m}$  in diameter, which is depicted in all sub-figures as a red vertical rectangle. The green curve is a Gaussian fit and the blue curve is a circle fit to the center values at the minimum of the measured data (black). At the boundaries, both curves deviate strongly (a,b), but they are in excellent agreement in the center area, where the cavity mode is formed (c,d). In this case, the mirror have a radius of curvature of  $r_{c,x}^{MM} \approx 79.2 \mu\text{m}$  and  $r_{c,y}^{MM} \approx 87.8 \mu\text{m}$ .

pulses. However a satisfying dielectric mirror coating is not achievable with such small radii of curvatures. Steep side walls of the depression causes probably tensions on the dielectric mirror coating and a partial detachment of the mirror (see Fig. A.22). This was observed for all cavity fibers with a  $780 \text{ nm}$  dielectric mirror coating and a radius of curvature  $r_c \leq 12 \mu\text{m}$ , which are available in our own laboratory. The  $\text{CO}_2$  pulse for the depression at the center does not only evaporate the material but it also melts the silica surface, resulting in a desirable low surface roughness of only  $\approx 0.2 \text{ nm}$  [87, 101]. Due to this tiny surface roughness at the atomic scale, very high finesses can be achieved in the fiber-based FP cavity (see cooperativity below).

**Dielectric mirror coating.** A dielectric mirror consists of alternating thin layers with different refractive indices  $n_L$  and  $n_H$ . At each interface, the incident light with the vacuum wavelength  $\lambda_0$  is reflected and transmitted. When the thickness of each layer is  $t_i = \lambda_0/(4n_i)$ ,

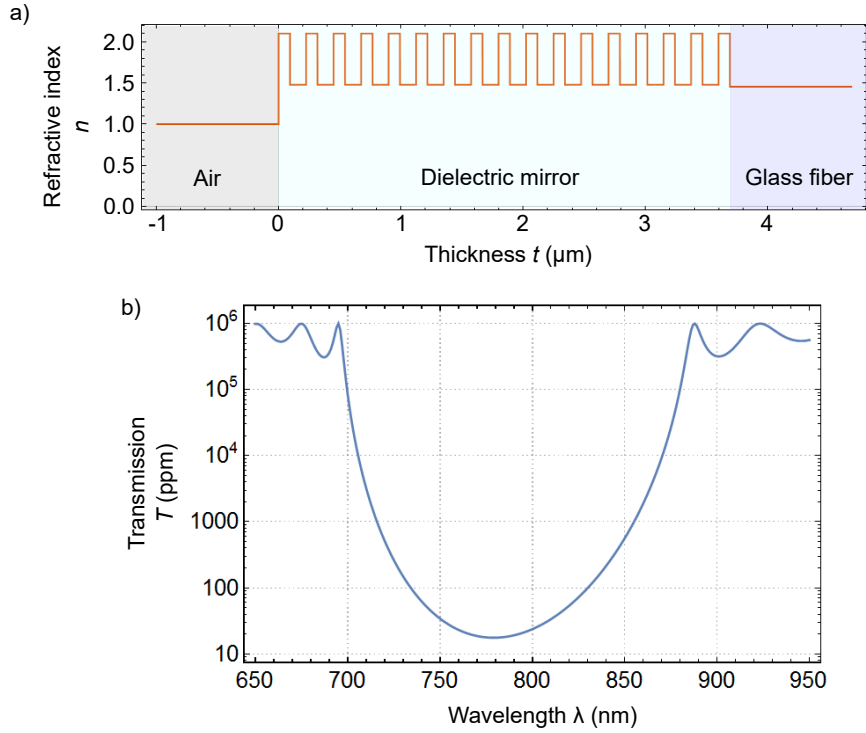


**Figure 3.4.:** Dielectric mirror coating of the cavity fibers used in this work. **a)** The coating consists of 16 alternating pairs of layer consisting of  $\text{Ta}_2\text{O}_5$  ( $n_{\text{Ta}_2\text{O}_5} = 2.10$ ) and  $\text{SiO}_2$  ( $n_{\text{SiO}_2} = 1.45$ ) and the final layer was chosen to be  $\text{Ta}_2\text{O}_5$ . In this case, the cavity fiber mirrors are in air. **b)** Transmission spectrum of the mirror. Both graphs were created with a Mathematica script written by Thomas Hümmer [111] and Julia Benedikter [103].

the reflected electrical fields interfere constructively and a high reflectivity is obtained. In this work, a mirror coating with 16 alternating pairs of layers consisting of tantalum pentoxide ( $\text{Ta}_2\text{O}_5$ ,  $n_{\text{Ta}_2\text{O}_5} = 2.10$ ) and  $\text{SiO}_2$  ( $n_{\text{SiO}_2} = 1.45$ ) was used. The final layer was chosen to be  $\text{Ta}_2\text{O}_5$  (see Fig. 3.4 a). Consequently, the mirror exhibit a transmission of  $T = 17.6$  ppm at the center wavelength  $\lambda_0 = 780$  nm and in air (see Fig. 3.4 b). The transmission spectrum and the following results were calculated by a transfer matrix method explained in the book [143] and performed with a Mathematica script written by Thomas Hümmer [111] and Julia Benedikter [103], which were two former PhD students of the same research group. With a FP cavity comprising two of such mirrors, a finesse of up to  $\mathcal{F} \approx 90000$  could be measured in air by the supervised bachelor student Julian Schaal [144]<sup>3</sup>. In his bachelor thesis he utilized a simplified cavity setup, which allowed him to precisely adjust the angular alignment of the fiber. Thus, the absolute maximum finesse could be measured without losses due to misalignment. Hence, according to Eq. 2.11, the mirror losses in air can be calculated and amount to  $A_1 = A_2 \approx 17$  ppm. When the same mirrors protrude in water, their transmission increases to  $T = 23.5$  ppm and the light penetration depth into the mirror changes from  $d_{p,a} = 323$  nm in air to  $d_{p,w} = 430$  nm in water. In addition, the absorption loss in water has

<sup>3</sup> Actually, he could measure larger finesse values at short cavity distances. However, these results are distorted, because the cavity length was measured via the higher-order transverse modes (see Chapter 3.3).

	Air	Water
Finesse $\mathcal{F}$	90000	$\geq 56710$ ( $d_{\text{opt}} = 5.4 \mu\text{m}$ )
Mirror transmission $T$ (ppm)	17.6	23.5
Mirror absorption and scattering loss $A$ (ppm)	17	$\leq 24$
Mirror penetration depth $d_p$ (nm)	323	430
Absorption of medium between mirrors $L_m$ (ppm)	0	16.2 ( $d_{\text{opt}} = 5.4 \mu\text{m}$ )
Cooperativity $C_0 \propto Q\lambda_m^3/V_m$	$5.1 \cdot 10^4$	$2.1 \cdot 10^4$

**Table 3.1.:** Dielectric mirror coating of the cavity fibers, which were used for the experiments. The absorption loss of the mirror in water was determined by assuming a perfect mirror alignment. With this mirror coating a high cooperativity of  $C_0 \propto 2.1 \cdot 10^4$  was achieved in water.

to be taken into account (see Chapter 2.1.1). At a cavity length of  $d_{\text{opt}} = 5.4 \mu\text{m}$ , the water absorption loss is

$$L_m = 2 \cdot 2.38 \text{ ppm}/\mu\text{m} \cdot d_{\text{geom}} \quad (3.1)$$

$$= 2 \cdot 2.38 \text{ ppm}/\mu\text{m} \cdot (d_{\text{opt}} - 2 \cdot d_{p,w})/1.33 \quad (3.2)$$

$$= 16.2 \text{ ppm} \quad . \quad (3.3)$$

Accordingly, the finesse in water decreases to  $\mathcal{F} \approx 65000$ , when an optical cavity length of  $d_{\text{opt}} = 5.4 \mu\text{m}$  and the same mirror losses as in air are assumed. However, as the scattering losses of the mirror increase with a shorter light wavelength<sup>4</sup>, a finesse  $< 65000$  is expected. In this work, a maximal finesse of  $\mathcal{F} = 56710$  could be achieved in water at the optical cavity length  $d_{\text{opt}} = 5.4 \mu\text{m}$ . Compared to the above mentioned setup of Julian Schaal, the fibers in the fiber-based FP sensing platform are automatically aligned by the precision hole of the ferrule. As there is a spacing of  $6 \mu\text{m}$  between the cavity fiber (diameter  $125 \mu\text{m}$ ) and the ferrule precision hole (diameter  $131 \mu\text{m}$ ), small misalignments can arise. The alignment can be improved by a rotation of the mirrors to each other. Consequently, when a perfect mirror alignment is assumed at the maximal measured finesse of  $\mathcal{F} = 56710$ , the increased mirror losses in water can be deduced:  $A_1 = A_2 = 24 \text{ ppm}$ . All results discussed in this section are summarized in Table 3.1.

**Cooperativity.** The smooth surface obtained by  $\text{CO}_2$  laser pulses in combination with high reflective dielectric mirrors reduces the mirror scattering losses significantly and is responsible for the high finesse of 90000 in air and 56710 in water achieved with the fiber-based FP cavity. The remaining losses of the mirror are dominated by absorption of the light in the dielectric mirror coating stack. The highest cooperativity achieved in this work amounts to  $C_0 \propto Q\lambda_m^3/V_m = 5.1 \cdot 10^4$  in air and  $C_0 \propto 2.1 \cdot 10^4$  in water. When dielectric mirrors with a higher reflectivity are used than those presented above, a finesse of even up to  $\mathcal{F} = 172000$  can be obtained in air [145]. Consequently, a FP cavity with a high cooperativity of up to

<sup>4</sup> The Rayleigh scattering cross-section  $\sigma_{\text{scat}}$  is proportional to  $n_m^4/\lambda_0^4$ .

$C_0 \propto 4.3 \cdot 10^5$  can be achieved in air (assumed parameters:  $\mathcal{F} = 172000$ ,  $r_c = 15 \mu\text{m}$ ,  $d_{\text{opt}} = 2 \mu\text{m}$  and  $\lambda_0 = 780 \text{ nm}$ ). The cooperativity  $C_0$  is the figure of merit for the signal enhancement of the fiber-based FP cavity.

**Mode matching.** Without the use of any additional coupling optics, the light propagating through the fiber is transmitted through the dielectric mirror and directly coupled into the cavity. However, only a fraction of light is coupled into the cavity mode depending on the overlap integral between the fiber mode and the cavity mode. This is called mode matching  $\epsilon$ . For well aligned cavity mirrors, meaning that the fiber mode and the cavity mode optical axis are not shifted to each other, and for a well centered mirror depression with respect to the center of the fiber core, the mode matching can be estimated by [87]

$$\epsilon \approx \left( \frac{2w_f w_m}{w_f^2 + w_m^2} \right)^2 . \quad (3.4)$$

Here,  $w_m$  is the cavity mode radius on the mirror and  $w_f$  is the mode field radius of the fiber. Consequently, for a SM fiber with  $w_f = 3 \mu\text{m}$  and  $n_f = 1.45$  and the cavity parameters  $w_m = 1.53 \mu\text{m}$ ,  $r_{c,1} = 49,6 \mu\text{m}$  and  $r_{c,2} = 83.5 \mu\text{m}$ , the maximal mode matching is  $\epsilon \approx 0.67$ . Here, the parameters of the cavity were inserted, which were used for the operated three-dimensional tracking experiment (see Chapter 5). The already high coupling efficiency can be increased to a theoretical maximum value of 0.979 by adapting the cavity mode size on the mirror. This is achieved by a larger cavity length or by an increased radius of curvature. However, the first option also increases the water absorption losses in the cavity and the second option increases the mode volume, both leading to a reduced cooperativity. A more elaborate option to increase the coupling efficiency would be the fabrication of cavity fibers with integrated mode matching optics [146].

In this work, a SM fiber was used for the light coupling into the cavity. Using a MM fiber instead would greatly reduce the mode matching due to the larger fiber mode, a non-planar phase wavefront inside the fiber core and consequently a worse mode overlap.

**Transmission efficiency.** The transmission efficiency of perfectly aligned cavity mirrors depends on the mode matching between the input fiber mode and cavity mode  $\epsilon_1$ , between the output fiber mode and cavity mode  $\epsilon_2$ , the transmission, scattering, and absorption losses of each mirror ( $T_1$ ,  $T_2$ ,  $A_1$ ,  $A_2$ ) and the absorption losses due to the liquid filling the cavity  $L_m$ . The transmission efficiency is then given by [147]

$$\frac{P_{T,\text{max}}}{P_{\text{in}}} = \epsilon_1 \epsilon_2 \frac{4T_1 T_2}{(2L_m + T_1 + T_2 + A_1 + A_2)^2} , \quad (3.5)$$

where  $P_{T,\text{max}}$  is the maximal transmitted power and  $P_{\text{in}}$  is the incident power. In case of the same coupling efficiencies  $\epsilon_1 = \epsilon_2 = 0.67$ , the maximal transmission efficiency amounts to 0.056 (remaining parameters are the same as discussed for the dielectric mirror coating:  $T_1 = T_2 = 23.5 \text{ ppm}$ ,  $A_1 = A_2 = 24 \text{ ppm}$ ,  $2L_m = 16.2 \text{ ppm}$ ). In this work, a ferrule with a precision hole of  $131 \mu\text{m}$  was used for an automatic alignment of the cavity mirrors. However, the spacing between the ferrules hole and the glass fibers (diameter:  $125 \mu\text{m}$ ) is  $6 \mu\text{m}$ . Accordingly, a lateral offset as well as an angular misalignment of the fiber cores can occur. If a SM fiber is used as

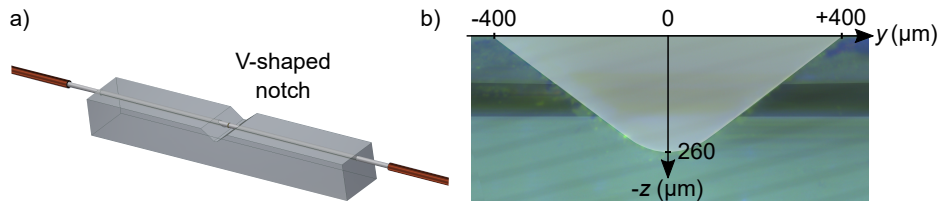


**Figure 3.5.:** Fabrication of a v-shaped notch into the glass ferrule. **a)** CAD drawing of the glass ferrule and the v-shaped notch. **b)** Micrograph of the sewed notch. Submitted to [95].

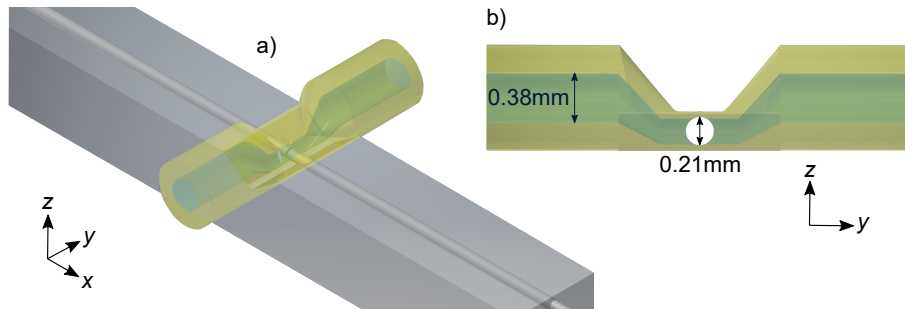


**Figure 3.6.:** CAD drawing of the polymer structure, which forms the microfluidic channel. **a)** The 3D structure is written into the v-shaped notch. **b)** Side view of the microfluidic channel. The outer hole with a diameter of 0.38 mm is designed to fit a syringe needle, which can be glued into that hole and acts as a microfluidic adapter. To provide a laminar flow, the microfluidic channel diameter is reduced to 0.2 mm at the center. The 0.21 mm perpendicular hole forms the transition to the precision hole of the ferrule.

outcoupling fiber instead of a MM fiber, the transmission efficiency can decrease significantly. This was analyzed by Jasmin Häberle and Shalom Palkhivala (both supervised students) in more detail [148, 149]. Consequently, if single-mode operation is required (e.g. for active stabilization measurements) a narrower precision hole of the ferrule is necessary in order to increase the transmission efficiency. However, all experiments conducted and presented in this work, were compatible to the MM-outcoupling-fiber and therefore were unsusceptible for misalignment and transmission losses.

### 3.1.2. Microfluidic channel

The microfluidic channel is an essential part of the fiber-based FP sensing platform. It allows the detection of nanoparticles dispersed in liquids, enables a laminar flow and significantly reduces the required sample volume for the measurement. Within this work, three different microfluidic channel versions were fabricated. As the first microfluidic version was not used for the conducted experiments, the information about its design and fabrication can be taken from Appendix A.1. The other two versions are described in the following. Both microfluidic designs have been submitted to [95].

**Polymer channel.** The second microfluidic channel version consists of a 3D polymer structure, which is written by two-photon direct laser writing (see Fig. 3.1 a) and c)). It was designed and fabricated together with Christian Kern, a former Ph.D. student in the Martin Wegener

research group at the Applied Physical Institute at the Karlsruhe Institute of Technology. In the following, the fabrication steps for the microfluidic channel are briefly explained. Detailed information can be taken from Appendix A.2.2.

At first, a v-shaped notch is cut into the glass ferrule<sup>5</sup>, which is 260  $\mu\text{m}$  deep and has a width of 800  $\mu\text{m}$  (see Fig. 3.5). In the second step, the 3D-polymer structure is written into the notch. For this purpose, a CAD design of structure was drawn (see Fig. 3.6). It consists of an outer hole, with a diameter of 0.38 mm, which narrows to 0.2 mm at the center. At the center is a crossing with a slightly thicker hole of 0.21 mm in diameter than the precision hole of the ferrule (0.131 mm). This is necessary in order to compensate for inaccuracies in the fabrication. The direct laser writing of the 3D polymer structure itself was carried out by Christian Kern (see Appendix A.2.2). In general, the 3D-writing of the microfluidic channel into a polymer allows for custom design and it is fabricated within  $\approx 5$  h.

**Quartz glass channel.** The third microfluidic channel version consists of a conical hole inside the glass ferrule, which is produced with femtosecond laser pulses (see Fig. 3.1 b) and d)). This was carried out by Heino Besser of the Laser Material Processing Facility (KNMF), a Helmholtz Research Infrastructure at the Karlsruhe Institute of Technology (KIT)<sup>6</sup>. Due to limitations of the aspect ratio in the fabrication and in order to create symmetrical conical holes, the ferrule is machined from both sides. This results in holes with an outer diameter of 0.56 mm and an inner diameter of 0.32 mm. At the center of the ferrule, the drilled hole intersects with the precision hole in order to allow the fiber ends to protrude into the microfluidic channel. The fabrication time of the microfluidic channel is only  $\approx 10$  min. An alternative fabrication way was also investigated in cooperation with Georg Gramlich from the Institute of high-frequency technology and electronics. In this case, the concave hole was produced with a laser cutter. Finally, those holes with similar quality can also be produced in our laboratory using a CO<sub>2</sub> pulsed laser, as it was shown by Shalom Palkhivala (supervised master thesis) [149].

**Laminar flow simulation.** For the first microfluidic channel design (see Appendix A.1) water flow simulations were carried out in the Autodesk computational fluid dynamics (CFD) simulation software (see Fig. A.2). This first microfluidic channel was not used for the conducted experiments and is therefore not further described in the rest of this work. The flow simulations were done to detect any turbulences that might occur inside the microfluidic channel depending on the applied pressure between channel inlet and channel outlet. Although the first microfluidic channel version was not used for the experiments shown in this work, the simulation results are transferable to the other two microfluidic channel versions (polymer and quartz glass channel). Turbulences are only expected, where the cavity fibers protrude into the microfluidic channel. In this respect, the different microfluidic versions are similar. Fig. 3.7 shows the water flow at a pressure difference of 140 Pa between the three inlets and

<sup>5</sup> Carried out by Lucas Radtke, a technician at the Center for Functional Nanostructures at the KIT.

<sup>6</sup> The conical hole in d) is similar to the hole fabricated by Heino Besser, however, in this case, the hole was drilled with a laser cutter. This was done in another collaboration with Georg Gramlich from the Institute of Radio Frequency Engineering and Electronics (IHE)

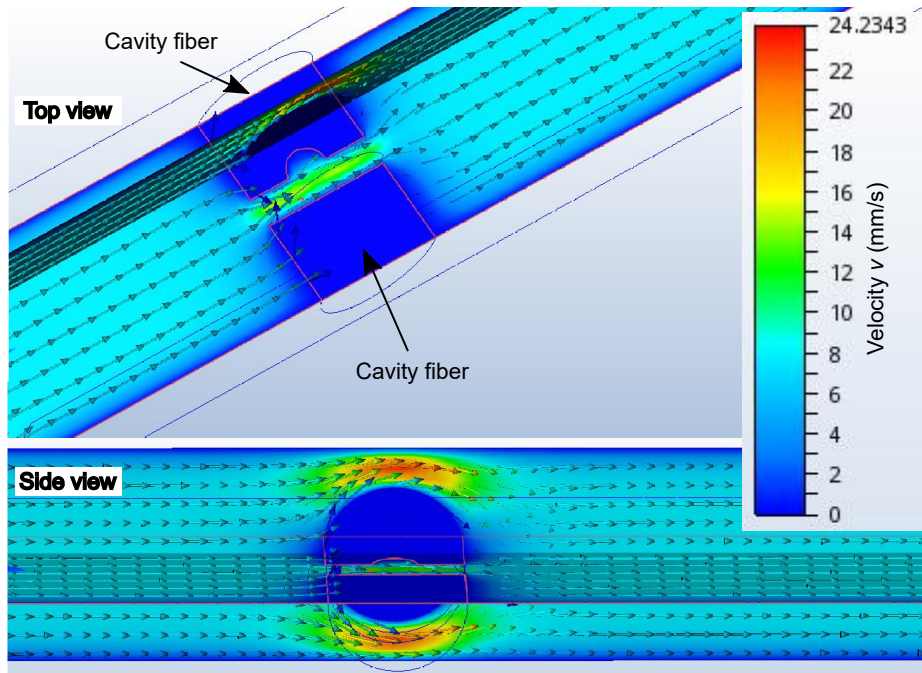


**Figure 3.7.:** Water flow simulation at a pressure difference of 140 Pa between the three inlets and the outlet. A top view as well as a side view on the microfluidic channel is shown. In the gap between the fiber ends and around the fibers the water velocity is increased, but no turbulences occur.

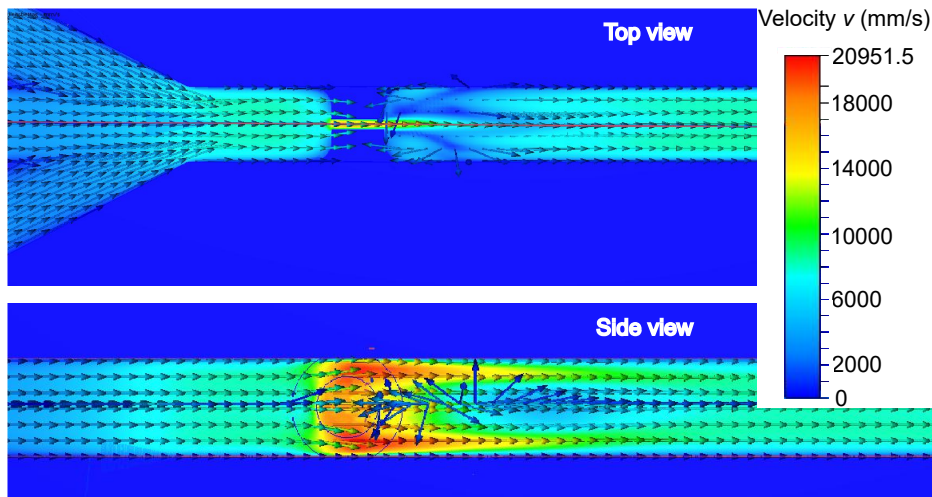


**Figure 3.8.:** Water flow simulation at a pressure difference of  $2.5 \cdot 10^5$  Pa between the three inlets and the outlet. A top view as well as a side view on the microfluidic channel is shown. In the gap between the fiber ends, around the fibers and after the constriction the water velocity is increased and turbulences occur.

the outlet. Since the cross-section for the water flow narrows at the fibers and the water is incompressible, the velocity is increased, when the water has to flow around the fibers and through the gap between the fiber ends. However, no turbulences occur and the fluid flow is laminar. On the other hand, if the pressure difference is increased to  $2.5 \cdot 10^5$  Pa, turbulences occur after the constriction caused by the cavity fibers protruding into the microfluidic channel (see Fig. 3.8).

All measurements presented in this work were performed without a liquid flow (zero pressure difference). However, if in the future measurements are to be carried out with liquid flow and a laminar flow is demanded, then low fluid velocities, much slower than  $v = 8000$  mm/s should be ensured inside the microfluidic channel. Under normal conditions, such low velocities are already achieved, which is why laminar flow is expected. The calculation of the fluid velocity in the microfluidic channel is explained in Appendix A.3.

**Hydrophobic versus hydrophilic microfluidic channel surface.** In the polymer microfluidic channel, as well as in the quartz glass microfluidic channel, SiO<sub>2</sub> nanoparticles were investigated. By comparing both channels with respect to the time of operation until the nanoparticles got stuck and the channel had to be mechanically cleaned, two major differences were observed: Whereas in the polymer channel the SiO<sub>2</sub> nanoparticles did not get stuck for at least 5 months<sup>7</sup>, they clogged the quartz glass channel within 1-3 weeks. As the surface of the polymer is hydrophobic and the surface of the hole inside the quartz glass ferrule is hydrophilic, it is assumed that the hydrophobic surface prevents the SiO<sub>2</sub> nanoparticles to adsorb at the surface of the polymer channel. In contrast, the free silanol groups on the surface of the SiO<sub>2</sub> nanoparticles presumably interact with the surface of the glass ferrule and tend of being adsorbed to the microfluidic channel wall (see Chapter 2.3.3). If the microfluidic channel is flushed, only the non-bound single nanoparticles and agglomerates can leave the ferrule through the microfluidic tubes. However, the bound nanoparticles remain and build ever-increasing SiO<sub>2</sub> agglomerates when new SiO<sub>2</sub> nanoparticles are introduced to the channel. This assumption is supported insofar as after about three weeks macroscopic sized glass structures could be resolved under the stereo microscope.

Therefore, it is assumed that a hydrophobization of the quartz glass ferrule surface could prevent the SiO<sub>2</sub> nanoparticles to bind to the surface and would enhance the sensors durability significantly. This can be achieved by a silanization with octadecyltrichlorosilane (OTS) (see Appendix A.8). However, the passivation of the microfluidic channel's surface depends on the kind of nanoparticle. Whereas the hydrophobization prevents SiO<sub>2</sub> nanoparticles to bind to the surface, unspecific protein binding at hydrophobic surfaces is observed for biological samples [150, 151].

---

<sup>7</sup> The polymer structure detached from the surface after 5 months.

	<b>Cavity A</b>	<b>Cavity B</b>	<b>Cavity C</b>
<b>Microfluidic channel</b>	polymer channel	quartz glass channel	quartz glass channel
<b>Material of the base</b>	aluminum	aluminum	Macor
<b>Sorbothane sheet</b>			×
<b>Hood</b>			×
<b>Microfluidic tubes</b>	removable	non-removable	removable

**Table 3.2.:** The different developed sensing platforms at a glance.

### 3.2. Combining all elements into the Fabry-Pérot sensing platform

The core of the FP sensor, consisting of the fiber-based FP cavity and the microfluidic channel (see Chapter 3.1) is embedded into a sensing platform. It is mounted on a base comprising all necessary components to operate the core of the FP sensor, such as microfluidic connectors and shear piezoelectric actuators for the cavity length modulation. As two of the three different microfluidic channel versions were used in the experiment (polymer and borosilicate channel) and the base was improved stepwise, the measurements presented in this work were carried out with three different sensing platforms. In the following, they are specified as cavity A, cavity B and cavity C and their main features are briefly summarized in Table 3.2. The principle of the sensing platform is described with cavity A, whereas only changes and improvements on cavity B and cavity C in respect to cavity A are highlighted. In all sensing platforms, liquid leaked out at the inlets of the precision hole, when it was pumped through the microfluidic channel. The precautions made in this context are explained in Appendix A.2. In the Appendix, also the exact details about the fabrication of the sensing platforms are given.

#### 3.2.1. Cavity A

Cavity A is the first cavity version and is shown in Fig. 3.9. Here, the core of the FP sensor is glued<sup>8</sup> on an aluminum base and the microfluidic channel consists of a direct laser-written polymer structure (see Chapter 3.1.2). Syringe needles<sup>9</sup> are glued<sup>10</sup> into the microfluidic channel inlet and outlet and an infusion extension line connector<sup>11</sup> enables a connection to commercial available microfluidic tubes<sup>12</sup>. The connectors and thus the long microfluidic tubes can be removed during nanoparticle measurements. For the modulation of the cavity length, each cavity fiber is clamped on a shear piezoelectric actuator<sup>13</sup>, which shear in opposite directions with an applied voltage. They are specified with a shear range of 3  $\mu\text{m}$  at an operating voltage of  $\pm 320$  V. Therefore, assuming a vacuum wavelength of 780 nm and the

<sup>8</sup> UHU plus schnellfest 2-Komponenten-Kleber

<sup>9</sup> Sterican Insulinkanüle gelb 30G, outer diameter: diameter of 0.3 mm.

<sup>10</sup> Epo-Tek OG116-31

<sup>11</sup> Braun 1 ProSet Verlängerungsleitung 0,5x2,35x300 mm PUR

<sup>12</sup> Upchurch 1561L PEEK tubing black; outer diameter: 1/16", inner diameter: 0.004".

<sup>13</sup> Noliac NAC2402-H2.3

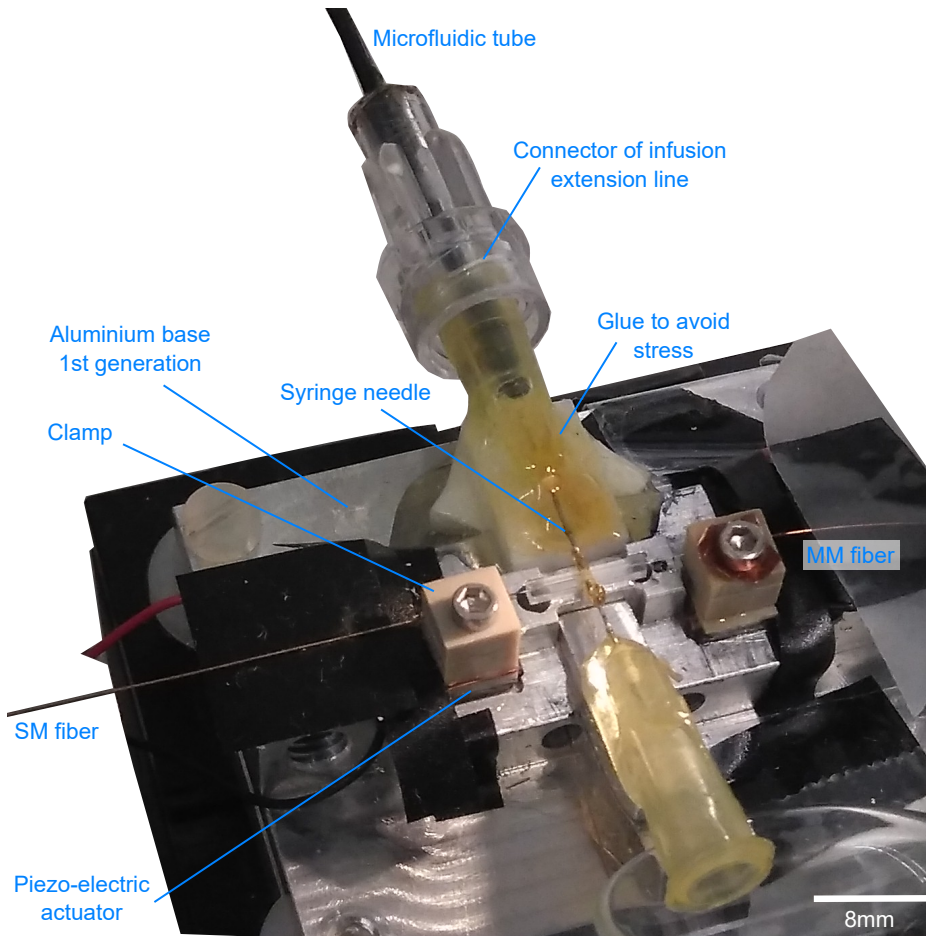


**Figure 3.9.:** Photograph of the first sensing platform (cavity A). The ferrule is glued on a aluminum base. Into the 3D-polymer structure syringe needles are glued in order to enable the connection to microfluidic tubes via the connector of an infusion extension line. Stress on the fragile 3D-polymer structure can be avoided by gluing the syringe on the aluminum base. Two piezoelectric actuators provide a modulation of the cavity length. For this purpose, clamps are glued on top to hold the cavity fibers.

cavity filled with water, the cavity length can be modulated more than 20 FSR. However, this specification applies only for unloaded piezoelectric actuators. In this case, clamps are glued on the piezoelectric actuators in order to mount the fibers and to allow fast unplugging of the fibers. Besides, the piezos are operated with a maximal voltage of  $\pm 175$  V. When taking the operation parameters as basis, a scanning range of 10 FSR is expected. As a matter of fact the cavity length could only be modulated by 4 FSR. The base is mounted on a 3-axis micropositioner<sup>14</sup>. This allows an adjustment of the cavity alignment via micrometer screws<sup>15</sup>. However, the positioning stage also increases the mechanical instability of the system, which becomes noticeable through a cavity length shift (see Chapter 3.5). For the adjustment of the

<sup>14</sup> Thorlabs MAX313D/M

<sup>15</sup> The precision hole is 6  $\mu\text{m}$  bigger than the fiber diameter. Therefore, small adjustments of the alignment can be made.

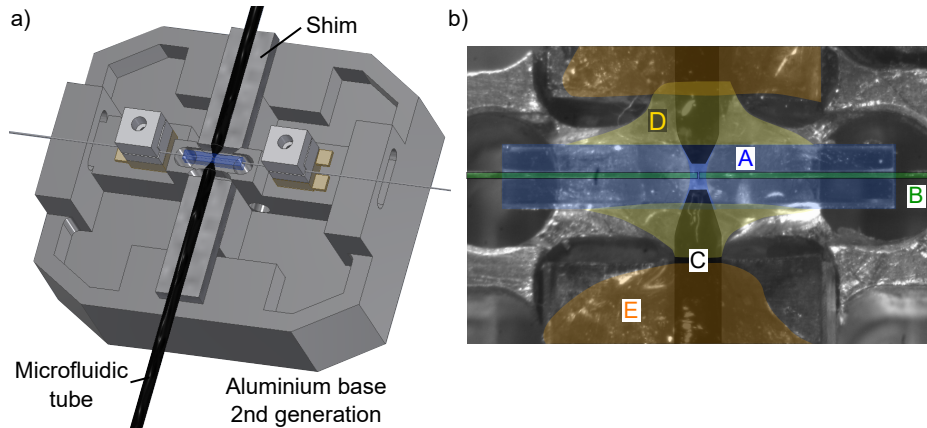


**Figure 3.10.:** The cavity B sensing platform. **a)** CAD drawing of the setup. The 2nd generation aluminum base consists of a drain for the microfluidics as well as of a catch basin. To prevent excessive forces on the drilled hole, the microfluidic tubes are glued to the aluminum base. Shims are used to adjust the height. **b)** Photograph of the ferrule (A), the inserted fibers (B), and the attached microfluidic tubes (C), which are tapered at the tip. The tube is glued into the hole (D) and on the shims (E).

cavity length, a second 3-axis micropositioner<sup>16</sup> is used, which is placed next to the sensing platform (compare Fig 3.12). During the preliminary adjustment, one fiber is already fixed to the clamp on the piezoelectric actuator and the second fiber is moved by clamping it on the 3-axis stage and via a micrometer screw. When the desired length is achieved, the second fiber is also fixed by the clamp on the piezoelectric actuator. During the measurements, the second fiber was still fixed on the micropositioning stage. Since the cavity length was only modulated by  $\approx 150$  pm, this had no influence on the movement of the fibers in the ferrule. The fixation on the micropositioning stage was necessary because, despite the clamping on the piezoelectric actuators, the cavity length changed several sub-micrometers independently from the piezoelectric modulation and had to be adapted by the micrometer screw after a few hours.

### 3.2.2. Cavity B

As the first sensing platform (cavity A) was assembled provisionally and the polymer microfluidic channel has detached from the ferrule after about 5 months, a new sensing platform was established. The section for the modulation of the cavity length remained the same, but the aluminum base became more professional and the polymer microfluidic channel was exchanged by a microfluidic channel consisting of a drilled hole into the ferrule (see Fig. 3.10). Into the quartz glass microfluidic channel, commercially available and tapered microfluidic tubes<sup>17</sup> are glued<sup>18</sup>. Therefore, they can't be removed during measurements. In this case, the

<sup>16</sup> Newport M-562-XYZ

<sup>17</sup> Upchurch 1561L PEEK tubing black; outer diameter: 1/16", inner diameter: 0.004".

<sup>18</sup> LOCTITE SI 5091

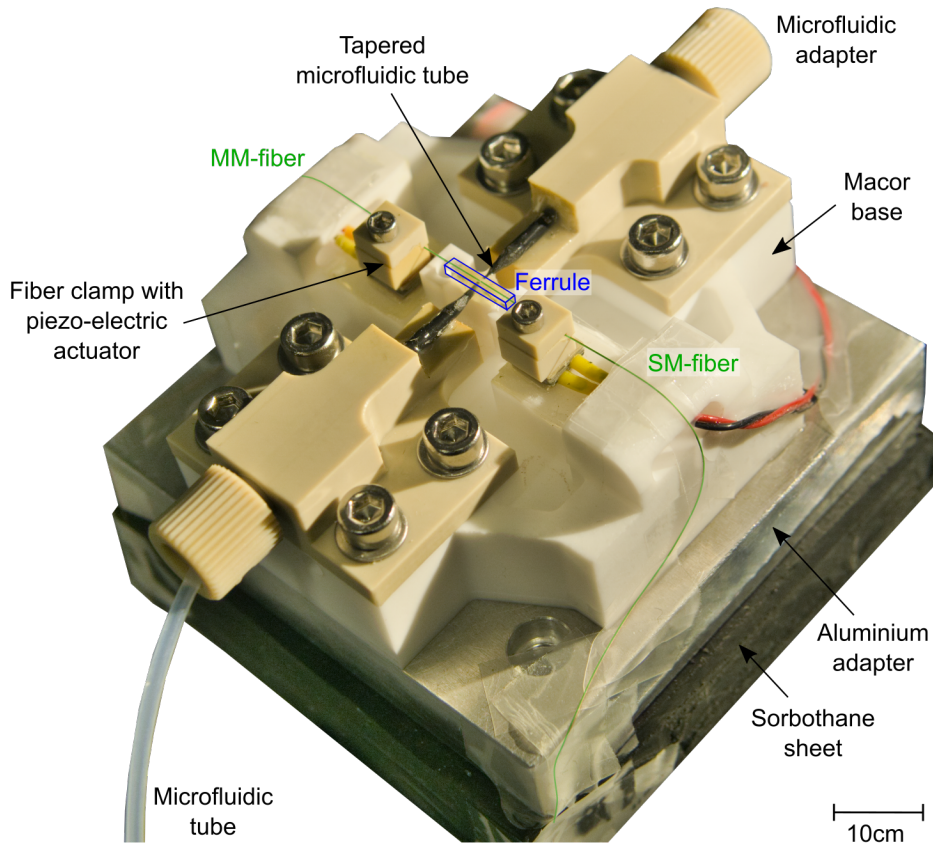


**Figure 3.11.:** Mount for the FP sensor. The Photograph shows the newest version of the cavity setup (cavity C). The core of the fiber-based FP microfluidic scanning cavity setup is mounted on a Macor base. Two clamps, each glued on a piezoelectric actuator, fix the cavity fibers, allowing the actuators to change the distance between the fiber end-facets. Tapered microfluidic tubes are glued into the conical holes of the ferrule in order to pass the liquid through the microfluidic channel. Microfluidic adapters allow the connection to additional microfluidic tubes, which in turn submerge in a liquid reservoir.

base is fixed on a massive aluminum block to avoid any mechanical noise generated by the mechanically unstable 3-axis micropositioner of cavity A.

### 3.2.3. Cavity C

Because of arising problems with cavity length drift in cavity A and B, a new version C was designed to eminently reduce the drifts and also to improve the measurement noise. (Fig. 3.11). The microfluidic channel is formed by a drilled hole in the quartz glass ferrule and the attachment of the tapered microfluidic tubes<sup>19</sup> (black color) to the ferrule is already explained for cavity B. This newest cavity version has the following new features:

First, the long tubes can be removed during measurements avoiding overhanging structures

<sup>19</sup> Upchurch 1561L PEEK tubing black; outer diameter: 1/16", inner diameter: 0.004".

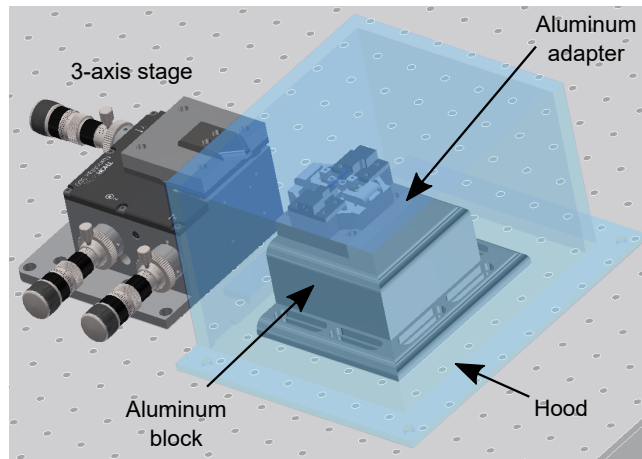


**Figure 3.12.:** Details of the sensor mount of cavity C. A 3-axis micropositioning stage is used to adjust the cavity length before both fibers are clamped and the piezoelectric actuators take over the fine-tuning. In order to increase the mechanical stability of the system, the 3-axis stage is removed and the FP sensor is covered by a hood.

and accordingly reducing the mechanical instability of the system. In contrast to cavity B, only a small piece of the tapered microfluidic tube is glued into the drilled hole of the quartz glass ferrule. On the opposite side of the tube, the tube is glued<sup>20</sup> into a microfluidic adapter<sup>21</sup>. In order to pump liquids through the microfluidic cell, long microfluidic tubes with an outer diameter of 1/16" can be connected to the adapter by commercial flangeless fittings<sup>22</sup>. Second, the new base consists of Macor instead of aluminum in order to reduce thermal drifts. Additionally, the corners of the fiber delivery are rounded, so that the fibers can be fixed to the base/socket. This avoids free-hanging glass fiber parts, reducing further vibrational noise. Finally, the base of cavity C is mounted on a massive aluminum block with a sorbothane sheet, which absorbs vibration from the table below. To reduce environmental influences, the complete sensing platform can be covered by a hood (see Fig. 3.12). Although the micropositioner was removed at measurements and both fibers were only fixed by the two clamps on the piezoelectric actuators, a cavity length drift was still observable independently from the cavity length modulation. Since the length changed only very slowly, this has negligible influence on individual measurements. In order to reduce this length changes in future, the clamping of the fibers has to be improved. For example a thin anti-friction coating on the clamps could provide remedy.

With the new sensing platform the cavity length shifts caused by the mechanical instability of the platform could be significantly improved. This is discussed in Chapter 3.5.1) in detail.

<sup>20</sup> LOCTITE SI 5091

<sup>21</sup> Milled by the workshop, material: polyetheretherketon (PEEK)

<sup>22</sup> Postnova XLT-111X

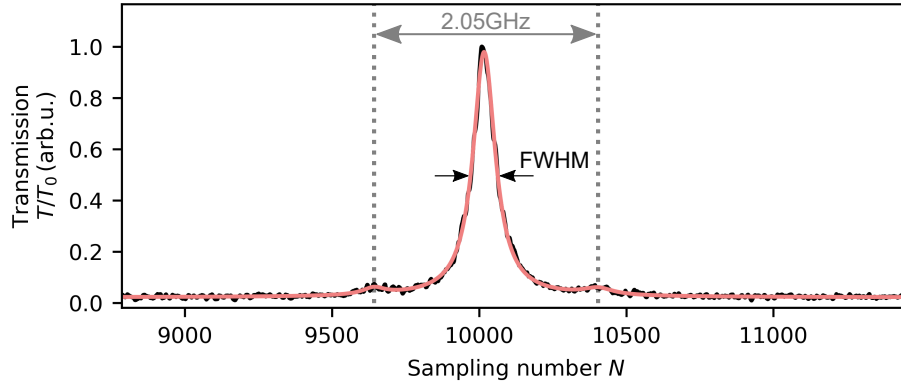


**Figure 3.13.:** Calibration of the resonance full width half maximum (FWHM). In addition to the  $TEM_{00}$  resonance two sidebands are excited, which are separated by 2.05 GHz. The gray vertical lines mark the maxima of the sidebands and the red curve is a fit to the measured data (black) by three Lorentzians.

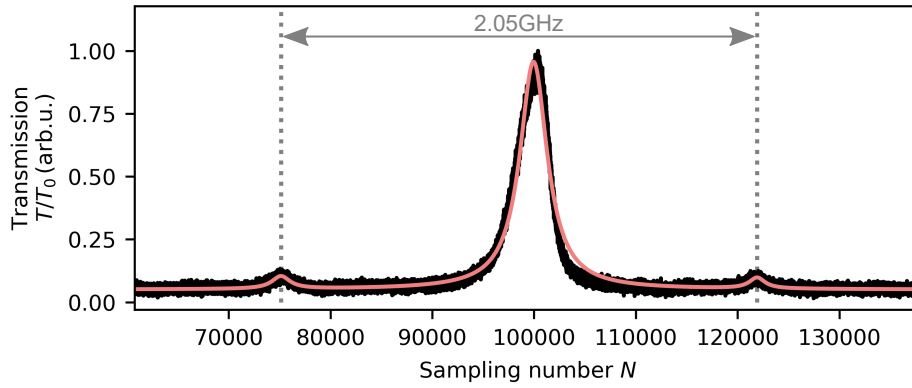


**Figure 3.14.:** Asymmetric resonance due to the photothermal effect. Three Lorentzians (red) are fitted to the resonance and the sidebands (black). The vertical dotted lines mark the sidebands, which are separated by 2.05 GHz.

### 3.3. Detection of the cavity finesse

Important properties of a FP resonator are the resonance full width half maximum (FWHM)  $\delta_\nu$  and the free spectral range (FSR)  $\Delta\nu_{\text{FSR}}$ . Both properties define the cavity finesse  $\mathcal{F}$ :

$$\mathcal{F} = \frac{\Delta\nu_{\text{FSR}}}{\delta_\nu} \quad (3.6)$$

(see Chapter 2.1.1), which is a figure of merit for the signal enhancement. The FSR itself depends on the optical cavity length (see Eq. (2.4)). In the following, the measurement of the FWHM and the optical length are explained in detail.

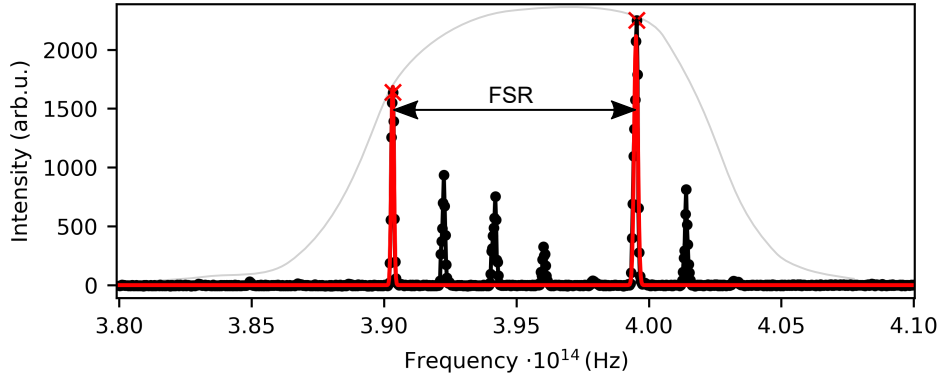


**Figure 3.15.:** Cavity free spectral range (FSR). At a fixed cavity length a superluminescent diode (SLED) is coupled into the resonator. The envelope of the SLED is sketched in gray. Two Gaussians (red) are fitted to the excited fundamental modes (black). The unfitted black curves are the excited higher-order modes.

### 3.3.1. Measurement of the full width half maximum

The FWHM of the resonance is measured with an electro-optic modulator (EOM)<sup>23</sup>, which creates sidebands with a known frequency distance. This allows the calibration of the measured FWHM from sampling numbers into frequency scales. The frequency distance of the sidebands is set by a signal generator<sup>24</sup>, which drives the EOM. In this case, it is set to 2.05 GHz. In Fig. 3.13 a recorded fundamental mode with sidebands is shown. The FWHM in sampling numbers  $\delta_N$  can be calculated into the FWHM in frequency units  $\delta\nu$  via the distance between the two sidebands  $\Delta N$ :

$$\delta\nu = \frac{2.05 \text{ GHz} \cdot \delta_N}{\Delta N} . \quad (3.7)$$

Here, a resonance with a  $\delta\nu = 490$  MHz FWHM is shown. With this cavity, the tracking of the three-dimensional motion of a single nanosphere was observed (see Chapter 5). The measurement of the FWHM has to be conducted at low laser<sup>25</sup> powers and at high scanning frequencies<sup>26</sup>. Otherwise, the cavity mirrors would absorb the high intracavity light and expand to such an extent that an asymmetric resonance occurs (see Fig. 3.14). This effect is also called "photothermal effect" [88]. By comparing the FP cavity operated in air and water, an increased photothermal effect could be observed in water due to water absorption.

### 3.3.2. Measurement of the cavity length

In order to measure the cavity length, the mirror distance is kept at a fixed value and a broadband light source is coupled into the cavity. In this case, the light source is a superluminescent

<sup>23</sup> Laser Components NIR-MPX800

<sup>24</sup> DS Instruments SG4400L

<sup>25</sup> The laser power was reduced so much that the sidebands were just visible.

<sup>26</sup> Usually, the cavity was scanned with a 1...3 kHz frequency.

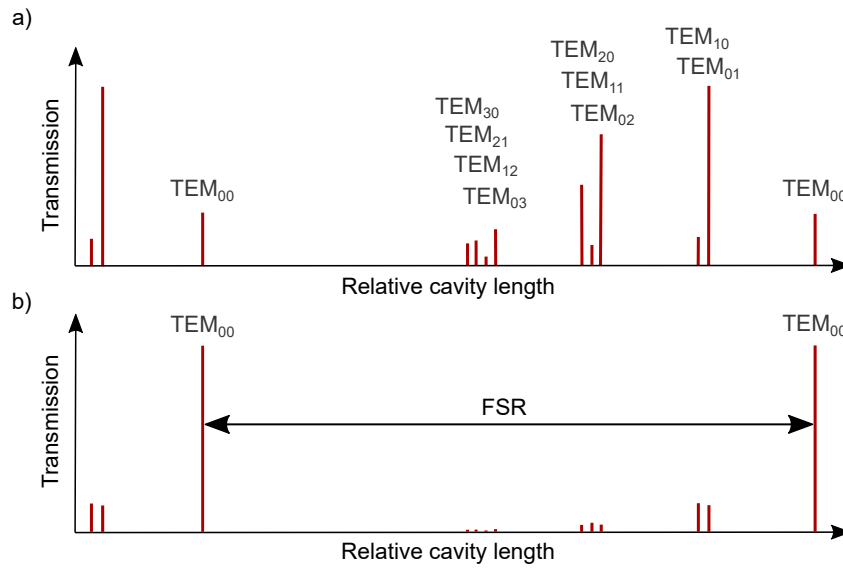


**Figure 3.16.:** Sketch of excited resonances with differently aligned cavity mirrors. **a)** A bad alignment of the mirrors results into a strong excitation of the higher-order modes (in this case the TEM<sub>01</sub> mode is strongest excited). **b)** A good cavity alignment is reached when especially the fundamental mode TEM<sub>00</sub> is excited and the higher-order transverse modes are almost not excited.

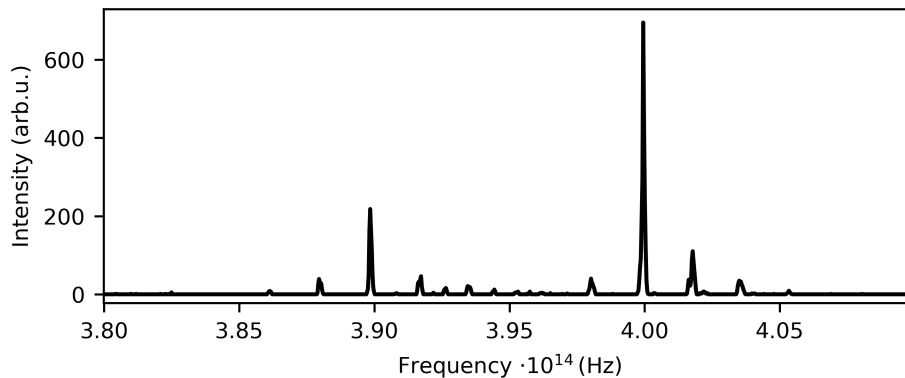


**Figure 3.17.:** Spectrum, when the cavity length is fixed and resonances are excited by a SLED. In this case, the cavity mirrors are poorly aligned.

diode (SLED) (see Fig. 3.19), which excites several resonances simultaneously in the cavity. The transmitted light is directed to a grating spectrometer via a magnetically mounted mirror. Fig. 3.15 shows such a recorded resonance spectrum. In this case, two fundamental modes are excited and the FSR can be measured and the optical cavity length deduced. However, the shorter the cavity length, the less fundamental modes are excited by the SLED and are visible in the spectrometer. With the SLED used in this work, at about 5.4  $\mu\text{m}$  optical cavity length only one fundamental mode, and the higher-order modes are detected. Then, the optical cavity length has to be determined by the distance between the higher-order transverse modes of same order. At first, the detection of the cavity length via the free spectral range is explained and then its detection via the higher-order transverse modes is discussed.

**Cavity length via the free spectral range.** Fig. 3.17 shows a recorded spectrum when the cavity length is constant and an SLED simultaneously excited several resonances in the fiber-based FP cavity. As the cavity mirrors were well-aligned, the two highest resonances can be assigned to two consecutive fundamental modes and their distance to each other is one FSR. According to Eq. (2.4), the cavity length can be deduced from the measured FSR  $\Delta\nu_{\text{FSR}}$  by

$$d_{\text{opt}} = \frac{c_0}{2n_m \Delta\nu_{\text{FSR}}} , \quad (3.8)$$

with  $\Delta\nu_{\text{FSR}} = \nu_{q+1,m,n} - \nu_{q,m,n}$ . In this case, the optical cavity length is  $d_{\text{opt}} = 16.3 \mu\text{m}$ . In general, perfectly aligned cavity mirrors are achieved when mainly the fundamental mode is excited and the higher-order modes are hardly excited. In contrast, a strong excitation of one of the higher-order transverse modes and a weak excitation of the fundamental mode is caused by badly aligned mirrors. Also, strongly different resonance amplitudes of the degenerated higher-order transverse modes provide evidence of poor alignment. In Fig. 3.16 the cases for a good and a bad alignment are schematically depicted. When the mirrors are badly aligned, the resonance spectrum recorded by the spectrometer is difficult to interpret. Fig. 3.17 shows such a recorded spectrum. Probably the first higher-order transverse mode is excited strongest, but quickly the spectrum is misinterpreted and thus a wrong cavity length is measured. In this case, the finesse can be estimated via the oscilloscope. Both, the FWHM as well as the FSR, are determined in sampling number units:

$$\mathcal{F} = \frac{\Delta\nu_{\text{FSR},N}}{\delta_N} . \quad (3.9)$$

However, the error on the measured FSR is large due to the piezoelectric actuators expanding non-linear and thus an error on the finesse of about 10 % has to be assumed. But if the finesse is approximately known and the FWHM is also measured in frequency units, the cavity length can be estimated. This can be thereupon used as a reference value for the hardly to interpret FSR spectrum.

**Cavity length via the higher-order transverse modes.** When at short cavity lengths ( $< 5.4 \mu\text{m}$ ) less than one FSR is excited in the FP cavity by the SLED, the optical cavity length and accordingly the FSR has to be determined via the distance between consecutive higher-order transverse modes of the same order  $q$ . According to Eq. (2.19) the following applies:

$$\nu_{q,m,n} - \nu_{q,m-1,n} = (\xi(z_2) - \xi(z_1)) \frac{\Delta\nu_{\text{FSR}}}{\pi} , \quad (3.10)$$

with the phase retardation

$$\xi(z) = \arctan \left( \frac{\lambda_0}{n_m \pi w_0^2 z} \right) . \quad (3.11)$$

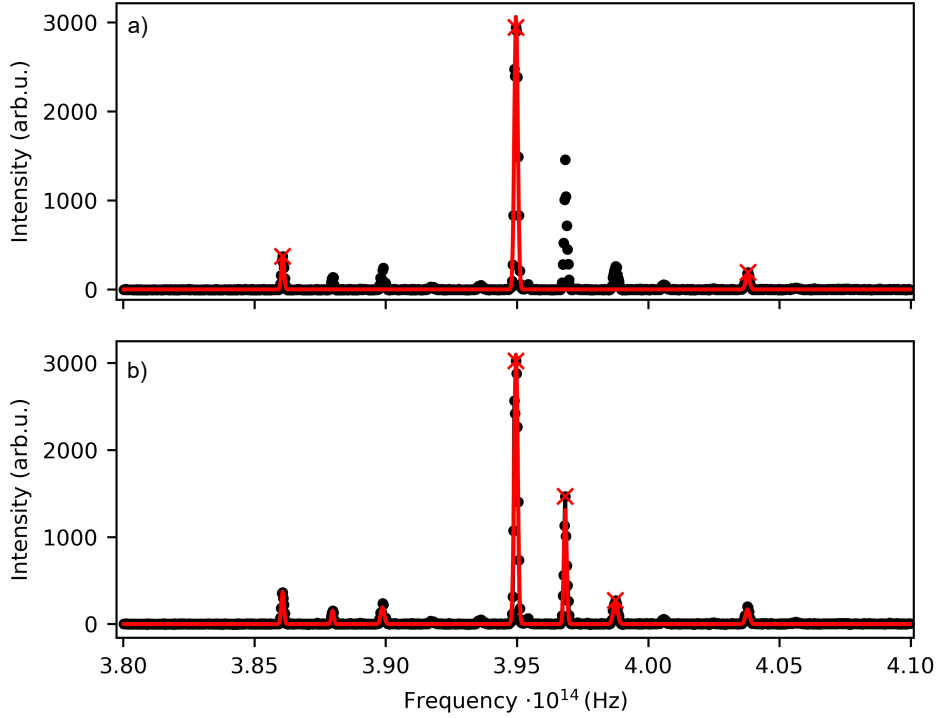


**Figure 3.18.:** Evaluation of the optical cavity length **a)** by taking the distance between consecutive fundamental modes and **b)** by considering the higher-order transverse modes of the same order  $q$ . The chosen modes are marked with red crosses.

Both, the waist  $w_0$  (see Eq. 2.16), as well as  $z_1$  and  $z_2$ , depend on the radii of curvatures  $r_{c,1}$ ,  $r_{c,2}$  of both mirrors as well as on the optical cavity length  $d_{\text{opt}}$  [100]:

$$w_0 = \sqrt{\sqrt{\frac{-d_{\text{opt}}(r_{c,1} + d_{\text{opt}})(r_{c,2} + d_{\text{opt}})(r_{c,1} + r_{c,2} + d_{\text{opt}})}{r_{c,1} + r_{c,2} + 2d_{\text{opt}}}} \frac{\lambda_0}{n_m \pi}} , \quad (3.12)$$

$$z_1 = \frac{-d_{\text{opt}}(r_{c,1} + d_{\text{opt}})}{r_{c,1} + r_{c,2} + 2d_{\text{opt}}} , \quad (3.13)$$

$$z_2 = z_1 + d_{\text{opt}} . \quad (3.14)$$

Since the used cavity mirror profiles are not rotationally symmetric but elliptical (see Chapter 3.1.1) and the higher-order transverse modes are radially expanded, different radii of curvatures have to be taken into account for the different modes. A more exact description of the higher-order transverse modes would be a series expansion of the Hermite-Gaussian modes as shown by Julia Benedikter [152]. Though, here it is shown that an empirical correction factor  $f_c$  to

$d_{\text{opt}}$ ( $\mu\text{m}$ ) via Eq. (3.8)	$d_{\text{opt}}$ ( $\mu\text{m}$ ) via Eq. (3.15)	$d_{\text{opt}}$ ( $\mu\text{m}$ ) via Eq. (3.10)
$16.9 \pm 0.1$	$16.7 \pm 0.8$	$22.6 \pm 1.1$
$16.3 \pm 0.003$	$16.3 \pm 1.0$	$22.1 \pm 1.5$
$12.8 \pm 0.0003$	$12.9 \pm 0.9$	$17.3 \pm 1.3$
$9.7 \pm 0.01$	$9.6 \pm 1.0$	$12.9 \pm 0.3$

**Table 3.3.:** Determination of the optical cavity length via the distance between consecutive fundamental modes (1st column), via the distance between consecutive higher-order modes including an empirical factor of  $f_c = 0.87$  (2nd column) and via the distance between consecutive higher-order modes without the consideration of an empirical factor (3rd column). Each column shows the averaged value as well as the standard deviation (five measurements at each cavity length).

the phase retardation in Eq. (3.10) gives good enough results for the determination of the optical cavity length. Hence, Eq. (3.10) is adapted to

$$v_{q,m,n} - v_{q,m-1,n} = f_c \cdot (\xi(z_2) - \xi(z_1)) \frac{\Delta v_{\text{FSR}}}{\pi} \quad (3.15)$$

for elliptical mirror profiles. The empirical factor  $f_c$  can be determined at longer cavity lengths, where the cavity length can also be measured via the FSR range. Such an example is shown in Fig. 3.18. For the same recorded spectrum, the cavity length is determined via the FSR (a) and via the higher-order transverse modes (b). Here, the empirical factor of  $f_c = 0.87$  has to be set in order to reach the same results for the optical cavity length. By reducing the cavity length, the same factor continues to lead to a good agreement between both evaluation methods (see Table 3.3). If, on the other hand, no empirical factor is assumed ( $f_c = 1$ ), the higher-order transverse modes deliver a result which deviates by up to 36 % from the value determined via the FSR (see third column of the table).

### 3.4. Detection of nanoparticle signals

This chapter provides the background information for the detection of nanoparticle signals. In this work, different kind of quartz glass nanospheres were investigated. At first, the preparation of the nanosphere colloidal solution is presented (Chapter 3.4.1). Chapter 3.4.2 deals with the optical and electrical peripherals. These components are required to operate the fiber-based cavity sensor. Finally, in Chapter 3.4.3 the detection principle of nanoparticle signals is discussed.

#### 3.4.1. Preparation of the nanoparticle colloidal solution

Three different quartz glass  $\text{SiO}_2$  nanosphere colloidal solutions with different sizes were used to conduct the measurements for the evaluation of the theoretical simulations. In the following, they are denoted as sample A, sample B and sample C (see Table 3.4). All manufacturers provide the  $\text{SiO}_2$  nanospheres dispersed in water and for detailed information see Appendix

	Sample A	Sample B	Sample C
$r_{\text{geom}}$ (nm)	$63.2 \pm 1.7$	$60.0 \pm 1.8$	$25.0 \pm 0.8$
$n_{\text{SiO}_2}$	1.42	1.45	1.45

**Table 3.4.:** SiO<sub>2</sub> nanospheres investigated in different experiments presented in this work. The intrinsic properties of the bare nanoparticle are given: Geometric radius  $r_{\text{geom}}$  and intrinsic refractive index  $n_{\text{SiO}_2}$ .

A.5.

SiO<sub>2</sub> nanoparticles tend to agglomerate within a short period of time (after  $\approx 1$  h, see 5.2). In order to separate the agglomerates and thereby increase the number of single particles inside the nanoparticle solution, an ultrasonic tip<sup>27</sup> is used<sup>28</sup>. First, 5  $\mu\text{l}$  of the nanoparticle solution is mixed with 2 ml of double-distilled water. Then, the solution is treated for 15 min with the ultrasonic tip at 90% of amplitude. The leftover agglomerates can be filtered out by a micrometer-pore filter with a suitable size, but this step can be also skipped, as the filters uncontrollably reduce the nanoparticle concentration. Eventually, the nanoparticle solution is pumped into the FP sensor microfluidic system via compressed air on a pressure vessel until it flushes the cavity at the center of the microfluidic channel. Subsequently, the pressure is turned off and after about 10 min to 1 h of waiting time, nanoparticle measurements are conducted. The waiting time is necessary in order to avoid drifts and to measure the free Brownian motion of single nanoparticles inside the FP cavity.

### 3.4.2. Optical and electrical components

In the following, the optical and electrical parts are explained, which are crucial for the operation of the cavity. Two different narrow-linewidth lasers and a broadband superluminescent diode (SLED)<sup>29</sup> can be coupled into the cavity single-mode (SM)-fiber (see Fig. 3.19). Here, the parts that are important for nanoparticle measurements are described.

Two narrow lasers, an external grating stabilized diode laser ( $\lambda = 780$  nm, laser linewidth  $< 1$  MHz on short time scales<sup>30</sup>) and a volume-holographic-grating stabilized laser diode ( $\lambda = 785$  nm, laser linewidth: 10 MHz<sup>31</sup>, laser head mount see Appendix A.4) are used to probe the cavity while the cavity length is modulated and single nanoparticles are diffusing through the cavity. At each optical path, a fiber-based polarization controller ( $\lambda/4 - \lambda/2 - \lambda/4$ ) allows the control of the polarization and thereby the control of the mode polarization inside the cavity (see Chapter 2.6). Via a 90/10-beam splitter<sup>32</sup>, both lasers are coupled into the input SM-cavity fiber at the same time. The transmitted light through the output multi-mode (MM)-cavity fiber is collimated into a free-space beam and focused on an avalanche photodiode (APD)

<sup>27</sup> Bandelin Sonopuls mini20 with a MS 1.5 sonotrode

<sup>28</sup> This only works for silicon dioxide nanoparticles. E.g. agglomerated polymethylmethacrylat (PMMA) agglomerates or polystyrol (PS) agglomerates are more difficult to separate since they can be destroyed at ultrasonic treatment. Here an anionic surfactant could help.

<sup>29</sup> About 40 nm broad spectrum at the center wavelength 755 nm.

<sup>30</sup> TOPTICA DLpro

<sup>31</sup> Thorlabs LP785-SAV50

<sup>32</sup> Thorlabs TN785R2A2

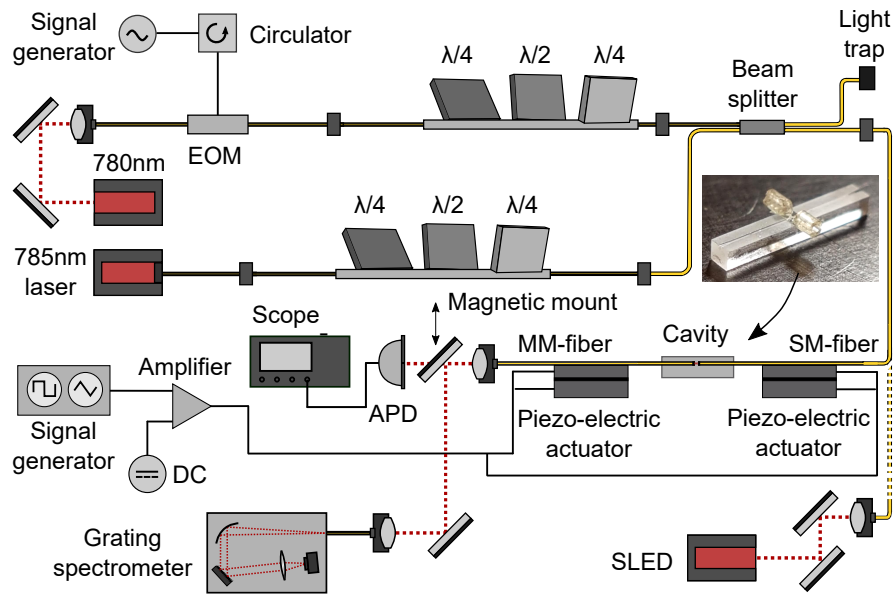


**Figure 3.19.:** Schematic drawing of the optical setup and the electrical components. The 780 nm and 785 nm lasers are used to probe the cavity and the transmitted light is detected by an APD and recorded by an oscilloscope. Two piezoelectric actuators shear in opposite directions, allowing a modulation of the cavity length. In order to measure the FWHM of the FP resonator, an EOM is used to calibrate the linewidth of the resonance in frequency units. The FSR can be measured by keeping the cavity length constant and coupling the SLED into the cavity. A magnetically mounted mirror is used to guide the transmitted light into a grating spectrometer. Sketch is similar to supplementary information of [95].

(bandwidth: 50 MHz). A 12 bit digital storage oscilloscope<sup>33</sup> records the APD signal. In order to modulate the cavity length during the measurement, two piezoelectric actuators are operated by a periodical high voltage waveform. The signal generator controls the shape of the voltage signal (e.g. sinusoidal or triangular) and provides the trigger signal in addition. The output of the signal generator is amplified<sup>34</sup> up to  $\pm 175$  V. In the following, the frequency of the modulated signal is called "scanning frequency".

### 3.4.3. Measurement principle

In this section, the basic measurement principle is explained, when the transmission signal is changed due to a nanoparticle diffusing through the standing-wave light field of the cavity (see Chapter 2.3). During the measurements, the cavity length is modulated either by a sinusoidal or a triangular signal in order to scan over the resonance. At higher scanning frequencies between 5 kHz and 15 kHz the sinusoidal signal produces less mechanical noise than the triangular signal. The non-linear expansion of the piezoelectric actuator can be overcome by

<sup>33</sup> LeCroy HRO66Zi

<sup>34</sup> Falco Systems WMA-280 for the three-dimensional tracking experiments and Falco Systems WMA-02 for the other experiments

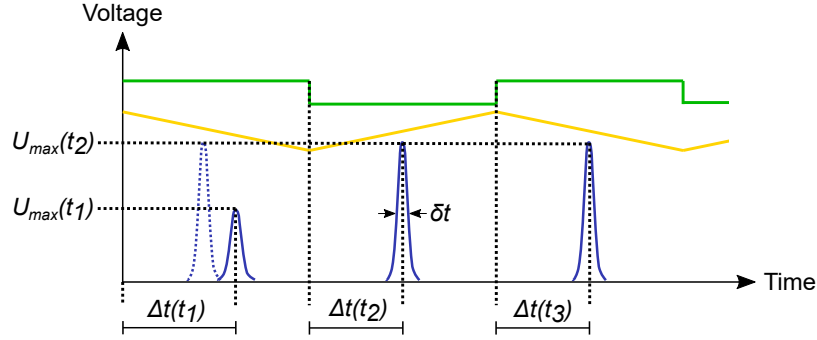


**Figure 3.20.:** Schematic drawing of the resonance (blue) occurring at each trigger event (green). In yellow, the triangular voltage signal, which drives the piezoelectric actuators, is depicted. The peak voltage  $U_{\max}(t)$ , FWHM  $\delta t(t)$  as well as the resonance peak time distance to the trigger  $\Delta t(t)$  change when a nanoparticle diffuses through the cavity standing-wave light field (dotted blue curve). Submitted to [95].

a local calibration of the slope with electro-optic modulator (EOM) sidebands. Below 5 kHz a triangular signal is preferable since the mechanical noise is low and the piezoelectric actuator expands approximately linear, when a correct voltage range is selected. The signal shape, as well as the corresponding trigger signal, stem from the frequency generator. In this case, the triangular signal (yellow) and the trigger signal (green) are schematically depicted in Fig. 3.20. At a certain cavity length, the resonance occurs (blue). Here, for the sake of simplicity, only one resonance (e.g. of the  $TEM_{00}$ ) with one polarization is shown<sup>35</sup>. At each trigger event, the resonance peak  $U_{\max}(t)$ , the FWHM  $\delta t(t)$  as well as the resonance peak time distance to the trigger  $\Delta t(t)$  is recorded by the oscilloscope<sup>36</sup>. If noise is neglected, the three parameters have a constant value, if the cavity is empty. However, when a nanoparticle diffuses into the cavity,  $U_{\max}(t)$  decreases,  $\delta t(t)$  broadens and  $\Delta t(t)$  shifts (see Chapter 2.3).

In Fig. 3.21 a typical time trace for  $\delta t(t)$ ,  $\Delta t(t)$  and  $U_{\max}(t)$  is shown. Here the calculation of the raw data into frequency shift ( $\Delta\nu$ ) units and the DOA is explained. Both, the frequency shift as well as the decrease of amplitude are related to the unperturbed, empty cavity parameters. As the cavity length drifts over time, the recorded time traces have to be fitted in order to determine the unperturbed cavity parameters at each time. First, a linear fit  $\delta t_{\text{fit}}$  is fitted to the unperturbed  $\delta t$ <sup>37</sup> (see a)). In b)  $\Delta t(t)$  is already plotted in units of the FWHM fit  $\delta t_{\text{fit}}$  and is called "lineshift". To get rid of the cavity length drift, a linear fit  $\Delta t_{\text{fit}}$  is fitted to the

<sup>35</sup> If both polarizations of the  $TEM_{00}$  are desired (see Chapter 6), the polarization controller can be used to change the polarization of the laser. The higher-order transverse mode of order 01 ( $TEM_{01}$ ) and higher-order transverse mode of order 01 ( $TEM_{10}$ ) can be detected together with the  $TEM_{00}$  mode by operating the second probe laser in addition (see Chapter 5).

<sup>36</sup> In order to record the three parameters at each trigger event, the oscilloscope is operated in sequence mode. In this mode, the oscilloscope first writes the full probe signal (blue) into its memory and then calculates the three parameters after the memory storage capacity is reached. In timebase mode, the oscilloscope would save the first trigger event, calculate the three parameters and then save the next trigger event. As the calculation takes about 0.01 s, data is getting lost if the scanning frequency is higher than 100 Hz.

<sup>37</sup> Meaning the  $\delta t_{\text{fit}}$  of the cavity filled with double distilled water, but none of the silica nanoparticles residing in the cavity standing-wave light field.

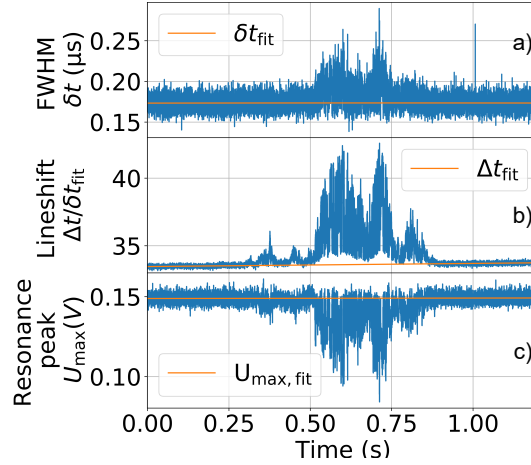


**Figure 3.21.:** Recorded time traces of the resonance FWHM  $\delta_t(t)$ , the time shifts  $\Delta t(t)$  and the resonance peak  $U_{\max}$ , when a  $\text{SiO}_2$  nanosphere of 75.3 nm hydrodynamic radius diffuses through the cavity standing-wave light field. The resonance parameters are explained in Fig. 3.20. **a)** Linear fit to the unperturbed  $\delta_t(t)$ , **b)** Linear fit to the unperturbed lineshifts  $\Delta t/\delta_{t,\text{fit}}$ , **c)** Linear fit to the unperturbed  $U_{\max}$ . Submitted to [95] (supplementary information).

unperturbed lineshifts. By subtracting  $\Delta t_{\text{fit}}$  and multiplying the FWHM in frequency units ( $\delta_\nu$ ), the time-dependent frequency shifts  $\Delta \nu$  are finally calculated:

$$\Delta \nu(t) = \left( \frac{\Delta t}{\delta_{t,\text{fit}}} - \Delta t_{\text{fit}} \right) \delta_\nu \quad . \quad (3.16)$$

In c) the recorded  $U_{\max}$  as well as a linear fit  $U_{\max,\text{fit}}$  to the unperturbed data is shown. The DOA is defined as the percentage deviation of the measured data to the fit at time  $t$ :

$$DOA(t) = 100\% \left( 1 - \frac{U_{\max}(t)}{U_{\max,\text{fit}}(t)} \right) \quad (3.17)$$

### 3.5. Resolution limit of the different cavity versions

Before nanoparticle signals are investigated with the FP fiber-based sensor, it is crucial to know the resolution limit of the sensor. The resolution limit depends on the signal enhancement as well as on the measurement noise. Various changes were made between the three different cavity designs cavity A, cavity B, and cavity C (see Chapter 3.2). Here, not only the design of the setup including the different microfluidic channel versions changed, but the fiber-based FP cavity itself was also operated with different cavity mirrors and at different optical cavity lengths (see Table 3.5). In the table, next to the FWHM in frequency units  $\delta_\nu$ , also the FWHM in cavity length units  $\delta_d$  is given. As the finesses are the same, the following relation applies

$$\frac{\Delta_d}{\delta_d} = \frac{\Delta \nu_{\text{FSR}}}{\delta_\nu} \quad , \quad (3.18)$$

	Cavity A	Cavity B	Cavity C (1 kHz)	Cavity C (14.1 kHz)
$\mathcal{F}$	18400	56710	52228	50469
$d_{\text{opt}}$ ( $\mu\text{m}$ )	27.3	5.4	5.1	8.14
$\delta_v$ (MHz)	299	490	561	365
$\delta_d$ (pm)	21.2	6.9	7.4	7.7
$\bar{r}_{\text{c,SM}}$ ( $\mu\text{m}$ )	59.3	49.6	49.6	37.1
$\bar{r}_{\text{c,MM}}$ ( $\mu\text{m}$ )	95.0	83.5	83.5	87.6
$w_0$ ( $\mu\text{m}$ )	2.27	1.53	1.51	1.60

**Table 3.5.:** Cavity geometry and finesse of the different cavity versions. Cavity C was operated with two different cavity fiber mirror pairs. They are specified by the operated modulation frequency of the cavity length of 1 kHz and 14.1 kHz. From each elliptically shaped cavity mirrors (see Appendix 3.6) the mean value of the radii of curvatures  $\bar{r}_{\text{c},i}$ , with  $i = \{\text{SM}, \text{MM}\}$  is given. The waist  $w_0$  was calculated by Eq. (2.16). Results of cavity A and cavity B have been submitted to [95].

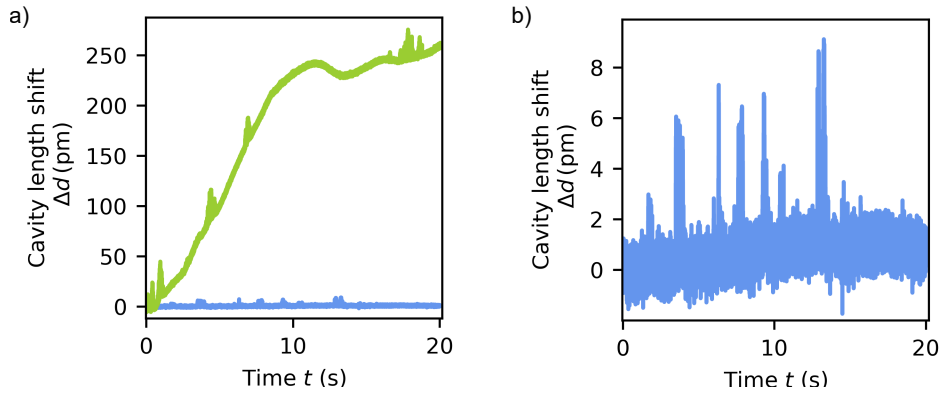


**Figure 3.22.:** Comparison of the drift behavior between cavity A and cavity C. **a)** Within 20 s of measurement time, the signal measured by cavity A (green) drifts about  $\Delta d = 268$  pm, whereas there is no significant signal drift observed with cavity C (blue) in this representation. **b)** Signal recorded with cavity C. Within 20 s it only drifts about  $\Delta d \approx 1$  pm.

with the free spectral ranges  $\Delta d_{\text{FSR}} = \lambda_0 / (2n_m)$  and  $\Delta v_{\text{FSR}} = c_0 / (2n_m d_{\text{opt}})$ . Therefore, when  $\Delta v_{\text{FSR}}$  and  $\delta_v$  are measured (see Chapter 3.3), the FWHM  $\delta_d$  can be calculated by

$$\delta_d = \frac{\delta_v \lambda_0}{\Delta v_{\text{FSR}} 2n_m} . \quad (3.19)$$

The construction of the sensing platform has an impact on the measurement noise, whereas the FP cavity geometry determines the signal enhancement. At first, the different cavity designs are compared in terms of their passive stability and their measurement noise. Then, the resolution limit of each cavity is discussed.

### 3.5.1. Passive stability and measurement noise

First, the drift behavior of cavity A and cavity C are compared (see Fig. 3.22). Both signals were recorded in a noisy laboratory when people were walking around. This is important to

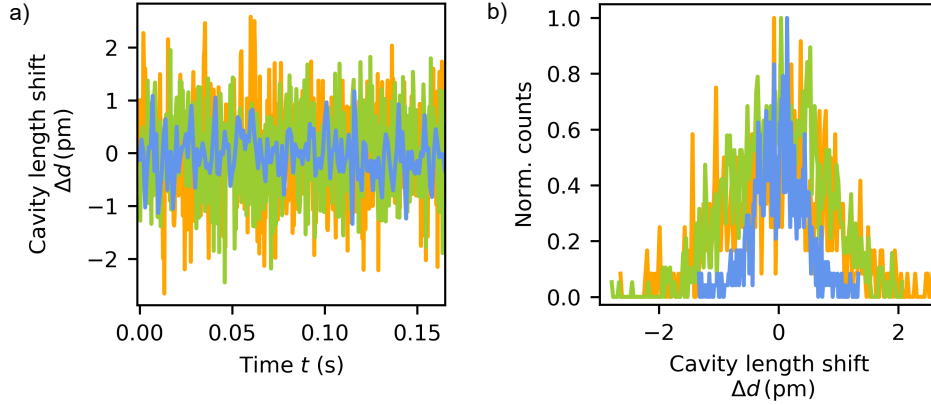


**Figure 3.23.:** Measurement noise of the signals recorded by three different setups. **a)** Time traces for the measured length shifts  $\Delta d$ . The signal of cavity A (green) shows an *rms*-noise of 0.77 pm and a peak-to-peak noise of 4.86 pm. Cavity B (orange) produces an *rms*-noise of 0.91 pm and a peak-to-peak noise of 5.21 pm and the noise of cavity C (blue) is significantly the lowest: the *rms*-noise is 0.43 pm and the peak-to-peak-noise is 2.66 pm. **b)** Histograms of the measured time traces in a).

mention since the mechanical instability can be significantly reduced in a quite laboratory and without people walking around. Thus, only signals within the same environmental conditions are compared. Within 20 s of measurement time, cavity A drifts about  $\Delta d \approx 268$  pm (see a)), which is about 12.6 times the FWHM  $\delta_{d,A}$  of the resonance, whereas cavity C hardly drifts ( $\Delta d \approx 1$  pm =  $0.13 \cdot \delta_{d,C}$ , see b)).

In order to compare the different background noises, the drifts are subtracted from the length shifts and only short, unperturbed<sup>38</sup> parts of the signal are taken (see Fig. 3.23 a)). In addition to the length shifts of cavity A (green) and C (blue), also cavity B (orange) is compared. The signal recorded by cavity A has an *rms*-value of  $rms_A = \sqrt{(\sum_i^{N_1} (\Delta d_i)^2) / N} = 0.77$  pm =  $0.04 \cdot \delta_{d,C}$ , the *rms*-value of the signal recorded with cavity B is slightly greater ( $rms_B = 0.91$  pm =  $0.13 \cdot \delta_{d,C}$ ) and the smallest *rms*-value could be measured with cavity C ( $rms_C = 0.43$  pm =  $0.06 \cdot \delta_{d,C}$ ). Fig. 3.23 b) shows the measured length shifts in an histogram. The peak-to-peak noise values of cavity A and B are similar with 4.86 pm and 5.21 pm, whereas the noise value for cavity C is significantly lower (2.66 pm). The signals of cavity A and B were taken with a 3 kHz and the signal of cavity C with a 1 kHz scanning frequency. In order to exclude that the better background noise of cavity C stems from the lower scanning frequency, the *rms*-value and peak-to-peak noise is also determined for a 14.1 kHz measurement with cavity C. Here, both values are even slightly smaller in comparison to the 1 kHz frequency measurement:  $rms = 0.39$  pm =  $0.05 \cdot \delta_{d,C}$  and 2.56 pm peak-to-peak noise.

**Discussion.** By comparing the drift behavior and the *rms* noises of cavity C with cavity A and cavity B, both could be significantly improved. In the following, the implemented

<sup>38</sup> Cavity is only filled with water, but no nanoparticle resides inside the light field.

mechanical improvements of cavity C, as well as general aspects, are discussed which provide an improved mechanical stability:

- The new sensor mount (cavity C) consists of a Macor base instead of an aluminum base (cavity A, B). Macor has a significantly smaller coefficient of linear thermal expansion ( $\alpha_L$ ) of  $\alpha_{L,Macor} = 9.3$  ppm/K in comparison to that of aluminum ( $\alpha_{L,Al} = 22.9$  ppm/K) [153, 154]. In all cavity versions, the piezoelectric actuators<sup>39</sup> are glued on the sensor mount and on top of the actuators, the cavity fibers are clamped. Therefore, an expansion of the sensor mount directly transfers into a drift of the mirror distance. Due to the smaller linear thermal expansion of Macor, this effect is reduced.
- A second source for length drifts stems from the movement of the cavity fibers due to environmental airflow. This happens for example if people are passing by, if the door is opened or if the air circulates due to air conditioning. The airflow has a greater impact on the length drifts in comparison to the thermal expansion of the sensor base. The effect of airflow on the cavity length drift is reduced by three measures: First, the free-standing parts of the cavity fibers are kept as short as possible by keeping the distance between clamp and ferrule short. Second, the cavity fibers are fixed to the setup and optical table with tapes. Besides the mechanical fixation, this also prevents the change of polarization of the guided mode in the fiber. Third, while running measurements, the outer microfluidic tubes (see Fig. 3.11, white color) are removed and a hood is put over the setup (see Fig. 3.12). The former reduces free-hanging parts and the latter reduces the airflow reaching the sensor.
- A third source for length drifts are mechanical vibrations of the hole sensing setup. This is on the one hand reduced due to the mount of the sensor on an optical table, which has a passive vibration damping. On the other hand, a sorbothane sheet<sup>40</sup> is used between the aluminum adapter and aluminum block in order to further reduce vibrations.

### 3.5.2. Resolution limit

The resolution limit of the cavity depends on the signal enhancement and the measurement noise. The resolution limit is achieved, when the length shift produced by the nanoparticle is equal to the *rms*-value of the length shift noise. At first, a general expression is deduced for the length shift produced by the nanoparticle  $\Delta d$  depending on the cavity finesse  $\mathcal{F}$ , the FWHM  $\delta_d$  and waist  $w_0$ . Inserting Eq. (2.10) and Eq. (2.60) into the frequency shift of the fundamental mode (Eq. 2.61) gives

$$\Delta\nu_{00}(x_0, y_0, z_0) = \frac{2\Re(\alpha) \cdot c_0}{\lambda_m \epsilon_0 \pi w_0^2 d_{opt}} \int_{V_{NP}} dV_{NP} \cdot \frac{I_{00}(x_0, y_0, z_0)}{I_0} . \quad (3.20)$$

<sup>39</sup> Noliac NAC2402-H2.3

<sup>40</sup> Thorlabs, SB12C, sorbothane sheet, 12" x 12" x 1/2", hardness 70 durometer

By inserting Eq. (2.10), this can be transformed to

$$\Delta v_{00}(x_0, y_0, z_0) = \frac{4\Re(\alpha)n_m}{\lambda_m \epsilon_0 \pi} \int_{V_{\text{NP}}} dV_{\text{NP}} \cdot \frac{I_{00}(x_0, y_0, z_0)}{I_0} \frac{\mathcal{F} \delta v}{w_0^2} . \quad (3.21)$$

Since the length shift depends on the frequency shift as  $\Delta d = \Delta v \delta_d / \delta_v$  the shift in length scales can be expressed by

$$\Delta d_{00}(x_0, y_0, z_0) = \frac{4\Re(\alpha)n_m}{\lambda_m \epsilon_0 \pi} \int_{V_{\text{NP}}} dV_{\text{NP}} \cdot \frac{I_{00}(x_0, y_0, z_0)}{I_0} \frac{\mathcal{F} \delta d}{w_0^2} , \quad (3.22)$$

Consequently, if a nanosphere is assumed, which is dispersed in water and has an effective refractive index of  $n_{\text{NP,eff}} = 1.45$ , the produced cavity length shift depending on the nanoparticle hydrodynamic radius can be derived for each cavity version (see Fig. 3.24). As the blue solid line (cavity C) and the dashed orange line cavity B are almost in line, their signal enhancements are almost the same. In contrast, the signal enhancement of cavity C (green solid line) is significantly smaller. Simultaneously, the *rms*-noise of cavity B (horizontal orange dotted line) and cavity C (horizontal green dotted line) are considerably larger than the *rms*-noise of cavity C (horizontal blue dotted line). Both, the improved signal enhancement (cavity A  $\rightarrow$  cavity B, C) and the improved mechanical stability (cavity A, B  $\rightarrow$  cavity C) enabled an improvement of the resolution size limit from  $r_{\text{hydr,min}} = 18.5$  nm (cavity A) to  $r_{\text{hydr,min}} = 15.1$  nm (cavity B) and  $r_{\text{hydr,min}} = 11.7$  nm (cavity C (1kHz)). The resolution size limit of cavity C (14.1 kHz) is not depicted in Fig. 3.24, but it is equal to the resolution size limit of cavity C (1kHz).

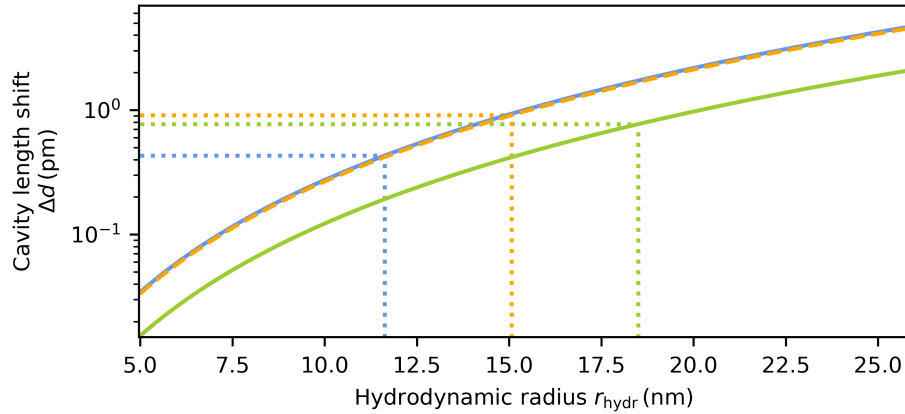


**Figure 3.24.:** Resolution size limit of each cavity version for a nanosphere with an effective refractive index of  $n_{\text{eff}}=1.45$ . The green (blue) solid and the orange dashed line shows the simulated cavity length shifts for cavity A (cavity C (1 kHz)) and cavity B depending on the nanospheres hydrodynamic radius  $r_{\text{hydr}}$ . The horizontal dotted lines mark the measured *rms*-noise and the vertical dotted lines the minimal hydrodynamic radius for cavity A (green), cavity B (orange) and cavity C (blue).

	CG 1	CG 2	CG 3	CG 4
Cavity version	A	B	C	C
Cooperativity $\propto Q\lambda^3/V_m$	$0.3 \cdot 10^4$	$2.1 \cdot 10^4$	$1.9 \cdot 10^4$	$1.7 \cdot 10^4$
Quality factor $Q$	$1.7 \cdot 10^6$	$1.0 \cdot 10^6$	$0.9 \cdot 10^6$	$1.4 \cdot 10^6$
Finesse TEM <sub>00</sub> $\mathcal{F}$	18400	56710	52228	50469
Finesse TEM <sub>01</sub> $\mathcal{F}_{01}$	-	47789	-	
Finesse TEM <sub>10</sub> $\mathcal{F}_{10}$	-	45668	-	
Optical cavity length $d_{\text{opt}}$ ( $\mu\text{m}$ )	27.3	5.4	5.1	8.14
FWHM $\delta\nu_{00}$ (MHz)	299	490	561	365
FWHM $\delta\nu_{01}$ (MHz)	-	581	-	-
FWHM $\delta\nu_{10}$ (MHz)	-	607	-	-
Radius of curvature $r_{c,x}^{SM}$ (m)	62.4	46.1	46.1	29.4
Radius of curvature $r_{c,y}^{SM}$ ( $\mu\text{m}$ )	56.2	53.1	53.1	44.7
Radius of curvature $r_{c,x}^{MM}$ ( $\mu\text{m}$ )	58.9	79.2	79.2	81.8
Radius of curvature $r_{c,y}^{MM}$ ( $\mu\text{m}$ )	131.0	87.8	87.8	93.4
Mirror transmission in air $T_{SM}$ (ppm)	17.6	17.6	17.6	17.6
Mirror transmission in air $T_{MM}$ (ppm)	77	17.6	17.6	17.6
Waist $w_0$ ( $\mu\text{m}$ )	2.3	1.5	1.5	1.6
Mode volume $V_m$ ( $\mu\text{m}^3$ )	110.0	10.0	9.7	16.3
Cavity length modulation frequency $f$ (kHz)	3	3	1	14.1

**Table 3.6.:** Cavity geometries (CG) of the different fiber-based FP cavities, which were used for the presented experiments in Chapter 4, 5, and 6. Cavity geometries of cavity A and cavity B have been submitted to [95].

### 3.6. Cavity geometries and signal enhancement of each cavity version

The presented experiments in this work have been operated with three different sensing platforms (cavity A-C) and four different cavity fiber geometries (CG 1-4). In Table 3.6, the important information, such as the cavity finesse and the cooperativity of the different established cavities are summarized. All parameters given are valid for the cavity filled with water if not stated otherwise. Due to the long cavity length in CG1 and thus increased water absorption losses and due to a higher transmission of the mirror on the outcoupling side ( $T_{MM} = 77$  ppm instead of  $T_{MM} = 17.6$  ppm), the cooperativity is significantly lower  $C \propto 0.3 \cdot 10^4$  compared to the cooperativities of the other cavity geometries ( $C \propto 1.7 \dots 2.1 \cdot 10^4$ ).

### 3.7. Discussion

In this chapter, a new sensing platform was presented, which includes the fiber-based FP microcavity and its easy integration into a microfluidic channel. Overall, two different types of microfluidic channels (polymer channel, quartz glass channel) have been developed, both of

which in principle allow the measurement of nanoparticles in a laminar flow (Chapter 3.1.2). However, all measurements presented in this work were operated without any liquid flow. In the case of the polymer channel, the FP sensor could be operated for 5 months with quartz glass nanoparticles. After this time, the polymer structure released from the quartz glass ferrule surface. On the other hand, in the case of the quartz glass channel, the FP sensor could only be operated for 1-3 weeks. After that time, the channel got stuck due to the agglomeration of quartz glass nanospheres and their adsorption to the channel surface. Both microfluidic versions, though, allowed the measurement of hundreds of single nanoparticle transit events. The fiber-based FP microcavity consists of two highly reflective dielectric mirrors attached to the end-facet of glass fibers with a Gaussian surface depression and a low surface roughness of  $\approx 0.2$  nm. Due to the low scattering losses and the high mirror reflectivities, a high cooperativity of  $C_0 \propto 2.1 \cdot 10^4$  could be achieved in water, which was already on par with the best reported WGM microcavities. A precision hole with a diameter of  $131 \mu\text{m}$  in a quartz glass ferrule provided a direct alignment of the cavity mirrors. However, the spacing of  $6 \mu\text{m}$  between glass fiber and the precision hole demanded a multi-mode-outcoupling fiber which was unsusceptible for misalignments and transmission losses. For the conducted measurements presented in this work, the phase did not have to be preserved. However, if phase measurements are carried out in future experiments, a single-mode-single-mode-configuration is required. In this case, the spacing between glass fiber and precision hole has to be reduced in order to prevent coupling losses and to increase the transmission efficiency. In terms of cavity length measurements with a SLED as a broadband light source, short cavity lengths had to be determined via the higher-order transverse modes of the same longitudinal order. It was shown that applying the theory for perfectly spherical cavity mirrors leads to a systematic error of up to 36 % at the determination of the cavity length. If instead the deviation of the used cavity mirrors from the spherical shape was taken into account by an empirical factor, the systematic error could be significantly reduced to 1.2 %.

Overall, three different sensing platforms have been operated. The drift of the passively stabilized cavity could be significantly improved from 268 pm to 1 pm within 20 s of recording time by exchanging the material of the base from aluminum to Macor and covering the sensing platform with a hood. In addition, the mechanical stability of the sensing platform could be improved from 0.91 to 0.43 *rms*-noise. Consequently, together with the high cooperativity of  $C_0 \propto 2.1 \cdot 10^4$ , the actual resolution limit of the FP sensor amounted to  $r_{\text{hydr,min}} = 11.7$  nm in the case of quartz glass nanospheres. With this resolution limit, already single biomolecules such as viruses, DNA origami, and exosomes can be detected.

## 4. Properties of quartz glass nanospheres dispersed in liquids and probed by the Fabry-Pérot cavity light field

Parts of the results presented in this chapter have been submitted to Nature Communications [95].

If a nanoparticle diffuses in water and is probed by the cavity standing-wave light field (see Fig. 4.1a), it generates a decrease of the transmission amplitude and a broadening and shift of the resonance due to its optical polarizability (see Chapter 2.3). Depending on the light intensity at the position of the nanoparticle, the nanoparticle has a weaker or stronger effect on the change of the transmission signal and it is maximal at the center of the antinode, where the intracavity intensity is greatest. Fig. 4.1 b) shows snapshots of the recorded transmission change when a single quartz glass ( $\text{SiO}_2$ ) nanoparticle diffuses in water and approaches the center of the antinode.

In Chapter 4.1, the measured frequency shifts and transmission amplitude changes produced by a single, or several single nanoparticle transit events, are evaluated in terms of the signal-to-noise ratios, the nanoparticles' dwell time in the cavity and it's shown in addition that most of the measured transit events stem from single nanoparticles residing in the cavity. In the next Chapter 4.2, the polarizability is deduced from the measured frequency shifts and transmission amplitude changes for three different quartz glass nanosphere samples (Sample A-C). An important result of this analysis is the sensitivity of the optical FP sensor to the

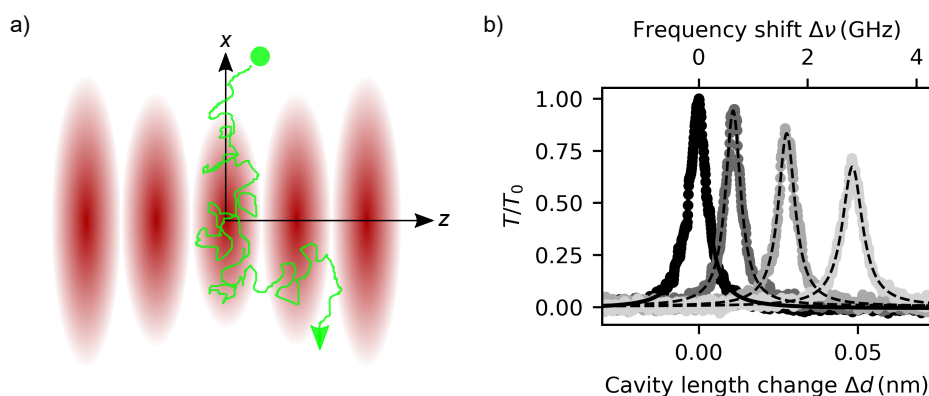


**Figure 4.1.:** a) Schematic of the cavity standing-wave light field and a diffusing nanoparticle. b) Snapshots of the recorded resonance when a nanoparticle diffuses in water. In black is the unperturbed resonance when the nanoparticle is absent. From dark gray to light gray the nanoparticle approaches regions of increasing intensities. Therefore, the amplitude decreases, the linewidth broadens, and the resonance shifts. [95]

increased size of the  $\text{SiO}_2$  nanoparticle in water (see hydrate shell, Chapter 2.3.3). Therefore, Chapter 4.4 is about the manipulation of the  $\text{SiO}_2$  hydrate shell with salt. In Chapter 4.5, the autocorrelation of several transit events is compared with the theoretical autocorrelation function for a punctiform nanosphere (see Chapter 2.5) and the simulated autocorrelation of several Monte-Carlo nanosphere tracks. Finally, in Chapter 4.6, the results are discussed.

#### 4.1. Single nanoparticle transit events

In Fig. 4.2 a typical single  $\text{SiO}_2$  nanosphere transit event is shown. The signal was recorded with cavity A, which had the lowest cooperativity of  $C \propto 0.3 \cdot 10^4$  (see CG1, Table 3.6) and with sample A (Table 4.1). Different frequency shifts and decreases of amplitudes are produced by the nanosphere over time, depending on its position inside the cavity standing-wave light field (see Chapter 2.3). The frequency shift  $\Delta\nu$  and the decrease of amplitude  $DOA$  are correlated: A larger shift also leads to a larger decrease of amplitude.

**Signal-to-noise ratios.** By comparing the signal-to-noise ratios ( $SNR$ )

$$SNR = \frac{\text{maximal measured value}}{\text{standard deviation of the noise}}, \quad (4.1)$$

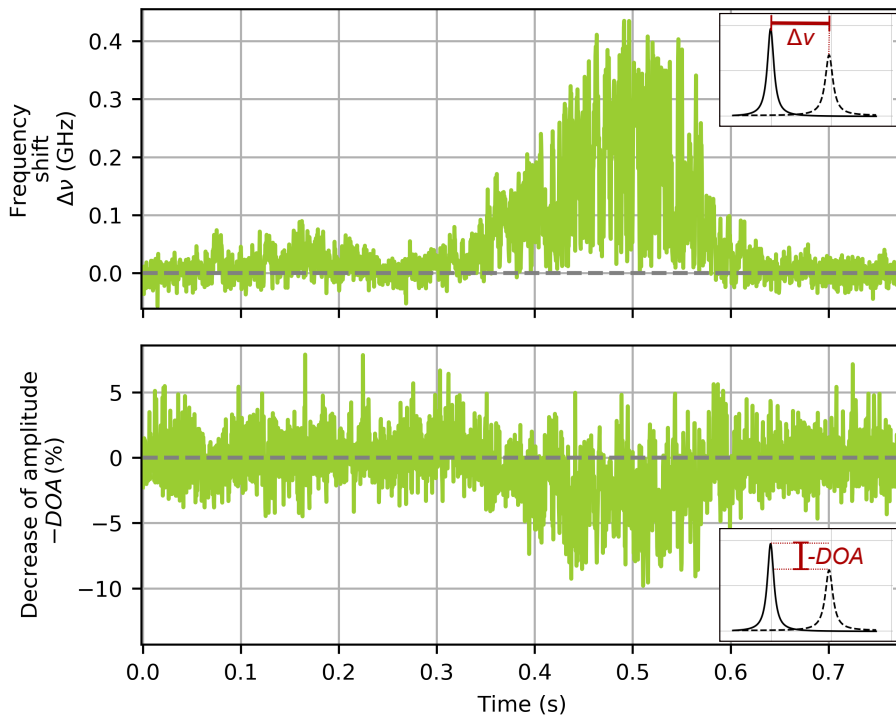


**Figure 4.2.:** Single  $\text{SiO}_2$  nanosphere transit event. At about 0.07 s the nanosphere enters the cavity standing-wave light field, at approximately 0.49 s it resides at the center of the antinode or at least it is close to the center and after 0.68 s the nanosphere leaves the cavity. Similar to [95].

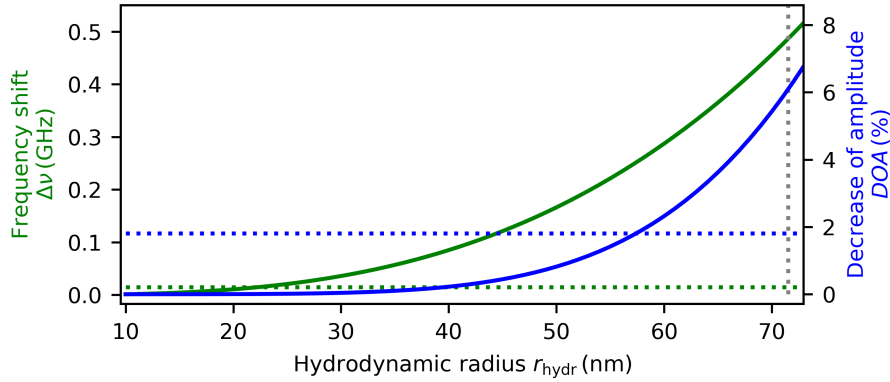


**Figure 4.3.:** Simulated maximal frequency shifts and decreases of amplitudes for different SiO<sub>2</sub> hydrodynamic radii. For the simulation, the parameters of cavity geometry 1 (CG1, Table 3.6) were used. The horizontal blue (green) dotted line marks the measured standard deviation of the decrease of amplitudes (frequency shifts) and the vertical gray dotted line marks the hydrodynamic radius of the SiO<sub>2</sub> sample, which produced the signal depicted in Fig. 4.2.

the frequency shift signal has a  $SNR_{fs}$  of 29 and the DOA has a significantly smaller  $SNR_{doa} = 5$ . This is in accordance with the theoretical consideration in Fig. 4.3. Following Eq. (2.61) and (2.46), the maximal decrease of amplitude produced by the SiO<sub>2</sub> nanosphere decreases more towards smaller hydrodynamic radii than the frequency shift. In the case of the decrease of amplitude, a  $SNR_{doa}$  value of 1 is already achieved at 58 nm hydrodynamic radius. In contrast, single SiO<sub>2</sub> nanospheres with a hydrodynamic radius down to 23 nm can be detected by the measured frequency shifts. In this case, an effective refractive index of  $n_{eff} = 1.41$  was assumed. This is why the result for the minimum detectable nanosphere radius differs from the result obtained in Chapter 3.5.2 for cavity A ( $r_{hydr} = 18.5$  nm at  $n_{eff} = 1.45$ ). The effective refractive index of  $n_{eff} = 1.41$  is also different to the intrinsic refractive index of  $n_{SiO_2} = 1.42$  given by the manufacturer. Later is shown that the nanospheres have a reduced effective refractive index in water due to a hydrate shell surrounding them. Besides, in Chapter 3.5.2 is shown that improved mechanical stability and increased cooperativity have lowered the resolution limit to a hydrodynamic radius as small as  $r_{hydr} = 11.7$  nm at an effective refractive index of  $n_{eff} = 1.45$  (cavity C).

**Dwell time in the cavity.** 330 different transit events are evaluated in order to determine the mean dwell time of the quartz glass nanoparticles (sample A) in the cavity. Fig. 4.4 shows an histogram of the nanospheres' dwell time  $t_D$ . A nanosphere stays in the cavity for  $t_D = 0.5$  s on average.

**Single or multiple nanospheres residing in the cavity.** In order to increase the probability of measuring single nanosphere transit events, the nanosphere concentration is chosen so low that transit events occur every 10 s on average. In Fig. 4.5, all measured frequency shifts are plotted in an histogram. By fitting a Gaussian distribution to the frequency shift distribution of the empty cavity originating from measurement noise (a), this contribution can be subtracted from the signal and only the nanoparticle signal remains (b). The measured signal can be compared with the theoretical frequency shift distribution produced by a single

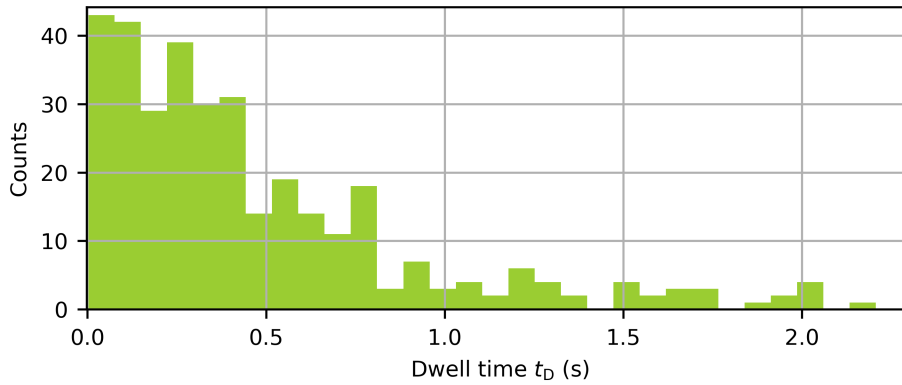


**Figure 4.4.:** Dwell times of about 330 single SiO<sub>2</sub> nanoparticle transit events. On average, a single particle is in the cavity for 0.5 s. Submitted to [95] (supplementary information).

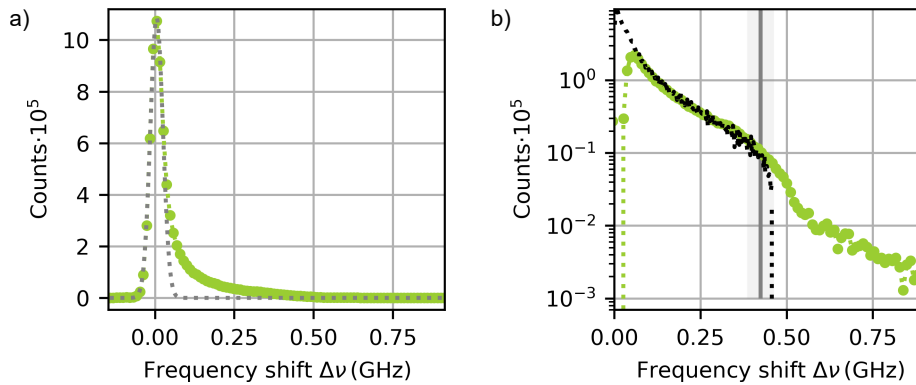


**Figure 4.5.:** Measured frequency shifts (green) of about 330 nanoparticle transit events. **a)** Gaussian fit to the noise (gray dotted line) in order to subtract the noise from the overall signal (green curve in **b**). **b)** The gray bar shows the maximal theoretical shifts for the mean nanosphere hydrodynamic radius of 71.5 nm (gray vertical line) and plus-minus the size standard deviation of 2 nm. In black are the simulated frequency shifts produced by a single nanosphere with a hydrodynamic radius of 73.5 nm and the intrinsic refractive index of  $n_{\text{SiO}_2} = 1.42$ . As the intrinsic refractive index instead of the effective refractive index is used, the simulated frequency shifts are slightly overestimated. Since in the measurement also larger frequency shifts occur than expected for single nanoparticle transit events, few of the 330 nanoparticle transit events are also multiple particle or agglomerate transit events. Similar to [95] (supplementary information).

nanosphere (black dotted curve<sup>1</sup>). The steep count decay at the maximal shift is slightly washed out as in sample A different nanosphere radii are contained ( $r_{\text{hydr}} = 71.5 \pm 2.0$ ). Besides, transit events can be included with multiple nanoparticles residing in the cavity at the same time or originating from agglomerates ( $\Delta\nu_{\text{meas}} > \Delta\nu_{\text{theo,max}}$ ). However, the simulation for a single nanosphere transit event is in good agreement with the smaller occurring frequency shifts and therefore it can be concluded that most of the detected events stem from single nanospheres.

<sup>1</sup> also see Fig. 2.12 for the theoretical frequency shifts

## 4.2. Quantitative evaluation of the nanoparticle optical properties

This section covers the evaluation of single nanosphere transit events in order to determine their effective averaged polarizability. A total of three different quartz glass nanosphere samples are investigated (sample A-C). Their properties given by the manufacturer (M) or measured with a scanning electron microscope (SEM) or by dynamic light scattering (DLS) are summarized in Table 4.1. Detailed information can be taken from Appendix A.5. As the mean hydrodynamic radius is known, the effective refractive index is deduced from the effective averaged polarizability. This also allows the determination of the hydrate shell refractive index. While in the following several transit events are evaluated in order to get information about the sample's averaged properties, in Chapter 4.3 a single nanosphere transit event is evaluated. It is shown that an increase in modulation frequency of the cavity length allows the determination of the single nanosphere properties.

### 4.2.1. Polarizability and effective refractive index

In the following, the polarizability is determined for three different quartz glass nanosphere samples (sample A-C, Table 4.1). As for sample A and B the cavity length was modulated with a frequency between  $f = 1$  kHz and 3 kHz (Measurement principle, see Chapter 3.4.3), a single nanosphere transit event doesn't include enough statistics. Therefore, for the determination of the nanosphere's polarizability, several single nanoparticle transit events have to be taken into account. At first, the mean polarizability of sample A is evaluated via the correlation between the decrease of amplitude  $DOA$  and the frequency shift  $\Delta\nu$ . Then, only the measured frequency shifts are evaluated for the determination of the polarizability of sample B and C. In addition, also the effective refractive index is determined for all three samples. The hydrodynamic radius required for this was either known from the manufacturer (sample A) or measured with dynamic light scattering (DLS, sample B,C).

	Sample A	Sample B	Sample C
$r_{\text{geom}}$ (nm)	$63.2 \pm 1.7$ (SEM)	$60.0 \pm 1.8$ (M)	$25.0 \pm 0.8$ (M)
$r_{\text{hydr}}$ (nm)	$71.5 \pm 2.0$ (M)	$75.3 \pm 9.5$ (DLS)	$46 \pm 30$ (DLS)
$n_{\text{SiO}_2}$	1.42 (M)	1.45 (M)	1.45 (M)

**Table 4.1.:** Properties of the different quartz glass nanospheres, which were investigated in the fiber-based FP microcavity. The geometric radius  $r_{\text{geom}}$  of sample A was measured by scattering electron micrographs (SEM) and the hydrodynamic radius  $r_{\text{hydr}}$  was specified by the manufacturer (M). In case of sample B and sample C the geometric radius was specified by the manufacturer and the hydrodynamic radius was measured by dynamic light scattering (DLS). All manufacturers made indications on the refractive index of the bare nanoparticle  $n_{\text{SiO}_2}$ . The intrinsic refractive index  $n_{\text{SiO}_2} = 1.45$  for cavity B and C is an estimation of the manufacturer: since they don't add any impurity to the silica nanospheres, the nanospheres should have the same refractive index as the bulk silica material. In Chapter 4.4 measurements are presented, which support their estimation. Detailed information about the samples can be taken from Appendix A.5.

**Sample A.** For the determination of the polarizability of sample A, about 330 transit events are evaluated in order to achieve an improved statistic. The measured frequency shifts and decrease of amplitudes (compare with Fig. 4.2 for a single transit event) are plotted in one density scattering plot (see Fig. 4.6). At larger shifts (decreases), the density of points decrease. This can be explained by the lower density of states at higher intensities of the cavity standing-wave light field and is therefore in accordance with the expected theory (see Fig. 2.12). The black curve shows the measured mean  $DOA$  and its slope depends on the nanosphere's polarizability and is independent of the cavity geometry [155]. This is shown in Fig. 4.7. Hence, by comparing simulated curves<sup>2</sup> with the measured mean  $DOA$ , the best agreement is achieved for the mean polarizability  $\bar{\alpha}/(4\pi\epsilon_0) = (14.5 \pm 1.8) \cdot 10^3 \text{ nm}^3$ . For the nanospheres studied in these measurements, the hydrodynamic radius of  $r_{\text{hydr}} = 71.5 \text{ nm}$  is specified by the manufacturer, whereby the effective refractive index is unknown. Fig. 4.8 shows the deviation of the simulated decreases of amplitudes from the mean value when the refractive index is changed and the hydrodynamic radius stays constant. Here, the  $\chi^2$ -function is defined as

$$\chi^2(n_{\text{eff}}) = \sum_i \frac{(DOA_{\text{sim}}(\Delta\nu_i, n_{\text{eff}}) - DOA_{\text{mean}}(\Delta\nu_i))^2}{DOA_{\text{mean}}(\Delta\nu_i)} \quad (4.2)$$

and best agreement between simulation and measured mean values is achieved for  $n_{\text{eff}} = 1.41 \pm 0.01$ . The uncertainty for the effective refractive index of 0.01 is deduced from the  $y$ -error of the parabola fit (= uncertainty for  $\chi^2$ ) and is transmitted into an  $x$ -error (= uncertainty for  $n_{\text{eff}}$ ). The measured effective refractive index of  $n_{\text{eff}} = 1.41 \pm 0.01$  is smaller than the intrinsic refractive index  $n_{\text{SiO}_2} = 1.42$  of the bare particle (definition see Chapter 2.3.3). The reason for this significant difference is due to the  $\text{SiO}_2$  nanosphere's hydrolysis in water. This results in a formation of a hydrate shell, which increases the overall particle size and is sensed by the FP resonator.

**Sample B.** If the decrease of amplitude is unknown or not measurable due to the weak  $SNR$  of nanoparticles with smaller polarizabilities (see Fig. 4.3), the mean polarizability can also be determined by the measured frequency shifts. This is discussed for a measurement with another type of  $\text{SiO}_2$  nanospheres (sample B, Table 4.1) and with another cavity geometry (CG2, Table 3.6). The new cavity has a larger cooperativity of  $C \propto 2.1 \cdot 10^4$  than the cavity before ( $C \propto 0.3 \cdot 10^4$ ). Fig. 4.9 shows the measured frequency shifts of about 59 transit events (orange curve). Because of the shorter cavity length ( $5.4 \mu\text{m}$  versus  $27.3 \mu\text{m}$ ), and the lower transmission of the cavity outcoupling mirror ( $T = 17.6 \text{ ppm}$  versus  $T = 77 \text{ ppm}$ ), the signal-to-noise ratio could be significantly increased in comparison to the measurement shown in Fig. 4.5, namely from  $SNR_{\text{fs,A}} = 29$  to  $SNR_{\text{fs,B}} = 50$ . The nanosphere hydrodynamic radius also increased from  $r_{\text{hydr}} = 71.5 \text{ nm}$  to  $r_{\text{hydr}} = 75.3 \text{ nm}$ , which was additionally responsible for the larger  $SNR$ , but had a minor effect. The steep decay at 8.05 GHz is more pronounced as in Fig. 4.5, because fewer transit events include larger shifts due to agglomerates or multiple particle events. Therefore, the maximal shift produced by single nanosphere transit events and accordingly the mean polarizability can be determined directly from the frequency shift distribution.

<sup>2</sup> The loss introduced by the nanoparticle is assumed to change linearly from  $L_{\text{NP}} = 0$  to  $L_{\text{NP}} = L_{\text{NP,max}}$  for increasing frequency shifts and the frequency shifts are calculated by Eq. 2.61.

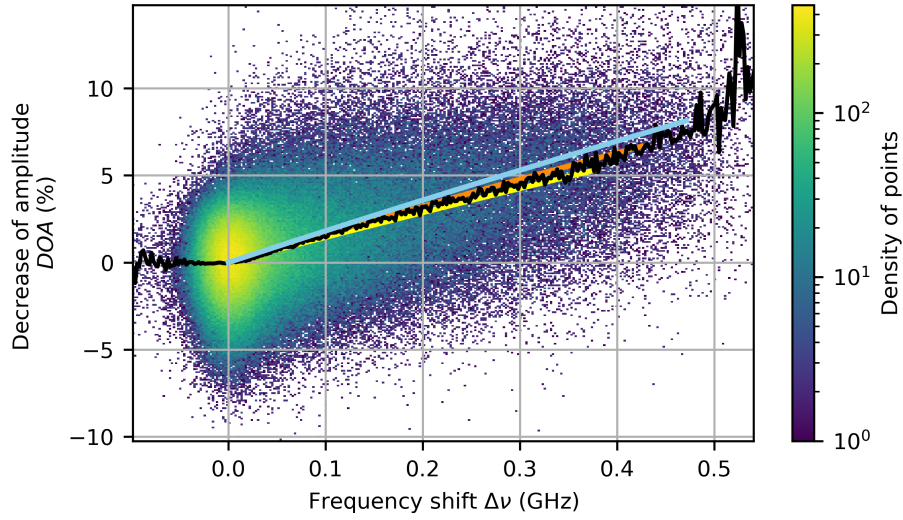


**Figure 4.6.:** Density scattering plot of about 330 SiO<sub>2</sub> nanoparticle transit events. By comparing the slope of the measured mean DOAs (black) with the simulated curves for  $r_{\text{eff}} = 71.5$  nm and  $n_{\text{eff}} = 1.41$  (yellow), 1.42 (orange) and 1.43 (blue), the effective refractive index can be determined. If both, the size and the refractive index are unknown, the slope gives the mean polarizability. Submitted to [95].

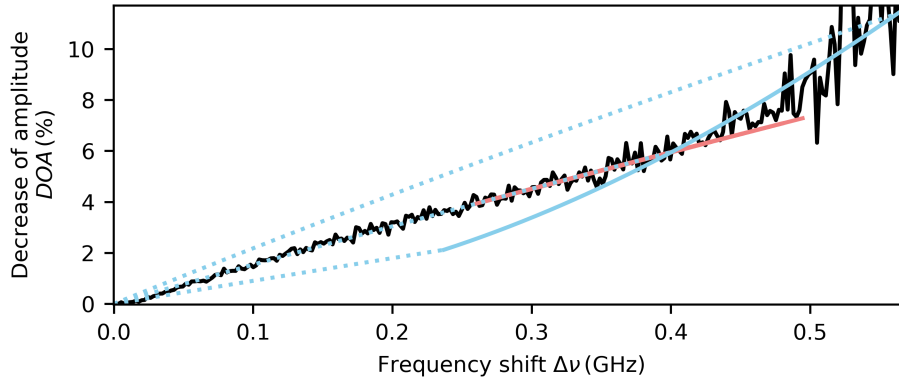


**Figure 4.7.:** Decrease of amplitude  $DOA$  versus Frequency shift  $\Delta\nu$ . Black solid line: measured mean  $DOAs$ . Red solid line: Maximal simulated  $DOA$  and  $\Delta\nu$  when the mirror radii of curvature  $r_{c,SM}$  and  $r_{c,MM}$  are varied between  $50 \mu\text{m}$  and  $150 \mu\text{m}$  and a constant effective refractive index ( $n_{\text{eff}} = 1.41$ ) is assumed. Blue dotted (solid) line: (Maximal) simulated  $DOA$  and  $\Delta\nu$  when the effective refractive index is varied between 1.38 and 1.5 and constant radii of curvature ( $r_{c,SM} = 59.3 \mu\text{m}$ ,  $r_{c,MM} = 95.0 \mu\text{m}$ ) are assumed. The remaining parameters assumed for the simulations can be taken from Table 3.6, CG1. The slope of the simulated curve increases with increasing effective refractive index. In contrast, the slope remains the same for different radii of curvatures.

In this case, the mean hydrodynamic radius of  $r_{\text{hydr}} = \bar{r}_{\text{hydr}} \pm \sigma_r = (75.3 \pm 9.5)$  nm is known from dynamic light scattering (DLS) measurements, and therefore the effective refractive index is directly deduced from the comparison between simulation and experimental data. It is assumed that the maximal shift of  $\Delta\nu_{\text{max}} = 8.05$  GHz is produced by nanospheres with the larger radius of the size distribution. This demands an effective refractive index of  $n_{\text{eff}} = 1.43$ . Since the DLS-size distribution is larger than the intrinsic one (9.5 nm versus 1.8 nm), a large systematic error is assumed. It is estimated by calculating the effective refractive index for the

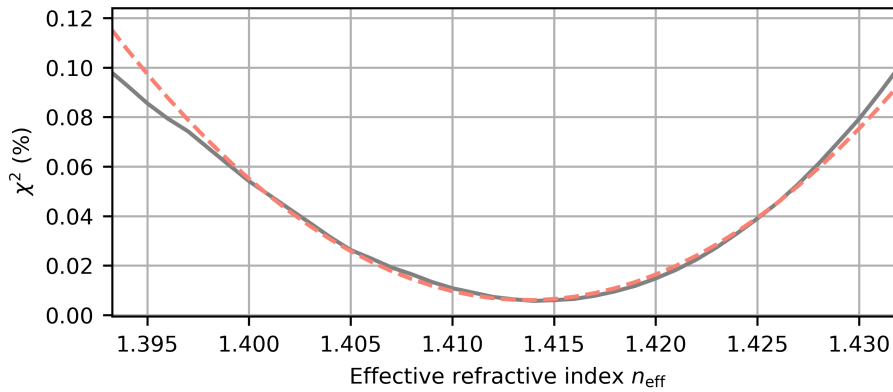


**Figure 4.8.:** Deviation between the simulated curves and the measured mean DOAs depicted in Fig. 4.6. The minimum of the parabola fit to the center values (between 1.388 and 1.430) gives the best agreement between theory and experiment. Here, the effective refractive index amounts to  $n_{\text{eff}} = 1.414$ . Submitted to [95], see supplementary information.

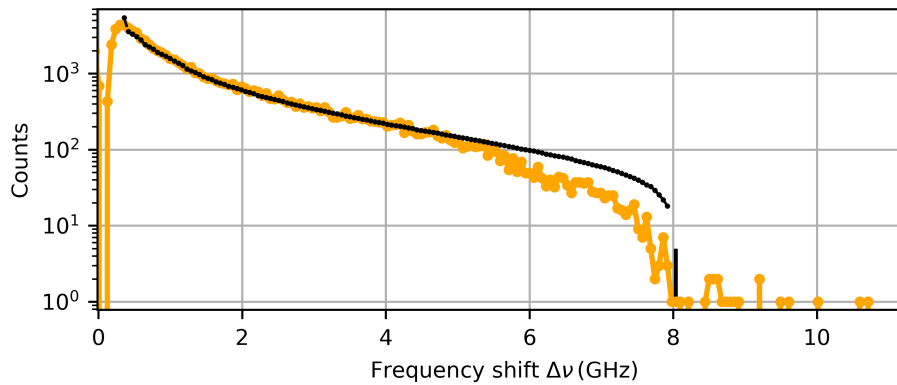


**Figure 4.9.:** Measured frequency shifts of about 59 transit events (orange). The black dots are the simulated frequency shifts for a refractive index-radius-combination producing the maximal frequency shift of 8.05 GHz (e.g.  $r_{\text{hydr}} = 84$  nm and  $n_{\text{eff}} = 1.43$ ). Submitted to [95].

largest size  $\bar{r}_{\text{hydr}} + \sigma_r$  and taking the difference to the refractive index derived at  $\bar{r}_{\text{hydr}} + \sigma_r/2$ . Hence, the result for the effective refractive index is  $n_{\text{eff}} = 1.43 \pm 0.02$ .

By determining the effective refractive index via the correlation between the decrease of amplitude and the frequency shifts, the value for the effective refractive index of sample B can be given with a smaller uncertainty of  $n_{\text{eff}} = 1.42 \pm 0.005$  (see Appendix A.5.2).

**Sample C.** The effective refractive index of a third type of silica nanospheres (sample C, Table 4.1) is determined with another cavity geometry (CG3, Table 3.6). This cavity has a similar cooperativity ( $C \propto 1.9 \cdot 10^4$ ) as the previous cavity. The investigated  $\text{SiO}_2$  nanospheres are specified with a mean geometric radius of  $r_{\text{geom}} = 25$  nm by the manufacturer and an increased hydrodynamic diameter of  $r_{\text{hydr}} = 46.2$  nm was measured by DLS. Since the small polarizability of the nanospheres doesn't produce a visible decrease of the resonance amplitude, the effective refractive index is determined by the measured frequency shifts of 25 transit

events and in a similar way as described for sample B (see Appendix A.5). Therefore, the result is given directly with  $n_{\text{eff}} = (1.39 \pm 0.03)$ .

#### 4.2.2. Refractive index of the hydrate shell

From the measured frequency shifts shown in Fig. 4.9, it can be concluded that the FP sensor is sensitive to the expanded size of the SiO<sub>2</sub> nanospheres dispersed in water: If the intrinsic radius of the bare nanosphere of  $r_{\text{SiO}_2} = 61.8$  nm (sample B)<sup>3</sup> instead of the hydrodynamic radius  $r_{\text{hydr}} = 80.1$  nm is assumed, the maximal measured frequency shift of  $\Delta\nu_{\text{max}} = 8.05$  GHz would demand a refractive index of 1.57, which is much larger than the expected refractive index of quartz glass (1.45). Therefore, the sensor is sensitive to the hydrodynamic size, as well as to the effective refractive index of the nanosphere. The effective refractive index consists of the intrinsic refractive index of the bare nanosphere and the refractive index of the hydrate shell, which surrounds the nanosphere (see Chapter 2.3.3). As the hydrodynamic radius of  $r_{\text{hydr}} = (75.3 \pm 9.5)$  nm, the intrinsic radius of  $r_{\text{SiO}_2} = (60 \pm 1.8)$  nm, the intrinsic refractive index of  $n_{\text{SiO}_2} = 1.45$  and the effective refractive index of  $n_{\text{eff}} = 1.42 \pm 0.005$  are known or measured with the fiber-based FP sensor, the refractive index of the hydrate shell can be calculated by Eq. (2.71) and amounts to  $n_{\text{h}} = 1.39 \pm 0.04$ . By the same approach, also the refractive index of the hydrate shell of sample A can be determined. Here, the 8.5 nm thick hydrate shell has a refractive index of  $n_{\text{h}} = 1.40 \pm 0.02$ . For sample C a 21.2 nm thick hydrate shell is measured and a refractive index of  $n_{\text{h}} = 1.38 \pm 0.04$  is deduced.

#### 4.2.3. Discussion

The results derived in this section are summarized in Table 4.2. For all sample types, the measured frequency shift histograms are in agreement with the simulated shifts for a diffusive nanosphere motion. If an additional force would act on the nanoparticle, e.g. an optical tweezer force (see Appendix A.10), a peak would occur in the histogram at larger frequencies due to the nanosphere being trapped in the center of the antinode [86]. Therefore, it can be concluded that the nanospheres behave purely diffusive.

A comparison between the different polarizabilities (Table 4.2) shows that nanospheres dispersed in water have a significantly higher polarizability than their intrinsic value. Therefore, for the determination of the minimal detectable nanosphere polarizability of optical sensors in liquids, the expanded size of the nanoparticle has to be taken into account. E.g. in Ref. [98] a minimum detectable silica radius of 20 nm was predicted in water. However, in measurements they were still able to resolve nanospheres with 5 nm radius due to a hydrate shell surrounding the nanospheres.

By comparing the three samples, the thickness of the hydrate shells vary greatly. The hydrate shell of sample A (8.5 nm) is significantly thinner than that of sample B (15.3 nm) and C

<sup>3</sup> The larger radius is used from the diameter distribution:  $60 \pm 1.8$  nm.

(21.2 nm). As the intrinsic refractive index of sample A (1.42) is smaller than that of the bulk material (1.45), it can be concluded that the material must contain impurities. In contrast, sample B and sample C have the same refractive index as the bulk material, thus the material is pure quartz glass. Therefore, the nanospheres of sample A have presumably less silanol groups covering their surface and accordingly a lower negatively surface charge is acquired, when the nanospheres are immersed in water (see Chapter 2.3.3). Thus, the reduced electrostatic field leads to a thinner hydrate shell. On the other hand, the hydrate shell of sample C is thicker than that of sample B despite of the same material (pure quartz glass). In Ref. [156] and Ref. [119] is shown that a stronger curvature of the silica nanosphere surface increases the surface charge density below a critical nanosphere radius. When the ratio hydrate shell thickness  $t_h$  to intrinsic nanosphere diameter  $2r_{\text{hydr}}$  is

$$\frac{t_h}{2r_{\text{hydr}}} < 0.2 \quad , \quad (4.3)$$

the surface charge density is independent of the nanoparticle size. At ratios

$$\frac{t_h}{2r_{\text{hydr}}} > 0.2 \quad , \quad (4.4)$$

the surface charge density increases with smaller nanosphere sizes. In case of sample B, the ratio amounts to  $\frac{t_h}{2r_{\text{hydr}}} \approx 0.13 < 0.2$  and in case of sample C it is  $\frac{t_h}{2r_{\text{hydr}}} \approx 0.42 > 0.2$ . Therefore it is assumed that the stronger curvature of the nanosphere's surface (sample C) consist of a denser surface charge than sample B and consequently, the higher electric field leads to a thicker hydrate shell. This only applies for deionized water. If the nanospheres would be dispersed in an electrolyte, the ions are attracted by the surface charge and screen the charge from the surrounding area (see Chapter 4.4).

	Sample A	Sample B	Sample C
$\bar{\alpha}_{\text{eff}}/(4\pi\epsilon_0) \text{ (nm}^3\text{)}$	$(14.5 \pm 1.8) \cdot 10^3$	$(19.0 \pm 1.0) \cdot 10^3$	$(2.9 \pm 1.4) \cdot 10^3$
$n_{\text{eff}}$	$1.41 \pm 0.01$	$1.42 \pm 0.005$	$1.39 \pm 0.03$
$n_h$	$1.40 \pm 0.02$	$1.39 \pm 0.04$	$1.38 \pm 0.04$
$t_h \text{ (nm)}$	8.5	15.3	21.2
$\bar{\alpha}_{\text{SiO}_2}/(4\pi\epsilon_0) \text{ (nm}^3\text{)}$	$(11.2 \pm 3.3) \cdot 10^3$	$(12.8 \pm 4.5) \cdot 10^3$	$(0.9 \pm 0.3) \cdot 10^3$
$r_{\text{geom}} \text{ (nm)}$	$63.2 \pm 1.7 \text{ (SEM)}$	$60.0 \pm 1.8 \text{ (M)}$	$25.0 \pm 0.8 \text{ (M)}$
$r_{\text{hydr}} \text{ (nm)}$	$71.5 \pm 2.0 \text{ (M)}$	$75.3 \pm 9.5 \text{ (DLS)}$	$46 \pm 30 \text{ (DLS)}$
$n_{\text{SiO}_2}$	1.42 (M)	1.45 (M)	1.45 (M)

**Table 4.2.:** Effective refractive indices  $n_{\text{eff}}$ , refractive indices of the hydrate shell  $n_h$  and thickness of the hydrate shell  $t_h$  of the different SiO<sub>2</sub> samples, which were measured with the FP fiber-based sensor. The geometric radius  $r_{\text{geom}}$ , the hydrodynamic radius  $r_{\text{hydr}}$  as well as the intrinsic refractive index of the bare nanoparticle  $n_{\text{SiO}_2}$  were either specified by the manufacturer (M) or measured with a scattering electron microscope (SEM) or by direct light scattering (DLS). The averaged polarizabilities  $\bar{\alpha}_{\text{eff}}$  and  $\bar{\alpha}_{\text{SiO}_2}$  were calculated by Eq. (2.68) and (2.32). Results for sample A and sample B have been submitted to [95].

### 4.3. Optical properties of a single quartz glass nanosphere

By increasing the modulation frequency of the cavity length from 3 kHz to 14.1 kHz, the recorded signal of a single nanosphere transit event already contains enough statistics for the determination of its polarizability and effective refractive index. Fig. 4.10 shows the signal of a quartz glass nanosphere (sample B, see Table 4.1), which is dispersed in  $1.5 \cdot 10^{-4}$  mM dulbecco's phosphate buffered saline (DPBS). In Chapter 4.4 is shown that the hydrodynamic radius is reduced to  $r_{\text{hydr}} = 71.2$  nm due to the salt (DPBS) ions providing a better shielding of the negative  $\text{SiO}_2$  surface charge. The signal was recorded with cavity geometry 4 (CG4, Table 3.6), which had a cooperativity of  $C \propto 1.7 \cdot 10^4$ . Due to the great signal enhancement, the change of the resonance produced by the nanosphere is also visible in the broadening of the resonance linewidth (FWHM). The mean effective refractive index of sample B was already determined in Chapter 4.2 and amounts to  $n_{\text{eff}} = 1.42 \pm 0.005$ . This predicts a maximal produced frequency shift of  $\Delta\nu_{\text{max}} = 3.22$  GHz at the center of the antinode (red horizontal line, Fig. 4.10) and a frequency shift of  $\Delta\nu_{\text{min}} = 0.42$  GHz at the node on the optical axis. Away from the optical axis, also smaller frequency shifts can be induced by the nanosphere. Hence, between 0 s and 0.95 s the envelope of the frequency shift signal shows that the nanosphere diffuses between neighboring antinodes or back into the same antinode. Fig. 4.11 shows a zoom into the data set of Fig. 4.10, marked with a yellow transparent vertical line. Also within an antinode, the nanosphere's position changes between the center of the antinode (red) and the node (gray) on millisecond time scale.

**Polarizability and refractive index.** The measured data shown in Fig. 4.10 are evaluated in the same way as in Chapter 4.2. It is crucial to note that in this case a single nanosphere transit event already contains the whole information in order to determine its polarizability or its effective refractive index if the diameter is known. Fig. 4.12a) shows the measured frequency shifts in an histogram (blue) and in comparison also the measured frequency shifts of 12 single transit events. In red is the simulated maximal shift for  $n_{\text{eff}} = 1.42$  and  $r_{\text{hydr}} = 71.2$  nm plus-minus the peak-to-peak measurement noise. It can be concluded, that a single transit event already displays the entire range up to the maximal frequency shift. Fig. 4.12b) shows the correlation between the decrease of amplitude and the frequency shifts for the single transit event (blue) and 12 single transit events (gray). The gray data cloud is broader in  $y$ -direction than the blue one. In black is a measurement for the same nanospheres, but dispersed in pure double distilled water. Therefore, the hydrodynamic radius is bigger and a larger shift is produced by the nanosphere (see Chapter 4.4). The data cloud obtained at this measurement is even broader. The reason is that the polarization-splitting of the fundamental mode was tracked (see Chapter 2.6 and Chapter 6) with similar heights of the resonance amplitudes, but only one amplitude was tracked by the oscilloscope. Here, only the greater amplitude was recorded, such that one of the polarization modes was selected randomly for the evaluation. The splitting between the two modes is thus added as noise and consequently, the data cloud is expanded in  $y$ -direction. The lines represent the simulation for  $r_{\text{hydr}} = 71.2$  nm and  $n_{\text{eff}} = 1.41$  (yellow), 1.42 (purple) and 1.43 (gray). Already the single nanosphere transit events delivers the result  $\alpha/(4\pi\epsilon_0) = 16.1 \cdot 10^3 \text{ nm}^3$  or  $n_{\text{eff}} = 1.42$  for sample B.

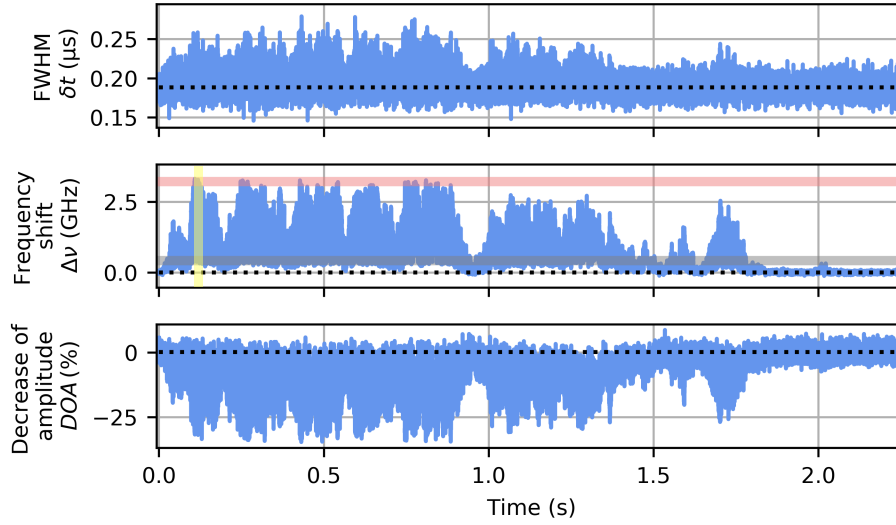


**Figure 4.10.:** Correlation between the FWHM  $\delta t$ , the frequency shifts  $\Delta\nu$  and the resonance peak  $U_{\max}$ . When the quartz glass nanosphere with  $r_{\text{hydr}} = 71.2$  nm enters the cavity at  $t = 0.01$  s,  $\delta t$  and  $\Delta\nu$  increase and  $U_{\max}$  decreases. At about  $t = 1.85$  s the nanoparticle leaves the cavity. The red (gray) horizontal line represent the maximal (minimal) theoretical shift produced by the nanosphere when it resides at the antinode (node) plus-minus the peak-to-peak measurement noise and the black dotted lines mark the unperturbed resonance values. The yellow vertical transparent line marks the section shown as zoom in Fig. 4.11.

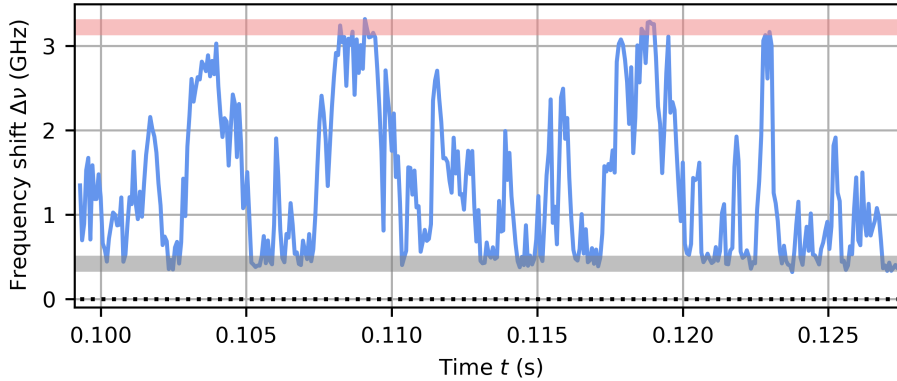


**Figure 4.11.:** Zoom into the data set marked with a vertical transparent line in Fig. 4.10. The red (gray) horizontal line represent the maximal (minimal) theoretical shift produced by the nanosphere when it resides on the optical axis and at the center of the antinode (node) plus-minus the peak-to-peak measurement noise. The black dotted line marks the unperturbed resonance value. It can be concluded that the nanoparticle resides in the center of the cavity mode.

**Frequency spectrum of the recorded signal generated by a single nanosphere.** In order to determine the frequency spectrum generated by a single nanosphere diffusing in water and probed by the FP cavity fundamental mode  $TEM_{00}$ , the detected frequency shifts are fast Fourier transformed (FFT) and calculated into the power spectral density (PSD) (see Appendix A.9). The result is shown in Fig. 4.13. The PSD of the nanosphere signal is shown in blue and the PSD of the measurement noise is shown in black. The overall signal is depicted in gray, where it lies behind the blue and black areas over a wide range. One observes frequency

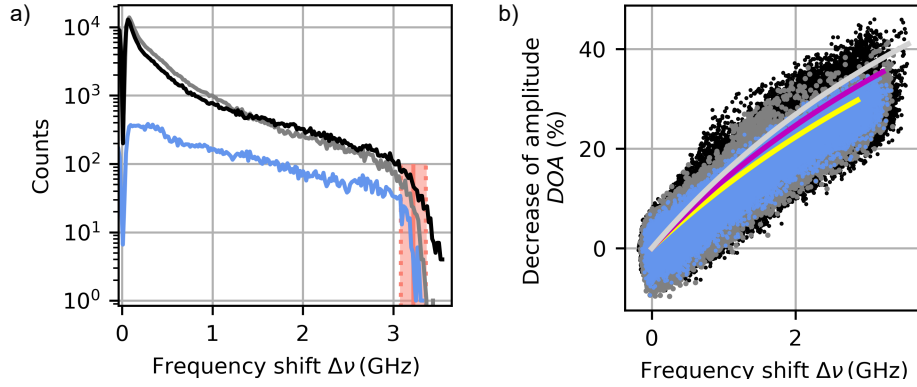


**Figure 4.12.:** Evaluation of the polarizability and refractive index of a single  $\text{SiO}_2$  nanosphere. **a)** Histogram of the detected frequency shifts for 12 transit events (gray, dispersed in  $1.5 \cdot 10^{-4}$  mM DPBS), 9 transit events (black, dispersed in double distilled water) and the single transit event shown in Fig. 4.10 (blue, dispersed in  $1.5 \cdot 10^{-4}$  mM DPBS). The red transparent rectangle marks the maximal simulated shift for  $n_{\text{eff}} = 1.42$  and  $r_{\text{hydr}} = 71.2$  nm plus-minus the peak-to-peak measurement noise. **b)** Decrease of amplitude versus the correlated frequency shifts for 9 transit events in double distilled water (black), 12 transit events in  $1.5 \cdot 10^{-4}$  mM DPBS (gray) and the single transit event in  $1.5 \cdot 10^{-4}$  mM DPBS (blue). The lines are simulations for  $r_{\text{hydr}} = 71.2$  nm and  $n_{\text{eff}} = 1.41$  (yellow), 1.42 (purple) and 1.43 (bright gray).

components of the nanosphere signal over the entire accessible spectral range. However, below 10 Hz the signal is dominated by an  $1/f$ -noise, which is attributed to frequency and amplitude noise of the probe laser. Between  $\approx 10$  Hz and  $\approx 200$  Hz the PSD consists of a plateau and at larger frequencies it decreases towards the background noise. The plateau arises due to the nanoparticle movement through the antinode in lateral and longitudinal direction. According to Eq. (2.76) the diffusion time in transversal direction amounts to

$$\tau_{D,xy} = \frac{w_0^2}{4 \cdot D} = 0.21 \text{ s} \quad . \quad (4.5)$$

Therefore, the nanoparticle signal is expected around 4.7 Hz, which is approximately at the middle of the measured plateau. On the other hand, the diffusion time in longitudinal direction can be calculated by

$$\tau_{D,z} = \frac{\left(\frac{\lambda_0}{4n_m}\right)^2}{2 \cdot D} = 3.6 \text{ ms} \quad . \quad (4.6)$$

The expected nanoparticle signal around 280.6 Hz is in the measured PSD where the signal already starts to decrease to the background noise.

#### 4.4. The impact of salt ions on the formation of the hydrate shell

In the previous sections it was shown that the FP sensor is sensitive to the hydrate shell of the nanosphere. In the following, the impact of salt ions on the formation of the hydrate shell is investigated. At a pH value larger than  $2 \pm 1$ , the surface of  $\text{SiO}_2$  nanoparticles is negatively charged, when they are immersed in water [157]. The reason is the dissociation

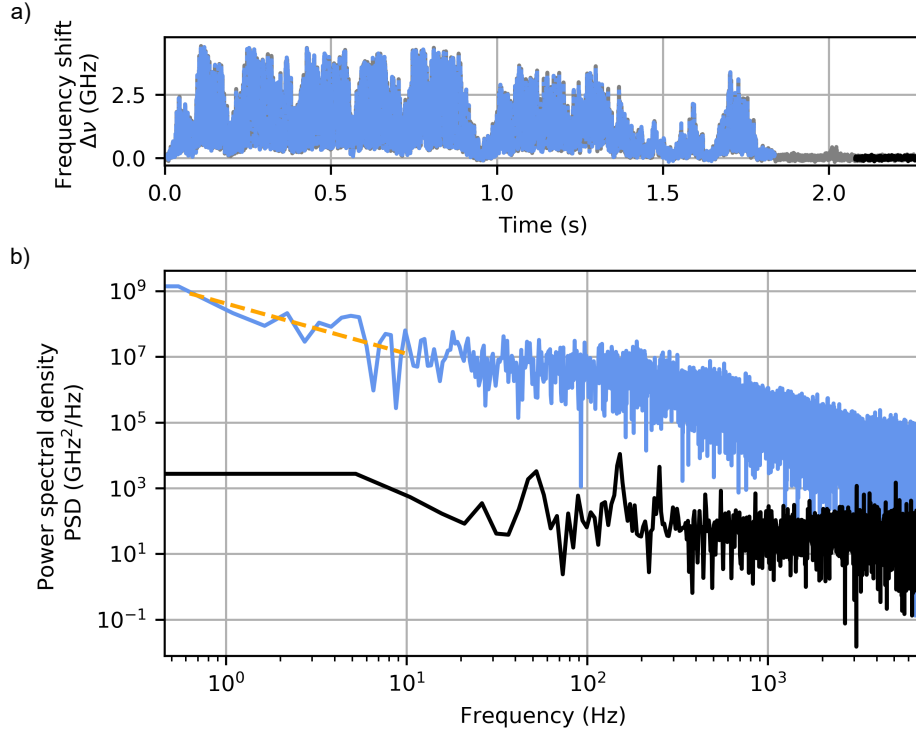


**Figure 4.13.:** Frequency range of a single SiO<sub>2</sub> nanosphere transit event. **a)** Time domain signal for the measured frequency shifts at a 14.1 kHz modulation frequency of the cavity length. The gray data depicts the whole signal (also hidden behind the blue and the black data), whereas the marked section in blue (black) shows the nanoparticle signal (noise). **b)** Power spectral density of the signal in a). The blue data represents the nanosphere signal and the black data represents the measurement noise. Below 10 Hz a 1/f-noise is visible (orange dashed line).

of the silanol groups, which cover the quartz glass surface, into SiO<sup>-</sup> and H<sup>+</sup> (see Chapter 2.3.3). In Ref. [119] the surface charge density of a SiO<sub>2</sub> nanosphere is modeled for different parameters. Barisik et al. could show that an increase in pH, a reduction of the nanosphere's radius below a critical value, or an increase in salt concentration increases the charge density of the negative charge on the nanosphere's surface. The reason is a decrease of the H<sup>+</sup> ion concentration at the surface. In case of double distilled water, no or negligible few ions are in the solution. Therefore, attracted water molecules form the hydrate shell, which increases in size as the surface charge density increases. On the other hand, if salt ions are in the solution, the positively charged ions of the salt are attracted by the negatively charged SiO<sub>2</sub> surface and thereby displace the H<sup>+</sup> ions at the surface. Simultaneously, the salt ions provide a better screening of the surface charge, leading to a reduction of the hydrate shell. According to the Debye-Hückel theory, the Debye length  $\lambda_D$  is related to the number density of the salt ions  $c_{b,i}$  by [158]

$$\lambda_D = \sqrt{\frac{\epsilon_0 n_m^2 k_B T}{\sum_i c_{b,i} e^2 z_i^2}}, \quad (4.7)$$

where  $k_B$  is the Boltzmann constant,  $T$  is the temperature,  $e$  is the elementary charge and  $z$  is the number of charges on an ion. The summation over  $i$  accounts for the different ions  $i$  in the

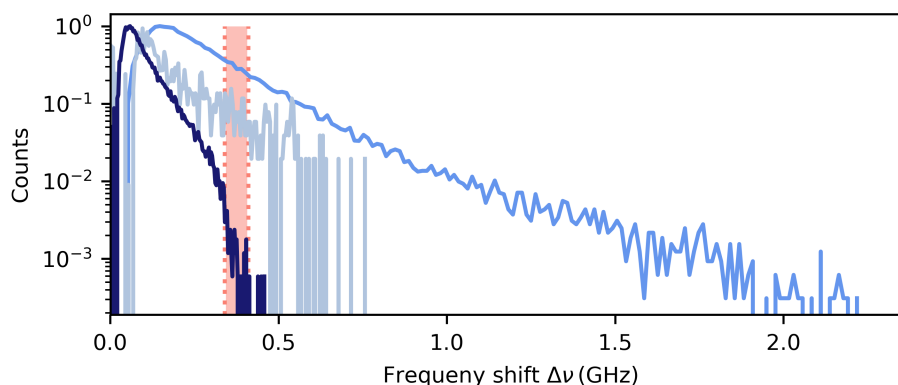


**Figure 4.14.:** SiO<sub>2</sub> Nanospheres dispersed in different salt concentrations and effect of the salt on the polarizability of the nanospheres. Medium blue: Nanospheres dispersed in pure double distilled water (25 transit events), light blue: dispersed in  $1.5 \cdot 10^{-4}$  mM DPBS (5 transit events) and dark blue: presumably higher (unknown) DPBS concentration than before (25 transit events). Red: maximal theoretical frequency shift produced by the bare nanosphere with  $(25 \pm 0.8)$  nm radius and a refractive index of  $n_{\text{SiO}_2} = 1.45$ .

solution, such as Na<sup>+</sup> or K<sup>+</sup>. The Debye length is defined as the length at which the potential from the negatively charged surface has dropped to  $1/e$ . Therefore, the decrease of the Debye length with increasing salt concentration is directly correlated to the thickness decrease of the hydrate shell. In addition, according to Ref. [159], a higher surface charge density leads to a decrease of the hydrate shell thickness, when the nanoparticle radius is kept constant. On the other hand, the surface charge density increases for a stronger surface curvature and thus smaller nanosphere radius [156, 119] and it increases for a larger pH value. The smaller the radius of the nanosphere, the more the surface charge density increases as the pH increases [119]. Consequently, when different SiO<sub>2</sub> nanosphere sizes of the same material (pure quartz glass, no impurities) are dispersed in a salt solution, a thinner hydrate shell is expected for the smaller nanospheres (Salt: pH=7.0...7.3, double distilled water: pH=5...7).

The effect of salt on the hydrate shell was investigated with two different SiO<sub>2</sub> nanosphere sizes:  $r_{\text{geom}} = 25$  nm and  $r_{\text{geom}} = 60$  nm. In the following, the first results are presented. However, these are still to be regarded as preliminary due to inconsistencies.

#### 4.4.1. Hydrate shell of 25 nm quartz glass nanoparticles

At first, the effect of salt on the expansion of the hydrate shell was investigated with sample C (see Table 4.2) and the cavity with the cooperativity  $C \propto 1.9 \cdot 10^4$  (CP3, Table 3.6). Fig. 4.14 shows the measured frequency shifts of several single SiO<sub>2</sub> transit events. The large shift of  $\Delta\nu_{\text{max}} = 2.2$  GHz stems from 101 SiO<sub>2</sub> nanosphere transit events, which were solved in pure double distilled water (medium blue). Here the hydrate shell is completely formed and increases the intrinsic nanosphere radius from  $r_{\text{SiO}_2} = 25$  nm to the hydrodynamic radius of  $r_{\text{hydr}} = 46$  nm. The effective refractive index was determined independently (see Appendix A.5.3) and amounts to  $n_{\text{eff}} = 1.39 \pm 0.03$ . This corresponds to an effective polarizability of

$\alpha/(4\pi\epsilon_0) = (2.9 \pm 1.4) \cdot 10^3 \text{ nm}^3$ . By adding  $1.5 \cdot 10^{-4} \text{ mM}$  of the salt DPBS<sup>4</sup>, the maximal produced frequency shift is smaller ( $\Delta\nu_{\text{max}} = 0.75 \text{ GHz}$ , light blue), but a precise statement can't be made due to the poor statistics (12 transit events). Between this measurement (light blue) and the last measurement (dark blue) the microfluidic cell was flooded with different liquids and air as follows:

- nanospheres dispersed in  $1.5 \cdot 10^{-4} \text{ mM}$  DPBS, no nanospheres could be detected,
- air,
- about 15 min with double distilled water,
- nanospheres dispersed in  $1.5 \cdot 10^{-4} \text{ mM}$  DPBS, no nanospheres could be detected,
- about 30 min with double distilled water,
- nanospheres dispersed in  $1.5 \cdot 10^{-4} \text{ mM}$  DPBS, no nanospheres could be detected,
- about 15 min with double distilled water,
- nanospheres dispersed in  $1.5 \cdot 10^{-4} \text{ mM}$  DPBS, no nanospheres could be detected,
- about 15 min with double distilled water,
- nanospheres dispersed in double distilled water, no nanospheres could be detected,
- double distilled water,
- air,
- nanospheres dispersed in double distilled water.

Although in the last step the nanospheres should have been dispersed in pure water, the typical steep decay in the frequency shift histogram occurs at about 0.4 GHz (dark blue, 42 transit events), which is much smaller than 2.2 GHz and corresponds to a polarizability of  $\alpha/(4\pi\epsilon_0) = 1.0 \cdot 10^3 \text{ nm}^3$ . By comparing this measurement result with the theoretical maximal shift produced by the bare SiO<sub>2</sub> nanosphere with  $(25 \pm 0.8) \text{ nm}$  radius and the refractive index of pure quartz glass  $n_{\text{SiO}_2} = 1.45$  (marked in red), the steep decay of the measured frequency shifts agrees with the bare nanosphere (=without a hydrate shell). This is contrary to the expectations. Although the same reservoir was used for each sample preparation, it was previously rinsed with plenty of double distilled water. In addition, the microfluidic channel was rinsed with plenty of water as well. Therefore, nanospheres with the fully developed hydrate shell would have been expected, however, nanospheres with the same polarizability as the bare nanosphere was measured.

**Discussion.** Presumably the hydrate shell was not developed because DPBS residues remained in the microfluidic cell. Similar effects were observed with different SiO<sub>2</sub> samples. Within the same setup, different samples could not be observed consecutively, because a

---

<sup>4</sup> SAFC, Cat. No. 56064C-10L, dry powder, DPBS Modified, without calcium, without magnesium, suitable for cell culture.

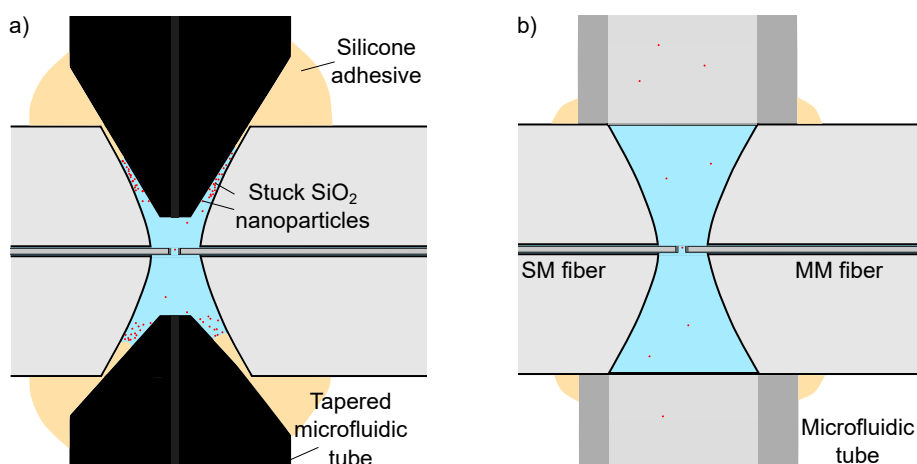


**Figure 4.15.:** Sketch with stuck SiO<sub>2</sub> nanospheres (red) inside the microfluidic channel. **a)** The tapered microfluidic tubes are glued into the concave-shaped hole with a silicone adhesive. Thereby, cavities are created between the tubes and the glass wall, where the SiO<sub>2</sub> nanospheres get stuck. **b)** Improved microfluidic connection avoiding cavities. This new connection was developed by Shalom Palkhivala, a supervised master student [149].

fraction of the old sample remained in the microfluidic channel. This is explained with Fig. 4.15a. In case of the quartz glass channel, tapered microfluidic tubes are glued into the drilled hole. Thereby, cavities are created, where the SiO<sub>2</sub> nanospheres can accumulate. Already an improved microfluidic connection has been developed by Shalom Palkhivala [149] (supervised student, see Fig. 4.15b), however, the hydrate shell measurements were conducted with the tapered connectors. The accumulated salt concentration in the cavities of the microfluidic channel could have been already high enough to screen the surface charge of the SiO<sub>2</sub> nanospheres to a large extent. In Ref. [98] an effect of salt on the hydrate shell was already measured at  $10^{-4}$  mM salt concentration. As the microfluidic channel was rinsed with  $1.5 \cdot 10^{-4}$  mM DPBS several times, presumably a higher concentration accumulated. Nevertheless, it remains contradictory since the microfluidic channel was flushed with a lot of water and the residual salt concentration should be very low. Therefore, the results are not fully reliable. However, a significant statistic was measured for the single nanosphere transit events in pure water (101 events) and the unknown salt concentration, where the characteristic slope at maximal frequency shift occurred (43, dark blue, Fig. 4.14). Since in the second case the maximum shift agrees with the polarizability of the bare nanosphere, this strengthens the assumption made by Alpha Nanotechne about the refractive index  $n_{\text{SiO}_2} = 1.45$  of the bare nanospheres (see Appendix A.5).

#### 4.4.2. Hydrate shell of 60 nm quartz glass nanoparticles

The measurement of the nanospheres polarizability depending on the salt concentration was also conducted with sample B ( $r_{\text{geom}} = 60$  nm,  $r_{\text{hydr}} = 75.3$  nm, Table 4.2) and with a cavity cooperativity of  $C \propto 1.7 \cdot 10^4$  (CP4, Table 3.6). At the measurements, the cavity length was modulated at a high frequency of 14.1 kHz. Therefore only a few transit events lead to sufficient statistics. Fig. 4.16 shows the result. The maximal shift of  $\Delta\nu = 3.55$  GHz is produced by

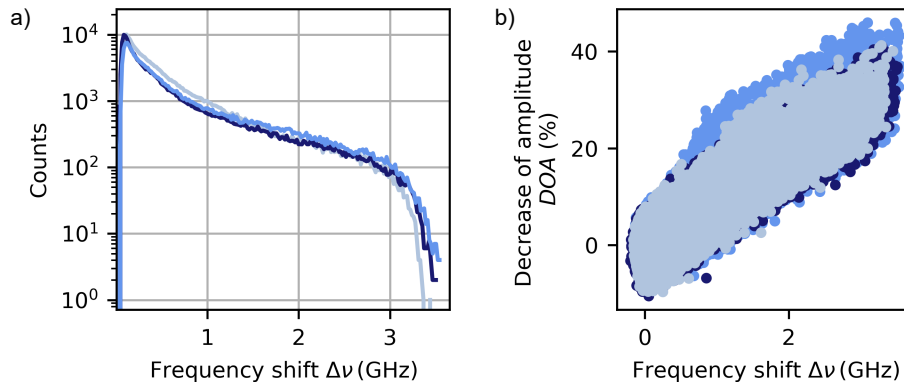


**Figure 4.16.:** Measured resonance change for several single  $\text{SiO}_2$  nanosphere transit events, when the nanospheres are dispersed in water (medium blue),  $1.5 \cdot 10^{-5}$  mM DPBS (dark blue) and  $1.5 \cdot 10^{-4}$  mM DPBS (light blue). **a)** Frequency shift histogram. **b)** Correlation between the decrease of amplitudes and frequency shifts.

the nanospheres dispersed in pure water (medium blue, 9 transit events) and doesn't change for a DPBS concentration of  $1.5 \cdot 10^{-5}$  mM (dark blue, 13 transit events). A small decrease of the shift is observed for  $1.5 \cdot 10^{-4}$  mM DPBS (light blue, 12 transit events). Here, the maximal shift amounts to  $\Delta\nu = 3.45$  GHz. By assuming that the effective refractive index has remained approximately the same, the hydrate shell has become thinner by 0.8 nm.

**Discussion.** By comparing both measurements, sample B (60 nm intrinsic radius) and sample C (25 nm intrinsic radius), the same DPBS concentration of  $1.5 \cdot 10^{-4}$  mM seems to reduce the hydrate shell thickness of sample C more than that of sample B. This is in accordance with the expectation that a presumably higher surface charge density of the 25 nm nanospheres (stronger curvature of the surface) leads to a stronger attraction of the salt ions and thus to a stronger screening of the surface charge. To what extent the hydrate shell could be reduced more in case of the 25 nm nanospheres compared to the 60 nm nanospheres can not be evaluated due to the poor statistics at the  $1.5 \cdot 10^{-4}$  mM DPBS concentration measurement. Presumably the maximal frequency shift when the nanosphere resides in the center of the antinode was not measured in case of sample C.

#### 4.5. Towards the determination of the hydrodynamic radius via the autocorrelation of the frequency shift signal

The autocorrelation of the produced frequency shifts of single nanospheres contains the information about their diffusivity and hydrodynamic radius. In this Chapter, the measured autocorrelation is compared in two different ways. First, it is compared with the analytical solution derived in Chapter 2.5 for a punctiform nanosphere diffusing or drifting in water and probed by the FP standing-wave light field. Second, the track of several nanospheres was Monte Carlo simulated and the produced frequency shifts autocorrelated (see Chapter 2.4.1).

This autocorrelation is compared with the measured one as well. Fig. 4.17 shows the different autocorrelations. The blue crosses depict the autocorrelation for about 33 transit events of single SiO<sub>2</sub> nanospheres ( $r_{\text{hydr}} = 75.3$  nm, sample B (Table 4.2)), which were measured with a cavity cooperativity of  $C \propto 1.7 \cdot 10^4$  (CG4, Table 3.6). The corresponding measured frequency shifts were already shown in Fig 4.16 dark blue (pure water) and medium blue ( $1.5 \cdot 10^{-5}$  mM DPBS). Although the nanoparticles were measured in different solutions, the same maximum frequency shift occurred. Therefore, the same hydrodynamic radius and autocorrelation were assumed. Both measurements were evaluated together for the autocorrelation in order to improve the statistic.

**Comparison with theoretical autocorrelation.** In case of the theoretical autocorrelation, purely diffusing nanospheres in water (no drift terms) with the same hydrodynamic radius as the investigated sample ( $r_{\text{hydr}} = 75.3$  nm) and the same cavity geometry (CG4, Table 3.6) were assumed. In Fig. 4.17 the result is depicted in green. Both, the measured autocorrelation as well as the theoretical one consist of two characteristic slopes at about  $10^{-3}$  s and  $10^{-1}$  s. However, especially for larger times, the two curves differ significantly. Since also the plateau height at  $10^{-2}$  s is different, an assumed drift in  $x, y$ -direction doesn't bring the curves into line. The main reason for the deviation is assumed to be that the theoretical description doesn't take into account the expansion of the nanosphere.

**Comparison with Monte Carlo simulated autocorrelation.** The Monte Carlo simulated tracks and the simulated frequency shifts produced by a nanosphere following this track take into account the nanosphere size (see Chapter 2.4). Here, the autocorrelation of 22 simulated tracks (orange curve) of single nanospheres with a hydrodynamic radius of  $r_{\text{hydr}} = 75.3$  nm is in good agreement with the experimental data (see Fig. 4.17). Especially between  $10^{-2}$  s and

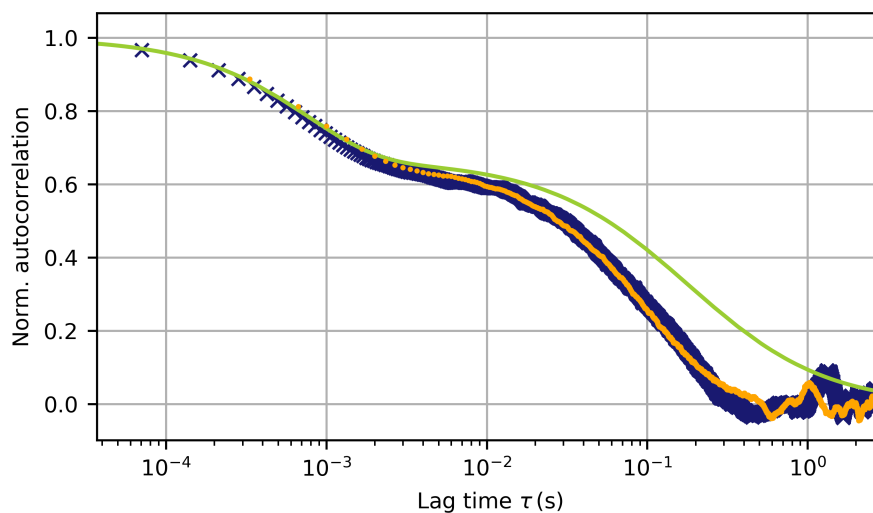


**Figure 4.17.:** Autocorrelation of 33 single nanosphere transit events (blue crosses) and comparison with the theoretical autocorrelation function (green) and the autocorrelation derived by Monte Carlo simulation (orange).

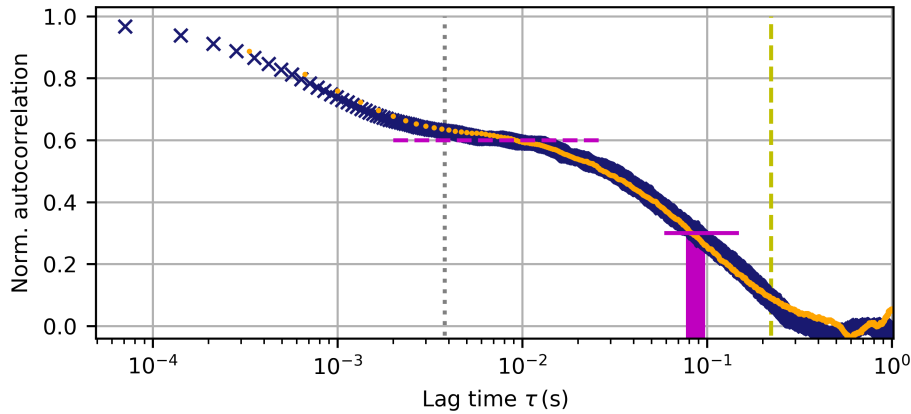


**Figure 4.18.:** Comparison of the lag time at half of the slope with the theoretical diffusion times. The experimental autocorrelation is depicted with blue crosses and the Monte Carlo simulated one with orange dots. Besides, the dashed horizontal magenta line marks the plateau and the solid horizontal line the value at half of the plateau. Here, the derived lag time at about  $\tau \approx 90$  ms is marked with a magenta rectangle. The gray (green) dotted (dashed) vertical line depicts the theoretical diffusion time if the nanosphere dispersed in water diffuses in longitudinal (transversal) direction.

$7 \cdot 10^{-2}$  s the two curves agree excellently. If there would be a drift in any direction, the slope at longer time scales would change (see Fig. 2.23).

**Discussion.** Only in Ref. [97] an analytical solution for the autocorrelation of a standing-wave light field is suggested. However, this solution contradicts the measured autocorrelation because it consists of only one slope instead of two. Therefore, an own analytical solution was derived. This solution follows the double-slope structure, though, at longer lag times the measured autocorrelation and the theoretical one deviate. Since the Monte Carlo simulated autocorrelation takes the nanoparticles size into account and is in good agreement with the measured data, the analytical solution still needs to be adapted in this respect.

On the other hand, because the Monte Carlo simulation agrees very well, it can be used to determine the nanoparticles diffusivity and hydrodynamic radius. Furthermore, it can be concluded that the nanospheres behave purely diffusive inside the microfluidic channel and intracavity forces like the optical tweezer force, the photothermal force<sup>5</sup>, or a force acting on the nanosphere due to the mirror movement can be neglected (see Appendix A.10).

In fluorescence correlation spectroscopy (FCS) the diffusion time can be read directly at half of the slope, if the different effects responsible for the different time scales can be treated independently [96]. In case of the measured autocorrelation with the fiber-based FP cavity, the two slopes occur due to the nanosphere's diffusion in longitudinal and transversal direction. According to Eq. (2.76) the diffusion time in transversal direction is expected at  $\tau_{D,xy} = w_0^2/(4D) = 0.22$  s and the diffusion time in longitudinal direction at  $\tau_{D,z} = (\lambda_0/(4n_m))^2/(2D) = 3.8$  ms. Fig. 4.18 shows a comparison between the theoretical expected diffusion times and the lag time derived at half of the second slope at the longer time scale. Neither the experimental derived lag time nor the Monte Carlo simulated one agree with the theoretical diffusion time.

<sup>5</sup> Heating of the liquid inside the cavity, causing a gradient in the liquid's density.

Consequently, the approach commonly used in FCS to read off the diffusion time at half the slope can't be applied to FP cavity-derived autocorrelations.

## 4.6. Discussion

In this chapter it was shown that the unlabeled quartz glass nanoparticles behaved purely diffusive in the cavity standing-wave light field of the FP cavity. This was, on the one hand, confirmed by the measured frequency shift histograms (Chapter 4.2.1) and, on the other hand, by the autocorrelation signal and its agreement with Monte Carlo simulations (Chapter 4.5). Therefore, the FP cavity is a promising candidate for the investigation of the natural behavior of nanoparticles and biomolecules.

In addition, the effective mean polarizability, the effective refractive index and the refractive index of the hydrate shell was determined for three different quartz glass nanoparticle samples (Chapter 4.2.1). At lower modulation frequencies (1...3 kHz) of the cavity length, several single nanoparticle transit events had to be taken into account. Improved statistics was achieved by an increase of the modulation frequency to 14 kHz such that the optical properties of a single nanoparticle could be determined from a single nanosphere transit event (Chapter 4.3). By considering the correlation between the decrease of amplitude and the frequency shift, the effective refractive index could be evaluated with a low uncertainty of 0.01 since the slope was widely independent of the cavity geometry (Fig. 4.7). However, the signal-to-noise ratio for the amplitude decrease was smaller than for the frequency shift (Chapter 4.1). Therefore, for particles with a smaller polarizability, only the frequency shift was measurable and a larger error arose for the determination of the refractive index (0.03 error). When the quartz glass nanospheres are dispersed in double-distilled water, their polarizability increases due to a formed hydrate shell around them. This significant increase of the polarizability was measured by the FP cavity (compare intrinsic and measured effective polarizability, Table 4.2). Furthermore, the refractive index of the hydrate shell could be estimated for three different samples (Chapter 4.2.2). The different hydrate shell thicknesses could be explained by impurities in the material (sample A) and different surface curvatures of the spheres (sample B versus sample C). Overall, it has been shown that the FP cavity enables the measurement of various optical properties of nanoparticles and therefore it is a powerful tool for the investigation of single nanoparticles.

In chapter 4.4 the impact of salt on the formation of the hydrate shell around the quartz glass nanosphere was investigated. In case of sample C, adding salt ions to the solution lead to a suppression of the hydrate shell as the intrinsic polarizability was evaluated from the measured frequency shifts. A downside of this measurement was the lack of control of the salt concentration in the FP cavity. Probably salt residuals remained in the microfluidic channel when it was rinsed with double distilled water. Therefore, no statements could be made about the actual salt concentrations in the cavity. In case of sample B, the salt concentration of  $\approx 1.5 \cdot 10^{-4}$  lead to a reduction of the hydrate shell thickness from 15.3 nm to 14,5 nm. Despite the lack of control of salt concentration, salt ions were shown to reduce the formation of the hydrate shell.

In chapter 4.5, the autocorrelation of the measured frequency shifts of several single nanoparti-

cle transit events was compared with the theoretical autocorrelation of a punctiform nanoparticle and with the Monte Carlo simulation of several single nanoparticle tracks. Whereas the theoretical autocorrelation contained the double-slope structure which arose due to the movement of the nanoparticle in the longitudinal and transversal direction inside the cavity standing-wave light field, especially at longer lag times the measured autocorrelation and the theoretical one differed. This strong deviation occurred because the geometric expansion of the particle has not yet been taken into account. In the Monte Carlo simulation, the expansion of the nanoparticle was considered instead. Especially between  $10^{-2}$  s and  $7 \cdot 10^{-2}$  s the measured autocorrelation and the Monte Carlo simulated one agreed excellently. Accordingly, by comparing Monte Carlo simulations with the measured autocorrelation, in principle, the hydrodynamic radius of the nanoparticles can be determined independently of their refractive index.

## 5. Three-dimensional tracking of a single quartz glass nanoparticle

All results presented in this chapter are submitted to Nature Communications for publication and content is therefore closely following [95].

In Chapter 2.4.1 it is theoretically explained, how the three-dimensional track of a spherical nanoparticle can be extracted from the recorded signal of the fundamental mode  $TEM_{00}$  and the two higher-order transverse modes  $TEM_{01}$  and  $TEM_{10}$ . The track itself contains the information of the nanosphere's diffusivity and consequently of its hydrodynamic radius (see Chapter 2.4.2). The determination of the hydrodynamic radius is thereby independent of the nanosphere's refractive index. In this chapter, the theory is applied to measured single nanosphere signals. The experimental data are based on the cavity with cooperativity  $C \propto 2.1 \cdot 10^4$  (CP2, Table 3.6) and sample B ( $r_{\text{geom}} = 60$  nm, Table 4.2). At first, a second laser is introduced, which enabled a simultaneous measurement of the three modes at low mechanical background noise (Chapter 5.1). In the next Chapter, the measured frequency shifts of several transit events are considered in order to select a transit event of a single nanosphere (Chapter 5.2). The single transit event is then evaluated and characterized. Besides, the localization, as well as the temporal resolution of the three-dimensional tracking, are analyzed (Chapter 5.3). Finally, the tracking algorithm for the position is applied to the measured frequency shifts resulting in the three-dimensional tracking path and the diffusivity and hydrodynamic radius are determined via the mean squared displacement (Chapter 5.4).

### 5.1. Reduction of the measurement noise by two probe lasers

In Chapter 3.5, the different cavity versions A-C are compared. For the measurements of their stabilities, the cavity length was changed by  $20 \cdot \delta_v \approx 0.2$  nm. If next to the fundamental mode  $TEM_{00}$  also the two higher-order transverse modes  $TEM_{01}$  and  $TEM_{10}$  are of interest, there are two possibilities for scanning over all three modes: Either one probe laser excites the three modes or two probe lasers are used, one excites the  $TEM_{00}$  mode and the second one excites the  $TEM_{01}$  and  $TEM_{10}$ . The former demands a larger range for the scanning of the cavity (see Fig. 5.1a). Using two lasers instead, the excited resonances can be shifted to each other by a tuning of the laser wavelength. This allows the shift of the fundamental mode in between of the two higher-order modes. Hence, the cavity length only has to be changed in the order of  $20 \cdot \delta_v$ , to scan over the three modes. Fig. 5.1b) shows the experimental difference in the detected measurement noise. By using two lasers instead of one, the mechanical noise of the cavity is greatly reduced from 25.3 pm *rms*-noise (gray) to 0.91 pm *rms*-noise (orange). For the definition of the *rms*-noise see Chapter 3.5.

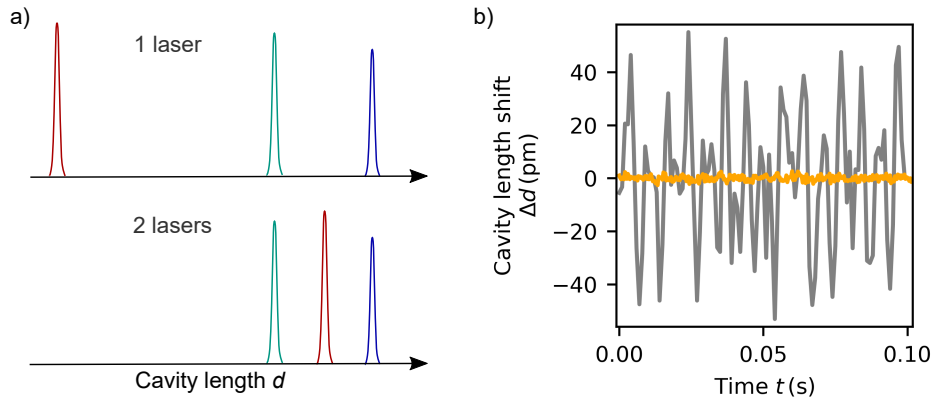


**Figure 5.1:** Reduction of the measurement noise by using two probe lasers. **a)** If one laser is used for the scanning over the TEM<sub>00</sub> (red), the TEM<sub>01</sub> (green) and the TEM<sub>10</sub> (blue) mode, the scanning range is larger than using two probe lasers instead. **b)** Measurement noise if one probe laser (gray) or two probe lasers (orange) are used.

## 5.2. Selection of a single transit event

In order to avoid an increased mechanical measurement noise, two probe lasers are operated when the cavity is scanned over the three modes TEM<sub>00</sub>, TEM<sub>01</sub> and TEM<sub>10</sub> (see Chapter 5.1). Fig. 5.2 shows the frequency shifts of several transit events, which were measured within 8 hours without changing the sample inside the cavity. Within the first two hours of measurement time (green,  $\approx 59$  transit events), the TEM<sub>00</sub> mode shows a steep decay at about 8 (GHz), which is typical for single nanosphere transit events and is in agreement with the simulated black dotted curve. However, the TEM<sub>01</sub> and TEM<sub>10</sub> mode don't agree with the simulated steep decay at about 5.8 GHz. Therefore it can be concluded that during the measurement the nanosphere concentration is too high, increasing the probability of detecting a single nanosphere in the TEM<sub>00</sub>, but simultaneously a second nanosphere in the radially expanded TEM<sub>01</sub> and TEM<sub>10</sub> modes. After 8 hours of measurement time (gray,  $\approx 210$  additional transit events), about double of the single nanosphere frequency shift is measured for the TEM<sub>00</sub> mode (gray transparent rectangle). This agrees with a dimer, consisting of two aggregated SiO<sub>2</sub> nanospheres<sup>1</sup>. The blue curve, however, represents a single nanosphere transit even. In this case, all three modes detect a single nanosphere at the same time, because all measured frequency shifts agree with the simulated histogram. The spreading of the simulated maximal frequency shifts at 6.4 GHz and 7.8 GHz for the TEM<sub>00</sub> mode stems from the size distribution of the sample.

The measured raw data of this single nanosphere transit event is shown in Fig. A.19 and the frequency shifts with the already subtracted drifts are shown in Fig. 5.3. It can be seen that each mode is reacting differently, depending on the nanosphere's position inside the standing-wave light field (see Fig. 2.14 for the qualitative explanation).

<sup>1</sup> For the estimation of the maximal frequency shifts produced by a dimer, two single spheres with the center distance  $2r_{\text{hydr}}$  are estimated. Any interaction fields are neglected, meaning the single produced shifts at  $x, y, z = 0$  and  $x = 2r_{\text{hydr}}, y, z = 0$  are summed up.

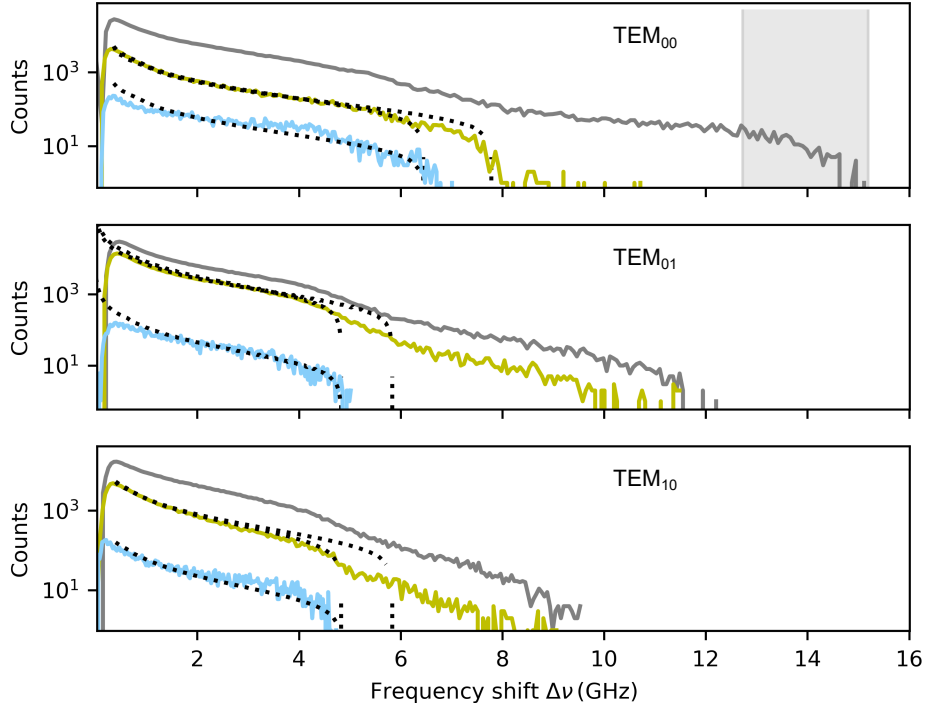


**Figure 5.2.:** Frequency shifts of a single nanosphere transit event (blue), of about 59 nanoparticle transit events (green, 2 hours measurement time) and of about 210 additional nanoparticle transit events (gray, 8 hours measurement time). The black dotted curves show the simulated frequency shifts for the single nanosphere polarizabilities  $\alpha/(4\pi\epsilon_0) = 23.3 \cdot 10^3 \text{ nm}^3$  and  $\alpha/(4\pi\epsilon_0) = 27.9 \cdot 10^3 \text{ nm}^3$ . Both values are within the range for the nanosphere size distribution and effective index uncertainty. The gray transparent rectangle shows the region of the expected maximum dimer shifts. Submitted to [95].

### 5.3. Characterization of the cavity and tracking resolution

In order to characterize the cavity's geometry, Fig. 5.4 shows the correlation between the  $\text{TEM}_{00}$  mode and the  $\text{TEM}_{01}$  (blue) and  $\text{TEM}_{10}$  (gray) mode. By comparing the measured correlations with the simulated one (red) the measured frequency shifts for the  $\text{TEM}_{01}$  and  $\text{TEM}_{10}$  mode seem to be slightly smaller than the theoretically expected ones. There are two possible reasons: On the one hand, the probability that the nanosphere resides at or close to the center of the antinode is low (see Fig. 2.12). Therefore small frequency shift values are measured more frequently than larger values. On the other hand, the non-perfect spherical-shaped mirrors<sup>2</sup> can cause small deviations between theory and experiment. Due to the radial expansion of the higher-order transverse modes, the radius of curvature for each mode can differ [152]. In the following, these possible, small deviations are neglected for the determination of the nanosphere's track.

<sup>2</sup> The mirrors used in this work are fabricated by  $\text{CO}_2$  laser pulses. [87].

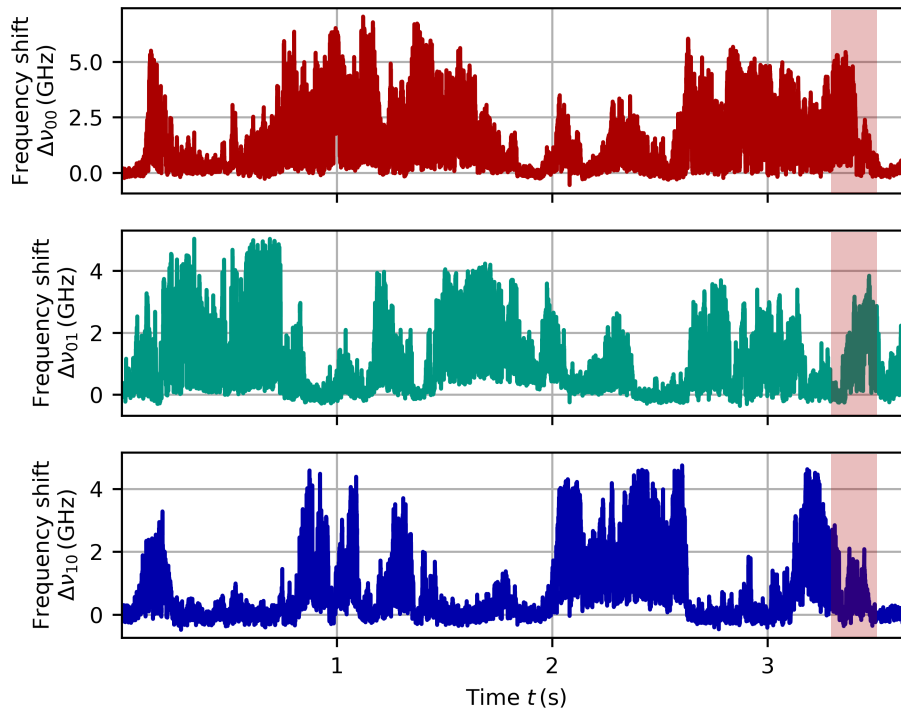


**Figure 5.3.:** Frequency shifts of the fundamental mode  $\Delta\nu_{00}$  (red) and the two higher-order transverse modes  $\Delta\nu_{01}$  (green) and  $\Delta\nu_{10}$  (blue) of a single nanosphere transit event. The red rectangle marks the time section of the three-dimensional track shown in Fig. 5.8. Submitted to [95].

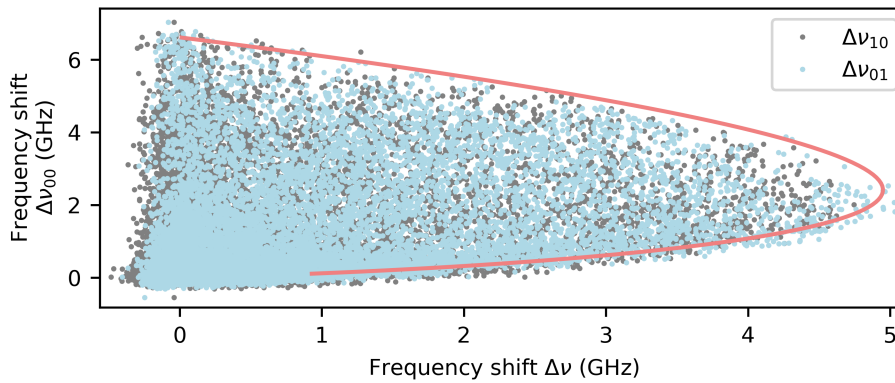


**Figure 5.4.:** Correlation between the frequency shifts of the  $TEM_{00}$  and the  $TEM_{01}$  (blue) or  $TEM_{10}$  (gray) mode generated by the nanosphere dispersed in water and diffusing through the modes. The red curve is the theoretical expectation, when the nanosphere changes its position along the  $x$ -axis at  $y, z=0$ . Submitted to [95], see supplementary information.

The measurement noise creates an uncertainty for the measured shifts and therefore plays an important role, when the nanosphere's track is derived from the shifts. Fig. 5.5 shows histograms of the measured frequency shifts of the three modes. Gaussian fits to the small frequency shift values gives the measurement noises:  $\sigma_{00} = 0.13$  GHz,  $\sigma_{01} = 0.15$  GHz and

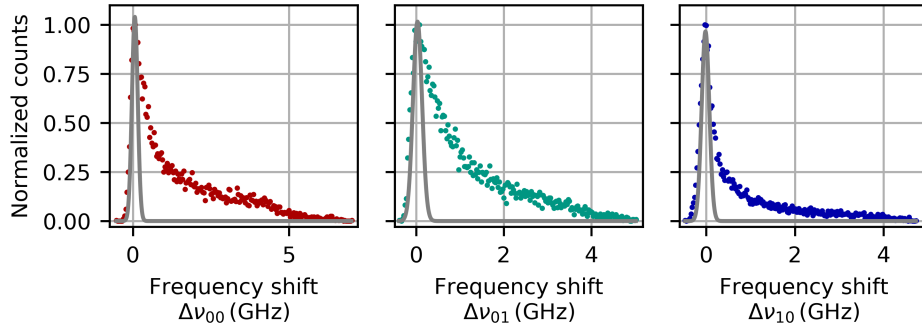


**Figure 5.5.:** Histograms for the measured frequency shifts of the TEM<sub>00</sub>, the TEM<sub>01</sub> and the TEM<sub>10</sub> mode produced by a single nanosphere. Submitted to [95], see supplementary information.

$$\sigma_{10} = 0.12 \text{ GHz.}$$

To deduce the the uncertainty of localization from the frequency measurement noise, the theoretical frequency shift matrices for each mode are calculated by Eq. (2.61), (2.65), and (2.66) with a  $\delta x = \delta y = 16.9 \cdot 10^{-3} \mu\text{m}$  pixel size in  $x$ - and  $y$ -direction and a  $\delta z = 1.6 \cdot 10^{-3} \mu\text{m}$  pixel size in  $z$ -direction. For each nanosphere position  $(x_i, y_i, z_i)$ , the theoretically produced frequency shift triples at this position are superimposed with the frequency measurement noises  $\sigma_{00} = 0.13 \text{ GHz}$ ,  $\sigma_{01} = 0.15 \text{ GHz}$ , and  $\sigma_{10} = 0.12 \text{ GHz}$ . Consequently, the exact theoretically produced frequency shifts at position  $(x_i, y_i, z_i)$  are compared with all other positions inside the matrix with superimposed frequency measurement noises. If the exact frequency shift triple values at position  $(x_i, y_i, z_i)$  lie within the uncertainty range at another position, the nanoparticle could also reside there. Finally, the localization uncertainty  $\delta r(x_i, y_i, z_i)$  is defined as the number of all positions  $N(x_i, y_i, z_i)$ , where the nanoparticle would produce the same frequency shift triples including the uncertainty, times the third root of the pixel volume  $V_{\text{pixel}} = \delta x \delta y \delta z$ :

$$\delta r(x_i, y_i, z_i) = N(x_i, y_i, z_i) \cdot (V_{\text{pixel}})^{1/3} . \quad (5.1)$$

Fig. 5.6a) shows the resulting localization uncertainty matrix for  $x \leq \sqrt{(w_0^2 - y^2)}$  and  $z \leq 143 \text{ nm}$ . Within this volume, the fundamental mode intensity is larger than  $I_0/e^2$ , where  $I_0$  is the maximal occurring intensity. Fig. 5.6b) and c) show a cross-section through the uncertainty matrix for  $y=0$  and  $z=0$ . At the largest intensity gradients, the localization uncertainty is only 8 nm. However, at the sensing octant border the uncertainty reaches its maximal value of 218 nm and the mean uncertainty inside the sensing volume is 43 nm.

The frequency shifts produced by the single SiO<sub>2</sub> nanosphere diffusing in water and probed by the cavity standing-wave light field were measured with a scanning frequency of 3 kHz. Therefore, the time resolution of the three-dimensional track is 0.3 ms.

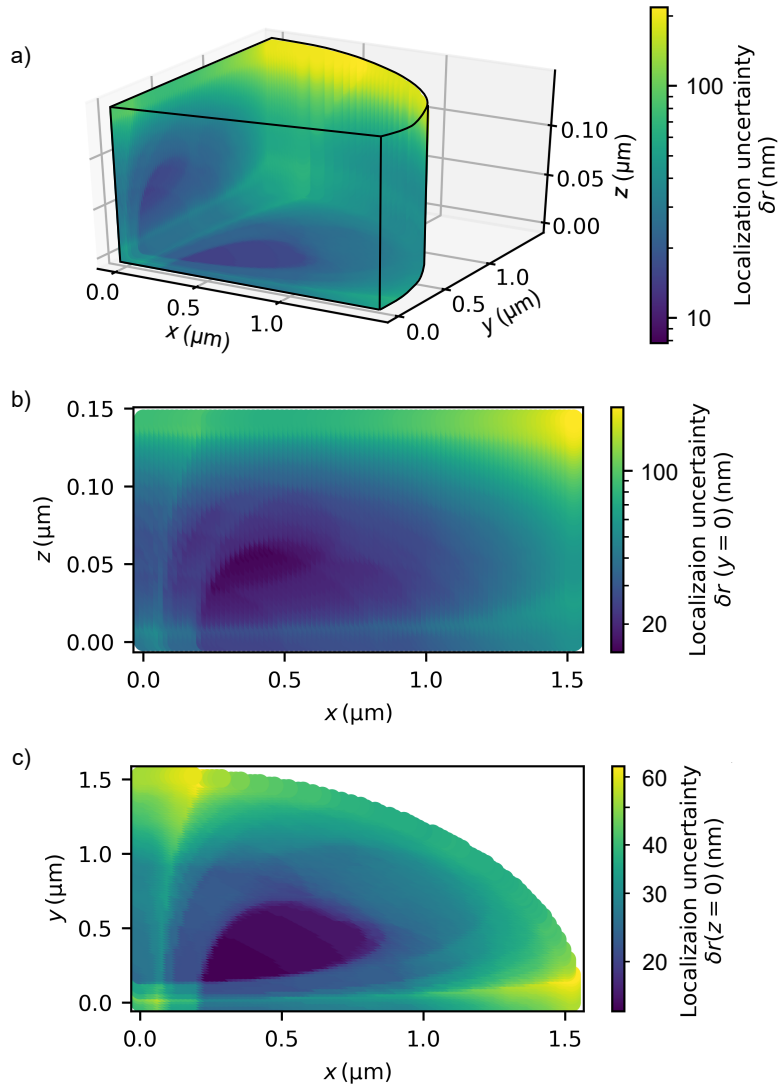


**Figure 5.6.:** Localization uncertainty due to measurement noise. **a)** Three-dimensional representation of the uncertainty matrix. Only the section of the sensing octant is shown, where the intensity of the fundamental mode is larger than the maximum intensity at the antinode divided by  $e^2$ . **b)** Cross-section through the uncertainty matrix at  $y = 0$  and **c)** cross section through the uncertainty matrix at  $z = 0$ . Submitted to [95].

#### 5.4. Three-dimensional track and mean squared displacement

Due to the measurement noise, the measured frequency shift triples at time  $t$  are afflicted with some uncertainty. Therefore, different possible positions inside the octant sensing volume can be found for the same frequency shift triple (see Chapter 5.3). The simulation of a single nanosphere transit event (see Chapter 2.4.1) yields the result that the mean of all possible positions within the uncertainty volume (Algorithm 3, Chapter 2.4.1) provides the best agreement between the actual track and the algorithm track. Consequently, this tracking algorithm is applied to the measured frequency shifts. Fig. 5.7 shows the resulting tracking path and Fig.

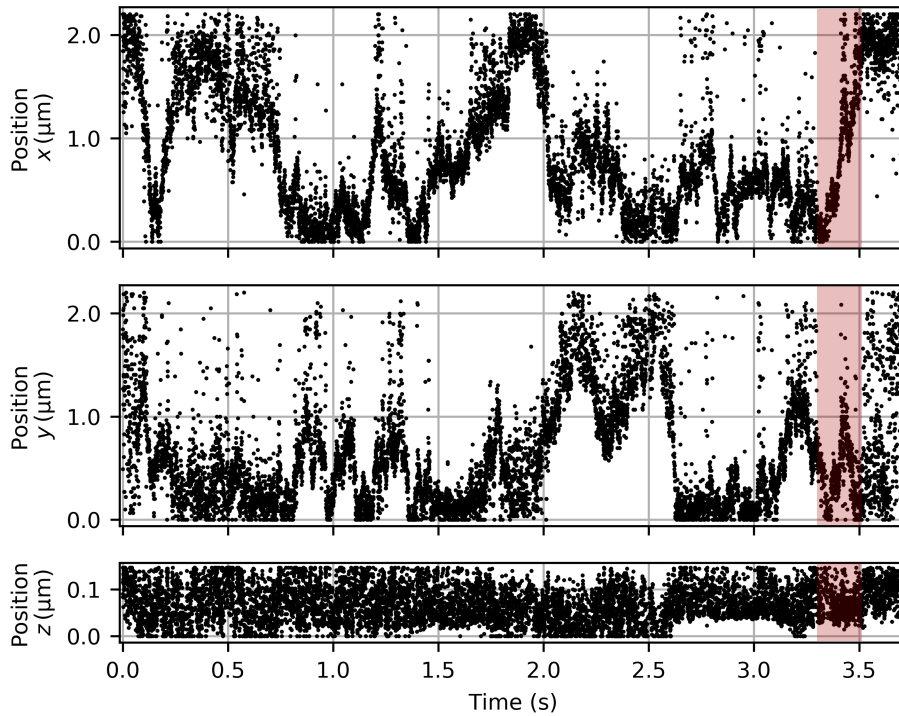


**Figure 5.7.:** Derived tracking path of a single  $\text{SiO}_2$  nanosphere transit event from the simultaneously measured frequency shifts of the  $\text{TEM}_{00}$ , the  $\text{TEM}_{01}$  and the  $\text{TEM}_{10}$  mode. The red rectangle marks the time section of the three-dimensional track shown in Fig. 5.8. Submitted to [95].

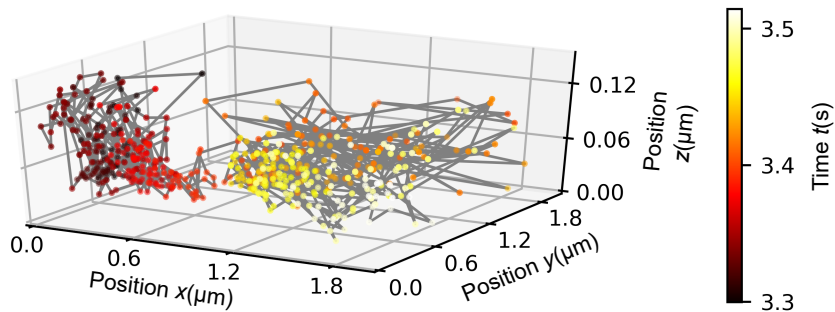


**Figure 5.8.:** Representation of the tracking path of a single nanosphere in the three-dimensional space. The time section shown here is marked in red in Fig. 5.3 and 5.7. Submitted to [95].

5.8 is a representation in the three-dimensional space. Here, only the time range marked in red in Fig. 5.3 and 5.7 is depicted for better visibility. As the expansion of the cavity mode in  $z$ -direction is about 15 times smaller than in  $x, y$ -direction, the nanosphere reaches faster the sensing octant's border and thus the track is folded back into the sensing octant more frequently. However, the information of the nanosphere's Brownian motion is still included.

In Chapter 2.4.2 it is explained, how the mean  $MSD$  is determined from the obtained three-dimensional track and how the values for the diffusivity are obtained from the linear fit. Therefore, only the results are given here. Fig. 5.9 a) shows the related  $\langle MSD \rangle$  to the single

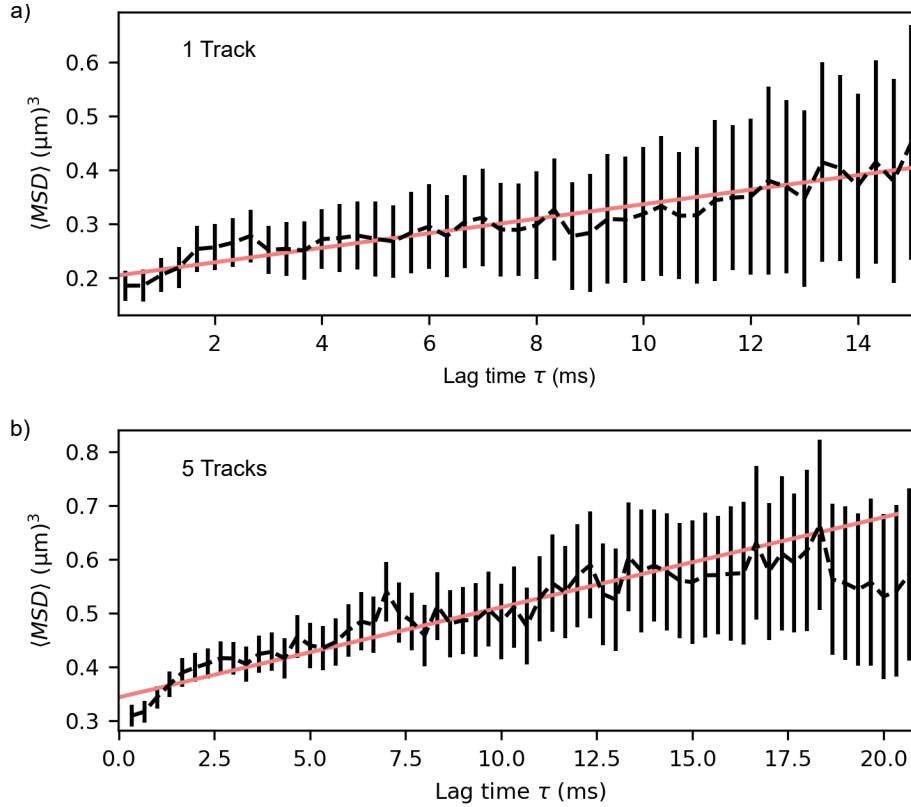


**Figure 5.9.:** Mean  $MSD$  **a)** for the single nanosphere track shown in Fig. 5.7 and **b)** for five single nanosphere tracks including the track depicted in Fig. 5.7. In both cases, the linear fit to the data points is shown in red. Submitted to [95].

nanosphere track depicted in Fig. 5.7. As the  $\langle MSD \rangle$  increases linearly with increasing lag times, the nanosphere's motion is purely diffusive. This is an additional confirmation of the result obtained via the autocorrelation (see Chapter 4.5). The slope of the linear fit to the first  $x_{ON} = 45$  data points [127] directly depends on the diffusivity. In this case, the diffusivity of  $D = (2.2 \pm 0.3) \mu\text{m}^2/\text{s}$  and the hydrodynamic radius of  $r_{\text{hydr}} = (95.7 \pm 14.6) \text{ nm}$  is obtained. Taking into account the uncertainty of the nanosphere's hydrodynamic radius of  $(75.3 \pm 9.5) \text{ nm}$ , both values are in agreement. An excellent agreement between both can be achieved by considering five single nanosphere tracks instead of one. The obtained mean  $MSD$  is shown in Fig. 5.9 b). In this case, the fit converges at the first  $x_{ON} = 62$  data points and the mean diffusivity of  $\langle D \rangle = (2.8 \pm 0.4) \mu\text{m}^2/\text{s}$  and the mean hydrodynamic radius of  $r_{\text{hydr}} = (76.9 \pm 10.0) \text{ nm}$  is derived.

Both  $\langle MSD \rangle$  are shifted along the  $y$ -offset due to the included measurement noise in the signal. From the offset, the static localization uncertainty can be estimated by Eq. (2.91). A fit to the first five data points gives  $\sigma_0 \approx 304 \text{ nm}$  in case of the single track and  $\sigma_0 \approx 361 \text{ nm}$  in case of the five tracks. Both uncertainties are on the same order as the result obtained by Monte Carlo simulation ( $\sigma_0 \approx 355 \text{ nm}$ , Chapter 2.4.2).

## 5.5. Discussion

In this work, three-dimensional tracking of nanoparticles with a microresonator was demonstrated for the first time. It was shown that nanoparticles can be tracked with a temporal resolution of 0.3 ms, a minimum spatial resolution of 8 nm and a mean spatial resolution of 43 nm. By detecting the diffusive motion, the diffusivity, as well as the hydrodynamic radius could be determined with only 2 % deviation to the obtained mean hydrodynamic radius via ensemble measurements. Thereby, the three-dimensional track provides the information about the nanoparticle's hydrodynamic radius independently from its refractive index. In addition, the recorded frequency shift of the  $TEM_{00}$  mode contains the information of the nanoparticle's effective polarizability (see 4.3). Consequently, the nanoparticle's effective refractive index can be deduced. Whereas previously only the polarizability could be determined with microresonators, detailed information is now obtained by the three-dimensional track.



## 6. Towards the determination of the rotational diffusion of nanoparticles

The temporal evolution of measured frequency shifts generated by single nanoparticle transit events is shown in Fig. 5.2. Within the first two hours of measurement, almost only single nanospheres reside in the cavity. With time progressed, larger frequency shifts are measured. As the larger frequency shifts have about twice the value of the maximal shift expected for a single nanosphere, these larger shifts are assumed to stem from dimers consisting of two agglomerated nanospheres. To further characterize both nanoparticle species, their rotational diffusion is investigated. In Chapter 2.6 the theory of the interaction between the polarization-split fundamental modes of a FP cavity and a rotating prolate spheroid is discussed. Here, this theoretical understanding is used in order to measure the rotational diffusion of single, not perfectly spherical nanospheres, of dimers and larger agglomerates. Due to their anisotropic shape, their rotational Brownian motion in water causes a change of the frequency splitting of the polarization-split fundamental modes. As the amount of frequency splitting also depends on the light intensity at the position of the nanoparticle, the frequency split signal contains the information about the nanoparticles translational diffusion as well. In Chapter 4.5 it was shown that the autocorrelation of the measured frequency shift signal consist of two slopes due to the nanosphere's translation in longitudinal and transversal direction of the standing-wave light field. The autocorrelation of the frequency splitting contains the additional information about the nanosphere rotation, thus, three slopes are expected in total.

In the following, two different nanosphere samples were used, with a geometric radius of either  $r_{\text{geom}} = 25 \text{ nm}$  (sample C, Table 4.2) or  $r_{\text{geom}} = 60 \text{ nm}$  (sample B, Table 4.2). Each sample contains different nanoparticle shapes due to the agglomeration of single nanospheres to dimers, consisting of two nanospheres, and larger agglomerates with unknown shape. These different nanoparticle types are investigated in their produced frequency shift and frequency splitting signal. Although, in case of sample C, a frequency splitting is detected for all nanoparticle species, rotational diffusion times can't be determined. In contrast, subsequent evaluation of the signals generated by nanoparticles of sample B provides information about rotation times. The first measurements with the smaller nanoparticles (sample C) were operated with a cavity cooperativity of  $C \propto 1.9 \cdot 10^4$  (CG3, Table 3.6) and the measurements with the larger nanoparticles (sample B) were performed with a slightly smaller cavity cooperativity of  $C \propto 1.7 \cdot 10^4$  (CG4, Table 3.6).

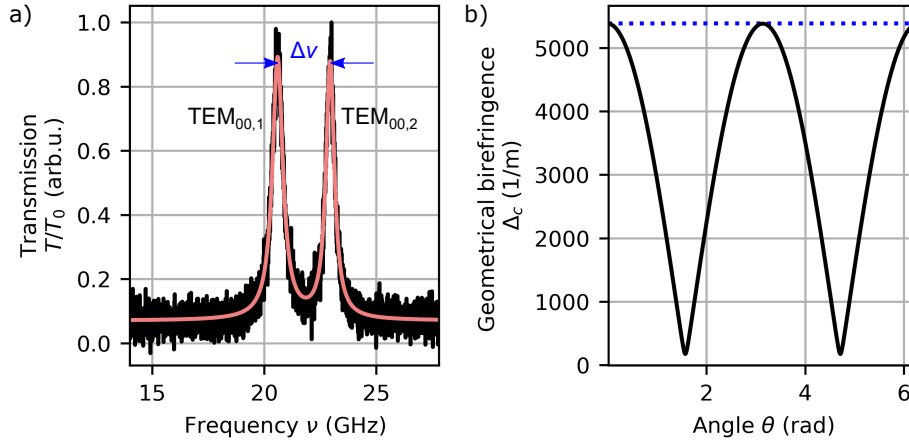


**Figure 6.1.:** Polarization splitting of the fundamental mode and geometric birefringence. **a)** Lorentzian fit (red) to the measured polarization-split fundamental mode  $TEM_{00,1}$  and  $TEM_{00,2}$  (black). The distance between the two resonances is  $\Delta\nu = 2.34$  GHz. **b)** Simulated geometrical birefringence depending on the rotation angle  $\theta$  of the mirrors relative to each other and for the mirror radii of curvature  $r_{c,M1,1} = 40.0 \mu\text{m}$ ,  $r_{c,M1,2} = 70.0 \mu\text{m}$ ,  $r_{c,M2,1} = 45.0 \mu\text{m}$  and  $r_{c,M2,2} = 85.6 \mu\text{m}$ . The blue dotted horizontal line marks the measured geometrical birefringence.

## 6.1. Rotational diffusion of 25 nm quartz glass nanoparticles

This section is divided into different parts. At first, the measured polarization splitting of the fundamental mode is evaluated. Then, the caused birefringence of different nanoparticle types is compared and eventually their rotational diffusion is investigated.

**Polarization-split fundamental mode.** Fig. 6.1a) shows the transmission signal of the polarization-split fundamental modes  $TEM_{00,1}$  and  $TEM_{00,2}$ . The frequency distance between both resonances of  $\Delta\nu = 2.34$  GHz is directly related to the geometrical birefringence of the cavity mirrors  $\Delta_c = 5385.7$  1/m via Eq. (2.21). The geometric birefringence in turn is related to the geometrical shape of the mirror at the position of the formed mode via Eq. (2.22). When the mode is formed at the center of the mirror depression, the mirror radii of curvatures (see MP3, Appendix 3.6) would cause a birefringence between  $\Delta_c = 1623$  1/m and  $\Delta_c = 4096$  1/m. As the measured value of  $5385.7$  1/m is not included in this range, this indicates that the mirrors are slightly misaligned and as a result, the mode is formed away from the center. Such a misalignment is possible since there is a cavity of 6 micrometers between the cavity fiber and the precision hole of the ferrule. Away from the center of the mirror depression, the radii of curvature can deviate from the radii of curvature at the center by several microns, because the used mirrors deviate from a spherical-shaped depression (see Chapter 3.1.1 and [152]). When the mirror radii of curvatures of  $r_{c,M1,1} = 40.0 \mu\text{m}$ ,  $r_{c,M1,2} = 70.0 \mu\text{m}$ ,  $r_{c,M2,1} = 45.0 \mu\text{m}$  and  $r_{c,M2,2} = 85.6 \mu\text{m}$  are assumed instead, the measured geometrical birefringence would be caused at the rotation angle  $\theta = 0$  (see Fig. 6.1b)).

**Birefringence produced by single quartz glass nanoparticles.** If an anisotropic nanoparticle resides inside the cavity light field, the frequency splitting between  $TEM_{00,1}$  and  $TEM_{00,2}$

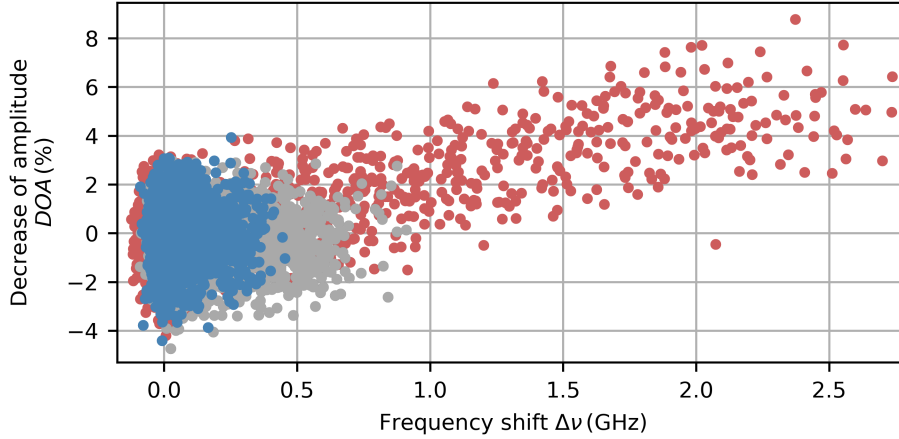


**Figure 6.2.:** Frequency shifts and decreases of amplitudes by different single nanoparticle transit events: Blue: a single nanosphere, gray: probably a dimer and red: a larger agglomerate.

changes. This is demonstrated for nanoparticles consisting of single or multiple nanospheres with a geometric radius of  $r_{\text{geom}} = 25$  nm (sample C). In this case, the nanoparticles were dispersed in a DPBS solution and a maximum frequency shift of  $\approx 0.45$  GHz for a single nanosphere transit event was measured (see Fig. 4.14). Thus, the frequency shift of a dimer is expected at  $\approx 0.9$  GHz. Following this theoretical expectations, three transit events are further investigated and assigned to the individual nanoparticle types (see Fig. 6.2). The smallest frequency shifts (blue) are assigned to a single nanosphere transit event. The approximately twice as large frequency shifts of the events in gray are assumed to stem from a dimer and the large frequency shifts (red) are caused by a large agglomerate consisting of several nanospheres.

The time evolution of the measured frequency shifts of the polarization-split modes  $\Delta\nu_{0,1}$  and  $\Delta\nu_{0,2}$ , the measured frequency splitting between the modes  $\Delta\nu_{0,2} - \Delta\nu_{0,1}$  and the decrease of amplitude *DOA* of  $\text{TEM}_{0,1}$  are depicted in Fig. 6.3. While the frequency shift and the frequency splitting signals increase with the nanoparticle size and with increasing anisotropy, the decrease of amplitude is too insensitive for the two smaller nanoparticle types. Only the larger agglomerate produces a detectable decrease of amplitude. In contrast, the frequency splitting is much more sensitive. Although the single nanospheres are specified with a roundness of better than 0.980 by the manufacturer (see TEM pictures A.13), this tiny asymmetry of the single nanosphere already produces a change of the frequency splitting.

**Investigation of diffusion times.** To extract the information about the diffusion times contained in the measured frequency splittings, the autocorrelation is calculated. Before that, however, only the sections containing the nanoparticle signal have to be determined from the overall frequency splitting measurement. This is shown in Fig. 6.4 for the dimer measurement. Only the black part of the signal is used to calculate the autocorrelation (see Fig. 6.5a, gray). The same procedure is done for the frequency splittings generated by the single sphere and the larger agglomerate. Their autocorrelation is shown in Fig. 6.5a) as well. The single nanosphere as well as the large agglomerate autocorrelation oscillate around zero in the entire lag time range, thus no slope is visible. Only the dimer autocorrelation slightly

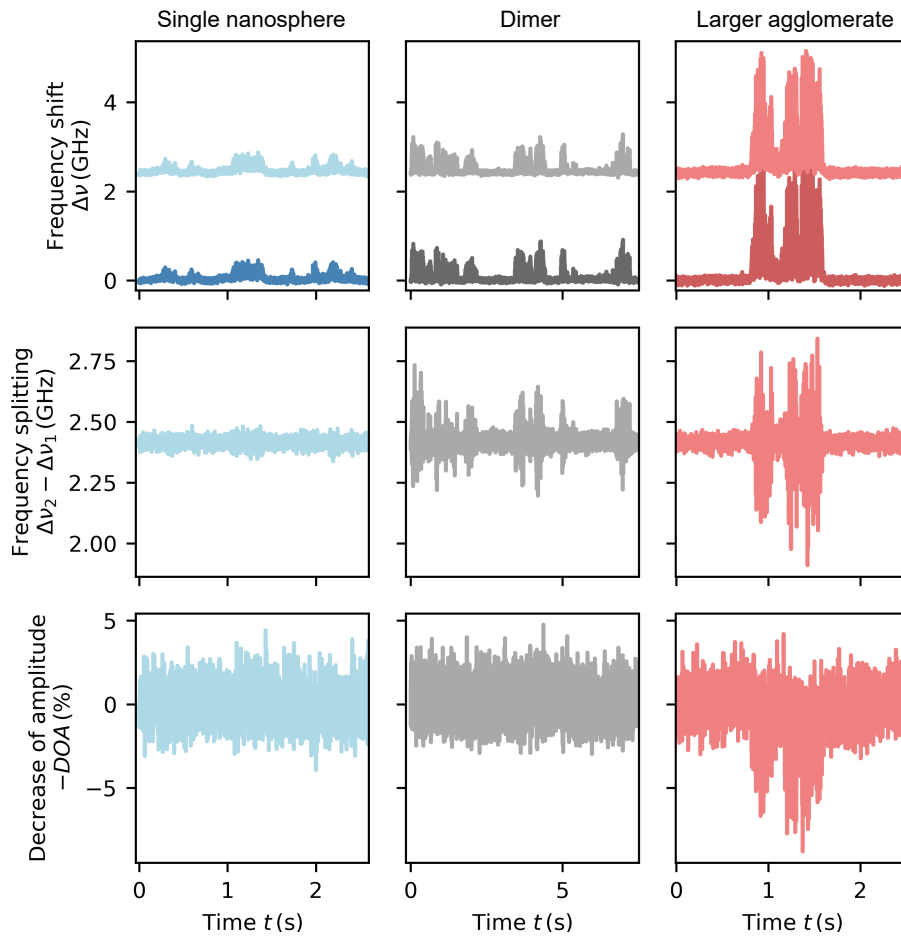


**Figure 6.3.:** Measured frequency shifts of the polarization-split fundamental modes  $\Delta_{00,1}$  and  $\Delta_{00,2}$ , frequency splitting between the two modes and measured decrease of amplitude of one of the modes over the time. Depicted are single nanoparticle transit events of different nanoparticle types: a single nanosphere (blue), a dimer (gray) and a larger agglomerate (red).

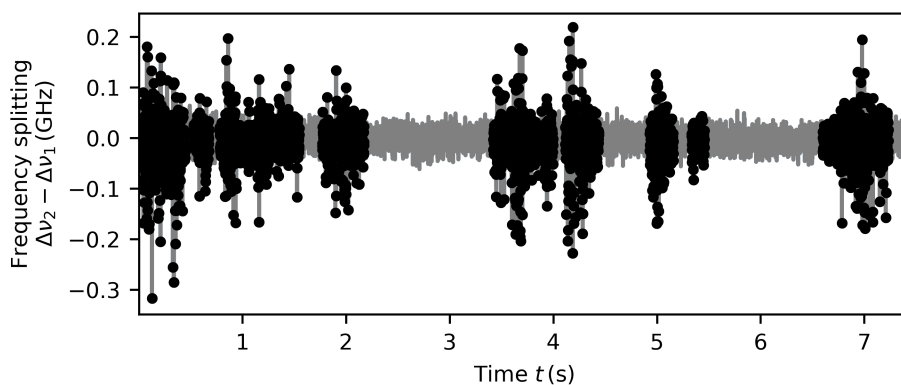


**Figure 6.4.:** Measured frequency splitting of the polarization-split fundamental modes when a dimer is diffusing in water. The black dots mark the data sections, which are different to the measurement noise and are generated by the rotation of the dimer.

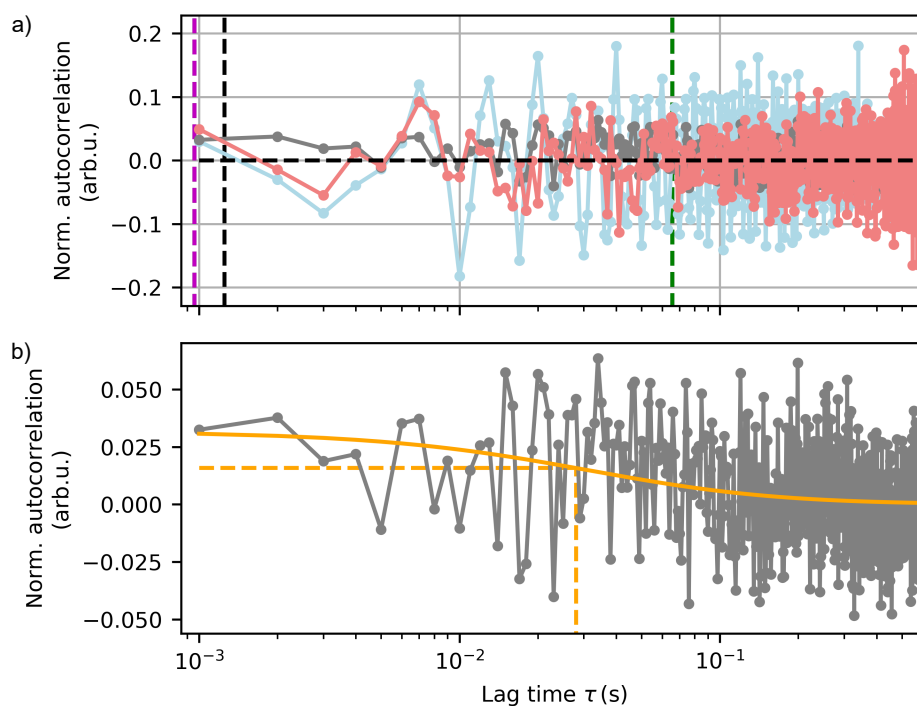


**Figure 6.5.:** **a)** Autocorrelation of the frequency splitting sections produced by the single nanosphere (blue), the dimer (gray) and the large agglomerate (red). The vertical dashed lines mark the theoretical diffusive rotation times for a nanosphere with the hydrodynamic radius  $r_{\text{hydr}} = 25$  nm (magenta) and its theoretical translational diffusion time in longitudinal (black) and transversal (green) direction. **b)** Evaluation of the lag time value at half of the plateau. The plateau is assumed at values equal or larger than 0.03. There, the lag time is  $\tau \leq 28$  ms.

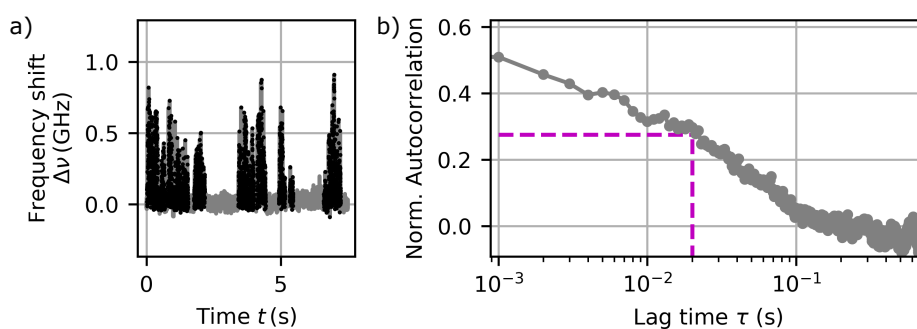


**Figure 6.6.:** Dimer frequency shift and corresponding autocorrelation. **a)** The black dots mark the section of the frequency shift signal (gray), which were caused by the dimer. **b)** Autocorrelation of the black sections marked in a). The magenta black horizontal line is the estimated value at half of the slope and the vertical magenta dashed line marks the corresponding lag time value.

increases with decreasing delay time (see Fig. 6.5b). Here, the autocorrelation consists of one slope instead of the expected three (one slope for the rotation and two slopes for the translational diffusion).

To find out where the slope comes from, the autocorrelation of the frequency shift produced by the dimer is calculated in addition. This is depicted in Fig. 6.6. Although two slopes are

expected of the translational diffusion, only one is visible. Consequently, the slope of the dimer translational diffusion in longitudinal direction is not resolved in time (expected at shorter time scales). The visible slope occurs due to the dimer diffusion in transversal direction. By comparing the value at half of the slope ( $\tau \approx 20$  ms) with the value at half of the slope of the frequency-split autocorrelation ( $\tau \approx 29$  ms, Fig. 6.5b), both values are similar. Therefore, it is assumed that the slope in the frequency-split autocorrelation of the dimer is caused by its translational diffusion in transversal direction.

In Fig. 6.5 also the theoretical diffusion times for a single nanosphere with  $r_{\text{hydr}} = 25$  nm hydrodynamic radius are shown. The dashed vertical lines mark the theoretical diffusive rotation time and its theoretical translational diffusion times in longitudinal (black) and transversal directions (green, compare with Eq. (2.101) and Eq. (2.76)). The rotational and transversal diffusion time in longitudinal direction are very close to each other ( $\tau_{D,r} \approx 1.0$  ms,  $\tau_{D,z} \approx 1.3$  ms), whereas the translational diffusion time in transversal direction is further apart ( $\tau_{D,xy} \approx 65.5$  ms). In case for the larger nanoparticles (dimer, agglomerate) larger diffusion times are expected due to the higher friction at rotation and translation. Because the two smaller diffusion times are so close together ( $\tau_{D,r} \approx \tau_{D,z}$ ), it is assumed that in the frequency-split autocorrelation only two slopes occur instead of three. One slope for the two smaller diffusion times ( $\tau_{D,r}$ ,  $\tau_{D,z}$ ) and the other slope for the diffusion in transversal direction ( $\tau_{D,xy}$ ). Furthermore, for all nanoparticles (single nanosphere, dimer, larger agglomerate) it is assumed that the slope at the smaller lag time would be further to the left of the lag time domain, but this time range is not contained in the frequency-splitting signal due to the low modulation frequency of the cavity length of 1 kHz. In addition, probably the slope at longer lag time caused by the translational diffusion in transversal direction of the single nanosphere and the agglomerate doesn't appear in the frequency-split autocorrelation due to the lack of statistics and because the autocorrelation is dominated by noise.

## 6.2. Rotational diffusion of 60 nm quartz glass nanoparticles

In the following the signals generated by a single nanosphere with geometric radius  $r_{\text{geom}} = 60$  nm and an event ascribed to a dimer consisting of two such agglomerated nanospheres are identified. Furthermore, their translational as well as their rotational diffusion are investigated. In comparison to the measurement results presented above in Chapter 6.1, the nanoparticle transit events are recorded with a significantly higher scanning frequency of 14.1 kHz versus 1 kHz. On the one hand, this improves the statistics of a single transit event and on the other hand, the autocorrelation signal also contains smaller lag times.

**Identification of different nanoparticle types.** Fig. 6.7 shows the comparison of decreases of resonance amplitudes and frequency shifts of two different nanoparticle transit events. As the same cavity setup was also used for the quantitative evaluation of the effective refractive index of several single nanosphere transit events of the same quartz glass nanosphere size (see Fig. A.15) the blue data can be directly assigned to a single nanosphere transit event. A dimer is assumed to produce about twice the shift than expected for a single nanosphere.

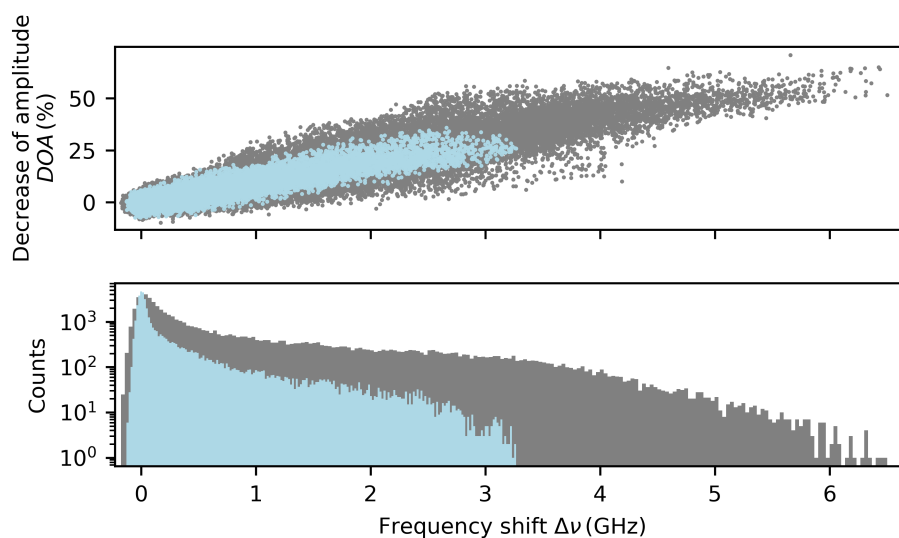


**Figure 6.7.:** Decreases of amplitude and frequency shifts produced by a diffusing single nanosphere (blue) and probably by a dimer (gray).

Therefore the gray signal is assigned to a dimer transit event.

**Translational diffusion.** The time evolution of both transit events is shown in Fig. 6.8a). Here, the data sections originating from the dimer (single nanosphere) are marked in red (blue). Fig. 6.8b) shows the autocorrelation of the marked sections of both transit events. Both autocorrelations consist of two slopes as expected. The first slope occurs due to the dimer (nanosphere) translational diffusion in longitudinal direction and the second slope at longer lag times occurs due to the diffusion in transversal direction. Furthermore, the second slope of the dimer is further to the right than that from the nanosphere. This is directly correlated with a larger diffusion time (compare with Fig. 2.23a), which is in agreement with the expectation, since a larger particle causes more friction and therefore diffuses slower.

**Rotational diffusion.** Fig. 6.8c) shows the frequency splitting of both transit events. Again the sections, which differ from the measurement noise, are marked in red and blue. Although the  $\text{SiO}_2$  nanoparticles are specified with a roundness of better than 0.980 by the manufacturer, a small anisotropy is detected via the frequency splitting. Compared to the dimer, the frequency splitting caused by the single nanosphere is smaller than that caused by the dimer. This is in agreement with the greater anisotropy of the dimer. In order to get information about the rotation time, the marked frequency splitting sections of the single nanosphere as well as of the dimer are autocorrelated and depicted in Fig. 6.8d). Two slopes appear for both nanoparticle types at about  $\tau = 10^{-3}$  s and  $\tau = 3 \cdot 10^{-2} \dots 10^{-1}$  s instead of the expected three slopes: one for the rotational diffusion and two for the translational diffusion in longitudinal and transversal direction. In contrast to the theoretical diffusion times of the 25 nm nanospheres, in this case, all theoretical values are further apart: The rotational diffusion time amounts to  $\tau_{D,r} = 26.2$  ms and the translational diffusion times are  $\tau_{D,z} = 3.8$  ms and  $\tau_{D,xy} = 224.4$  ms.

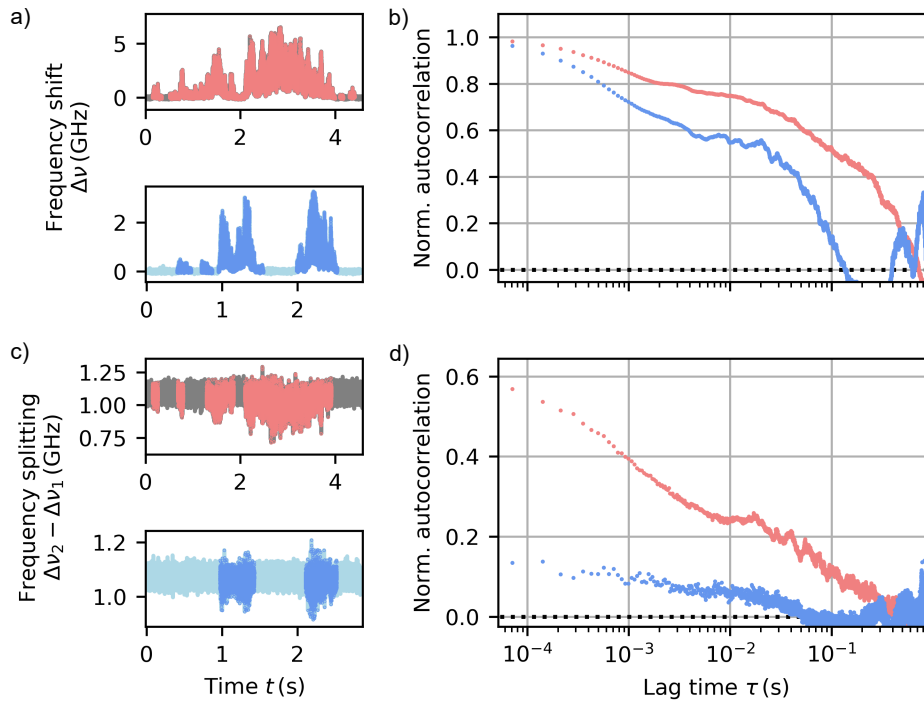


**Figure 6.8.:** Investigation of the translation and rotation of a  $\text{SiO}_2$  single nanoparticle with a geometric radius of 60 nm and a hydrodynamic radius of 75.3 nm (blue) and a dimer (gray/red) consisting of two agglomerated  $\text{SiO}_2$  nanoparticles of the same type. **a)** Time evolution of the measured frequency shift. In red and dark blue the sections are marked, which contain the dimer (nanoparticle) signal. **b)** Autocorrelation of the frequency shift sections, which are marked in red and dark blue in a). **c)** Time evolution of the frequency splitting of the polarization-split fundamental mode. **d)** Autocorrelation of the frequency splitting sections, which are marked in red and dark blue in c).

Presumably three slopes don't occur in the frequency-split autocorrelation due to the lack of statistics at longer time scales. Thus, the second slope at longer lag times could include the dimer (nanosphere) rotational diffusion as well as its diffusion in transversal direction. In order to investigate this in detail, the autocorrelation of the measured frequency shift is directly compared with the autocorrelation of the frequency splitting for both nanoparticle types (see Fig. 6.9). In the case of the dimer (a), as well as in the case of the nanosphere (b), the frequency-split autocorrelation and the frequency shift autocorrelation, consist of a plateau from about 7 ms to 20 ms (depicted as horizontal lines in black, blue (dimer) and black, orange (nanosphere)). At half value of the second slope, the lag time value of the frequency-split autocorrelation is smaller than that of the frequency shift autocorrelation. This applies for both cases: for the dimer (a) as well as for the nanosphere (b). It is assumed that the slopes shifted to the left due to the frequency-split signal containing the rotational diffusion in addition. As the rotational diffusion ( $\tau_{D,r} = 26.2$  ms) is faster than the transversal diffusion ( $\tau_{D,xy} = 224.4$  ms), a shift of the second slope to the left is conceivable. By comparing the frequency-split autocorrelation of the nanosphere and the dimer, the second slope of the nanosphere is further left than that of the dimer. This is in agreement with the expectation as the dimer causes more friction at rotation.

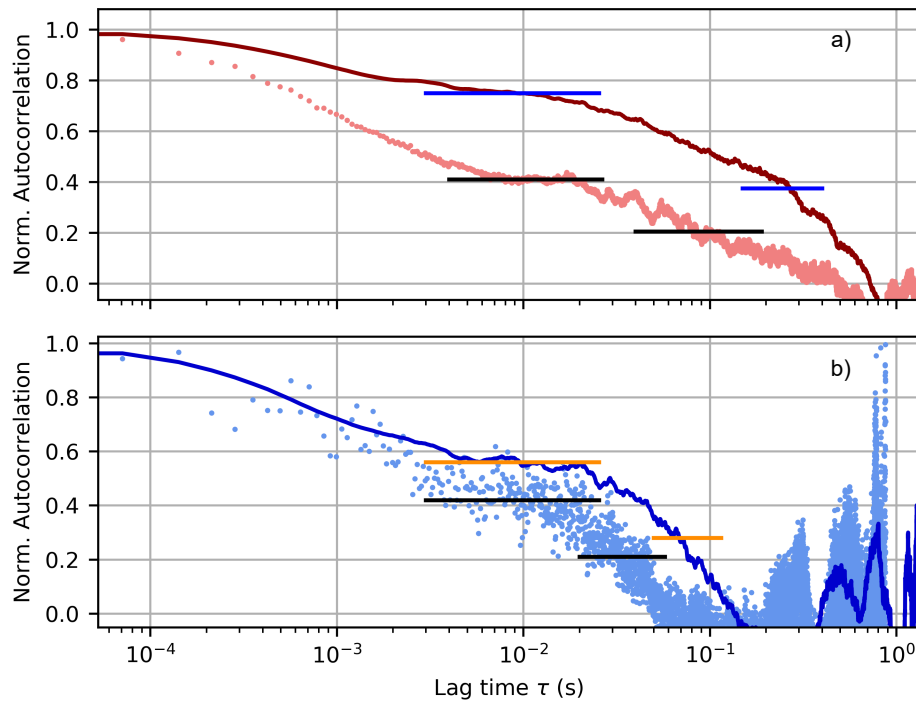


**Figure 6.9.:** Comparison of the frequency-split autocorrelation with the frequency shift autocorrelation for the dimer (a) and the single nanosphere (b)- In both cases the frequency-split autocorrelation was scaled in y-direction with a factor to better compare both autocorrelations. **a)** Dimer autocorrelations of the frequency-split signal (red dots) and the frequency shift signal (brown). The horizontal lines in blue (black) mark the plateau and the value at half of the slope. **b)** Single nanosphere autocorrelations of the frequency-split signal (medium blue dots) and the frequency shift signal (dark blue). The horizontal lines in blue (orange) black mark the plateau and the value at half of the slope.

### 6.3. Discussion

It has been shown that simultaneous measurement of the two polarization-split fundamental modes provides information on the rotational diffusion of anisotropically shaped nanoparticles in water. This detection method is highly sensitive as already nanospheres with a specified roundness of  $> 0.980$  could be detected in their rotational diffusion. However, the frequency-split signal still contains the information about the translational diffusion. So far, the rotational and translational diffusion can't be separated reliably. In addition, lack of statistics made the evaluation difficult. As a consequence, no precise statements could be made about the rotational diffusivity and diffusion time. In case of the dimer, a comparison with the theoretical rotation time could not be made due to the lack of information on the exact shape. Therefore future experiments need to be conducted with known nanoparticle shapes, such as gold nanorods, and with increased statistics. Furthermore the self-induced back-action (SIBA) optical trapping [160] of the nanoparticle in the center of the antinode could significantly reduce the impact of the translational movement on the measurement. Here, the effect of the increased cavity light field intensity on the nanoparticle's rotational movement could be investigated.



## 7. Summary and outlook

An open-access fiber-based Fabry-Pérot (FP) microcavity for the characterization and three-dimensional tracking of label-free single nanoparticles dispersed in liquids has been built up and its functionality evaluated in this work. In order to achieve high passive stability and a controllable laminar flow, a robust cavity setup with different microfluidic channel solutions has been developed. This opened up the possibility to measure the cavity resonance changes of several modes produced by a single nanosphere and thus the measurement of the nanosphere's polarizability, the change of its hydrate shell, the tracking of its three-dimensional Brownian transversal diffusion and the detection of its rotational diffusion at high bandwidth.

### 7.1. Characterization of the cavity

**Microfluidic channel.** Two different microfluidic channels have been demonstrated. Both allow an integration of the fiber-based FP cavity into the channel and an easy exchange of the fibers. The first microfluidic channel consists of a polymer, hydrophobic structure, and the second channel is built by a drilled hole into the glass ferrule [95]. Whereas the first channel has the advantage of a customized shape, the latter is fabricated in 30 times the time and can be fabricated in the own laboratory. Concerning the long-term stability as soon as SiO<sub>2</sub> nanoparticles are passed through the channel, the hydrophobic polymer channel isn't clogged after 5 months whereas the hydrophilic drilled hole is clogged after 1-3 weeks due to higher tendency of the SiO<sub>2</sub> nanoparticles adsorbing at the inner surface of the channel and agglomerating to macroscopic structures. Nevertheless, both kinds of channels enable the detection of hundreds single nanoparticle transit events within a few hours in order to achieve statistical data.

**Cooperativity.** By comparing the cavity filled with air and filled with water, the finesse is decreased in water due to the additional water absorption loss. Therefore, in air, a high finesse of ~ 90000 and in water a lower, but still high finesse of 56710 were achieved. Consequently, the highest cooperativity obtained in water was  $C \sim Q\lambda_0^3/(n_m^3 V_m) = 2.1 \cdot 10^4$ , with a high quality factor of  $Q = 1 \cdot 10^6$ , at the excitation wavelength of  $\lambda_0 = 780$  nm and the mode volume of  $V_m = 10 \mu\text{m}^3$ . [95]

**Passive stability and resolution limit.** In total, three sensing platform generations, cavity A-C, have been developed. As from cavity A to cavity B mainly the microfluidic channel was changed but the rest of the setup almost stayed the same, they consist of a similar mechanical

stability. In contrast, for cavity C, the cavity drifts have been drastically improved from 268 pm to  $\approx 1$  pm due to different kinds of changes: First, the material of the base was changed from aluminum to Macor, reducing thermal expansions of the material. Second, the fiber fixation on the setup mount was improved and finally, a hood over the setup was introduced. These changes also improved the measurement noise by a factor of 2.3. Consequently, a high passive stability of 0.39 pm *rms* and 2.56 pm peak-to-peak noise were achieved. In addition, different cavity geometries were used. Whereas cavity A had a cooperativity of  $C \propto 0.3 \cdot 10^4$ , the highest cooperativity of  $C \propto 2.1 \cdot 10^4$  was achieved with cavity B and similar cooperativities with cavity C. Therefore, due to the improved *rms*-noise in combination with an improved cavity cooperativity, the minimal detectable nanosphere radius could be reduced from  $r_{\text{hydr}} = 18.5$  nm to  $r_{\text{hydr}} = 11.7$  nm for SiO<sub>2</sub> nanospheres dispersed in water. Comparing this resolution limit with different kind of molecules, already the dynamics of single ribosomes, exosomes, DNA origami, and viruses could be detected [64, 68, 77, 161].

## 7.2. Characterization of different quartz glass nanospheres

From several tens to hundreds nanoparticle transit events, the mean polarizabilities of three different SiO<sub>2</sub> nanospheres, sample A-C, have been determined. It was shown that the extended nanosphere size (bare nanosphere + hydrate shell) instead of its intrinsic size (bare nanosphere) was measured. As a result, the mean effective refractive index of the extended nanosphere and the mean thickness and mean refractive index of its hydrate shell was deduced. The thickest hydrate shell of 21 nm was measured for sample C, with a shell refractive index of  $1.38 \pm 0.04$ . In this case, the effective refractive index amounted to  $1.39 \pm 0.03$ , which was smaller than the intrinsic refractive index of  $n_{\text{SiO}_2} = 1.45$ . In Table A.2, the results for each sample are summarized. [95]

In addition, it was shown that an increase of the scanning frequency from 3 kHz to 14.1 kHz allowed the determination of the polarizability of a single nanosphere.

Furthermore, the influence of the salt dulbecco's phosphate buffered saline (DPBS) on the hydrate shell was investigated. Upon repeated alternate pumping of air, pure water, and SiO<sub>2</sub> nanospheres dispersed in  $1.49 \cdot 10^{-4}$  mM DPBS through the microfluidic channel, the hydrate shell of the SiO<sub>2</sub> nanospheres presumably vanished as the polarizability of the bare nanosphere was measured. However, this contradicted the expectation since the nanoparticles were dispersed in pure water in the final step. Therefore, the fully developed hydrate shell was expected. Probably, the repeated pumping of the channel led to an accumulation of salt and thus to an increase of its concentration in the microfluidic channel.

Finally, the autocorrelation of several single nanosphere transit events was investigated both theoretically and experimentally. With mathematical support from Kevin Müller<sup>1</sup> a numerical solution of the autocorrelation of a punctiform nanosphere drifting and diffusing in water and probed by the FP standing-wave light field was derived. In contrast to [97] two characteristic

---

<sup>1</sup> Ph.D. student at the École Polytechnique Fédérale de Lausanne (EPFL).

slopes appeared in the autocorrelation. This double-slope structure was experimentally confirmed. However, the experimental autocorrelation differed from the theoretical one due to the nanosphere's expanded size in the real case. By considering the nanosphere's expansion and simulating the autocorrelation by Monte Carlo three-dimensional tracks, the measured autocorrelation could be brought in coincidence with the simulated one. This confirmed that the transversal motion of the nanosphere was purely diffusive and the effect of the light field on the nanosphere's motion could be neglected.

### 7.3. Three-dimensional tracking of the Brownian motion

The simultaneous scanning over the fundamental mode  $TEM_{00}$  and the two higher-order transverse modes  $TEM_{01}$  and  $TEM_{10}$  allowed the three-dimensional tracking of a single nanosphere's diffusive motion through the FP cavity standing-wave light field. First, this was shown theoretically by Monte Carlo simulations. Different tracking algorithms were evaluated and the best one was chosen, which deviated the least from the original track. Then, via the mean squared displacement (MSD) the diffusivity and hydrodynamic radius of the nanosphere was determined. Second, this established evaluation method was applied to the measured signals. This allowed the tracking of a single  $SiO_2$  nanosphere with a spatial resolution of 8 nm at the largest intensity gradients and with 44 nm mean spatial resolution within the octant's sensing volume for intensities greater than  $I_0/e^2$ . The track was recorded with a time resolution of 0.3 ms, but in principle, also a time resolution of 0.07 ms would be possible without losing mechanical stability (see rotational diffusion signals). From the single nanosphere track, the diffusivity  $D = (2.2 \pm 0.3) \mu m^2/s$  as well as the hydrodynamic radius  $r_{hydr} = (96 \pm 15) nm$  were deduced. A better statistic could be achieved by the evaluation of 5 different single nanosphere tracks. The obtained mean diffusivity of  $\langle D \rangle = (2.8 \pm 0.4) \mu m^2/s$  and mean hydrodynamic radius of  $\langle r_{hydr} \rangle = (76.9 \pm 10.0) nm$  were in excellent agreement with the measured hydrodynamic radius determined by DLS measurements ( $r_{hydr} = (75.3 \pm 9.5) nm$ ) and the diffusivity calculated from it ( $D = (2.85 \pm 0.37) \mu m^2/s$ ). Consequently, via the measurement of the three-dimensional single nanosphere track, the hydrodynamic radius could be determined independently from its refractive index. Together with the evaluation of the polarizability, thus, the nanosphere's effective refractive index can be derived. [95]

### 7.4. Rotational diffusion

The rotational diffusion of a nanosphere (sample B, C), a probable dimer (sample B, C) and a larger agglomerate (sample C) could be investigated by the detection of the polarization-split fundamental modes. Although the nanospheres were specified with a roundness larger than 0.98, even the rotational motion of a single nanosphere could be detected by the frequency splitting with a signal-to-noise (SNR) ratio of 5. As expected, with increasing anisotropic shape the SNR ratio also increased to  $SNR = 10$  in the case of the dimer and to  $SNR = 28$

in the case of the larger agglomerate. From the frequency-split signals, the autocorrelation was calculated in order to get information about the different diffusion times contained in the signal. As the amount of frequency splitting produced by the rotation of the nanoparticle also depends on the light field intensity at its position, three diffusion times and accordingly three slopes were expected in the autocorrelation: one due to the nanoparticle's rotation and two due to its diffusion in longitudinal and transversal direction. Interestingly, in the case of sample C, only the dimer autocorrelation showed a slight increase to smaller delay times. This increase was assigned to the transversal motion of the dimer. Both, the nanosphere as well as the larger agglomerate autocorrelation stayed the same (around zero) in the considered time period. An increase in scanning frequency from 1 kHz to 14.1 kHz allowed the investigation of the diffusion at smaller lag times of a nanosphere and a dimer (both sample B). Instead of the three expected slopes, the autocorrelation of both nanoparticle types only consisted of two slopes. Presumably, due to the lack of statistics, the slope at longer lag times contained the rotational as well as the transversal diffusion.

## 7.5. Outlook

The **resolution limit** of the cavity can be further improved by different approaches. First, the water absorption loss can be reduced by decreasing the wavelength of the probe laser to 630 nm. Within this work, new cavity fibers with attached dielectric mirrors for this wavelength were already prepared. Second, the signal enhancement can be increased by plasmonic nanoparticles. As on the one hand, plasmonic nanoparticles benefit from a tiny mode volume and on the other hand, microcavities consist of a high quality factor, both in combination would improve the signal enhancement. Such hybrid microcavities are already demonstrated for WGM [61, 162, 163, 164] and PhC cavities [165]. Third, the measurement noise can be further decreased. For instance, this would be achieved by establishing several cavities in the very same setup by using multi-core fibers instead of single-core fibers. Then, each cavity would measure the same background noise and this would allow a subtraction of the noise from the detected nanoparticle signal [86]. Alternatively, an active stabilization of the cavity length would improve the measurement noise. Within two supervised student works, a Pound-Drever-Hall lock [166], as well as a phase drift compensation lock, were already established [148, 149]. For this purpose, a second laser with a wavelength of 860 nm was introduced, which was simultaneously resonant with the 780 nm laser. The reflected signal of the 860 nm laser at the fiber-based cavity was used for active stabilization of the cavity length (Pound-Drever-Hall lock). In addition, a Mach-Zehnder interferometer was set up to measure phase changes when the nanoparticle resides in the cavity. Since phase drifts also occurred without nanoparticles, a phase stabilizer was introduced in addition (phase lock). To maintain phase in the fibers, the fiber-based cavity was established with two SM fibers instead of one SM for the incoupling and one MM fiber for the outcoupling. First nanoparticle signals could be measured in an active lock. However, the signal-to-noise ratio was still worse in comparison to the passively measured signals presented in this work. This is due to a very noisy lockbox, which must be replaced in the future by a low-noise device. Also, the SM-SM

fiber alignment has to be improved to obtain similar high cooperativities. This can be achieved by a smaller precision hole diameter of the ferrule.

Furthermore, the **recording of the nanoparticle signal** could be improved by replacing the oscilloscope with a field-programmable gate array (FPGA). This would offer the advantage that the recording of the signal and the evaluation of the resonance amplitude, resonance full width half maximum (FWHM), and resonance position could be performed in parallel and not consecutively. Hence, not only the waiting time during evaluation would be saved, but also the recording time would not be limited by the memory depth of the oscilloscope. Besides, for the evaluation of the resonance, a Lorentzian fit to the resonance could be implemented by using an FPGA for the readout. This would improve the determination of the resonance properties.

Regarding the **effect of salt on the hydrate shell**, the decrease in hydrate shell as a function of salt concentration as well as the SiO<sub>2</sub> nanosphere size could be further investigated. The effect on other nanoparticle materials, especially biomolecules, would also be interesting.

Besides, a further theoretical consideration of the **autocorrelation function** for a non-punctiform nanosphere moving inside a FP standing-wave light field would be valuable. Then, the type of nanosphere movement could be further investigated, independent of the measurement of the three-dimensional track.

Due to symmetry reasons, the **three-dimensional track** of the nanoparticle is folded back into the sensing octant of the antinode. Therefore, in the longitudinal direction, the sensing octant is only  $\lambda_0/(4n_m) = 147$  nm extended. To be able to detect a positional change between different antinodes and thus expand the sensing volume, an additional beat laser with a different frequency than the probe laser could be introduced. Then the new sensing octant would be extended to a half-period of the beating pattern. In addition, the symmetry within an antinode could be repealed by perfectly spherical mirror profiles. Thus, the degeneracy of the higher-order mode families would be broken by the nanoparticle and the phase-sensitive interference measurement of the different transverse modes would contain the full lateral particle position inside an antinode [167].

The **rotational diffusion** of different nanoparticle types inside the FP standing-wave light field is not well understood yet. To analyze the rotation, first, a change of the nanoparticle sample with a known anisotropic shape is recommended. For instance, single gold nanorods with a plasmon resonance far away from 780 nm could be investigated. Second, a measurement at higher bandwidth would improve the resolution of the first plateau in the autocorrelation. This could be achieved by actively stabilizing the cavity length and simultaneously exciting both polarization modes of the fundamental mode with an electro-optic modulator (EOM). In addition, it has to be investigated if the polarization direction of the split modes changes due to the birefringent nanoparticle [139, 140]. A change in rotation can be detected, by introducing a polarizing beamsplitter for the read-out of the signal. Finally, it would be interesting to

which extend different intracavity light intensities and nanorod lengths affect the rotational movement.

In order to expand the sensor's functionalities, an active stabilization of the cavity length would enable the investigation of the **self-induced back-action (SIBA) optical trapping** [160]. This would allow the trapping of nanoparticles or molecules at lower powers than needed for conventional optical tweezers. When the nanoparticle is trapped, its interaction with other nanoparticles or its change over time due to environmental changes could be investigated.

The first step towards the **measuring of biological samples** could be done by the investigation of the unfolding process of DNA origami at different temperatures and different salt concentrations [168, 169]. In addition, drug-loaded nanoparticles and molecules could be examined [170, 171]. Once, the cavity resolution is improved such that even SiO<sub>2</sub> nanospheres with a hydrodynamic radius between 1 nm to 10 nm are detectable, the dynamics of individual unlabeled proteins with a small molecular mass would provide insights into an unknown world of biological processes that occur in living species.

However, before biological samples can be examined, first, the passivation of the microfluidic channel has to be investigated. Whereas SiO<sub>2</sub> nanoparticles tend to agglomerate at hydrophilic surfaces, unspecific protein binding at hydrophobic surfaces is observed for biological samples [150, 151]. Therefore, in this case, another surface passivation has to be investigated. Good advances were achieved by other groups with dichlorodimethylsilane (DDS)-Tween-20 [172] or with bovine serum albumin (BSA) [173]. Probably nanometer-thin layers of polytetrafluoroethylene (PTFE) [174] could be used as an allrounder surface passivator, to prevent the adsorption of both, SiO<sub>2</sub> nanoparticles as well as biomolecules.

Finally, a **surface scanning FP cavity in liquids** would allow the investigation of biological processes e.g. on a cell membrane. In this case, one of the cavity fibers has to be exchanged by a planar mirror that would act as both, the second cavity mirror as well as the sample holder [87, 89, 175].

In conclusion, with the discussed current and future methods, the fiber-based Fabry-Pérot microcavity can be used for future studies of nanoparticles in liquids to learn more of this still largely unknown world. Such detection methods are important because, on the one hand, we can derive a benefit from nanoparticle properties, e.g. in nanomedicine or technological applications. But on the other hand, we can also investigate possible negative effects of nanoparticles on our health and the environment.

## A. Appendix

### A.1. The first fiber-based Fabry-Pérot cavity for sensing in liquids

The first version of the fiber-based FP cavity setup is shown in Fig. A.1. The design was created by Matthias Mader [108] and fulfills the requirement of integrating the cavity into a microfluidic channel. With the setup, the first signal of SiO<sub>2</sub> nanospheres diffusing through the cavity could be recorded with a locked cavity. The setup was first rebuilt with minor changes (see Fig. A.2), however, the fabrication of the setup is complex, time-consuming and a good cavity alignment, and thus a high quality factor, is only attainable through luck. In the following, the problems are discussed in more detail:

The microfluidic channel consists of a channel milled in macor<sup>1</sup>. This channel is sealed by gluing a quartz glass pane on top as a lid. In order to prevent the glue from flowing into the channel, the channel is first filled with polyethylenglycol 2000 (PEG2000) and then the quartz glass plane is glued on top<sup>2</sup>. Afterward, the PEG2000 is melted out of the channel again. Here, the first problem arises: As the PEG2000 consists of a rough surface and it's difficult to fill up the channel evenly, glue also extends into the channel and may cause turbulent flow. In addition, when the PEG2000 is melted out, residues can remain in the channel, which can

<sup>1</sup> The channel has a square cross-section with 200  $\mu\text{m}$  side length. The length of each inlet is 53.7 mm and the outlet has the length 6 mm.

<sup>2</sup> The silica plane is cut by the CO<sub>2</sub> laser setup with single laser pulses. As the bar in the middle has a diameter of only 2.2 mm, the plane breaks easily at its fabrication.

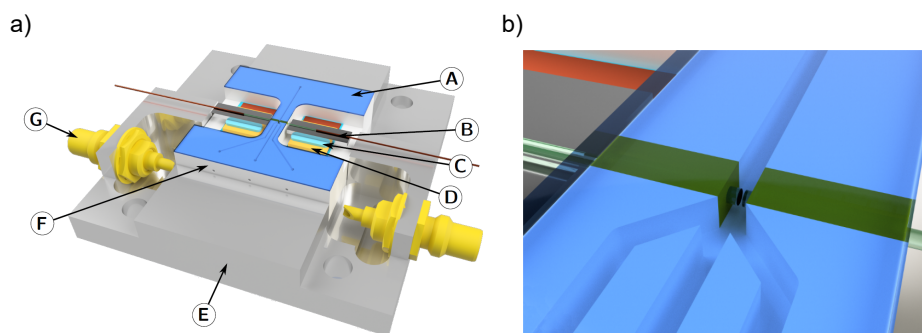


**Figure A.1.:** Overview of the cavity setup design by Matthias Mader. a) The microfluidics consists of a milled macor block (F), which is glued on top of an aluminum pedestal. A quartz glass panel seals the channel (A). The cavity fibers are glued on a v-groove (B), which in turn is glued (C) to piezoelectric actuators (D). Through SMC-connectors (G), the piezos are electrically connected to an external voltage. b) Zoom into the crossing, where the cavity fibers protrude into the microfluidic channel. Taken from [108].

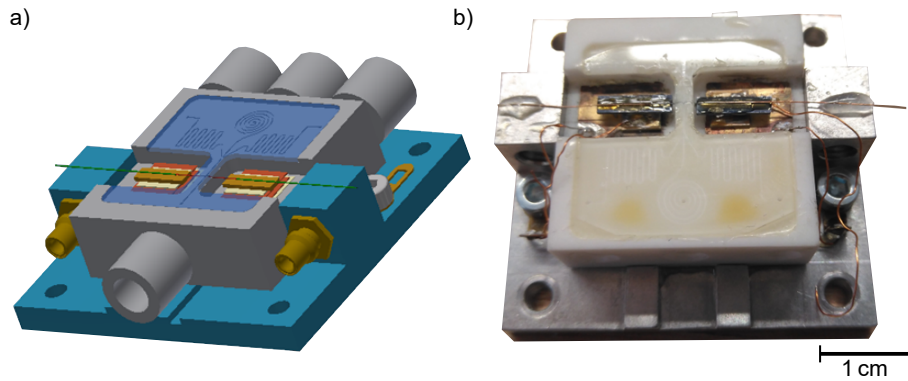


**Figure A.2.:** Own cavity setup inspired by Matthias Mader's design. a) CAD drawing of the setup. The microfluidic channel consists of three inlets and one outlet. b) Photograph of the setup.

contaminate the cavity when the experiments are conducted. The most critical part of the fabrication is the gluing of the fibers into the microfluidic channel. The gluing is in this case required because otherwise, the liquid could leave the microfluidic channel through the fiber openings and thus reach the electronics. However, gluing the fibers into the channel has the following disadvantages: First, although the glue cures under UV light<sup>3</sup>, it can happen very quickly that the glue gets onto the mirror end facets. This means that the whole setup has to be taken apart again and started from scratch. Second, the glue shrinks when it dries, causing a change in the cavity alignment. This generally deteriorates the cavity finesse without being able to control it. The glue's stiffness also reduces the scanning range of the piezos, which means that in the worst case, less than one FSR can be scanned. Lastly, when the fiber mirrors get dirty at the experiments, the fibers can't be taken out for cleaning in an ultrasonic bath or the mirrors also can't be exchanged. Instead, the whole setup has to be rebuilt.

Because of these problems, a new, simplified, controllable setup was developed and refined (see Chapter 3).

## A.2. Construction of the core sensor

This chapter deals with additional information about the different cavity setup versions. In Appendix A.2.1 the protection system for the electronics on the sensing platform is presented. This is necessary because water can leak out at the precision hole openings and is located there in the vicinity of the electronics of the piezoelectric actuators.

### A.2.1. Protection of electronics from getting wet

The fibers are inserted into the ferrule's precision hole without sealing the openings. Since untreated quartz glass consists of a hydrophilic surface, the water, which is pumped through

<sup>3</sup> EPO-TEK 113-91-5

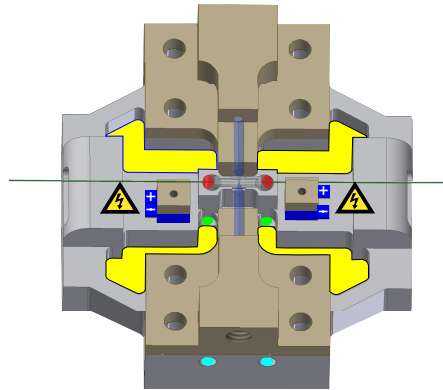


**Figure A.3.:** Details of the sensor mount of cavity C. To prevent the liquid from reaching the piezoelectric actuators, the sensor mount consists of a drainage system. The liquid leaking out of the ferrule's precision hole (red) is lead through a hole inside the Macor base (from red to green) and is collected in a catch basin (yellow). If the liquid level exceeds a certain height, it finally leaves the Macor base through two outlets (turquoise).

the microfluidic channel, can leave the ferrule through the precision hole by capillary forces (see Fig. A.3, red). Directly next to the ferrule precision hole openings, piezoelectric actuators (blue) are located, which are operated at high voltages. In order to prevent the electronics from getting wet, the aluminum bases (cavity A, cavity B), as well as the Macor base (cavity C), consist of a drain at the ferrule precision hole openings. In case of cavity B and cavity C, the drain leads to a catchment basin (Fig. A.3, green and yellow). Before the liquid level can exceed the piezoelectric actuator's pedestal, the liquid expires the Macor base at the outlet (only implemented in cavity C, Fig. A.3 turquoise).

A hydrophobization of the microfluidic channel and of the ferrule's precision hole (see Appendix A.8) could also prevents water from leaking out at the fiber precision hole openings. For this purpose, the polymer microfluidic channel (cavity C) was silanized and different pressure experiments conducted. As the Polymer microfluidic channel was directly silanized at its fabrication, at first, a non-silanized quartz glass ferrule was investigated. When a water bubble at the end of a syringe tip was held to the opening of the drilled hole, the typical capillary column was observed, which allowed the water to escape through all openings (microfluidic channel as well as precision hole) without any applied pressure. In the next step, the same approach was performed for the hydrophobic polymer microfluidic channel (see Fig. A.7a). The water did not flow through the channel nor through the precision hole, but came out on the same side. A microfluidic connector was then glued to one side of the polymer microfluidic channel (Fig. A.7b) and the water was pumped through, by applying a pressure of 0.5 bar to the pressure vessel (see Fig. A.5). Besides, glass fibers were inserted into the precision hole from both sides. In this case, the water flowed through the microfluidic channel and the opening on the other side. The capillary column also increased in length in the precision hole, but the water did not leak out at the precision hole openings. Finally, a connector was glued to the other side of the polymer microfluidic channel as well (see A.7c). As the length of the microfluidic channel increased, the water leaked out at the other side of the microfluidic channel, but also at the precision hole openings, when a pressure of 0.5 bar was applied. Experiments at lower pressures were not carried out. However it is assumed

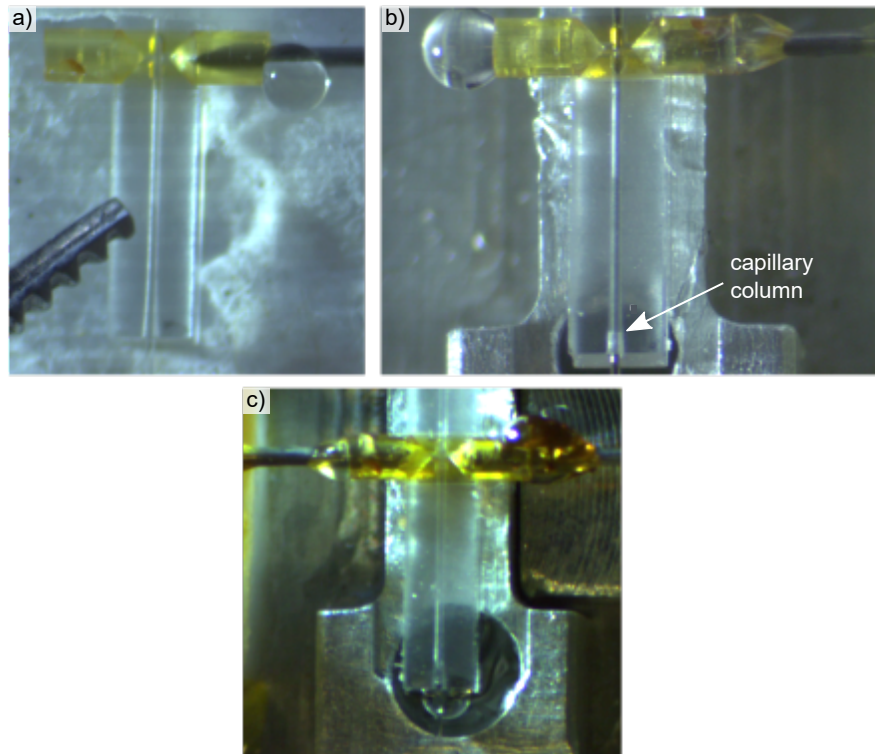


**Figure A.4.:** Water pressure experiments on the hydrophobized polymer microfluidic channel. a) The hydrophobic surface prevents the water from flowing through the channel. b) Gluing a connector into the inlet of the microfluidic channel and pumping water through under pressure forces the water flowing through the channel. The water leaves the channel on the other side, but it doesn't leak out at the precision hole openings, although the length of the capillary column increases. c) The outlet of the microfluidic is connected as well. Due to the increased length of the microfluidic channel, the water also leaks out at the precision hole openings.

that a significantly lower pressure in combination with a smaller precision hole diameter (the latter would also improve the SM-SM fiber alignment, which is necessary for active lock measurements) would prevent the water from leaking out at the precision hole openings.

### A.2.2. Construction of the different cavity versions

The main parts of the core sensor and the different sensing platforms cavity A (Fig. 3.9), cavity B (Fig. 3.10) and cavity C (Fig. 3.11) are already presented in Chapter 3. Here, the detailed fabrication steps as well as the used materials are described.

For all setup versions, the same quartz glass ferrule<sup>4</sup> is used. It is glued on the aluminum (cavity A, B) or the Macor base (C; see Fig. 3.11) with a 2-component epoxy glue<sup>5</sup>. To enable

<sup>4</sup> OZ Optics, FER 1.225-1.225-131, material: quartz glass

<sup>5</sup> UHU plus schnellfest 2-Komponenten-Kleber

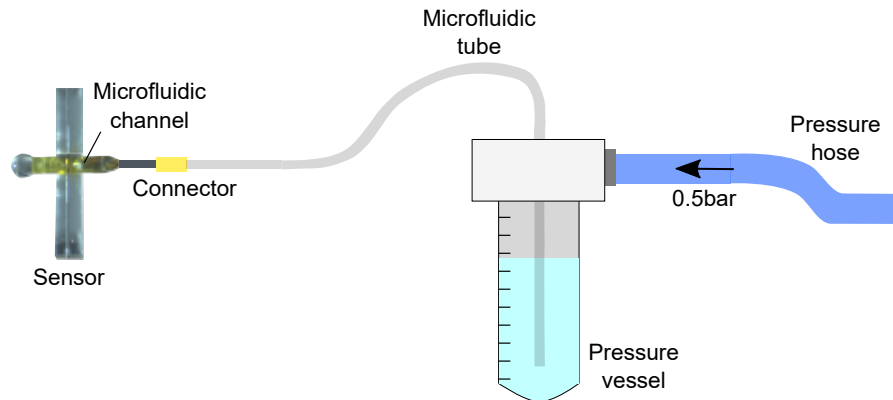


**Figure A.5.:** Microfluidic pump. The microfluidic channel is flushed with a liquid by applying pressure on a vessel. This forces the liquid to flow through the microfluidic tube into the microfluidic channel.

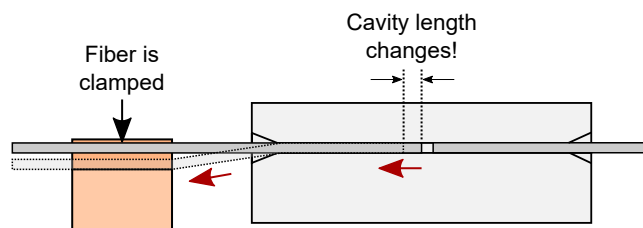


**Figure A.6.:** Sketch of the fiber clamp at lower height than the ferrule's precision hole. When the fiber is clamped down (black arrow) it is pulled back (red arrows) and therefore the cavity length increases.

a modulation of the cavity length, two Piezos are glued on the base with the same epoxy glue. Before the fiber clamps<sup>6</sup> are glued on top, the height between the fiber clamp and the ferrule precision hole has to be adapted. This is necessary because if the clamp was lower than the precision hole of the ferrule, the fiber would be pulled back when it was clamped (see Fig. A.6). This would increase the cavity length by several micrometers and therefore short resonator lengths would not be achievable. Long resonator lengths, on the other hand, lead to greater water absorption losses and consequently to lower signal enhancements (cooperativities) of the fiber-based FP cavity. The height of the clamp can be increased by cluing thin metal sheets on the piezoelectric actuator as a spacer or if the clamp is too high, the thickness of the clamp can be reduced by grinding its bottom side with sandpaper.

**Polymer channel (Cavity A).** The microfluidic channel of cavity A consists of a 3D polymer structure. It was designed and fabricated together with Christian Kern, a former Ph.D. student in the Martin Wegener research group at the Applied Physical Institute at the Karlsruhe Institute of Technology. In the following, the fabrication steps for the microfluidic channel are explained in detail.

At first, a v-shaped notch is cut into the glass ferrule (see Fig. 3.5). This is done with a wafer

<sup>6</sup> Material: PEEK.

$y$ -position ( $\mu\text{m}$ )	Sawing depth (mm)
0	250
$\pm 32.5$	225
$\pm 65.0$	201
$\pm 97.5$	176
$\pm 130.0$	151
$\pm 162.5$	127
$\pm 195.0$	102
$\pm 227.5$	78
$\pm 260.0$	53
$\pm 292.5$	28
$\pm 325.0$	4

**Table A.1.:** Parameters for the sawing of the v-shaped notch into the ferrule. At the middle ( $y = 0$ ) the sawing depth is greatest and decreases towards the outside symmetrically in  $\pm y$ -direction.

saw<sup>7</sup> and was carried out by Lucas Radtke, a technician at the Center for Functional Nanostructures at the KIT. The wafer saw has a saw blade width of about  $220 \mu\text{m}$ <sup>8</sup>, the spindle speed is set to 25000 rpm and the feed is set to 2 mm/s. To prevent the ferrule from moving around during the sawing process, the ferrule is fixed on an adhesive film<sup>9</sup> and it is additionally fixed with adhesive tape. In order to cut a v-shaped notch, different sawing depths are cut into the glass at different  $y$ -positions (see Fig. 3.5 for the definition of the  $y$ -position and Table A.1 for the sawing depths). In Fig. 3.5 b) a micrograph of the cut v-shaped notch is shown.

In the second step, the 3D-polymer structure is written into the notch. For this purpose, a CAD design of the wanted structure is necessary (see Fig. 3.6). It consists of an outer hole, with a diameter of 0.38 mm, which narrows to 0.2 mm at the center. At the center is a crossing with a slightly thicker hole of 0.21 mm in diameter for the cavity fibers. The designed hole of 0.21 mm is  $79 \mu\text{m}$  thicker than the precision hole of the ferrule. This is necessary since the fabricated hole diameter deviates from the designed hole, and also the center of the written hole can be slightly misaligned from the center of the precision hole. The writing of the 3D polymer structure was carried out by Christian Kern. Therefore, its verbatim description of the fabrication process is taken from [95]: "[...] we fabricate the microfluidic channel using a commercial direct laser writing setup (Photonic Professional GT, Nanoscribe GmbH) with a  $25\times$  NA 0.8 objective lens (LCI Plan-Neofluar Imm Corr DIC M27, Carl Zeiss Microscopy GmbH) and the liquid negative-tone photoresist IP-S (Nanoscribe GmbH). The total writing time is about 3.5 h. Due to the large dimensions of the polymer structure, several measures have to be taken: First, we use a galvanometer mirror scanning system to increase the writing speed. Second, we use the so-called dip-in configuration, which means that the objective lens is immersed in the liquid photoresist itself, thereby removing the constraint on the height of the structure imposed by the working distance of the objective lens. Third, instead of

<sup>7</sup> DISCO DAD3350

<sup>8</sup> Minitron elektronik GmbH Microkerf 2.187-8-45H

<sup>9</sup> UHP 0805M6 E2

polymerizing the whole structure during the actual writing process, we only polymerize an outer shell as well as an internal support scaffold. Following the development of the structure in mrDev 600 (micro resist technology GmbH), the liquid photoresist inside of the structure is cured using a UV flood-exposure. In the third and last step, in order to ensure that the system is watertight, we apply a hydrophobic coating in a two-step process: First, the structure is conformally coated with a  $\text{Al}_2\text{O}_3$  layer with a thickness of several ten nanometers using atomic-layer deposition. Second, following a brief air-plasma treatment, the structure is immersed in a 3 mM solution of octadecyltrichlorosilane (CAS 112-04-9) in toluene."

In the last step, external microfluidic tubes are connected to the microfluidic channel. First, syringe needles<sup>10</sup> with a diameter of 0.3 mm are shortened with a dremel and then glued into the 0.38 mm holes of the 3D-polymer structure with a UV-curing adhesive<sup>11</sup>. The rapid hardening of the adhesive under UV light is necessary, otherwise, there is a risk of the adhesive clogging the microfluidic channel. To avoid stresses on the 3D-polymer structure, the syringe needle is glued on the aluminum base with a 2-component epoxy adhesive<sup>12</sup>. Here, shims are used to adjust the height of the aluminum base. The microfluidic connection to the needle consists of the connector of an infusion extension line<sup>13</sup>, which are used as standard in the medical sector and a microfluidic tube<sup>14</sup> with an inner diameter of 100  $\mu\text{m}$ . The connection at the end of the extension line is cut off and the microfluidic tube is glued<sup>15</sup> into the resulting hole. The finished microfluidic connection is shown in Fig. 3.9.

**Quartz glass channel (cavity B, cavity C).** To the drilled hole, commercially available microfluidic tubes<sup>16</sup> are directly attached (see Fig. 3.10). First, the tube ends are conically sharpened with a razor blade so that the tip diameter is smaller than the outer diameter of the drilled hole and then the tubes are glued into the hole with a UV-curing silicone adhesive<sup>17</sup>. The silicon adhesive is used instead of the epoxy adhesive<sup>18</sup> because it is more elastic and provides a long-lasting seal. In case of cavity B, the long microfluidic tube is glued on the aluminum base with an epoxy glue<sup>19</sup> in order to reduce stress on the drilled hole. Shims are used to adjust the height between tube and aluminum base. On the other hand, the short microfluidic tubes of cavity C are glued on and into the microfluidic adapters with the silicone adhesive.

If the microfluidic cell gets clogged by solid, insoluble nanoparticles (see Chapter 3.1.2), the fibers as well as the microfluidic tubes have to be removed in order to mechanically clean the channel. In case of cavity C the following was tried once: The microfluidic adapters were

<sup>10</sup> Sterican Insulinkanüle gelb 30G

<sup>11</sup> Epo-Tek OG116-31

<sup>12</sup> UHU plus schnellfest 2-Komponenten-Kleber

<sup>13</sup> Braun 1 ProSet Verlängerungsleitung 0,5x2,35x300 mm PUR

<sup>14</sup> Upchurch 1561L PEEK tubing black; outer diameter: 1/16", inner diameter: 0.004".

<sup>15</sup> Epo-Tek OG116-31

<sup>16</sup> Upchurch 1561L PEEK tubing black; outer diameter: 1/16", inner diameter: 0.004".

<sup>17</sup> LOCTITE SI 5091

<sup>18</sup> Epo-Tek OG116-31

<sup>19</sup> UHU plus schnellfest 2-Komponenten-Kleber

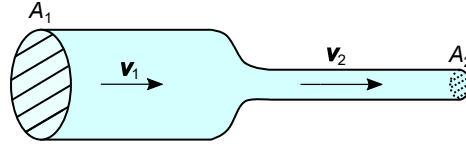


**Figure A.7.:** Schematic for the continuity law of incompressible fluids.

pulled simultaneously in opposite directions. This lead to an even breaking of the silicone adhesive and next time, they could be carefully pressed on the ferrule again without gluing.

### A.3. Pressure inside the microfluidic channel

Of the two different microfluidic designs, only the polymer microfluidic channel is silanized in order to prevent the water from leaking out through the precision hole. To estimate the pressure inside the microfluidic channel at which the channel remains water tight, two different physical laws are important [176]: The first one is the law of continuity for incompressible fluids. Fig. A.7 shows a sketch for a fluid flowing in a pipe with a cross-section  $A_1$  decreasing to a smaller cross-section  $A_2$ . The corresponding flow velocities through cross-section  $A_1$ ,  $\vec{v}_1$  and through cross-section  $A_2$ ,  $\vec{v}_2$  relate to each other as follows

$$|\vec{v}_2| = \frac{A_1}{A_2} |\vec{v}_1| \quad . \quad (\text{A.1})$$

In a microfluidic channel, the fluid flow is laminar. If the channel has a fixed radius of  $r$  and a length  $l$ , the volume flow can be calculated by Hagen-Poiseuille:

$$\frac{dV}{dt} = \frac{\pi r^4 \Delta p}{8 \eta l} \quad , \quad (\text{A.2})$$

whereas  $\eta$  is the dynamical viscosity and  $\Delta p$  is the pressure difference between the inlet and outlet. With the volume  $V = A \cdot l = \pi r^2 l$ , the volume flow can be transformed to

$$\frac{dV}{dt} = \frac{dA}{dt} l + \frac{dl}{dt} A = v \cdot \pi r^2 \quad (\text{A.3})$$

and with Eq. (A.2) the pressure difference can be expressed as

$$\Delta p = \frac{8 \eta l v}{r^2} \quad . \quad (\text{A.4})$$

By neglecting the outlet through the precision hole, the microfluidic system consist of the microfluidic tube (MT, inner radius  $r_{\text{MT}} = 0.1$  mm), the syringe needle (SN, inner radius  $r_{\text{SN}} = 1.4$  mm), the polymer microfluidic channel (PC), the syringe needle and the microfluidic tube (see Fig. A.8). At the outlet (0), the atmosphere pressure of  $p_0 \approx 1$  bar is assumed. Via Eq. A.4, the pressure at the intersection 1 can be calculated by

$$p_1 = \frac{8 \eta l_{\text{MT}} v_{10}}{r_{\text{MT}}^2} + p_0 \quad . \quad (\text{A.5})$$

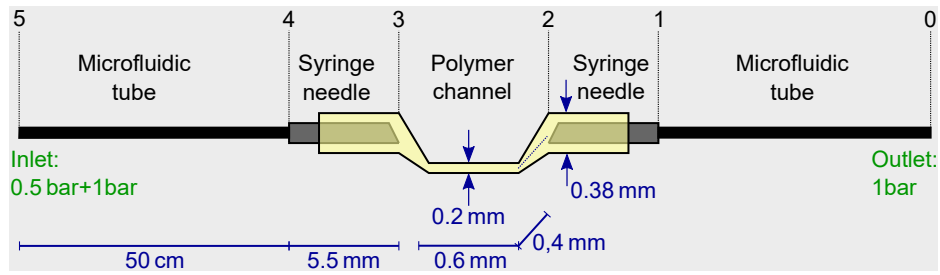


**Figure A.8.:** Sketch of the microfluidic system.

At intersection 1, the tube cross-section is changing from  $A_{MT} = \pi r_{MT}^2$  to  $A_{SN} = \pi r_{SN}^2$ . Here, the new velocity  $v_{21}$  is derived by Eq. (A.1):

$$v_{21} = \frac{r_{MT}^2}{r_{SN}^2} v_{10} \quad . \quad (A.6)$$

By repeating step (A.5) and step (A.6) for the other intersections 2-5, the pressure difference inside the polymer channel  $\Delta p_{32}$  as well as the fluid velocity  $v_{32}$  can be estimated. If the inlet pressure of 1.5 bar =  $1.5 \cdot 10^5$  Pa is applied, the pressure is  $\Delta p_{32} \approx 0.01 \dots 0.14$  Pa and the fluid velocity is  $v_{32} \approx 0.12 \dots 0.24$  mm/s.

For the estimation of the pressure difference and velocity, any height differences and friction at the internal surfaces were neglected.

#### A.4. CAD design for the electric current and temperature control of the laser

As a second probe laser, a wavelength-stabilized laser diode is used, which is already fiber coupled<sup>20</sup>. In order to establish a current and temperature control, a housing was CAD designed and fabricated by the mechanical workshop (see Fig. A.9). The laser diode (yellow) is clamped into a copper laser head mount and is fixed on a copper adapter. Copper is used to provide a good heat conduction. Under the copper adapter is a Peltier element clamped with its warm side facing upwards. Simultaneously, the Peltier element serves as a spacer between the copper adapter and the aluminum base, which is cooled by the Peltier element. The Peltier element is connected to a D-sub 9 connector (male) by electronic cables. Besides, the laser diode is electronically connected by an adapter mounted on an electronic board<sup>21</sup> and the electronic board itself is connected to a D-sub 9 connector (female) by electronic cables. All electronic cables are lead through the passage and are hidden under the cover. In order to thermally encapsulate the laser diode from the environment, an aluminum hood is imposed on the laser head mount. A passage through the hood provides an outlet for the fiber (laser output).

<sup>20</sup> Thorlabs LP785-SAV50

<sup>21</sup> Fabricated by Jannis Ret from the electronic workshop at the Physical Institute, KIT.

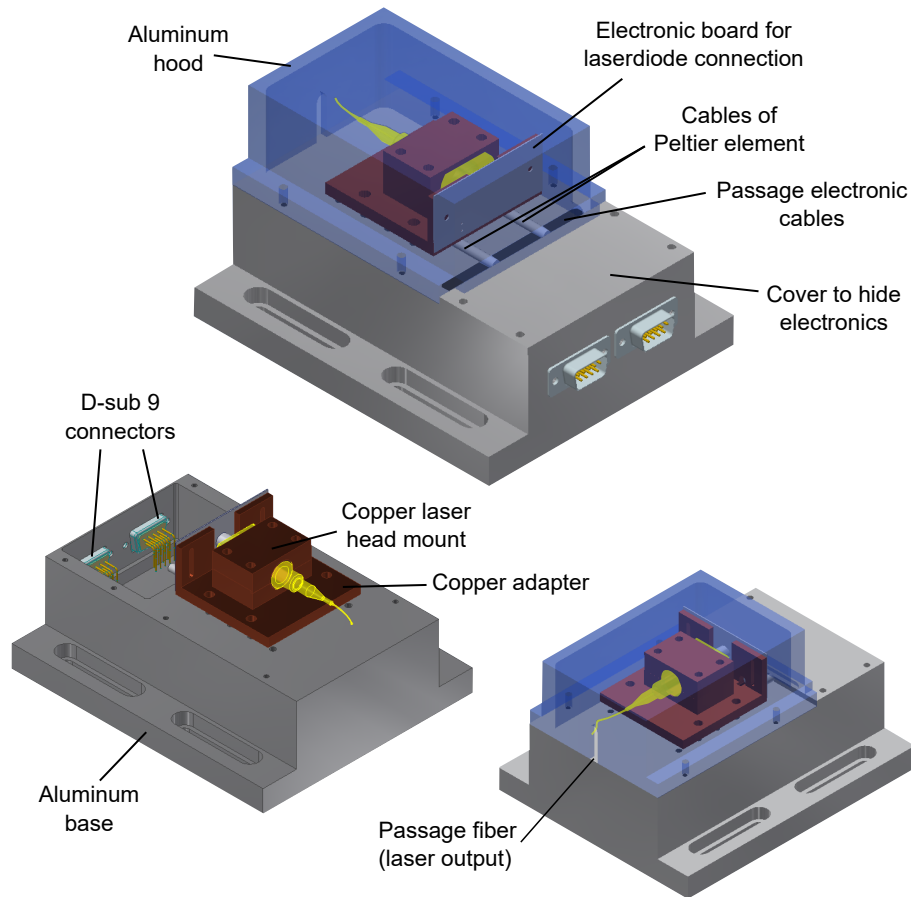


**Figure A.9.:** Laser head housing designed with Autodesk Inventor CAD software. The housing provides an aluminum hood for thermal encapsulation of the laser head to the environment and an electronic connection of the laser diode (electronic board, D-sub 9 connector). In addition, a Peltier element can be operated for an active temperature stabilization of the laser.

Both, the Laser diode and the Peltier element can be connected to an electric current controller and a temperature controller. In the conducted experiments, the laser was not temperature stabilized because the proportional integral derivative (PID) control loop settings of the temperature controller would have to be adapted to the new thermal mass. However, in the long term, the same temperature controller was used for another laser with a different thermal mass and therefore the PID settings have not been adjusted. However, for the conducted three-dimensional tracking events, the laser was stable enough. For the operation of the laser diode, a current controller from Toptica<sup>22</sup> was used. When connecting and operating the laser diode for the first time, several things must be considered: First, when touching the laser head, the person must be grounded to prevent damage to the laser diode. Second, the laser diode ground, cathode, and anode have to be connected to the correct inputs of the current controller. Consequently, custom-made cable connectors have to be soldered for the correct

<sup>22</sup> Toptica, DCC 110

assignment. Finally, the maximal current and maximal voltage for the laser diode must be set in the current controller. When the laser diode is operated the first time, a low current is advisable, which is slowly increased, until the lasing regime is achieved.

## A.5. Quartz glass nanoparticle samples

Within this work, three different quartz glass nanosphere samples were investigated. They are denoted as sample A, sample B, and sample C. In Table A.2 the different properties are summarized. The black numbers are given by the companies, the gray numbers were measured with commercial measurement techniques and the blue numbers were measured with the FP sensor. In the following, the sample properties are investigated in more detail.

### A.5.1. Sample A

The SiO<sub>2</sub> nanospheres are provided by the company microParticles GmbH<sup>23</sup>. The general specifications of the SiO<sub>2</sub> nanospheres given by the company are summarized in Fig. A.10. Especially for the acquired nanosphere diameter distribution, the following properties are specified: They have a mean diameter of 143 nm, a standard deviation of 0.004 nm and a 5% solids content in an aqueous solution. The following additional information could be received via email contact: The SiO<sub>2</sub> nanospheres are fabricated by a sol-gel process (hydrolysis/condensation reaction according to Stöber).

	Sample A	Sample B	Sample C
$r_{\text{geom}}$ (nm)	63.2 ± 1.7	60.0 ± 1.8	25.0 ± 0.8
$r_{\text{hydr}}$ (nm)	71.5 ± 2.0	75.3 ± 9.5	46 ± 30
$n_{\text{eff}}$	1.41 ± 0.01	1.420 ± 0.005	1.39 ± 0.03
$n_{\text{SiO}_2}$	1.42	1.45	1.45
$n_{\text{h}}$	1.40 ± 0.02	1.39 ± 0.04	1.38 ± 0.04

**Table A.2.:** Quartz glass nanospheres investigated in this work. The different parameters are the geometric radius  $r_{\text{geom}}$ , the hydrodynamic radius  $r_{\text{hydr}}$ , the effective refractive index  $n_{\text{eff}}$ , the intrinsic refractive index  $n_{\text{SiO}_2}$  and the refractive index of the hydrate shell  $n_{\text{h}}$ .

**Refractive index of the bare nanosphere.** The intrinsic refractive index of  $n_{\text{SiO}_2} = 1.42$  was measured by customers by increasing the transmission intensity through the solution for different solvent mixture ratios. More details about this method can be found in [177].

<sup>23</sup> microParticles GmbH, SiO<sub>2</sub>-F-0.15

Properties	Silica-Particles
Density	1.85 g/cm <sup>3</sup>
Refractive index	1.42
Particle diameter	100 nm – 25 μm
Monodispersity	CV < 5%
Particle shape	spherical
Surface charge	anionic
Functional groups	silanol
Hydrophilicity/Hydrophobicity	hydrophilic
Crosslinking	crosslinked
Porosity	non-porous
Temperature stability	to 1000 °C
Mechanical strength	robust
Solubility in acids and bases	soluble in HF and bases
Stability in solvents without swelling	water, alcohols, all solvents and oils
Biocompatibility	biocompatible

**Figure A.10.:** General properties of the SiO<sub>2</sub> nanospheres provided by the microParticles GmbH company. Screenshot taken from the official website [178].

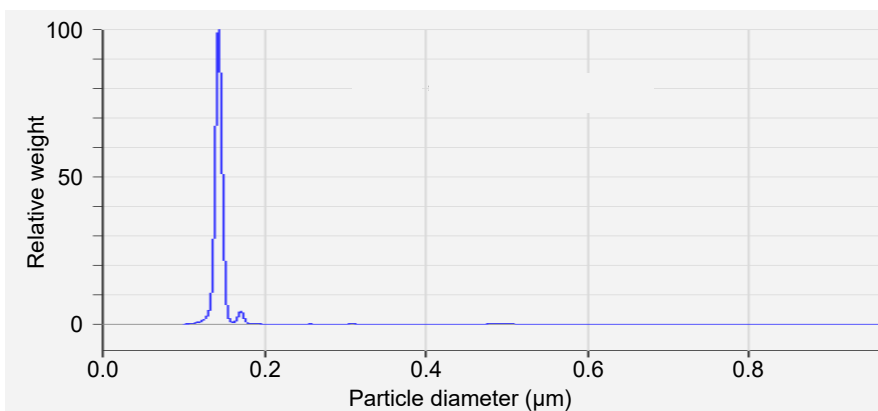


**Figure A.11.:** Nanosphere size distribution measured by differential sedimentation. This Plot was provided by the company and is from another batch than used in this work.

**Hydrodynamic size.** The diameter distribution of the SiO<sub>2</sub> particles was determined by the company via differential sedimentation (cps disc centrifuge) in aqueous suspension. Therefore, the hydrodynamic size distribution is measured instead of the intrinsic size. In Fig. A.11 the diameter distribution for another batch but the same nanosphere size is shown.

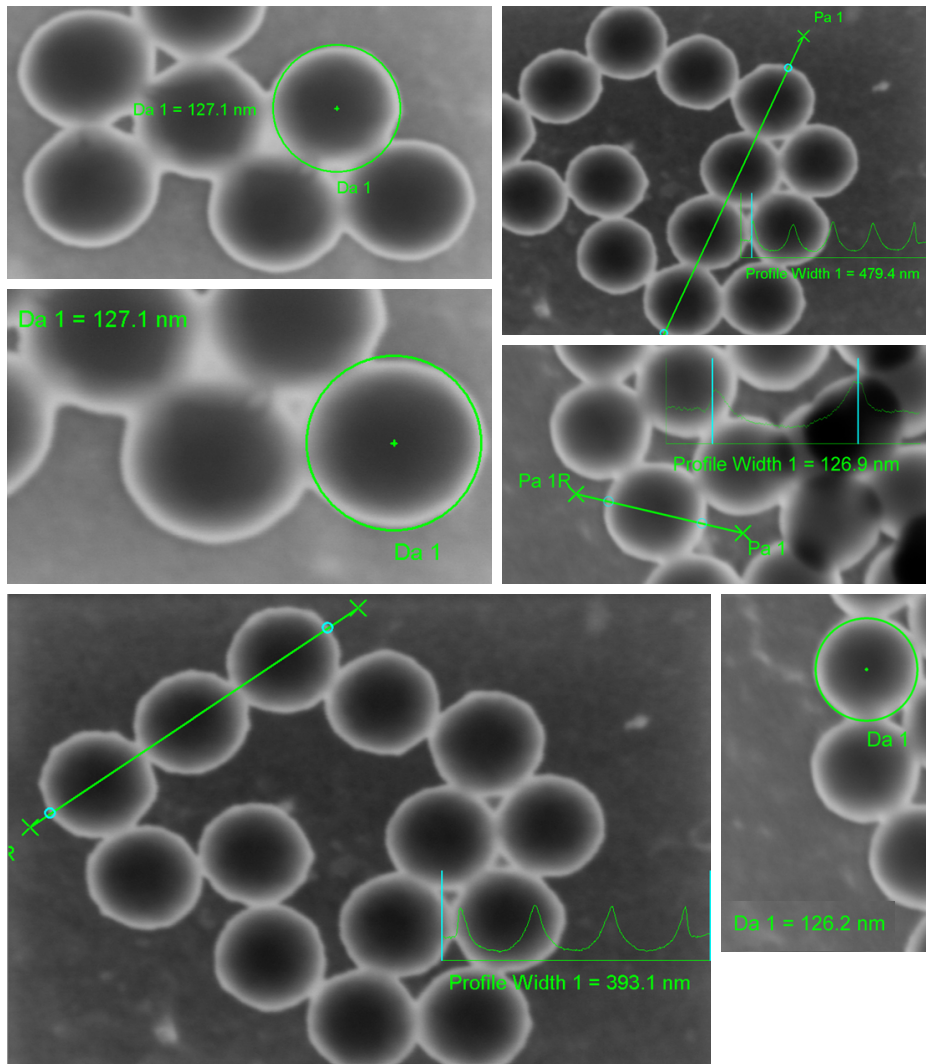


**Figure A.12.:** SEM pictures of sample A. The SiO<sub>2</sub> nanospheres have a mean intrinsic radius of  $r_{\text{geom}} = 63.2$  nm and a standard distribution of  $\sigma_r = 1.7$  nm. [95], see supplementary information

**Intrinsic size.** In order to determine the intrinsic size distribution of the nanospheres, scattering electron micrographs were taken from the nanospheres. This measurement was done by Patrice Brenner from the CFN nanostructure service lab at the Karlsruhe institute of technology (KIT) and the results are shown in Fig. A.12. From the different measured sizes a mean intrinsic radius of  $r_{\text{geom}} = 63.2$  nm and a standard distribution of  $\sigma_r = 1.7$  nm could be obtained.

**Effective refractive index and refractive index of the hydration shell.** The determination of the effective refractive index and the refractive index of the hydration shell is described in Chapter 4.2.

### A.5.2. Sample B

This kind of quartz glass nanospheres is provided by the company ALPHA Nanotech<sup>24</sup>. Since the company determines the size distribution by transmission electron micrographs (see Fig. A.13), the given size distribution accounts for the intrinsic size of the bare SiO<sub>2</sub> nanosphere. They specify the nanospheres with a mean diameter if  $D_{\text{geom}} = 120$  nm and a variation coefficient of  $cv < 3\%$ . The nanospheres are diffracted in Milli-Q water and are non-functionalized.

**Hydrodynamic radius.** In order to measure the hydrodynamic size of the nanospheres, DLS measurements were carried out by Mark Rutschmann from the Institute of Inorganic Chemistry at the Karlsruhe Institute of Technology (KIT). The measurement result is shown in Fig. A.14 and yield a hydrodynamic radius of  $r_{\text{hydr}} = 75.3$  nm and a standard deviation of  $\sigma_r = (\sqrt{PDI} \cdot D_{\text{hydr}})/2 = 9.5$  nm.

**Refractive index of the bare nanosphere.** Via email contact the following additional information about the intrinsic refractive index of the nanospheres could be received: "We haven't measured the refractive index [...], however, we expect the value is very close to the refractive index of silica surfaces, as there is no impurity added into the silica nanospheres, the silica nanospheres should have the same physical parameters as silica materials." (21.08.2019, contact: Edward from ALPHA Nanotech Team). Concerning the agglomeration of glass beads, the following information was given: "We did a number of tests for different sizes (SiO<sub>2</sub> 50 nm, SiO<sub>2</sub> 500 nm, and SiO<sub>2</sub> 1000 nm) and different materials (PS 100 nm, PS 500 nm, and PS 1000 nm) and found that silica nanospheres are NOT easy to get aggregated if prolonged ultrasonication/vortexing is applied. On the other hand, for polymeric materials like polystyrene or poly(methyl methacrylate), the re-suspended nano-/microspheres cannot be back to the originally suspended state, regardless of the length and power of ultrasonication/vortexing. This indicates the aggregation of silica nanospheres is reversible while the aggregation of polymeric nanospheres is not. Silica nanospheres can be considered as miniaturized glass beads and they are much more "robust than what we thought they would be. So, ultrasonication/vortexing at 40 to 80 kHz for 10 to 15 minutes is sufficient for colloidal silica nanospheres to reach a completely colloidal state. If the silica nanospheres ever undergo temperature shocks or come to the partially or completely powdered state, ultrasonication/vortexing at 100 kHz for 30 mins in the new solvent (while controlling the temperature no higher than 35 Celcius degrees) is sufficient for reversing any aggregations. If you wish to add surfactants (although not necessary based on our experience), we would say always start by a tiny amount and see how it would respond to the colloidal silica." (21.08.2019, contact: Edward from ALPHA Nanotech Team)

**Effective refractive index.** The determination of the effective refractive index via the frequency shift histogram is described in Chapter 4.2. Due to a later quantitative measurement with another cavity geometry (CG4, Table 3.6), the correlation between the decrease of

---

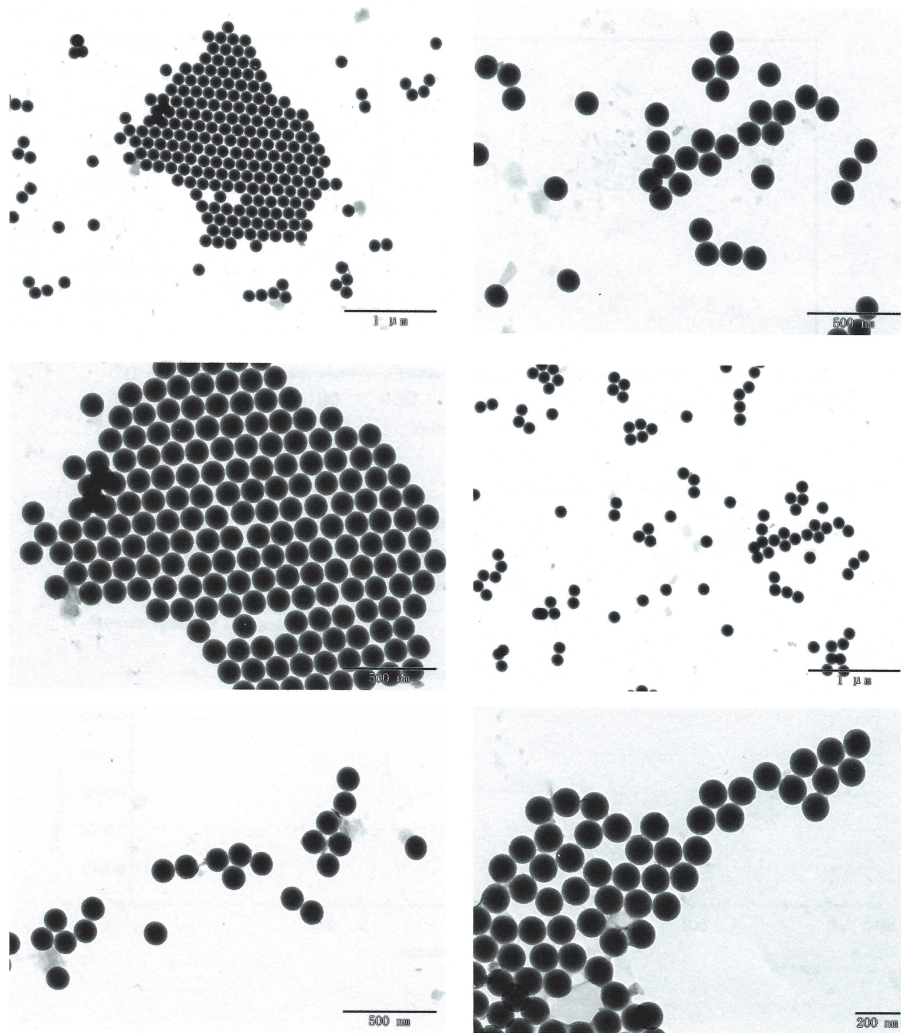
<sup>24</sup> ALPHA Nanotech, non-functionalized colloidal quartz glass nanospheres, size: 120 nm.



Aug 20, 2019

**Non-Functionalized Colloidal Silica Nanospheres (120 nm)**

**Transmission electron micrographs:**



Page 6 of 11

**Figure A.13.:** Transmission electron micrograph of sample B provided by ALPHA Nanotech.

Results

	Size (d.n...	% Intensity:	St Dev (d.n...
Z-Average (d.nm): 150,6	Peak 1: 156,7	100,0	34,22
PdI: 0,016	Peak 2: 0,000	0,0	0,000
Intercept: 0,963	Peak 3: 0,000	0,0	0,000

Result quality Good

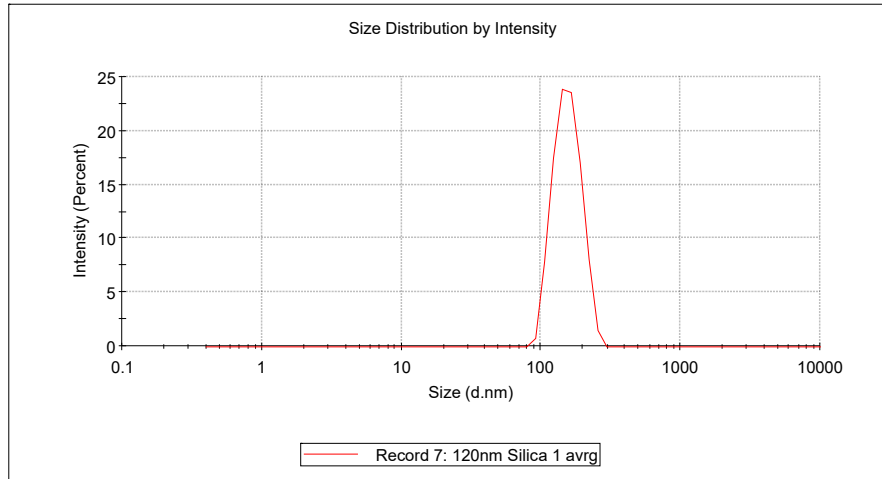


**Figure A.14.:** a) Dynamic light scattering (DLS) measurement of the SiO<sub>2</sub> nanospheres with an intrinsic diameter of  $D_{\text{geom}} = 120$  nm. The nanospheres have an expanded averaged diameter of  $D_{\text{hydr}} = 150.6$  nm when they are dispersed in water and the polydispersity index is  $PDI = 0.016$  nm.

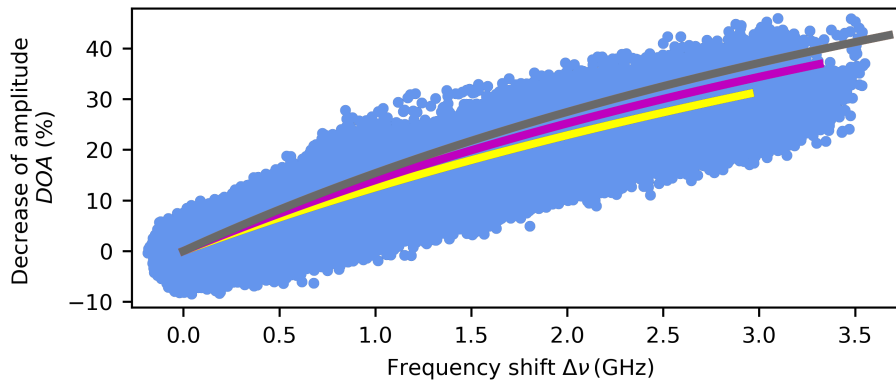


**Figure A.15.:** Correlation between the decrease of amplitudes and the frequency shifts of 9 transit events (blue). In colors are the simulated curves depicted for the hydrodynamic radius of  $r_{\text{hydr}} = 75.3$  nm and the effective refractive index of  $n_{\text{eff}}$  1.41 (yellow), 1.42 (purple) and 1.43 (gray).

amplitude and frequency shifts could be measured (see Fig. A.15). In this case, the polarization splitting of the fundamental mode was measured with resonances of a similar height. Therefore, the data point cloud is slightly expanded on  $y$ -direction. By comparing the experimentally derived data with the simulated curves, the best agreement is achieved for  $n_{\text{eff}} = 1.420$ . The systematic error is estimated by  $\Delta n_{\text{eff}} = 0.005$ .

**Refractive index of the hydration shell.** The determination of the refractive index of the hydration shell is described in Chapter 4.2.

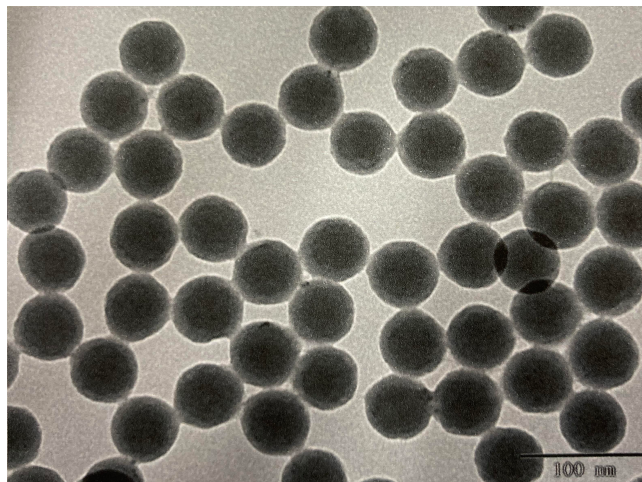


**Figure A.16.:** Transmission electron micrograph of SiO<sub>2</sub> with an intrinsic mean diameter of  $D_{\text{geom}} = 50$  nm (sample C) provided by ALPHA Nanotech.

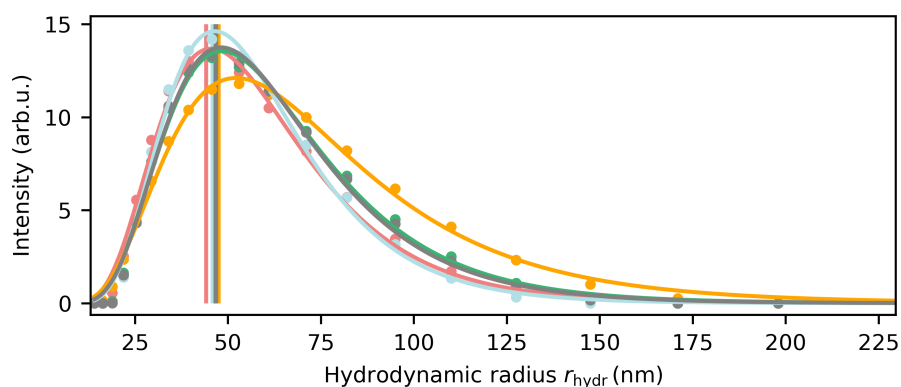


**Figure A.17.:** DLS measurement of sample C. The solid lines represent lognorm-fits to the data points and the vertical lines define the z-average value.

### A.5.3. Sample C

Sample C is provided by the same company as sample B (ALPHA Nanotech)<sup>25</sup>. Here, the nanospheres are specified with a mean intrinsic diameter of  $D_{\text{geom}} = 50$  nm and a variation coefficient of  $cv < 3\%$  (see Fig. A.16). The rest of the properties given by the company are the same as for sample B.

<sup>25</sup> ALPHA Nanotech, non-functionalized colloidal quartz glass nanospheres, size: 50 nm.

**Hydrodynamic radius.** From DLS measurements<sup>26</sup> the intensity weighted mean hydrodynamic size  $r_z$  (also called "z-average") of an ensemble nanosphere measurement can be derived by [179]

$$r_z = \frac{\sum I(r_{\text{hydr}})}{\sum \frac{I(r_{\text{hydr}})}{r_{\text{hydr}}}} \quad . \quad (\text{A.7})$$

This is done for each measurement and is shown in Fig. A.17 by vertical lines. By averaging over all  $r_z$ , the averaged harmonic mean of the hydrodynamic radius is calculated, namely  $r_{\text{hydr}} = 46.2$  nm. In order to deduce the standard deviation for the hydrodynamic radius  $\sigma_r$ , a log-normal distribution is fitted to the measured intensities. The linewidth of the fit directly indicates the standard deviation and averaging over all linewidths give the standard deviation  $\sigma_r = 29.6$  nm.

**Effective refractive index.** The effective refractive index is determined by the FP fiber sensor (see Fig. A.18). Since the polarizability of the nanospheres is so small that the amplitude of the resonance doesn't change, the effective refractive index is derived from the frequency shift histogram, where the maximal measured frequency is  $\Delta\nu = 2.2$  GHz (see Fig. A.18). In this case, agglomerates and multiple nanospheres being in the cavity at the same time could be sorted out in advance via the polarization contrast (see Chapter 6). Due to the large hydrodynamic radius distribution of  $r_{\text{hydr}} = (46.2 \pm 29.6)$  nm, the occurring maximal frequency shift is assumed to stem from nanospheres with radius  $r_{\text{hydr}} = (46.2 + 29.6/2)$  nm and the systematic error is estimated by  $\Delta n = n_{\text{eff}}((46.2 + 29.6) \text{ nm}) - n_{\text{eff}}((46.2 + 29.6/2) \text{ nm})$ . Therefore, the effective refractive index is  $n_{\text{eff}} = 1.39 \pm 0.03$ . The determination of the refractive index of the hydrate shell is described in Chapter 4.2.

<sup>26</sup> Carried out by Mark Rutschmann from the Institute of Inorganic Chemistry at the Karlsruhe institute of technology (KIT).

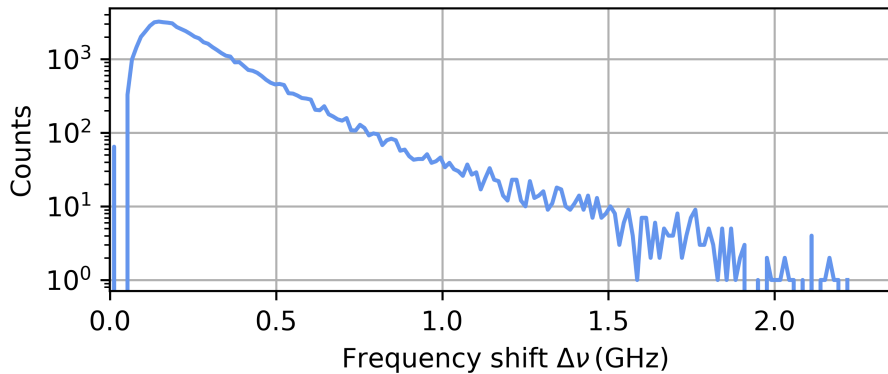


**Figure A.18.:** Measured frequency shift of 25 nanosphere transit events. The maximal measured frequency shift is at  $\Delta\nu = 2.2$  GHz, whereby an effective refractive index of  $n_{\text{eff}} = 1.39$  can be derived.

## A.6. Raw data of the single quartz glass nanosphere transit event

Measured resonance full width half maxima (FWHMs)  $\delta t$  and time shifts  $\Delta t$  for the TEM<sub>00</sub>, the TEM<sub>01</sub> and the TEM<sub>10</sub> mode. The calculation into frequency shifts is already explained in Chapter 3.4.

## A.7. Cavity preparation and occurring sensor problems

When the cavity is adjusted and flooded with a liquid, several problems may occur. In the following, those problems are discussed, and possible solutions are offered.

### Problem 1:

Despite a short cavity length, the finesse in air is lower than the theoretical one. When the cavity fibers are inserted into the ferrule, the precision hole basically ensures the alignment. However, various reasons lead to a misalignment: 1. the mirrors' convex profiles are not perfectly centered to the fiber cores, 2. the fiber cores itself may not be perfectly centered, and 3. the precision hole is 6  $\mu\text{m}$  larger than the diameter of the uncoated fibers, allowing them to tilt and shift against each other.

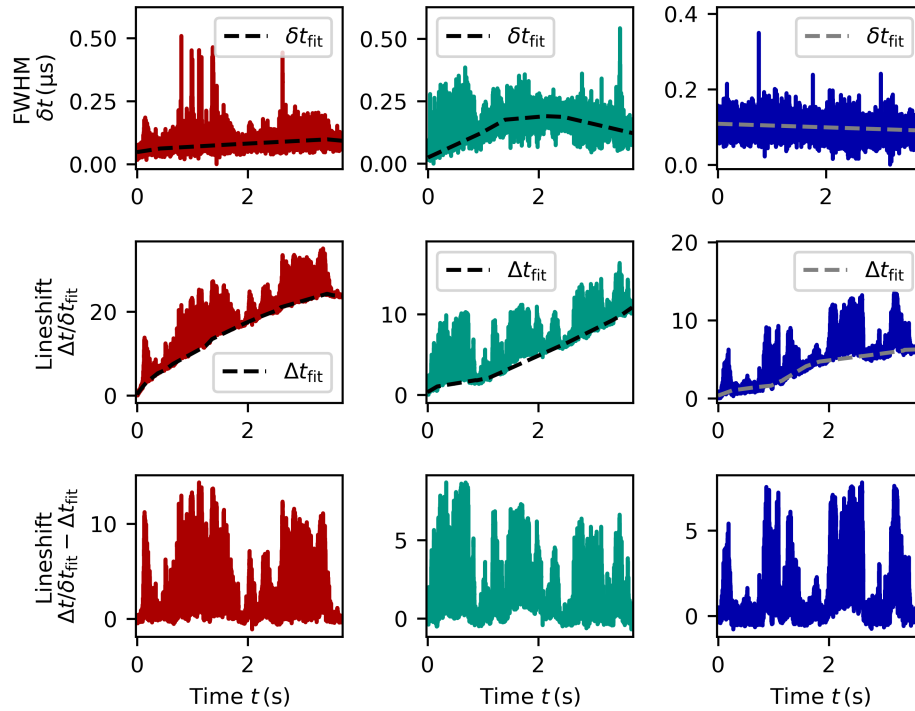


**Figure A.19.:** FWHMs  $\delta t$  and time shifts  $\Delta t$  for the TEM<sub>00</sub> (red), the TEM<sub>01</sub> (green) and the TEM<sub>10</sub> (blue) mode. The black/gray dashed lines are fits to the unperturbed FWHMs or lineshifts  $\Delta t/\delta t_{\text{fit}}$ . The third row shows the drift subtracted lineshifts  $\Delta t/\delta t_{\text{fit}} - \Delta t_{\text{fit}}$ . [95], see supplementary information.

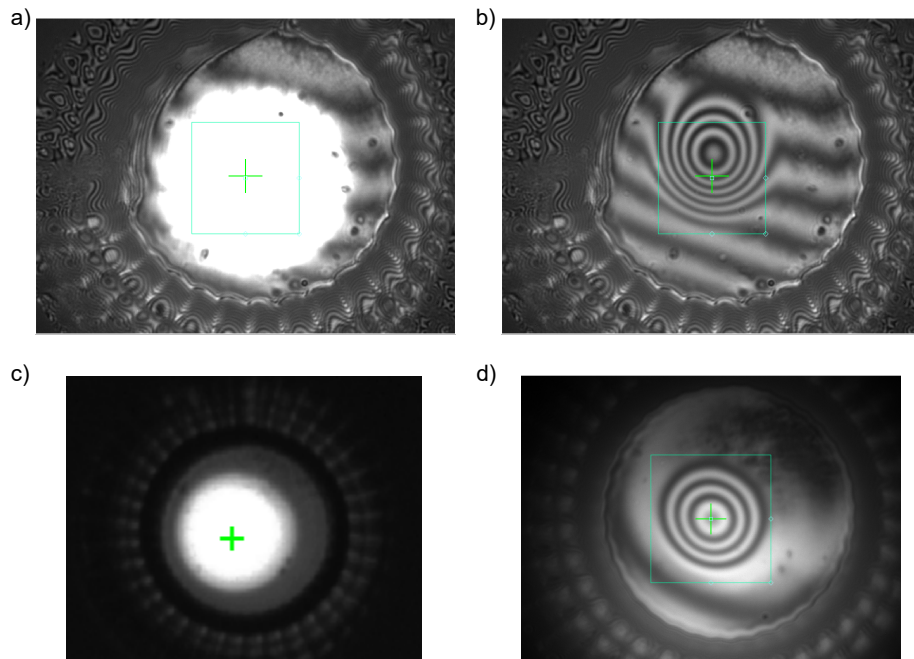


**Figure A.20.:** Investigation of the fiber core distance to the center of the mirror depression by the WLI. a) The green cross is aligned to the center of the fiber core (white circle). b) When the fiber core isn't illuminated anymore, the center of the mirror profile appears, which seems to be shifted to the center of the fiber core. However, the mirror is tilted, which can be seen by the many interference fringes. Therefore, only a reconstruction of the profile can clarify whether the core of the fiber is shifted in relation to the mirror depression. The same procedure is applied to another mirrored fiber (c,d). In this case, the mirror is hardly tilted and the center of the mirror depression is at the center of the fiber core .

Possible solutions:

1.: Only use fiber mirrors that consist of sufficiently good centered mirror profiles (see Fig. A.20). If one mirror is well centered and the other one is strongly shifted to the core, a low finesse can't be avoided. 2., and 3.: Alignment can be improved by an adjustment of the rotation angle of one cavity mirror to the other.

**Problem 2:**

Don't get light into the cavity.

Possible solutions:

Is the glass fiber in the fiber plug broken? Is the fiber plug dirty? Is the light in-coupling into the cavity fiber optimized?

**Problem 3:**

Don't detect light in the photodiode.

Possible solutions:

Couple light with another wavelength into the cavity, which is not reflected by the mirror coating. If the photodiode detects a signal, then adjust the coupling and collection optics until

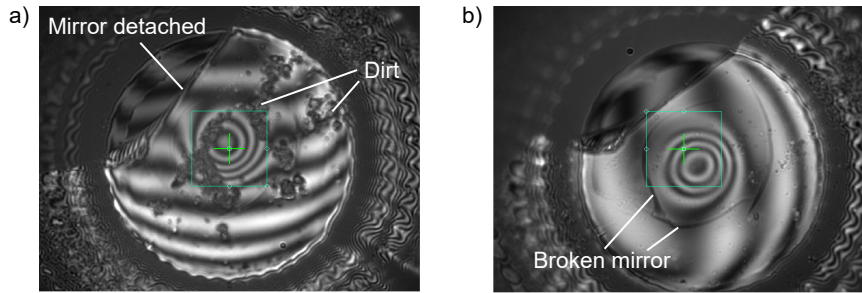


**Figure A.21.:** Broken and dirty fiber mirror. a) WLI picture of the cavity fiber mirror, directly after it was pulled out of the microfluidic channel. Both liquid residues on the mirror as well as a detachment of the mirror at the edge are observed. b) The same fiber after it was cleaned in the ultrasonic bath. Although there is no more dirt at the center, the cavity finesse is still low due to the broken mirror coating.

the signal is maximized. Afterward couple into the cavity input fiber the probe laser light. If the photodiode detects a signal, adjust the coupling optics and collection optics again, until the signal is maximized. However if the photodiode doesn't detect a signal, the cavity mirrors may be dirty or have been detached from the fiber ends.

#### Problem 4:

No resonances are detected although the coupling and collection optics are built correctly. Or: Broad resonances are detected with a low amplitude.

##### Possible solutions:

The mirrors could be dirty. Have a look at the fiber end facet with a white light interferometer (WLI) (see Fig. A.21a). If there are residues close or at the fiber core (radius twice the waist of the beam), clean the fiber end facets in the ultrasonic bath: 3 min in 20% hydrochloric acid and afterward 3 min in ethanol for spectroscopy. Slowly lift the fibers back up vertically out of the bath. Control the result in the WLI and repeat the procedure, if there are still residues close to the core. However, if the mirrors look clean, also the mirror coating itself could have come off slightly (see Fig. A.21a). This has been observed after the fiber cleaning as well as for mirrors with small radii of curvatures ( $r_c < 20 \mu\text{m}$ ). In this case, exchange the fiber mirror (see Fig. A.22). Recommendation: Don't clean the fibers with hydrochloric acid inside the setup. In this case, bubbles appear in the microfluidic channel (see below) and the hydrochloric acid attacks the piezoelectric actuators destroying them over time<sup>27</sup>.

#### Problem 5:

Less than one FSR is scanned, although the piezoelectric actuators should expand more according to the datasheet

##### Possible solutions:

1. Cables soldered on the piezoelectric actuators correctly? Check the resistors. 2. Are the piezoelectric actuators intact? Check the capacity. Do the piezo electrodes look differently as

<sup>27</sup> This observation was made in the context of a supervised master's thesis [149]

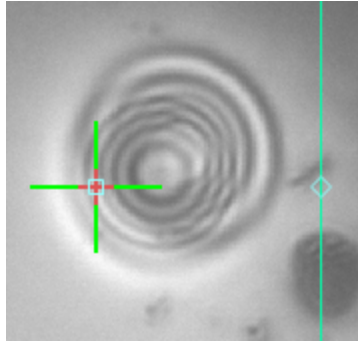


**Figure A.22.:** WLI picture of the cavity mirror profile. In this case, the mirror radius of curvature is only  $11.6\ \mu\text{m}$  and a double-ring structure is visible in the WLI. Such double-ring structures were also observed for mirrors with similar and smaller radii of curvature. Presumably, due to the steep mirror walls, the dielectric mirror coating has come off slightly.

before?<sup>28</sup> Exchange the piezoelectric actuators. 3. Do the piezoelectric actuators expand as described in the datasheet? Check the expansion with the WLI<sup>29</sup> 4. Does the fiber get stuck in the ferrule? This can happen if nanoparticles are used in the experiments and if these block the cavity between fiber and precision hole.<sup>30</sup> 5. Do the piezoelectric expand in opposite directions? Check each piezoelectric actuator individually and change the polarity of the contacts if necessary.

**Problem 6:**

When the clamps are tightened, the alignment and cavity length changes.

Possible solutions:

1. If the cavity length changes strongly, check if the clamp height is on the same level as the ferrule's precision hole (see Fig. A.6). 2. Be careful when tightening the clamp. Observe the change of the signal in the oscilloscope during this time and adjust the cavity length if necessary by the micro-positioning stage, before the clamp is fully tightened.

**Problem 7:**

The measurement noise is increased although the setup is the same. Only the fiber clamps have been opened and closed.

Possible solutions:

Cavity changes in the sub-micrometer range have been observed, especially when a liquid was pumped through the microfluidic channel. This may be improved by coating the clamp

---

<sup>28</sup> This observation was made in the context of a supervised master's thesis [149]. In this case, hydrochloric acid was pumped through the microfluidic channel whereby the electrodes degraded over time.

<sup>29</sup> Several Thorlabs PL5FBP3 piezoelectric actuators were tested, but they could not hold the expansion properties described in the datasheet. Some only expanded in the sub-micrometer range.

<sup>30</sup> In the context of a supervised bachelor and master's thesis [148, 149], ferrules with a smaller hole diameter ( $128\ \mu\text{m}$ ) also lead to a greater friction between fiber and glass ferrule and therefore parts of the mirror coating were broken and got stuck in the precision hole. Over time, the fibers couldn't be moved anymore.

with a higher friction material.

**Problem 8:**

When measuring the cavity length in the spectrometer, it's difficult to identify the fundamental modes.

Possible solutions:

This problem occurs with a poor alignment. If e.g. the 2nd order mode is more excited than the fundamental mode or if the  $x$ -polarization of the 2nd order mode is much more excited than the  $y$ -polarization, this causes a spectrum in the spectrometer which is difficult to interpret (see Chapter 3.3).

**Problem 9:**

There are bubbles inside the microfluidic channel through which gives rise to an unstable cavity.

Possible solutions:

Gas bubbles were mainly observed when Tween 20<sup>31</sup> or hydrochloric acid<sup>32</sup> were used in the microfluidic channel. Also after much rinsing with double-distilled water or ethanol for spectroscopy, the bubbles remained in the channel. The bubbles can be flushed out by repeatedly increasing and decreasing the pressure inside the microfluidic cell. Thereby the bubbles shrink and expand allowing them to detach from the wall and leaving the cavity through the tubes or the precision hole. If the microfluidic is not glued into the ferrule (see Chapter A.2.2), the microfluidic adapters can also be dipped in a double-distilled water bath and the remaining liquid can be blown out. By repeating this several times, the residuals are sufficiently removed and in a faster way than by the repeated pressure change.

Recommendation: Either don't use liquids that outgas at low pressures, or if it is unavoidable, degassing of the liquids in advance may help.

**Problem 10:**

Don't get rid of the old SiO<sub>2</sub> sample, although the cavity is rinsed with plenty of double-distilled water. This leads to ever-increasing agglomerates, which build macroscopic glass residues inside the channel and the FP cavity.

Possible solutions:

1. The SiO<sub>2</sub> nanoparticles get stuck between the tapered microfluidic tube and the ferrule wall (see Fig. 4.15a). This can be improved by a new tube connection (b). 2. The SiO<sub>2</sub> surface is covered with silanol groups [180]. Those hydrophilic groups cause an adsorption of water molecules to the surface (hydration), however, they also form a bond with other SiO<sub>2</sub> glass surfaces. This is how agglomerates are formed and how the ferrule surface is covered with SiO<sub>2</sub> nanoparticles. The latter can be avoided by the hydrophobization of the ferrule surface with a hydrophobic silane (see Appendix A.8).

---

<sup>31</sup> Merck, TWEEN 20, CAS-number: 9005-64-5.

<sup>32</sup> Observed in supervised master thesis [149].

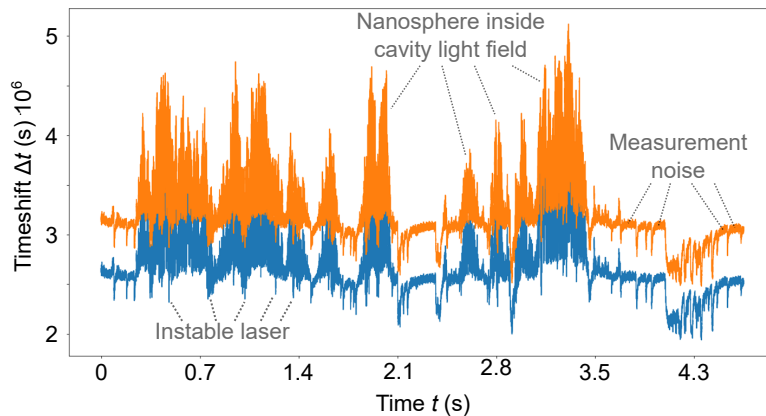


**Figure A.23.:** Example signal when the laser is running unstable. The upwards jumps are produced by the nanoparticle, which diffuses through the cavity standing-wave light field. However, the signal jumps downward occur due to the unstable laser.

### Problem 11:

How to get rid of the 50 Hz noise on the measurement signal.

Possible solutions:

1. Use cables between the electronic devices which are as short as possible.
2. Twist all electronic cables together in order to avoid any electronic loops.
3. Ensure that all electronic devices have the same earthing (try different power plugs).

### Problem 12:

The measured resonance shift signal has both upward and downward jumps (see Fig. A.23).

Possible solutions:

The laser runs unstable. Slightly change the current of the laser current controller.

## A.8. Silanization

Here, the process for the silanization of glass or tantalum pentoxide ( $\text{Ta}_2\text{O}_5$ )<sup>33</sup> surfaces is described. The process was developed by the Wegener group (Applied Physics, Karlsruhe Institute of Technology) and shared by Christian Kern, a former Ph.D. student of this group. At first, a 3 mM silane solution in toluene is prepared. There are different kinds of silanes with different functional groups available. In this case, for the hydrophobization of the surface, octadecyltrichlorosilane (OTS)<sup>34</sup> is used. The mixture of toluene and the 90 % silane is done under a nitrogen outlet flow because the silane alters if oxygen enters the solution. A part of the prepared solution is poured into a breaker and another breaker is placed over the first

<sup>33</sup> This was done in a supervised Bachelor thesis [144].

<sup>34</sup> CAS 112-04-9

one. The rest of the prepared solution is sealed as airtight as possible with sealing foil. In the second step, the quartz glass or the tantalum pentoxide surface is treated in a plasma oven in order to increase the number of -OH groups on the surface. This is also called activation of the surface. Both kinds of materials are treated with an O<sub>2</sub> plasma for 5 min<sup>35</sup>. After the surface activation, the sample is immersed into the 3 mM silane and afterward rinsed with isopropanol and blown off with nitrogen. This last step, after the plasma oven, has to be carried out as fast as possible, because the activation of the surface holds only for a short time under ambient air condition.

Additional practical tips:

- Whether the silanization has worked can be checked by measuring the contact angle of a water drop on the silanized surface (see Fig. A.24). A contact angle of about 98 degrees is expected.
- If silanization didn't work, a treatment of the same surface is not possible. It is therefore recommended to first try silanization with a test substrate (e.g. cover glass) and then use the actual sample.

<sup>35</sup> This is different depending on the plasma oven and the O<sub>2</sub> concentration.

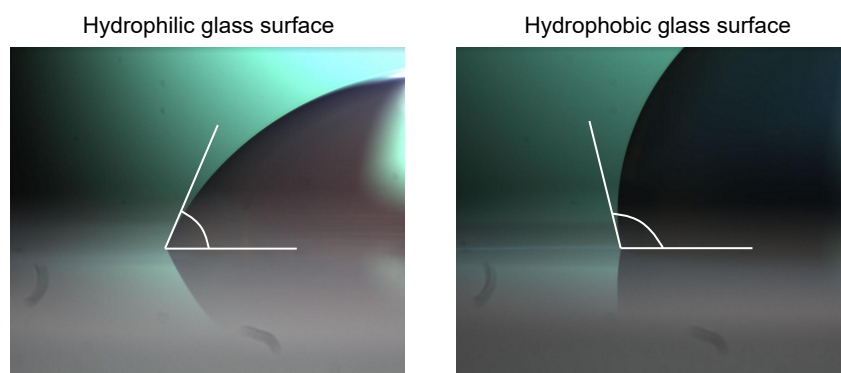


**Figure A.24.:** Measurement of the contact angle of a water drop on a glass substrate. Before the silanization, the contact angle between water drop and hydrophilic glass substrate surface is below 90 degrees. After the hydrophobic silanization of the glass surface, the contact angle is larger than 90 degrees. The pictures were taken by Andreas Wickberg, a former Ph.D. student in the Wegener group at the Applied Physical Institute at the Karlsruhe Institute of Technology.

## A.9. Fast Fourier transformation and power spectral density

If a time domain signal  $x(t)$  is fast Fourier transformed (FFT), the amplitude spectrum  $x(f)$  is derived. However, the y-axis is uncalibrated. In order to calibrate the y-axis, the *rms*-values for the time domain signal, as well as for the frequency domain signal are calculated by

$$rms_t = \sqrt{\frac{x(t_1)^2 + x(t_2)^2 + \dots + x(t_{N-1})^2}{N}} \quad \text{and} \quad (\text{A.8})$$

$$rms_f = \sqrt{\frac{|x(f_1) + x(f_2) + \dots + x(f_{N-1})|^2}{N^2}} \quad . \quad (\text{A.9})$$

As Parseval's theorem states that [181]

$$rms_t \stackrel{!}{=} rms_f \quad , \quad (\text{A.10})$$

the amplitude of the FFT can be calibrated by

$$x(f) \rightarrow \frac{rms_t}{rms_f} x(f) \quad . \quad (\text{A.11})$$

Eventually, the power spectral density is the squared amplitude and normalized to the frequency bin width  $df = f_2 - f_1$ :

$$PSD(f) = \frac{\left(\frac{rms_t}{rms_f} \cdot x(f)\right)^2}{df} \quad . \quad (\text{A.12})$$

## A.10. Possible acting forces inside the Fabry-Pérot cavity

Although the SiO<sub>2</sub> nanospheres behave purely diffusive in the operated experiments, here different forces, are discussed, which could act on the nanospheres' motion inside the cavity. At first, the optical tweezer force is illuminated in more detail and then the cavity mirror movement is considered.

### A.10.1. Optical tweezer force

The FP standing-wave light field generates an attractive force on the dielectric SiO<sub>2</sub> nanosphere. Here it is shown that for the used intracavity powers in the experiments the attractive force is negligible.

At first, the measured peak power of the resonance  $P_T$  by the APD is converted to the intracavity power via the transmission of the output-coupling cavity mirror  $T_{MM}$ <sup>36</sup> [104]:

$$P_{Cav} = \frac{P_T}{T_{MM}} . \quad (\text{A.13})$$

The maximal intracavity intensity at the center of the antinode is then calculated by [145]

$$I_{Cav} = \frac{8P_{Cav}}{\pi w_0^2} \quad (\text{A.14})$$

and the maximal trapping potential is [160]

$$U_{Trap} = \frac{\alpha I_{Cav}}{n_m c} . \quad (\text{A.15})$$

Here,  $\alpha$  is the polarizability of the nanosphere (see Eq. (2.68)). Stable trapping occurs when the trapping potential exceeds about three times the thermal energy

$$U_{Trap} > 3k_B T , \quad (\text{A.16})$$

but also below up to  $\approx 1k_B T$  the attractive forces act on the nanosphere significantly [60].

In the experiments, peak voltages of up to 0.33 V are measured by the APD. This corresponds to a measured transmitted power of  $P_T = 0.25 \mu\text{W}$ . The intracavity power then amounts to  $P_{Cav} = 14.2 \text{ mW}$  and the trapping potential is  $U_{Trap} = 2.7k_B T$ . Although the condition in Eq. (A.16) is fulfilled, in the experiment, this force only acts for a short time, because the cavity length is scanned by the frequency  $f = 3 \dots 14.1 \text{ kHz}$ . In the following, it is estimated by how much the nanosphere is moved within this short time when the optical force is acting:

The optical force is calculated by

$$F_{Opt}(z) = -\frac{d}{dz}(U_{Trap} (\cos(k_m z))^2) = 2U_{Trap} \cos(k_m z) \sin(k_m z) k_m . \quad (\text{A.17})$$

If the maximal force  $F_{Opt}(\pi/(4k))$  is assumed and the full width half maximum  $\delta t \approx 0.3 \mu\text{s}$  is assumed for the time span that this force acts on the nanosphere, the distance traveled by the nanosphere can be calculated by

$$s = \frac{1}{2} \frac{F_{Opt}(\pi/(4k_m)) \delta t^2}{m_{SiO_2} + 6\pi r_{SiO_2} \eta_m \delta t} \quad (\text{A.18})$$

Here, the Stokes friction force  $F_S = 6\pi r_{SiO_2} \eta_m v$  is considered, which acts against the optical force. The velocity can be expressed as  $v = at$  and  $m_{SiO_2}$  is the mass of the  $\text{SiO}_2$  nanosphere. This gives a distance traveled of  $s = 2.0 \cdot 10^{-14} \text{ m} \ll \lambda/(4 \cdot n_m)$ . That means in this short time

---

<sup>36</sup> Any incoupling losses into the APD or mode matching losses are neglected.

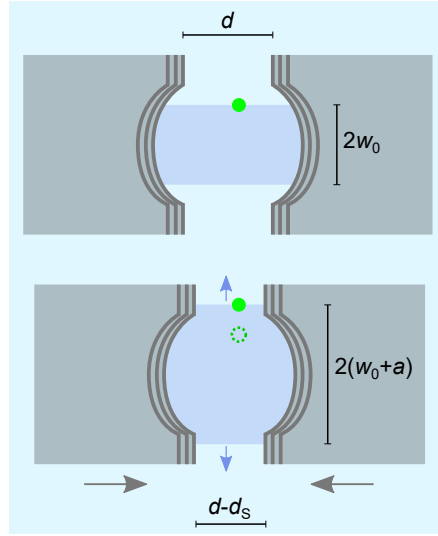


**Figure A.25.:** Illustration of the lateral movement of the nanosphere due to the periodically changed cavity length.

span, where the optical force is acting, the movement of the nanosphere is negligible. In addition, the mean trapping potential can be considered<sup>37</sup> by

$$\langle U_{\text{Trap}} \rangle = \frac{\alpha \langle I_{\text{Cav}} \rangle}{n_m c} \quad \text{and} \quad (\text{A.19})$$

$$\langle I_{\text{Cav}} \rangle = \frac{8 \langle P_{\text{Cav}} \rangle}{\pi w_0^2} \quad \text{with} \quad (\text{A.20})$$

$$\langle P_{\text{Cav}} \rangle \approx \frac{P_T \delta_t f}{T_{\text{MM}}} . \quad (\text{A.21})$$

In the experiments, this gives a mean trapping potential of  $\langle U_{\text{Trap}} \rangle = 0.007 k_B T$ , which is three orders below the condition for stable trapping.

### A.10.2. Mirror movement

The movement of the cavity mirrors is already discussed in [182]. If the mirror distance  $d$  is decreased by  $d_s$ , the assumed incompressible liquid is displaced in lateral direction (see Fig. A.25). This is the lateral force, which acts on the nanosphere. The transversal movement is given by

$$a = r \sqrt{\frac{d}{d - 2d_s} - 1} , \quad (\text{A.22})$$

when the concave mirror profile is neglected and the liquid column is assumed to have a cylindrical shape with cross section  $A = \pi w_0^2$  at the beginning and  $A = \pi (w_0 + a)^2$  after the

---

<sup>37</sup> Similar to the consideration of a pulsed laser.

mirror movement. In the experiments presented in this work, the scanning amplitude of the mirrors amounts to  $d_s \approx 0.1$  nm and typical cavity parameters are  $d = 5$   $\mu\text{m}$  and  $w_0 = 1.5$   $\mu\text{m}$ . This results into a lateral nanosphere movement of  $a = 0.03$  nm  $\ll \lambda/(4n_m)$  due to the scanning of the resonance length. As this moved distance is much shorter than the expansion of the antinode, this effect is negligible.



## B. Abbreviations and symbols

### B.1. Abbreviations

<b>STORM</b>	stochastic optical reconstruction microscopy
<b>PALM</b>	photoactivated localization microscopy
<b>STED</b>	stimulated emission depletion
<b>iScat</b>	interference scattering
<b>PhC</b>	photonic crystal
<b>FP</b>	Fabry-Pérot
<b>SP</b>	surface plasmon
<b>LSP</b>	localized surface plasmon
<b>WGM</b>	whispering gallery mode
<b>DLW</b>	direct laser writing
<b>SM</b>	single-mode
<b>MM</b>	multi-mode
<b>FSR</b>	free spectral range
<b>FWHM</b>	full width half maximum
<b>SNR</b>	signal-to-noise ratio
<b>ppm</b>	parts per million, $10^{-6}$
<b>SEM</b>	scanning electron microscope
<b>DLS</b>	dynamic light scattering
<b>SiO<sub>2</sub></b>	silicon dioxide
<b>APD</b>	avalanche photodiode
<b>SLED</b>	superluminescent diode
<b>EOM</b>	electro-optic modulator
<b>TEM<sub>00</sub></b>	fundamental mode

<b>TEM<sub>01</sub></b>	higher-order transverse mode of order 01
<b>TEM<sub>10</sub></b>	higher-order transverse mode of order 01
<b>FFT</b>	fast fourier transform
<b>PEG2000</b>	polyethylenglycol 2000
<b>WLI</b>	white light interferometer
<b>PBS</b>	phosphate buffered saline
<b>DPBS</b>	dulbecco's phosphate buffered saline
<b>D<sub>2</sub>O</b>	heavy water
<b>PEEK</b>	polyetheretherketon
<b>PS</b>	polystyrol
<b>OTS</b>	octadecyltrichlorsilane
<b>DDS</b>	dichlorodimethylsilane
<b>PTFE</b>	polytetrafluoroethylene
<b>BSA</b>	bovine serum albumin
<b>SIBA</b>	self-induced back-action
<b>PID</b>	proportional integral derivative

## **B.2. Symbols**

$V_s$	effective sensing volume
$V_m$	mode volume
$\lambda$	wavelength
$\mathcal{F}$	finesse
$d_{\text{opt}}$	optical cavity length
$d_{\text{geom}}$	geometrical cavity length
$d_{\text{pen}}$	penetration depth
$V_{\text{NP}}$	sphere volume of the nanosphere
$\alpha$	optical polarizability
$\alpha_{\text{eff}}$	effective optical polarizability
$n_{\text{SiO}_2}$	intrinsic refractive index of the SiO <sub>2</sub> nanosphere

$n_{\text{eff}}$	effective refractive index of the nanosphere
$n_{\text{m}}$	refractive index of the liquid
$r_{\text{hydr}}$	hydrodynamic radius
$r_{\text{SiO}_2}$	intrinsic radius of the SiO <sub>2</sub> nanosphere
$T$	mirror transmission
$\alpha_L$	coefficient of linear thermal expansion
$DOA$	decrease of amplitude
$\Delta\nu$	frequency shift
$MSD$	mean squared displacement
$MSAD$	mean square angular displacement
$Q$	quality factor
$\delta_\nu$	FWHM in frequency units
$\delta_t$	FWHM in time units
$\Delta_t$	time shift
$\Delta_\nu$	frequency shift
$\Delta_s$	length shift
$rms$	root mean square
$r_c$	radius of curvature
$U_{\text{max}}$	resonance peak in volt units
$\Delta\nu_{\text{FSR}}$	free spectral range



## Bibliography

- [1] Minhan Park, Hung Soo Joo, Kwangyul Lee, Myoseon Jang, Sang Don Kim, Injeong Kim, Lucille Joanna S. Borlaza, Heungbin Lim, Hanjae Shin, Kyu Hyuck Chung, Yoon Hyeong Choi, Sun Gu Park, Min Suk Bae, Jiye Lee, Hangyul Song, and Kihong Park. Differential toxicities of fine particulate matters from various sources. *Scientific Reports*, 8(1):1–11, 2018.
- [2] Eidgenössische Kommission für Lufthygiene (EKL). Feinstaub in der Schweiz. Status-Bericht. 2007.
- [3] C. Chellaram, G. Murugaboopathi, A.A. John, R. Sivakumar, S. Ganesan, S. Krithika, and G. Priya. Significance of Nanotechnology in Food Industry. *APCBEE Procedia*, 8(Caas 2013):109–113, 2014.
- [4] K. A. Abbas, A. M. Saleh, A. Mohamed, and N. MohdAzhan. The recent advances in the nanotechnology and its applications in food processing: A review. *Journal of Food, Agriculture and Environment*, 7(3-4):14–17, 2009.
- [5] H. J. Lee, S. Y. Yeo, and S. H. Jeong. Antibacterial effect of nanosized silver colloidal solution on textile fabrics. *Journal of Materials Science*, 38(10):2199–2204, 2003.
- [6] Yuyang Liu, Xiaowen Wang, Kaihong Qi, and J. H. Xin. Functionalization of cotton with carbon nanotubes. *Journal of Materials Chemistry*, 18(29):3454–3460, 2008.
- [7] A. P. Popov, A. V. Priezhev, J. Lademann, and R. Myllylä. TiO<sub>2</sub> nanoparticles as an effective UV-B radiation skin-protective compound in sunscreens. *Journal of Physics D: Applied Physics*, 38(15):2564–2570, 2005.
- [8] Anuradha Patel, Parixit Prajapati, and Rikisha Boghra. Overview on Application of Nanoparticles in Cosmetics. *Asian Journal of Pharmaceutical Sciences and Clinical Research (AJPSCLR)*, 1(2):40–55, 2011.
- [9] Catherine J.E. Ingram, Charlotte A. Mulcare, Yuval Itan, Mark G. Thomas, and Dallas M. Swallow. Lactose digestion and the evolutionary genetics of lactase persistence. *Human Genetics*, 124(6):579–591, 2009.
- [10] Barbara E. Goodman. Insights into digestion and absorption of major nutrients in humans. *American Journal of Physiology - Advances in Physiology Education*, 34(2):44–53, 2010.
- [11] Richard A. Forsgård. Lactose digestion in humans: Intestinal lactase appears to be constitutive whereas the colonic microbiome is adaptable. *American Journal of Clinical Nutrition*, 110(2):273–279, 2019.

- [12] Wahala M.P.B. Wahala and Aravinda M. de Silva. The human antibody response to dengue virus infection. *Viruses*, 3(12):2374–2395, 2011.
- [13] Florian Krammer. The human antibody response to influenza A virus infection and vaccination. *Nature Reviews Immunology*, 19(6):383–397, 2019.
- [14] Stephanie Tran, Peter-Joseph DeGiovanni, Brandon Piel, and Prakash Rai. Cancer nanomedicine: a review of recent success in drug delivery. *Clinical and Translational Medicine*, 6(1), 2017.
- [15] Rashmirekha Pati, Maxim Shevtsov, and Avinash Sonawane. Nanoparticle vaccines against infectious diseases. *Frontiers in Immunology*, 9(OCT), 2018.
- [16] Dominik Huster, Tina D. Purnat, Jason L. Burkhead, Martina Ralle, Oliver Fiehn, Franziska Stuckert, N. Erik Olson, Daniel Teupser, and Svetlana Lutsenko. High copper selectively alters lipid metabolism and cell cycle machinery in the mouse model of Wilson disease. *Journal of Biological Chemistry*, 282(11):8343–8355, 2007.
- [17] David C Kennedy, Rodney K Lyn, and John Paul Pezacki. Copper. *JACS communications*, pages 2444–2445, 2009.
- [18] Sophie Lanone, Françoise Rogerieux, Jorina Geys, Aurélie Dupont, Emmanuelle Maillot-Marechal, Jorge Boczkowski, Ghislaine Lacroix, and Peter Hoet. Comparative toxicity of 24 manufactured nanoparticles in human alveolar epithelial and macrophage cell lines. *Particle and Fibre Toxicology*, 6:1–12, 2009.
- [19] Andreas Elsaesser and C. Vyvyan Howard. Toxicology of nanoparticles. *Advanced Drug Delivery Reviews*, 64(2):129–137, 2012.
- [20] Nicholas Dias Robert Cronin Yung Peng, Rose Khavari. Mycobacteria inactivation using Engineered Water Nanostructures (EWNS). *Physiology & behavior*, 176(3):139–148, 2017.
- [21] Adam J M Wollman, Richard Nudd, Erik G Hedlund, Mark C Leake, and Mark C Leake. IX. An account of Mr. Leeuwenhoek’s microscopes. *Philosophical Transactions of the Royal Society of London*, 41(458):503–519, 2015.
- [22] Manuela Malatesta. Transmission electron microscopy for nanomedicine: Novel applications for long-established techniques. *European Journal of Histochemistry*, 60(4):8–12, 2016.
- [23] Syed Mahmood, Uttam Kumar Mandal, Bappaditya Chatterjee, and Muhammad Taher. Advanced characterizations of nanoparticles for drug delivery: Investigating their properties through the techniques used in their evaluations. *Nanotechnology Reviews*, 6(4):355–372, 2017.
- [24] Daniel Martín-Yerga. Electrochemical detection and characterization of nanoparticles with printed devices. *Biosensors*, 9(2), 2019.

- [25] Lizhou Xu, Nahid Shoaie, Fatemeh Jahanpeyma, Junjie Zhao, Mostafa Azimzadeh, and Khuloud T. Al Jamal. Optical, electrochemical and electrical (nano)biosensors for detection of exosomes: A comprehensive overview. *Biosensors and Bioelectronics*, 161(April), 2020.
- [26] Daeun Sung and Jahyun Koo. A review of BioFET's basic principles and materials for biomedical applications. *Biomedical Engineering Letters*, 11(2):85–96, 2021.
- [27] Christopher M. Hoo, Natasha Starostin, Paul West, and Martha L. Mecartney. A comparison of atomic force microscopy (AFM) and dynamic light scattering (DLS) methods to characterize nanoparticle size distributions. *Journal of Nanoparticle Research*, 10(SUPPL. 1):89–96, 2008.
- [28] Andrew D. Hughes, Ian C. Glenn, Andrew D. Patrick, Andrew Ellington, and Eric V. Anslyn. A pattern recognition based fluorescence quenching assay for the detection and identification of nitrated explosive analytes. *Chemistry - A European Journal*, 14(6):1822–1827, 2008.
- [29] Gael Moneron and Stefan W. Hell. Two-photon excitation STED microscopy. *Optics Express*, 17(17):14567, 2009.
- [30] O. Shimomura, F. H. Johnson, and Y. Saiga. Extraction, purification and properties of aequorin, a bioluminescent. *Journal of cellular and comparative physiology*, 59(165):223–239, 1962.
- [31] Mikhail V. Matz, Arkady F. Fradkov, Yulii A. Labas, Aleksandr P. Savitsky, Andrey G. Zaraisky, Mikhail L. Markelov, and Sergey A. Lukyanov. Fluorescent proteins from nonbioluminescent Anthozoa species. *Nature Biotechnology*, 17(10):969–973, 1999.
- [32] Nathan C. Shaner, Robert E. Campbell, Paul A. Steinbach, Ben N.G. Giepmans, Amy E. Palmer, and Roger Y. Tsien. Improved monomeric red, orange and yellow fluorescent proteins derived from *Discosoma* sp. red fluorescent protein. *Nature Biotechnology*, 22(12):1567–1572, 2004.
- [33] Sviatlana Shashkova and Mark C. Leake. Single-molecule fluorescence microscopy review: Shedding new light on old problems. *Bioscience Reports*, 37(4):1–19, 2017.
- [34] W. E. Moerner. New directions in single-molecule imaging and analysis. *PNAS*, 104(31), 2007.
- [35] Steffen J. Sahl and W. E. Moerner. Super-resolution fluorescence imaging with single molecules. *Current Opinion in Structural Biology*, 23(5):778–787, 2013.
- [36] Samuel T. Hess, Thanu P.K. Girirajan, and Michael D. Mason. Ultra-high resolution imaging by fluorescence photoactivation localization microscopy. *Biophysical Journal*, 91(11):4258–4272, 2006.
- [37] Peter Mock, Dirk Hülsebusch, Jörg Ungethüm, and Stephan A. Schmid. Electric vehicles - A model based assessment of future market prospects and environmental impacts. *World Electric Vehicle Journal*, 3(1):793–795, 2009.

- [38] Eva Rittweger, Kyu Young Han, Scott E. Irvine, Christian Eggeling, and Stefan W. Hell. STED microscopy reveals crystal colour centres with nanometric resolution. *Nature Photonics*, 3(3):144–147, 2009.
- [39] Francisco Balzarotti, Yvan Eilers, Klaus C Gwosch, Arvid H Gynnå, Volker Westphal, Fernando D Stefani, Johan Elf, and Stefan W Hell. With Minimal Photon Fluxes. *Science*, 355(February):606–612, 2017.
- [40] Klaus C. Gwosch, Jasmin K. Pape, Francisco Balzarotti, Philipp Hoess, Jan Ellenberg, Jonas Ries, and Stefan W. Hell. MINFLUX nanoscopy delivers 3D multicolor nanometer resolution in cells. *Nature Methods*, 17(2):217–224, 2020.
- [41] Michael Weber, Marcel Leutenegger, Stefan Stoldt, Stefan Jakobs, Tiberiu S Mihaila, Alexey N Butkevich, and Stefan W Hell. MINSTED fluorescence localization and nanoscopy. *bioRxiv*, page 2020.10.31.363424, 2020.
- [42] Marek Piliarik and Vahid Sandoghdar. Direct optical sensing of single unlabelled proteins and super-resolution imaging of their binding sites. *Nature Communications*, 5:1–8, 2014.
- [43] Carlo Manzo and Maria F. Garcia-Parajo. A review of progress in single particle tracking: From methods to biophysical insights. *Reports on Progress in Physics*, 78(12), 2015.
- [44] Chia Lung Hsieh, Susann Spindler, Jens Ehrig, and Vahid Sandoghdar. Tracking single particles on supported lipid membranes: Multimobility diffusion and nanoscopic confinement. *Journal of Physical Chemistry B*, 118(6):1545–1554, 2014.
- [45] Matz Liebel, James T. Hugall, and Niek F. Van Hulst. Ultrasensitive Label-Free Nanosensing and High-Speed Tracking of Single Proteins. *Nano Letters*, 17(2):1277–1281, 2017.
- [46] Philipp Kukura, Helge Ewers, Christian Müller, Alois Renn, Ari Helenius, and Vahid Sandoghdar. High-speed nanoscopic tracking of the position and orientation of a single virus. *Nature Methods*, 6(12):923–927, 2009.
- [47] Katelyn M. Spillane, Jaime Ortega-Arroyo, Gabrielle De Wit, Christian Eggeling, Helge Ewers, Mark I. Wallace, and Philipp Kukura. High-speed single-particle tracking of gm1 in model membranes reveals anomalous diffusion due to interleaflet coupling and molecular pinning. *Nano Letters*, 14(9):5390–5397, 2014.
- [48] Yanyan Zhi, Xiao Chong Yu, Qihuang Gong, Lan Yang, and Yun Feng Xiao. Single Nanoparticle Detection Using Optical Microcavities. *Advanced Materials*, 29(12), 2017.
- [49] Da Quan Yang, Bing Duan, Xiao Liu, Ai Qiang Wang, Xiao Gang Li, and Yue Feng Ji. Photonic crystal nanobeam cavities for nanoscale optical sensing: A review. *Micromachines*, 11(1), 2020.
- [50] Cheng Wang, Qimin Quan, Shota Kita, Yihang Li, and Marko Lončar. Single-nanoparticle detection with slot-mode photonic crystal cavities. *Applied Physics Letters*, 106(26), 2015.

- 
- [51] Giampaolo Pitruzzello and Thomas F. Krauss. Photonic crystal resonances for sensing and imaging. *Journal of Optics (United Kingdom)*, 20(7), 2018.
- [52] Jens M Dobrindt. *Bio-sensing using toroidal microresonators Theoretical cavity optomechanics*. Dissertation, Ludwig-Maximilians-Universität München, 2012.
- [53] M. G. Scullion, A. Di Falco, and T. F. Krauss. Slotted photonic crystal cavities with integrated microfluidics for biosensing applications. *Biosensors and Bioelectronics*, 27(1):101–105, 2011.
- [54] B. Gagianut. Beitrag zur Wirkung von Deuteriumoxyd (D<sub>2</sub>O) auf das Wachstum. *Brèves communications*, V(1938):48–50, 1948.
- [55] Andrea M. Armani, Rajan P. Kulkarni, Scott E. Fraser, Richard C. Flagan, and Kerry J. Vahala. Label-free, single-molecule detection with optical microcavities. *Science*, 317(5839):783–787, 2007.
- [56] Siyka I Shopova. Whispering Gallery Mode Biosensor. *ResearchGate*, (November):24, 2014.
- [57] W. Bogaerts, P. de Heyn, T. van Vaerenbergh, K. de Vos, S. Kumar Selvaraja, T. Claes, P. Dumon, P. Bienstman, D. van Thourhout, and R. Baets. Silicon microring resonators. *Laser and Photonics Reviews*, 6(1):47–73, 2012.
- [58] M. Ghulinyan, D. Navarro-Urrios, A. Pitanti, A. Lui, G. Pucker, and L. Pavesi. Whispering-gallery modes and purcell effect in a Si-nanocrystal-based single microdisk resonator. *2008 5th International Conference on Group IV Photonics, GFP*, 16(17):225–227, 2008.
- [59] F. Vollmer, S. Arnold, and D. Keng. Single virus detection from the reactive shift of a whispering-gallery mode. *Proceedings of the National Academy of Sciences of the United States of America*, 105(52):20701–20704, 2008.
- [60] S. Arnold, D. Keng, S. I. Shopova, S. Holler, W. Zurawsky, and F. Vollmer. Whispering gallery mode carousel – a photonic mechanism for enhanced nanoparticle detection in biosensing. *Optics Express*, 17(8):6230, 2009.
- [61] Martin D. Baaske and Frank Vollmer. Optical observation of single atomic ions interacting with plasmonic nanorods in aqueous solution. *Nature Photonics*, 10(11):733–739, 2016.
- [62] Yong Yang, Jonathan Ward, and Sile Nic Chormaic. Quasi-droplet microbubbles for high resolution sensing applications. *Optics Express*, 22(6):6881, 2014.
- [63] Jon D. Swaim, Joachim Knittel, and Warwick P. Bowen. Detection of nanoparticles with a frequency locked whispering gallery mode microresonator. *Applied Physics Letters*, 102(18), 2013.
- [64] Judith Su, Alexander F.G. Goldberg, and Brian M. Stoltz. Label-free detection of single nanoparticles and biological molecules using microtoroid optical resonators. *Light: Science and Applications*, 5(August 2015):2–7, 2016.

- [65] Tao Lu, Hansuek Lee, Tong Chen, Steven Herchak, Ji Hun Kim, Scott E. Fraser, Richard C. Flagan, and Kerry Vahala. High sensitivity nanoparticle detection using optical microcavities. *Proceedings of the National Academy of Sciences of the United States of America*, 108(15):5976–5979, 2011.
- [66] Bei Bei Li, William R. Clements, Xiao Chong Yu, Kebin Shi, Qihuang Gong, Yun Feng Xiao, and Oskar J. Painter. Single nanoparticle detection using split-mode microcavity Raman lasers. *Proceedings of the National Academy of Sciences of the United States of America*, 111(41):14657–14662, 2014.
- [67] Lina He, Şahin Kaya Özdemir, Jianguang Zhu, Woosung Kim, and Lan Yang. Detecting single viruses and nanoparticles using whispering gallery microlasers. *Nature Nanotechnology*, 6(7):428–432, 2011.
- [68] F. Vollmer, S. Arnold, and D. Keng. Single virus detection from the reactive shift of a whispering-gallery mode. *Proceedings of the National Academy of Sciences of the United States of America*, 105(52):20701–20704, 2008.
- [69] Ying Jen Chen, Ulrike Schoeler, Chung Hsuan Benjamin Huang, and Frank Vollmer. Combining Whispering-Gallery Mode Optical Biosensors with Microfluidics for Real-Time Detection of Protein Secretion from Living Cells in Complex Media. *Small*, 14(22):1–8, 2018.
- [70] Yuye Wang, Shuwen Zeng, Georges Humbert, and Ho Pui Ho. Microfluidic Whispering Gallery Mode Optical Sensors for Biological Applications. *Laser and Photonics Reviews*, 14(12):1–20, 2020.
- [71] Peter Zijlstra, Pedro M.R. Paulo, and Michel Orrit. Optical detection of single non-absorbing molecules using the surface plasmon resonance of a gold nanorod. *Nature Nanotechnology*, 7(6):379–382, 2012.
- [72] Shavkat Nizamov, Vitali Scherbahn, and Vladimir M. Mirsky. Detection and Quantification of Single Engineered Nanoparticles in Complex Samples Using Template Matching in Wide-Field Surface Plasmon Microscopy. *Analytical Chemistry*, 88(20):10206–10214, 2016.
- [73] Sarah Unser, Ian Bruzas, Jie He, and Laura Sagle. Localized surface plasmon resonance biosensing: Current challenges and approaches. *Sensors (Switzerland)*, 15(7):15684–15716, 2015.
- [74] Larissa Kohler. *Untersuchung der oberflächenverstärkten Ramanstreuung in mikrofluidischen Analysesystemen*. Masterarbeit, Karlsruhe Institute of Technology, 2016.
- [75] Vincenzo Amendola, Roberto Pilot, Marco Frasconi, Onofrio M. Maragò, and Maria Antonia Iatì. Surface plasmon resonance in gold nanoparticles: A review. *Journal of Physics Condensed Matter*, 29(20), 2017.
- [76] Alexander Zybin, Yurii A. Kuritsyn, Evgeny L. Gurevich, Vladimir V. Temchura, Klaus Überla, and Kay Niemax. Real-time detection of single immobilized nanoparticles by surface plasmon resonance imaging. *Plasmonics*, 5(1):31–35, 2010.

- [77] Xiao Li Zhou, Yunze Yang, Shaopeng Wang, and Xian Wei Liu. Surface Plasmon Resonance Microscopy: From Single-Molecule Sensing to Single-Cell Imaging. *Angewandte Chemie - International Edition*, 59(5):1776–1785, 2020.
- [78] Wencheng Yue, Peijun Yao, Huiwen Luo, and Wen Liu. Surface plasmon polariton nanocavity with ultrasmall mode volume. *Journal of Physics D: Applied Physics*, 50(31), 2017.
- [79] Govinda Lilley, Manuel Messner, and Karl Unterrainer. Improving the quality factor of the localized surface plasmon resonance. *Optical Materials Express*, 5(10):2112, 2015.
- [80] Baoqing Wang, Peng Yu, Wenhao Wang, Xutao Zhang, Hao Chung Kuo, Hongxing Xu, and Zhiming M. Wang. High-Q Plasmonic Resonances: Fundamentals and Applications. *Advanced Optical Materials*, 2001520:1–30, 2021.
- [81] Chengjun Huang, Kristien Bonroy, Gunter Reekmans, Wim Laureyn, Katarina Verhaegen, Iwijn De Vlaminck, Liesbet Lagae, and Gustaaf Borghs. Localized surface plasmon resonance biosensor integrated with microfluidic chip. *Biomedical Microdevices*, 11(4):893–901, 2009.
- [82] Jhih Siang Chen, Pin Fan Chen, Hana Tzu Han Lin, and Nien Tsu Huang. A Localized surface plasmon resonance (LSPR) sensor integrated automated microfluidic system for multiplex inflammatory biomarker detection. *Analyst*, 145(23):7654–7661, 2020.
- [83] Michael A. Beuwer, Menno W.J. Prins, and Peter Zijlstra. Stochastic protein interactions monitored by hundreds of single-molecule plasmonic biosensors. *Nano Letters*, 15(5):3507–3511, 2015.
- [84] Gary A. Baker and David S. Moore. Progress in plasmonic engineering of surface-enhanced Raman-scattering substrates toward ultra-trace analysis. *Analytical and Bioanalytical Chemistry*, 382(8):1751–1770, 2005.
- [85] Lamyaa M. Almeahmadi, Stephanie M. Curley, Natalya A. Tokranova, Scott A. Tenenbaum, and Igor K. Lednev. Surface Enhanced Raman Spectroscopy for Single Molecule Protein Detection. *Scientific Reports*, 9(1):1–9, 2019.
- [86] A. A.P. Trichet, P. R. Dolan, D. James, G. M. Hughes, C. Vallance, and J. M. Smith. Nanoparticle Trapping and Characterization Using Open Microcavities. *Nano Letters*, 16(10):6172–6177, 2016.
- [87] D. Hunger, T. Steinmetz, Y. Colombe, C. Deutsch, T. W. Hänsch, and J. Reichel. A fiber Fabry-Perot cavity with high finesse. *New Journal of Physics*, 12, 2010.
- [88] Johannes F. S. Brachmann, Hanno Kaupp, Theodor W. Hänsch, and David Hunger. Photothermal effects in ultra-precisely stabilized tunable microcavities. *Optics Express*, 24(18):21205, 2016.
- [89] Matthias Mader, Jakob Reichel, Theodor W. Hänsch, and David Hunger. A scanning cavity microscope. *Nature Communications*, 6:1–7, 2015.

- [90] Stefan Kuhn, Georg Wachter, Franz Ferdinand Wieser, James Millen, Michael Schneider, Johannes Schalko, Ulrich Schmid, Michael Trupke, and Markus Arndt. Nanoparticle detection in an open-access silicon microcavity. *Applied Physics Letters*, 111(25), 2017.
- [91] Lukas Greuter, Sebastian Starosielec, Daniel Najer, Arne Ludwig, Luc Duempelmann, Dominik Rohner, and Richard J. Warburton. A small mode volume tunable microcavity: Development and characterization. *Applied Physics Letters*, 105(12):1–5, 2014.
- [92] Manuel Uphoff, Manuel Brekenfeld, Gerhard Rempe, and Stephan Ritter. Frequency splitting of polarization eigenmodes in microscopic Fabry-Perot cavities. *New Journal of Physics*, 17, 2015.
- [93] Hrishikesh Kelkar, Daqing Wang, Diego Martín-Cano, Björn Hoffmann, Silke Christiansen, Stephan Götzinger, and Vahid Sandoghdar. Sensing nanoparticles with a cantilever-based scannable optical cavity of low finesse and sub- $\lambda^3$  volume. *Physical Review Applied*, 4(5):1–11, 2015.
- [94] A. A.P. Trichet, J. Foster, N. E. Omori, D. James, P. R. Dolan, G. M. Hughes, C. Vallance, and J. M. Smith. Open-access optical microcavities for lab-on-a-chip refractive index sensing. *Lab on a Chip*, 14(21):4244–4249, 2014.
- [95] Larissa Kohler, Matthias Mader, Christian Kern, Martin Wegener, and David Hunger. Tracking Brownian motion in three dimensions and characterization of individual nanoparticles using a fiber-based high-finesse microcavity. *arXiv: 2008.12173, submitted to Nature Communications*, pages 1–8, 2020.
- [96] Petra Schwille and Elke Haustein. Fluorescence Correlation Spectroscopy An Introduction to its Concepts and Applications Petra Schwille and Elke Haustein Experimental Biophysics Group Max-Planck-Institute for Biophysical Chemistry Am Fassberg 11 D-37077 Göttingen. *ResearchGate*, (January 2001), 2001.
- [97] Ipsita Saha and Saveez Saffarian. Interferometric fluorescence cross correlation spectroscopy. *PLoS ONE*, 14(12):1–12, 2019.
- [98] N. P. Mauranyapin, L. S. Madsen, M. A. Taylor, M. Waleed, and W. P. Bowen. Evanescent single-molecule biosensing with quantum-limited precision. *Nature Photonics*, 11(8):477–481, 2017.
- [99] Evan P. Perillo, Yen Liang Liu, Khang Huynh, Cong Liu, Chao Kai Chou, Mien Chie Hung, Hsin Chih Yeh, and Andrew K. Dunn. Deep and high-resolution three-dimensional tracking of single particles using nonlinear and multiplexed illumination. *Nature Communications*, 6(91), 2015.
- [100] Bahaa E. A. Saleh. *Fundamentals of photonics*. Wiley, Hoboken, NJ, third edit edition, 2020.
- [101] D. Hunger, C. Deutsch, R. J. Barbour, R. J. Warburton, and J. Reichel. Laser micro-fabrication of concave, low-roughness features in silica. *AIP Advances*, 2(1), 2012.
- [102] George M. Hale and Marvin R. Querry. Optical Constants of Water in the 200-nm to 200- $\mu\text{m}$  Wavelength Region. *Applied Optics*, 12(3):555, 1973.

- 
- [103] Julia Benedikter. *Microcavity Enhancement of Silicon Vacancy Centres in Diamond and Europium Ions in Yttria*. Dissertation, Ludwig-Maximilians-Universität München, 2019.
- [104] Christina J. Hood, H. J. Kimble, and Jun Ye. Characterization of high-finesse mirrors: Loss, phase shifts, and mode structure in an optical cavity. *Physical Review A - Atomic, Molecular, and Optical Physics*, 64(3):7, 2001.
- [105] Sébastien Garcia, Francesco Ferri, Konstantin Ott, Jakob Reichel, and Romain Long. Dual-wavelength fiber Fabry-Perot cavities with engineered birefringence. *arXiv*, 26(17):22249–22263, 2018.
- [106] Stefan A. Maier. *Plasmonics: Fundamentals and Applications*.
- [107] John David Jackson. *Klassische Elektrodynamik*. *Klassische Elektrodynamik*, 2011.
- [108] M. Mader. *A scanning cavity microscope*. Doktorarbeit, Ludwig-Maximilians-Universität München, 2018.
- [109] Ari Sihvola. Dielectric polarization and particle shape effects. *Journal of Nanomaterials*, 2007, 2007.
- [110] Matthias Mader, Jakob Reichel, Theodor W. Hänsch, and David Hunger. A scanning cavity microscope. *Nature Communications*, 6:1–7, 2015.
- [111] Thomas Hümmer. *Cavity-enhanced hyperspectral Raman and Absorption Microscopy*. Dissertation, Ludwig-Maximilians-Universität München, 2019.
- [112] Craig F Bohren and Donald R Huffman. *Absorption and scattering of light by small particles*. Wiley-VCH, Weinheim, 2004.
- [113] I. Wayan Sudiarta and Petr Chýlek. Mie scattering by a spherical particle in an absorbing medium. *Applied Optics*, 41(18):3545, 2002.
- [114] Carsten Sönnichsen. Plasmons in metal nanostructures. *Dissertation*, 27(June):134, 2001.
- [115] Jon D. Swaim, Joachim Knittel, and Warwick P. Bowen. Detection of nanoparticles with a frequency locked whispering gallery mode microresonator. *Applied Physics Letters*, 102(18), 2013.
- [116] Andreas Muller, Edward B Flagg, John R Lawall, and Glenn S Solomon. Fabry – Perot microcavity. *Optics letters*, 35(13):2293–2295, 2010.
- [117] F.G.K Baucke. The Glass Electrode - Applied Electrochemistry of Glass Surfaces. *Journal of Non-Crystalline Solids*, 73:215–231, 1985.
- [118] Sven H Behrens, David G. Grier, Sven H Behrens, David G. Grier, Peter Carmichael, Jabez J. McClelland, J. Alexander Liddle, Andrew J. Berglund, Matthew D. McMahon, Fook Chiong Cheong, Bhaskar Jyoti Krishnatreya, David G. Grier, Sang-Hyuk Lee, David G. Grier, Yohai Roichman, Gi-Ra Yi, Shin-Hyun Kim, Seung-Man Yang, Alfons van Blaaderen, Peter van Oostrum, David G. Grier, Ferréol Soulez, Éric Thiébaud, Loïc Denis, Corinne Fournier, Charles Goepfert, Ke Xiao, Fook Chiong Cheong, Lisa Dixon, David G. Grier, Bo Sun Rémi Dreyfus, and Jesse Amato-Grill. Characterizing and

- tracking single colloidal particles with video holographic microscopy. *Optics Express*, 15(13):13071, 2007.
- [119] Murat Barisik, Selcuk Atalay, Ali Beskok, and Shizhi Qian. Size dependent surface charge properties of silica nanoparticles. *Journal of Physical Chemistry C*, 118(4):1836–1842, 2014.
- [120] Matthew A. Brown, Zareen Abbas, Armin Kleibert, Richard G. Green, Alok Goel, Sylvio May, and Todd M. Squires. Determination of surface potential and electrical double-layer structure at the aqueous electrolyte-nanoparticle interface. *Physical Review X*, 6(1):1–12, 2016.
- [121] Si Han Chen and Sherwin J. Singer. Molecular Dynamics Study of the Electric Double Layer and Nonlinear Spectroscopy at the Amorphous Silica-Water Interface. *Journal of Physical Chemistry B*, 123(29):6364–6384, 2019.
- [122] Y. T.C. Ko, J. P. Huang, and K. W. Yu. The dielectric behaviour of single-shell spherical cells with a dielectric anisotropy in the shell. *Journal of Physics Condensed Matter*, 16(3):499–509, 2004.
- [123] N. V. Brilliantov, V. P. Denisov, and P. L. Krapivsky. Generalized Stokes-Einstein-Debye relation for charged Brownian particles in solution. *Physica A: Statistical Mechanics and its Applications*, 175(2):293–304, 1991.
- [124] Thorsten Köddermann, Ralf Ludwig, and Dietmar Paschek. On the validity of Stokes-Einstein and Stokes-Einstein-Debye relations in ionic liquids and ionic-liquid mixtures. *ChemPhysChem*, 9(13):1851–1858, 2008.
- [125] Marcello Toschi, Federico and Sega. *Flowing Matter*. 2019.
- [126] Vincent Tejedor, Olivier Bénichou, Raphael Voituriez, Ralf Jungmann, Friedrich Simmel, Christine Selhuber-Unkel, Lene B. Oddershede, and Ralf Metzler. Quantitative analysis of single particle trajectories: Mean maximal excursion method. *Biophysical Journal*, 98(7):1364–1372, 2010.
- [127] Xavier Michalet. Mean square displacement analysis of single-particle trajectories with localization error: Brownian motion in an isotropic medium. *Physical Review E - Statistical, Nonlinear, and Soft Matter Physics*, 82(4):1–13, 2010.
- [128] Morikazu Toda. On the Theory of the Brownian Motion. *Journal of the Physical Society of Japan*, 13(11):1266–1280, 1958.
- [129] Charles Hagwood, Yudaya Sivathanu, and George Mulholland. The DMA Transfer Function with Brownian Motion a Trajectory/Monte-Carlo Approach. *Aerosol Science and Technology*, 30(1):40–61, 1999.
- [130] Jim C. Chen and Albert S. Kim. Brownian dynamics, molecular dynamics, and monte carlo modeling of colloidal systems. *Advances in Colloid and Interface Science*, 112(1-3):159–173, 2004.

- [131] R. H. Köhler, P. Schwille, W. W. Webb, and M. R. Hanson. Active protein transport through plastid tubules: Velocity quantified by fluorescence correlation spectroscopy. *Journal of Cell Science*, 113(22):3921–3930, 2000.
- [132] Oleg Krichevsky and Grégoire Bonnet. Fluorescence correlation spectroscopy : the technique. *Review of Modern Physics*, 65:251–297, 2002.
- [133] Mahdi Mazaheri, Jens Ehrig, Alexey Shkarin, Vasily Ziburdaev, and Vahid Sandoghdar. Ultrahigh-Speed Imaging of Rotational Diffusion on a Lipid Bilayer. *Nano Letters*, 20(10):7213–7219, 2020.
- [134] Gary L. Hunter, Kazem V. Edmond, Mark T. Elsesser, and Eric R. Weeks. Tracking rotational diffusion of colloidal clusters. *Optics Express*, 19(18):17189, 2011.
- [135] Y. Han, A. M. Alsayed, M. Nobili, J. Zhang, T. C. Lubensky, and A. G. Yodh. Brownian motion of an ellipsoid. *Optics InfoBase Conference Papers*, (October):626–631, 2006.
- [136] Fook C. Cheong and David G. Grier. Rotational and translational diffusion of copper oxide nanorods measured with holographic video microscopy. *Optics Express*, 18(7):6555, 2010.
- [137] Lehui Xiao, Yanxia Qiao, Yan He, and Edward S. Yeung. Imaging translational and rotational diffusion of single anisotropic nanoparticles with planar illumination microscopy. *Journal of the American Chemical Society*, 133(27):10638–10645, 2011.
- [138] Philipp Kukura, Helge Ewers, Christian Müller, Alois Renn, Ari Helenius, and Vahid Sandoghdar. High-speed nanoscopic tracking of the position and orientation of a single virus. *Nature Methods*, 6(12):923–927, 2009.
- [139] S. Moriwaki, H. Sakaida, T. Yuzawa, and N. Mio. Measurement of the residual birefringence of interferential mirrors using Fabry-Perot cavity. *Applied Physics B: Lasers and Optics*, 65(3):347–350, 1997.
- [140] F. Brandi, F. Della Valle, A. M. De Riva, P. Micossi, F. Perrone, C. Rizzo, G. Ruoso, and G. Zavattini. Measurement of the phase anisotropy of very high reflectivity interferential mirrors. *Applied Physics B: Lasers and Optics*, 65(3):351–355, 1997.
- [141] Hanno S Kaupp. *Coupling Nitrogen-Vacancy Centers in Diamond to Fiber-based Fabry-Pérot Microcavities*. Dissertation, Ludwig-Maximilians-Universität München, 2017.
- [142] Jonathan Körber. *Fabrication and characterization of optimized surface shapes for optical micro mirrors with multi-pulse CO2 laser machining*. Bachelorarbeit, Karlsruher Institut für Technologie, 2018.
- [143] Šmul Abramovič Furman and A. V. Tichonravov. *Basics of optics of multilayer systems*. Ed. Frontieres, 1992.
- [144] Julian Schaal. *Charakterisierung eines faserbasierten, silanisierten optischen Resonators mit hoher Finesse Bachelorarbeit von*. Bachelorarbeit, Karlsruhe Institute of Technology, 2018.

- [145] Johannes F. S. Brachmann, Hanno Kaupp, Theodor W. Hänsch, and David Hunger. Photothermal effects in ultra-precisely stabilized tunable microcavities. *Optics Express*, 24(18):21205, 2016.
- [146] Gurpreet Kaur Gulati, Hiroki Takahashi, Nina Podoliak, Peter Horak, and Matthias Keller. Fiber cavities with integrated mode matching optics. *Scientific Reports*, 7(1):1–6, 2017.
- [147] J. Gallego, S. Ghosh, S. K. Alavi, W. Alt, M. Martinez-Dorantes, D. Meschede, and L. Ratschbacher. High-finesse fiber Fabry–Perot cavities: stabilization and mode matching analysis. *Applied Physics B: Lasers and Optics*, 122(3):1–14, 2016.
- [148] Jasmin Häberle. *Cavity-enhanced homodyne detection for sensing of individual nanosystems*. Bachelorarbeit, Karlsruhe Institute of Technology, 2020.
- [149] Shalom Palkhivala. *Active Cavity Stabilisation for Nanosensing in a Microfluidic Environment*. Master’s thesis, Karlsruhe Institute of Technology, 2021.
- [150] Marie Wahlgren and Thomas Arnebrant. Marie Wahlgren and Thomas Arnebrant. *Scanning*, 9(June):201–208, 1991.
- [151] Jeong Wong and Chih Ming Ho. Surface molecular property modifications for poly(dimethylsiloxane) (PDMS) based microfluidic devices. *Microfluidics and Nanofluidics*, 7(3):291–306, 2009.
- [152] Julia Benedikter, Thomas Hümmer, Matthias Mader, Benedikt Schlederer, Jakob Reichel, Theodor W. Hansch, and David Hunger. Transverse-mode coupling and diffraction loss in tunable Fabry–Pérot microcavities. *New Journal of Physics*, 17(5), 2015.
- [153] Morgan Advanced Materials. [www.morgantechincalceramics.com](http://www.morgantechincalceramics.com), 2021.
- [154] F. R. Kroeger and C. A. Swenson. Absolute linear thermal-expansion measurements on copper and aluminum from 5 to 320 K. *Journal of Applied Physics*, 48(3):853–864, 1977.
- [155] Jiangang Zhu, Sahin Kaya Ozdemir, Yun Feng Xiao, Lin Li, Lina He, Da Ren Chen, and Lan Yang. On-chip single nanoparticle detection and sizing by mode splitting in an ultrahigh-Q microresonator. *Nature Photonics*, 4(1):46–49, 2010.
- [156] Ya Rong Shi, Man Ping Ye, Lu Chao Du, and Yu Xiang Weng. Experimental Determination of Particle Size-Dependent Surface Charge Density for Silica Nanospheres. *Journal of Physical Chemistry C*, 122(41):23764–23771, 2018.
- [157] Benjamin M. Lowe, Chris Kriton Skylaris, and Nicolas G. Green. Acid-base dissociation mechanisms and energetics at the silica-water interface: An activationless process. *Journal of Colloid and Interface Science*, 451:231–244, 2015.
- [158] Prudhvidhar Gaddam and William Ducker. Electrostatic Screening Length in Concentrated Salt Solutions. *Langmuir*, 35(17):5719–5727, 2019.
- [159] Hadi Saboorian-Jooybari and Zhangxin Chen. Calculation of re-defined electrical double layer thickness in symmetrical electrolyte solutions. *Results in Physics*, 15(June):102501, 2019.

- [160] Lukas Neumeier, Romain Quidant, and Darrick E. Chang. Self-induced back-action optical trapping in nanophotonic systems. *New Journal of Physics*, 17(12):123008, 2015.
- [161] Linda Karoline Brützel. *Structure and Conformational Dynamics of 3D DNA Origami Objects Probed by Small-Angle X-Ray Scattering*. Dissertation, Ludwig-Maximilians-Universität München, 2017.
- [162] Venkata R. Dantham, Stephen Holler, Curtis Barbre, David Keng, Vasily Kolchenko, and Stephen Arnold. Label-free detection of single protein using a nanoplasmonic-photonic hybrid microcavity. *Nano Letters*, 13(7):3347–3351, 2013.
- [163] Martin D. Baaske, Matthew R. Foreman, and Frank Vollmer. Single-molecule nucleic acid interactions monitored on a label-free microcavity biosensor platform. *Nature Nanotechnology*, 9(11):933–939, 2014.
- [164] H. Nadgaran and M. Afkhami Garaei. Enhancement of a whispering gallery mode microtoroid resonator by plasmonic triangular gold nanoprism for label-free biosensor applications. *Journal of Applied Physics*, 118(4), 2015.
- [165] Feng Liang, Yuzheng Guo, Shaocong Hou, and Qimin Quan. Photonic-plasmonic hybrid single-molecule nanosensor measures the effect of fluorescent labels on DNA-protein dynamics. *Science Advances*, 3(5):1–10, 2017.
- [166] Eric D. Black. An introduction to Pound–Drever–Hall laser frequency stabilization. *American Journal of Physics*, 69(1):79–87, 2001.
- [167] P. Horak, H. Ritsch, T. Fischer, P. Maunz, T. Puppe, P. W. Pinkse, and G. Rempe. Optical kaleidoscope using a single atom. *Physical Review Letters*, 88(4):436011–436014, 2002.
- [168] Sequence-coated DNA Origami, Verena J Schu, Simon Heidegger, Nadja Sandholzer, Philipp C Nickels, and Nina A Suhartha. Cellular Immunostimulation by CpG- Structures. *ACS Nano.*, 5(12):9696–9702, 2011.
- [169] Taiki Watanabe, Yusuke Sato, Hayato Otaka, Ibuki Kawamata, Satoshi Murata, and Shin Ichiro M. Nomura. DNA origami "quick" refolding inside of a micron-sized compartment. *Molecules*, 25(1):1–10, 2020.
- [170] Binbin Li, Qinghua Li, Jingxin Mo, and Honglian Dai. Drug-loaded polymeric nanoparticles for cancer stem cell targeting. *Frontiers in Pharmacology*, 8(FEB):1–12, 2017.
- [171] Asya Ozkizilcik, Aruna Sharma, Dafin F. Muresanu, José V. Lafuente, Z. Ryan Tian, Ranjana Patnaik, Herbert Mössler, and Hari S. Sharma. Timed release of cerebrolysin using drug-loaded titanate nanospheres reduces brain pathology and improves behavioral functions in Parkinson's disease. *Molecular Neurobiology*, 55(1):359–369, 2018.
- [172] Boyang Hua, Kyu Young Han, Ruobo Zhou, Hajin Kim, Xinghua Shi, Sanjaya C. Abeyesiri-gunawardena, Ankur Jain, Digvijay Singh, Vasudha Aggarwal, Sarah A. Woodson, and Taekjip Ha. An improved surface passivation method for single-molecule studies. *Nature Methods*, 11(12):1233–1236, 2014.

- [173] Jae Hyeon Park, Joshua A. Jackman, Abdul Rahim Ferhan, Gamaliel Junren Ma, Bo Kyeong Yoon, and Nam Joon Cho. Temperature-Induced Denaturation of BSA Protein Molecules for Improved Surface Passivation Coatings. *ACS Applied Materials and Interfaces*, 10(38):32047–32057, 2018.
- [174] Lei Li, Paul M. Jones, and Yiao Tee Hsia. Characterization of a nanometer-thick sputtered polytetrafluoroethylene film. *Applied Surface Science*, 257(9):4478–4485, 2011.
- [175] Thomas Hummer, Jonathan Noe, Matthias S. Hofmann, Theodor W. Hansch, Alexander Hogele, and David Hunger. Cavity-enhanced Raman microscopy of individual carbon nanotubes. *Nature Communications*, 7:1–7, 2016.
- [176] Robert T Sataloff, Michael M Johns, and Karen M Kost. *Laminare Schichtströmungen*.
- [177] Zhongyue Wang, Ning Wang, Dongdong Wang, Zihui Tang, Kehan Yu, and Wei Wei. Method for refractive index measurement of nanoparticles. *Optics Letters*, 39(14):4251, 2014.
- [178] MicroParticles GmbH (August 2020). <https://www.microparticles-shop.de>.
- [179] Hervé Cottet, Jean Philippe Biron, and Michel Martin. Taylor dispersion analysis of mixtures. *Analytical Chemistry*, 79(23):9066–9073, 2007.
- [180] Silvina Cervený, Gustavo A. Schwartz, Jon Otegui, Juan Colmenero, Juliane Loichen, and Stephan Westermann. Dielectric study of hydration water in silica nanoparticles. *Journal of Physical Chemistry C*, 116(45):24340–24349, 2012.
- [181] Dylan F Williams, Tracy S Clement, Paul D Hale, and Andrew Dienstfrey. Terminology for High-Speed Sampling- Oscilloscope Calibration. 2006.
- [182] A. A.P. Trichet, P. R. Dolan, D. James, G. M. Hughes, C. Vallance, and J. M. Smith. Nanoparticle Trapping and Characterization Using Open Microcavities. *Nano Letters*, 16(10):6172–6177, 2016.

# Danksagung

Zu guter Letzt möchte ich noch Danke sagen...

Erst einmal bin ich total dankbar, dass ich 4 ½ Jahre die Gelegenheit bekommen habe, auf einem Thema zu forschen, welches bei der Grundlagenforschung einzuordnen ist und in mir eine große Begeisterung und Leidenschaft hervorgerufen hat. Andererseits bin ich den Leuten dankbar, die mich in dieser spannenden Zeit begleitet haben.

Hier ist zuallererst mein Doktorvater Prof. David Hunger zu nennen, der mindestens genauso viel Begeisterung für dieses Thema hatte und mir stets mit viel Optimismus und wertvollen Tipps zur Seite gestanden hat. Ebenso möchte ich meinem Zweitbetreuer Prof. Heinz Kalt danken. Er war stets interessiert an dem Fortschritt meiner Arbeit und stand mir für die eine oder andere Diskussion zu Verfügung.

Den ersten Teil meiner Promotion habe ich in der Münchner Gruppe an der LMU verbracht. Hier möchte ich Matthias Mader danken, der mich anfangs betreut hat, um mich in das mir noch fremde Themengebiet einzuführen und mir seine vorangegangenen ersten Schritte für eine integrierte Fabry-Pérot Cavity in einen Mikrofluidikkanal zu zeigen. Schließlich konnte ich aus den damals aufgetretenen Problemen lernen und so schneller einen neuen, verbesserten Sensor entwickeln. Ebenfalls erinnere ich mich sehr gerne an Thomas Hümmer, Bernardo Casabone, Julia Benedikter und Christian Gebhardt zurück. Die gemeinsamen Kletteraktionen, Radeltouren nach Garching, das Baden in der Isar oder sonstige Freizeitgestaltungen haben meine Zeit in München sehr bereichert. Danke dafür!

Nun ist natürlich auch noch meine Gruppe in Karlsruhe zu erwähnen. Anfangs waren David und ich in Karlsruhe alleine, aber mit der Zeit hat sich die Gruppe deutlich vergrößert und es ist dabei ein richtig cooler „Haufen“ entstanden, mit dem ich viel Spaß hatte. Leute ihr seid zu viele, um euch alle namentlich zu nennen. Daher beschränke ich das auf die länger Beständigen in der Gruppe (Timon Eichhorn, Evgenij Vasilenko, Jonas Grammel, Maximilian Pallmann, Sören Bieling und Jannis Hessenauer) und auf diejenigen, die ich direkt betreuen durfte (Julian Schaal, Jasmin Häberle und Shalom Palkhivala). Mit den auch nicht namentlich genannten Leuten in der Gruppe entstanden lebhaftige Diskussionen über politische und sozialkritische Themen, sportliche Aktionen wie gemeinsames Volleyball spielen, Langlaufen, Wandern, Radeln oder Schwimmen. Selbst musikalisch konnte man uns nicht bremsen-danke für diese spaßigen Abende an der alljährlichen PHI-Weihnachtsfeier! Vielleicht werde ich ja nochmal eingeladen. Der Höhepunkt war für mich mein 30. Geburtstag, den ihr alle zu einem wahnsinnig witzigen und ausgelassen Abend mitgestaltet habt. Von diesem Abend konnte ich noch lange Zeit zehren im Corona Lockdown. (David ich hoffe du bist mir nicht böse, dass darunter die Bürostühle ein bisschen gelitten haben.) Ein besonderes Augenmerk möchte ich in unserer Gruppe darauf legen, dass auch in fachlicher Hinsicht ein enges Miteinander herrscht. So ist unser Arbeitsalltag durch gegenseitige Hilfestellungen dominiert ohne jegliches Konkurrenzdenken. Das ist nicht in jeder Arbeitsgruppe so der Fall, weshalb ich das immer sehr geschätzt habe.

Weiterhin möchte ich mich bei Andreas Wickberg, Martin Schumann und Christian Kern aus der Wegener Gruppe bedanken. Andreas hat für mich Silanisierungstests am dielektrischen Spiegel durchgeführt. Für das direkte Laserschreiben des Mikrofluidikkanals in ein Polymer stand mir für die ersten Schritte Martin zur Seite und nachdem er das Institut verlassen hatte, hat Christian die gemeinsame Kollaboration übernommen. Vielen Dank euch beiden, für euren wertvollen Beitrag zu meinem ersten funktionierenden Sensoraufbau. Hier auch ein Dank an Prof. Martin Wegener, dass Sie diese Kollaboration unterstützt haben.

Außerdem möchte ich mich noch bei Heino Besser bedanken, der mir im Rahmen der KNMF Löcher mit einem Femtosekundenlaser in die Ferrule geschossen und so eine zweite Version des Mikrofluidikkanals ermöglicht hat. In diesem Zuge möchte ich mich auch bei Georg Gramlich vom IHE bedanken. Dieser hat für mich erfolgreich getestet, ob die Mikrofluidiklöcher in der Ferrule auch mit einem Laserschneidegerät hergestellt werden können. Bei Antonia Eckert aus der Nienhaus Gruppe möchte ich mich bedanken, dass sie mit mir ihre Erfahrungen im Bereich Fluoreszenzkorrelationspektroskopie und bei sonstigen „Biothemen“ geteilt hat. Ein Dank geht auch an Lucas Radtke für das Schneiden des Keils in die Ferrule und an Patrice Brenner für die durchgeführten SEM Messungen.

Zudem möchte ich mich bei dem gesamten physikalischen Institut bedanken. Die Institutsausflüge und Weihnachtsfeiern waren stets ein soziales Miteinander zwischen Profs, (PhD-) Studenten und Mitarbeitern. Bedanken möchte ich mich speziell bei der AG Ustinov, dass ich anfangs bei euch immer Kaffee trinken durfte, bevor wir in der eigenen Gruppe eine Kaffeemaschine hatten und dass mich Jan Brehm und Steffen Schlör mit in ihr Büro aufgenommen haben, als bei uns in der Gruppe Platzmangel herrschte. Ein besonderer Dank geht auch an die Feinmechanik- und Elektronikwerkstatt. Durch eure kompetenten Hilfestellungen (v.a. Michael Meyer, Roland Jehle und Jannis Ret) kam ich immer sehr schnell zu praktischen Lösungen, was meinen Sensoraufbau oder aufkommende elektronische Probleme betroffen hat. Auch möchte ich mich bei Claudia Alaya und Steffi Baatz für stets schnelle und unkomplizierte Abwicklungen im Sekretariat bedanken, Kornelia Hügler für Hilfestellungen bei Chemiebedarf und Lars Behrens für die anfänglich IT-Unterstützung beim Aufbau der Büro- und Laborinfrastruktur. Ebenso möchte ich mich bei Richard Gebauer bedanken, der uns (Julian und mir) bezüglich FPGAs geholfen hat. Bedanken möchte ich mich bei Freunden wie Alexander Bilmes, Jan Brehm, Sebastian Schulz und Felix Hahl, mit denen ich mich, da alle Physiker, auch über fachliche Themen austauschen konnte.

Zu guter Letzt geht noch ein großer Dank an meine super Familie. Meiner Mutter möchte ich danken, da sie mich von jungen Jahren an in jeglicher Hinsicht gefördert hat. Ihr habe ich es zu verdanken, dass ich am liebsten alle Hobbies und Handwerkertätigkeiten dieser Welt erlernen möchte. Meinem Vater möchte ich für das Erwecken meiner Neugierde zur Physik danken. Schon in frühen Jahren habe ich so Fragen gestellt bekommen, wie zum Beispiel warum der Regenbogen verschiedene Farben hat, warum die Weihnachtsmühle bei angezündeten Kerzen sich dreht, oder warum der Teelöffel über einer Kerze schwarz wird. Zwar habe ich dabei öfters meine Augen verdreht, aber schließlich habe ich trotz des Abratens ("Überlege es dir gut, das Physikstudium ist kein Zuckerschlecken") das Physikstudium begonnen. Dann sind da noch meine lieben Schwestern Carmen und Daria. Wie auch meine Eltern und meine (Zukunfts-) Schwager Daniel und Maximilian, sind meine Schwestern immer für mich da, wenn einmal

Probleme auftreten. Danke für eure Unterstützung und Beratung! Danke auch Daria, dass du mir den Weg am Anfang des Studiums geebnet hast, indem du mir bei den ersten Übungsblättern in der theoretischen Physik geholfen hast. Meinen zukünftigen Schwiegereltern möchte ich danken, dass sie in der Endphase meiner Promotion viel Verständnis aufgebracht haben und mir auch sonst sehr ans Herz gewachsen und mir emotional eine Stütze sind. Dann zum Abschluss wäre da noch mein Partner Robert. Ich nenne ihn „der Fels in der Brandung“. Robert, du stehst mir immer liebevoll zur Seite und bereicherst mein Leben in allen Facetten sowohl als Freund als auch als Partner. Ich bin froh, dass wir uns während des Studiums gefunden haben und dass sich zwischen uns so ein tiefes Vertrauen aufgebaut hat. Während der Promotion hast du es die ganze Zeit geschafft mich zu erden, sodass ich, wenn mal etwas nicht funktioniert hat, sehr entspannt damit umgehen konnte. Einen riesen Dank dafür! Danke auch, dass du mir bei physikalischen Problemstellungen als Diskussionspartner zur Seite stehst. Sorry für die angespannte Phase in den letzten zwei Monaten meiner Promotion und danke, dass du das mit ertragen hast :\* .

Vielen lieben Dank euch allen!